A Structural Study of Host-Guest Chemistry in Zeolites

A thesis submitted for the degree of Doctor of Philosophy

in Inorganic Chemistry

Tsz Woon Benedict Lo

St John's College

Hilary Term 2017

Declaration

I confirm that this is my own work and the use of all material from other sources has been properly and fully acknowledged.

Tsz Woon Benedict Lo

Dedication

To my parents.

Abstract

The conversion of crude gas and oil into platform chemicals like olefins and aromatics is essential for the syntheses of numerous polymer materials and commodity chemicals that have played a key role in the activity of mankind since the turn of the last century. In the future, it is likely that concerns over the widespread use of fossil fuels will require the switch to alternative feedstocks such as biomass.

In both cases conversion to platform chemicals is carried out using catalysts, often based on zeolites. These porous materials possess an inherent acidity caused by the presence of both Lewis (LAS) and Brønsted acid sites (BAS), in addition to shape and size selective adsorption from internal channels and pore mouths. These properties make them great candidates for catalysis reactions. The chemistry is far from simple, however, with zeolites catalysing many reactions of hydrocarbons, such as isomerisation, oligomerisation, alkylation and cracking, to name but a few.

This thesis therefore focuses on elucidating the structural chemistry associated with the BAS chemistry of zeolites. Using high-resolution synchrotron powder X-ray diffraction (SXRD) as the primary characterisation technique, we propose a novel methodology for understanding the molecular chemistry in zeolites (with H-ZSM-5 as an illustration) from the structural perspective, which is discussed in a systematic manner.

The fundamentals, and the structure and acidity characterisation techniques of zeolites are introduced in Chapter 1. The procedures of the experimental and theoretical studies used in this thesis are provided in Chapter 2.

Chapter 3 investigates a microporous H-ZSM-5 that hosts pyridine, methanol and ammonia as guest molecules for the elucidation of their adsorption geometries and interactions with the BAS. By carefully studying the interatomic distances and angles, the locations of the BAS are identified at the framework T6 and O18 sites. More interestingly, in the case of ammonia in H-ZSM-5, the storage capability and sorption kinetics are reported in Chapter 4.

Consequently, based on the structural understanding of the BAS of H-ZSM-5, Chapter 5 reports the rational design of a novel biomass conversion reaction from biomass-derived furan and ethanol to aromatics. The use of liquid ethanol instead of high-pressure gaseous ethylene as the source of dienophile in this one-pot synthesis makes the aromatics production much simpler and renewable. The key facilitating step is studied accordingly by experimental and theoretical techniques.

Chapter 6 demonstrates a study of the mechanism of an industrially important catalytic process. By monitoring the catalytic conversion of methanol using *operando* SXRD, we demonstrate *for the first time*, that the concerted associative mechanism is responsible for dimethyl ether production via an activated protonated methanol intermediate species over H-ZSM-5 in an early stage of the reaction at 200 °C. The minor contribution from the dissociative mechanism of the adsorbed methoxy intermediate species at the BAS, renders their accumulation during the late stage of reaction. The accumulation of the methoxy species leads to a build-up of the 'hydrocarbon pool' and eventually to 'carbon' through C-C bonds formation.

Acknowledgements

First I would like to express my deep gratitude to Prof Edman Tsang for his continuous guidance and inspiration throughout my Part II and DPhil over the last four and half years. His ideas are truly inspiring, and without his advice and support, it would have been nearly impossible to reach this stage I am. Equally importantly, I wish to thank Prof Chiu Tang who offers me support and unlimited technical guidance. Not only his incredible expertise in synchrotron X-ray powder diffraction, but also his kindness and cooking skill will always motivate me.

Many thanks to everyone in the Tsang group, to make me feel extremely comfortable in the lab and office. A special thank you to Lin for spending days-and-nights with me in figuring out all the work from scratch. A deep gratitude to Ivo for the amazing discussion that we spent on the DA project and design. A notable thank you to Will for physically supporting me in the gym. To Ian, Harry and Josh for their generous proof-reading. To the others of the Tsang group, Linda, Aaron, Ieuan, Pu, Hannah, Lizzie, Molly, Yusuke, Simon, Bin, Simson, and every member of the group, thank you for all the time that we spent together.

Many thanks to all the beamline staff at beamline I11, for all the valuable guidance and support from such a world-class facility. A thank you to Claire for teaching me essentially everything in Diamond. Not to mention Jonathan, the magician at I11, who makes everything perfect. To the others of I11, Sarah, Annabelle, Steve, Anna, Chris, and every member of the group, for all fun time in the conferences that we attended together!

Also, I would like to thank EPSRC (UK) and Diamond Light Source (UK) for the funding of my DPhil studentship.

Last but not least, I wish to express my deepest gratitude to my family and Winky for their endless love and support.

List of Abbreviations

2,5-dimethylfuran (DMF)

Ab initio molecular dynamics (AIMD)

Brønsted acid sites (BAS)

Brunauer, Emmett and Teller (BET)

Covalent-organic-framework (COF)

Cross polarisation magic angle spinning solid state nuclear magnetic resonance (CP MAS ssNMR)

Crystallographic information file (CIF)

Density functional theory (DFT)

Diels-Alder (DA)

Extra-framework aluminium (EFAl)

Flame ionisation detector (FID)

Fluid catalytic cracking (FCC)

Fourier transformed – infrared (FT-IR)

Gas chromatography-mass spectrometry (GC-MS)

Inductive coupled plasma atomic emission spectroscopy (ICP-AES)

Intrinsic reaction coordinate (IRC)

Isotropic displacement factors (B_{eq})

Metal-organic-framework (MOF)

Methanol-to-olefins (MTO)

Molecular mechanics (MM)

Multi-analyser crystals (MAC)

Neutron diffraction (ND)

Our own N-layered integrated molecular orbital (ONIOM)

Potential energy surface (PES)

Proton affinities (PA)

Quantum mechanics (QM)

Scanning electron microscopy (SEM)

Site occupancy factor (SOF)

Synchrotron powder X-ray diffraction (SXRD)

Thermogravimetric analysis (TGA)

Transmission electron microscopy (TEM)

Trimethylphosphine (TMP)

Zero-point energy (ZPE)

Table of Contents

Chapter 1. Introduction

The fundamentals, structure and acidity characterisation techniques of zeolites are introduced in this chapter.

1.1 Zeolites

1.1.1 What and Why?

Silicate in origin, zeolites occur naturally or can be synthesised commercially. As of July 2015, there are 229 unique zeolite frameworks, including two recently identified by Corma et al.: ITQ-54[1] and ITQ-40[2]. The most value-added application of zeolites is in the petroleum refining and catalysis industries. Zeolites are composed of TO_4 (where T = Si or Al) interconnecting tetrahedra via the corner O atoms. The tetrahedra form distinct 3-D structures dependent on synthesis, substrate composition and reaction conditions.

Naturally occurring zeolites are of limited value in catalysis for various reasons. In contrast, synthetic zeolites are more valuable and exploited in numerous areas. The most commercially important ones are: A (a commercial drying and gas separation agent), X and Y (mainly used in fluid catalytic cracking (FCC)) and ZSM-5 (important for xylene isomerisation, disproportionation of toluene, production of crude-oil-derived hydrocarbons, such as the methanol-to-hydrocarbons (MTH), methanol-to-gasoline (MTG) and methanol-to-aromatics (MTA)).[3,4]

Zeolites are microporous materials that possess pores (or channels) ranging from 3 Å (zeolite A) to 13 Å (zeolite Y), see Figure 1.1. Aside from the difference in the pore sizes, the pore shapes are also dramatically different from each other. For example, ZSM-5

zeolite which adopts the MFI framework is built upon many pentasil units, resulting in interconnecting straight (5.6 Å × 5.3 Å) and sinusoidal (5.5 Å × 5.1 Å) channels. But zeolites X and Y which adopt the Faujasite structure are built upon sodalite units. This results in supercages interconnecting with channels (13 Å and 7.4 Å in diameter, respectively). During most zeolite catalysed reactions, a combination of the inherent zeolitic acidity, intrinsic shape and size selectivity[5], and mass transport effects[6] significantly alters the product distribution.

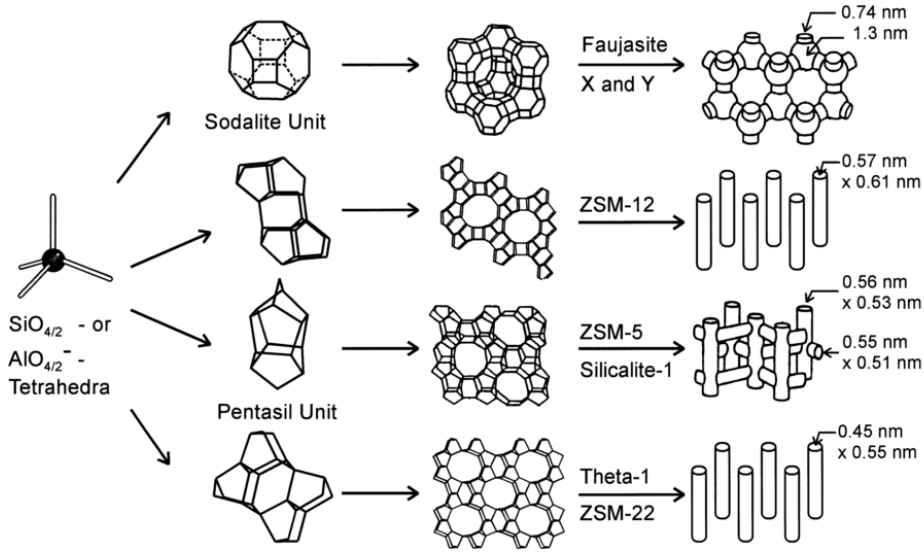

Figure 1.1. Various structures and physical properties of some common zeolites.[7] the vertices in the structure represent the T atoms (where T = Si or Al), whereas the lines between the vertices represent the bridging O atoms. The O atoms are not shown for clarity.

Zeolite ZSM-5 is used as an illustration in this thesis for the structural study of the chemistry in zeolites. The crystal structure was determined using single-crystal X-ray diffraction (XRD) by van Koningsveld in 1990.[8] ZSM-5 has an orthorhombic crystal system and the space group symmetry of *Pnma* (equivalents to a total of 8 special positions in a unit cell). The crystal structure of ZSM-5 contains 12 T and 26 O sites. Hence, its chemical formula is $Na_nAl_nSi_{96-n}O_{192}$ (for the Na^+-exchanged form). As seen in Figure 1.2, the straight channel can clearly be seen.

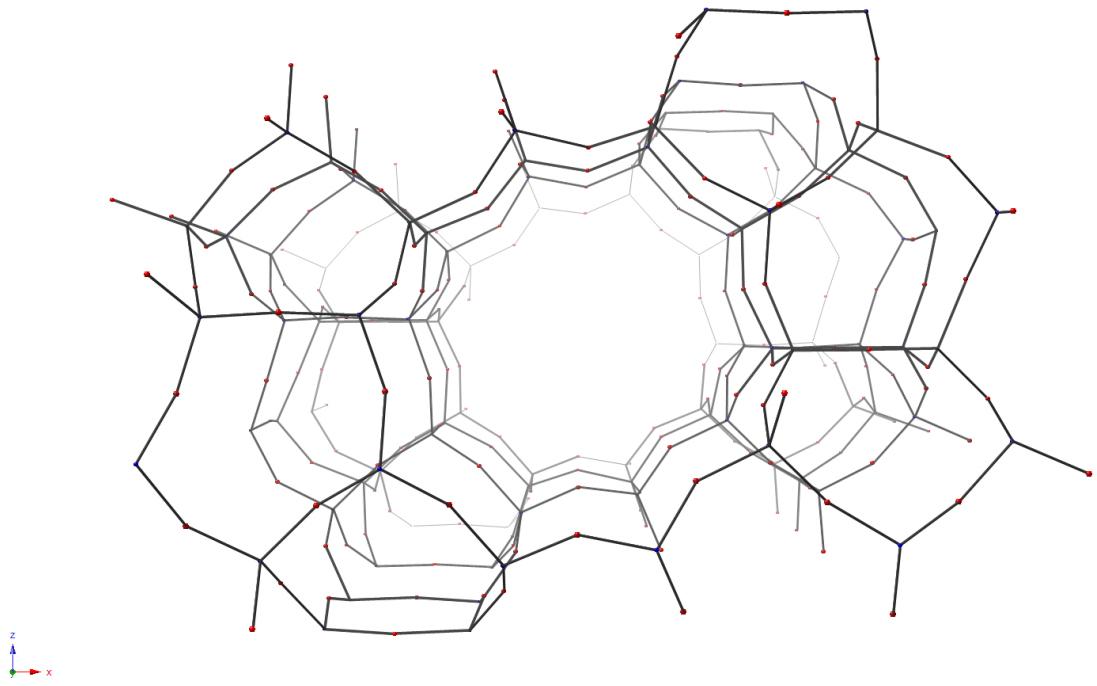

Figure 1.2. Published crystal structure of H-ZSM-5 by von Koningsveld[9], showing a unit cell viewing from the [010] (straight channel). Atoms are presented using the stick model.

Zeolites can also soften water in domestic and commercial applications (see Figure 1.3). In an ion-exchange water softener, hard water (i.e., Ca^{2+} and Mg^{2+} rich) exchange with Na^{+}-containing zeolites in a column. This makes the water 'softer' by removing the 'harder' metal cations (at the expense of more Na^{+}). Zeolites are also present in commercial detergents to remove the water 'hardness'.

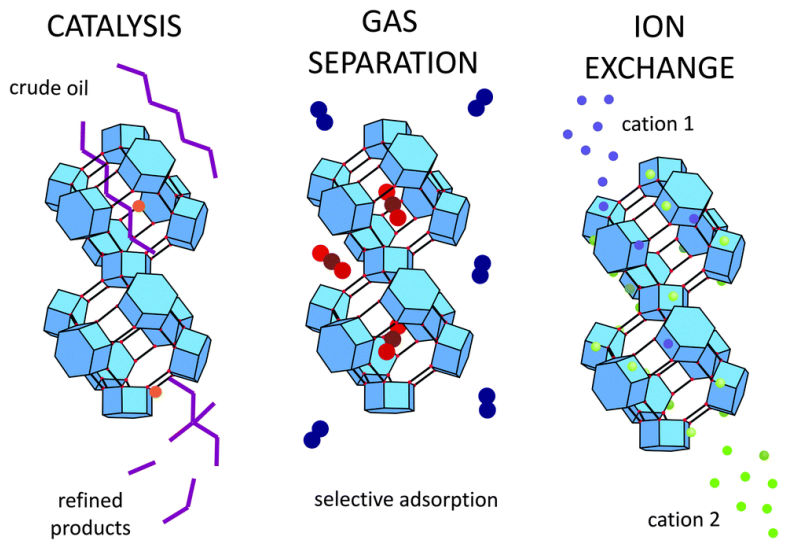

Figure 1.3. The most common applications of zeolites, namely catalysis, gas separation, and ion-exchange.[10]

1.1.2 Applications in Modern Catalysis

The petrochemical industry is playing a crucial role in the global economy and lifestyle of mankind. For example, the direct consumption of fossil fuels accounts for more than 80% of total energy consumption worldwide.[11] The petrochemical derivative products, i.e., commodity chemicals and polymer materials, are also of great importance. In fact, most of these processes involve the use of zeolite catalysts. The wide application of zeolite catalysts in industry is due to their unique framework structures and tuneable acid-base properties.

The earliest application of zeolites in catalysis was by Mobil during the early 1960s. They converted long-chain petroleum into shorter chain hydrocarbons such as gasoline using zeolite X (see Scheme 1.1 for the schematic of the FCC process). It was then found that rare earth metal ion-exchanged zeolites X and Y can increase the hydrothermal stability and improve their catalytic properties. Later in the 1970s, dealuminated zeolite Y, USY (Ultra-Stable Y), was made and found to produce gasoline with higher octane rating.[12] With further optimisation, USY with ion-exchanged rare earth metal ions is the major component nowadays for the FCC process.[12]

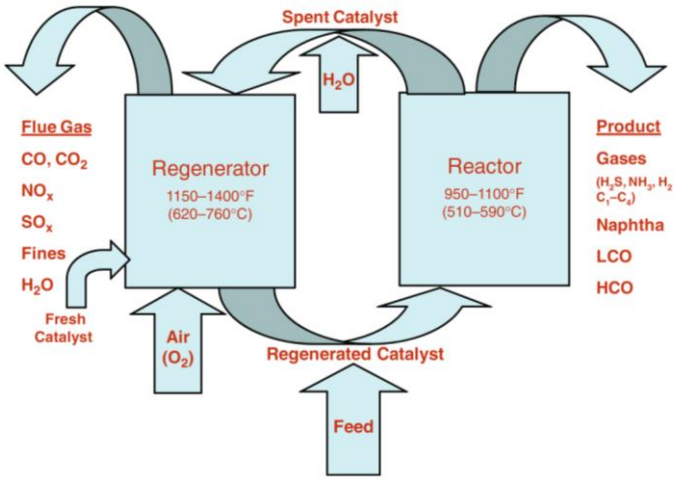

Scheme 1.1. Schematic of the fluid catalytic cracking (FCC) process.[12]

Following the success in FCC of long-chain hydrocarbons, many petrochemical companies have focused on the development and application of new zeolites. The most prominent example is high-silica ZSM-5, which is found to be applicable in many catalysis reactions, such as xylene isomerisation, MTA, and MTG.[12] Later in 2010, Dalian Institute of Chemical Physics (China) successfully developed the coal-to-olefins technology (via MTO) and built an industrial plant over SAPO-34 zeolite.[13]

At present, researchers are still actively developing new zeolites, as well as new applications using existing/modified zeolites. For example, various forms of zeolites are used to mimic the special atomic and spatial arrangements in enzymes; Cu-exchanged ZSM-5 and mordenite are receiving great attention in the selective oxidation of methane.[14–16]

1.1.3 Applications in Gas Separation and/or Storage

Due to the well-defined molecular-sized pores, high-porosity, high-thermal and chemical stability and intrinsic acidities, zeolites are widely used for gas separation, and are a potential candidate for gas storage.

Their gas separation properties are summarised as follows: [17]

(i) Size exclusion – direct molecular sieving, when the kinetic diameters of one gas are greater than the pore, e.g., the separation of H_2 from *i*-butane using DD3R zeolite membrane.[18]

(ii) Diffusion selectivity – when the smaller gas diffuses much faster than the larger gas, with respect to the corresponding kinetic diameters. This effect increases at elevated temperatures due to faster diffusion kinetics. Many 8-membered-ring zeolite membranes are effective in separating H_2 from CH_4.[19]

(iii) Adsorption strengths – the basicities of gas molecules are noticeably different, and can easily be distinguished by acid-base interactions with the acid sites in zeolites. For instance, Venna and Carreon have recently engineered zeolite ZIF-8 for the separation of CO_2 and CH_4.[20]

For gas storage capabilities in zeolites, the latest research has focused on how to effectively store functional gases that are mostly related to energy supply and storage. During the 1990s, when hydrogen storage was proposed as a viable alternative for mobile energy provision, zeolites have been considered a candidate with high potential for storing hydrogen. Ernst et al. first investigated extensively the chemistry of hydrogen storage in various zeolites.[21] Yaghi et al. designed a zeolite-like metal-

organic-framework (MOF) material, MOF-5, with improved hydrogen storage properties.[22] Yildirim et al. investigated another MOF material, ZIF-8, whereas Mokaya et al. studied microporous carbon synthesised by a zeolite templating method.[23–25]

Another great example is ammonia storage in zeolites. Aside from the extensive use of ammonia as a fertiliser precursor chemical, ammonia is a possible carbon-free fuel candidate. This offers exciting potential for ammonia to be used in energy storage with higher energy density than liquid hydrogen.[26,27] Recently, zeolites[26], covalent-organic-frameworks (COFs)[27], and MOFs[28] are used to store ammonia. These materials show great ammonia storage properties by using the Lewis (LAS) or Brønsted acid sites (BAS) to interact with the basic ammonia molecules. It has been postulated that the ammonia molecules are interconnected via their H moieties by a forming H-bonding network, hence behaving as a 'liquid' inside zeolites.[29] However, the highest ammonia uptake (15 mmol g^{-1}) achieved to date is still not satisfactory for industrial requirements. At the ammonia release stage, some ammonia may be released under low energy input condition, but some may need high temperature without clear rationale.

1.2 Acid Sites

The unique chemical/physical properties of zeolites in adsorption, gas separation and, catalysis, are caused by their microporous framework structures and inherent surface Brønsted and/or Lewis acidities.

1.2.1 Brønsted Acid Sites (BAS)

Zeolites are aluminosilicate compounds. When tetravalent Si(IV) is substituted with trivalent Al(III), the substitution creates charge imbalance that is compensated by cations (e.g., H^+ and Na^+). In the H^+-form, a H^+ moves close to the substituted Al atom to form a BAS. In principle, this H^+ can be populated on either one of the four O atoms bonded to each framework-Al site, as demonstrated in the early work by Haag et al. (see Figure 1.4).[30] However, these substituted sites are found to be synthesis condition dependent, where control measures like the use of organic templates, have been employed to alter the location of substitution sites.[31–34]

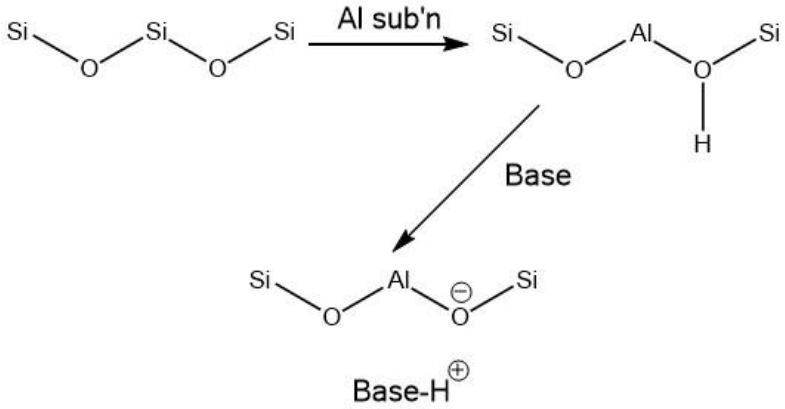

Figure 1.4. The Brønsted acid sites (BAS) in zeolites, and the formation of an acid-base adduct with a Brønsted basic molecule.

The strengths of the BAS are drastically different in various forms of zeolites. The BAS catalyses many reactions, such as hydrocarbon cracking and isomerisation, and methanol conversion reactions (to olefins, aromatics, or gasoline).[35,36] The BAS have intrinsic acid strengths defined by their ability to interact with Brønsted base molecules, but their strengths differ according to the chemical composition and framework structure. In addition, the location of the substituted Al also plays a role in determining the Brønsted acidity.[7,30] But neither the Al location nor the Al distribution within the zeolite framework is random or controlled by simple theoretical rules. The Al location and distribution instead depend on the conditions of the zeolite synthesis.[37,38] Meanwhile, the acidity depends on the location, distribution, and bonding geometry (bond length and angle) of the Al with respect to the framework.[39,40] Hence, the location of the BAS is extremely crucial to the understanding the chemistry of zeolites.

1.2.2 Lewis Acid Sites (LAS)

The LAS are well known to be generated from (i) the dehydration of the BAS at high temperature (Scheme 1.2) and (ii) mild steaming of zeolites leading to the dislodging of the framework-Al (where the extra-framework-Al (EFAl) species are Lewis acidic):

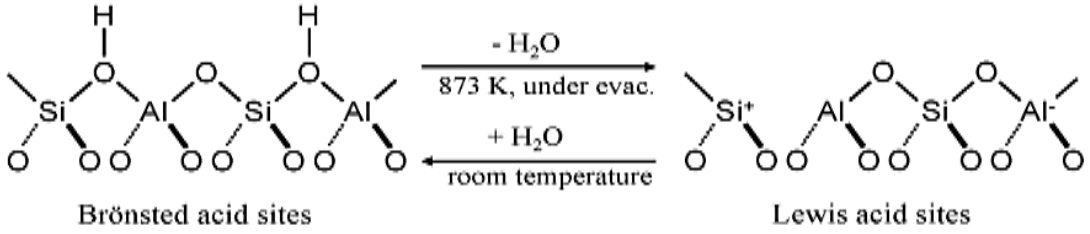

Scheme 1.2. The formation schematics of framework Lewis acid sites (LAS) from BAS.[41]

By definition, a LAS is a site that accepts a lone pair of electrons. As shown in Scheme 1.2, upon dehydration, the vacant Si^{+} moiety does not carry any Lewis acidity; rather, the vacant Al moiety now has an empty orbital which accepts a pair of electrons. Whereas for EFAl that has high charge density (which exists in the form of $Al(OH)_3$ or $AlOH^{2+}$, usually generated from the steaming process or directly from synthesis 'defects'), it acts as a LAS naturally. Moreover, coordination of the EFAl species to the O atom(s) adjacent to the framework-Al enhances the Brønsted acidity of dealuminated zeolites, which is called the BAS/LAS synergy (see Figure 1.5).[42] Equally, the LAS are broadly applied in adsorption, catalysis, gas sensing, etc.

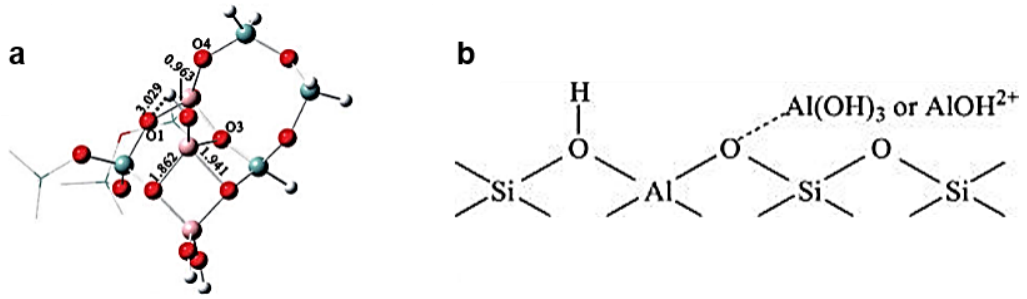

Figure 1.5. (**a**) The optimised geometries for the BAS/LAS synergy, obtained from 9T cluster density functional theory (DFT) calculation; (**b**) the corresponding schematic.[42]

This thesis will however mainly focus on the discussion of the catalysis chemistry related to the BAS. To adequately understand how the BAS and LAS govern the catalysis chemistry, it is extremely important to understand their nature, strength and concentration, as well as precise location.

1.3 Traditional Characterisation of BAS

In this section, four traditional characterisation techniques for BAS will be introduced.

1.3.1 Fourier Transformed-Infrared (FT-IR) spectroscopy

FT-IR is commonly used to directly measure the strength of the BAS in zeolites. FT-IR is an absorption spectroscopy based technique. As different molecules possess different bond energies, the FT-IR measures the frequency of the absorbed radiation that matches with the various transition energies of a bond, e.g., bond vibration and bending. In addition, these energies vary with different atomic masses, molecular potential energy surfaces and vibronic coupling.

In fact, FT-IR spectroscopy is the most basic identification tool for any fundamental study of BAS and LAS. There are two ways that are commonly used to compare with literature, namely (i) direct measurement of the O-H stretching frequencies (for the H-forms) and (ii) measurement of the stretching frequencies between the interaction of the framework zeolites and probing molecules, such as pyridine and ammonia. In this thesis, pyridine probed FT-IR spectroscopy has been used to identify the interactions between the acid sites and pyridine, where the corresponding modes have been well assigned in previous literature.[43–46]

1.3.2 Thermogravimetric Analysis (TGA)

TGA is a simple and direct thermal analysis technique, which measures the amount and rate of change in the weight of a sample is measured as a function of temperature or time. Any weight change by effects such as oxidation, reduction, desorption, and decomposition can be observed in the TGA. This can predict the thermal stability of a material at elevated temperatures. Upon heating, any adsorbed molecules on zeolites, such as water and ammonia, desorb accordingly. Hence, the strength (by plotting the difference TGA curve) and quantity (by measuring the total change in mass) of the sorption interaction between the adsorbed molecules and the framework can be identified. Conventionally, isothermal and constant heating rate TGA have been used to obtain additional kinetic information. Although other TGA methods, such as dynamic heating rate TGA[47], have also been developed, the constant heating rate method developed by Flynn and Wall[48] is generally used because if requires less experimental time. By applying the Arrhenius equation to the TGA of zeolite materials, the apparent activation energy of desorption can be estimated.

1.3.3 Solid State Nuclear Magnetic Resonance (ssNMR) Spectroscopy

ssNMR spectroscopy has been generally regarded as the 'ultimate' technique in understanding the global information of zeolite acidity. It can readily differentiate BAS and LAS, the coordination of Al (framework-Al or EFAl), the distribution of Al among the T-sites, etc.

The principle of ssNMR spectroscopy is like that of the solution state analogues. Under an applied magnetic field, a spin (an unpaired electron) interacts with another spin (of other atoms) in close proximity to the first nuclei. In contrast to traditional

solution state NMR spectroscopy where the interactions between the nuclei are isotropic, the interactions in ssNMR are anisotropic due to the absence of sample mobility. The anisotropy leads to peak broadening in the ssNMR spectra, which means that there will be significant peak overlap if the peaks are in close proximity. There are various techniques for reducing the problems of line broadening, hence increasing the resolution of the ssNMR spectra. In the modern high-resolution ssNMR instruments, the following techniques are mostly pre-installed, unless otherwise specified; magic angle spinning, macroscopic sample orientation, and radio frequency irradiation.

In this thesis, ^{27}Al, ^{15}N-pyridine probed and ^{31}P-trimethylphosphine (TMP) probed ssNMR experiments are performed. ^{27}Al ssNMR experiment directly measures the ratio of framework-Al and EFAl. Together with ICP-AES, the exact number of framework-Al can be determined by simple arithmetic calculation. The ^{15}N-pyridine experiment distinguishes various modes of pyridine adsorption behaviour with the BAS, with the integrated peak intensity giving quantitative information. Whereas for the ^{31}P-TMP probed ssNMR experiment, the peak position reflects the adsorption environment of the TMP molecule, and the peak area suggests the quantity ratio between the interaction of TMP and acid sites. All in all, ssNMR is an excellent technique sufficiently accurate in determining the acid properties of zeolites. But the major limitation is its deficiency in understanding the sorption chemistry from the structural perspective, i.e., the location of the acid sites and adsorbed molecules cannot be easily elucidated without other supporting techniques.

1.3.4 Powder X-ray Diffraction (PXRD)

The traditional characterisation techniques can only give limited information about the acid strength and quantity, but without the necessary local atomic arrangement. Whereas PXRD and various microscopy techniques have been generally used to determine the topology of zeolites, and some other crystallographic information. On the one hand, PXRD is well established for structural refinements, particularly when sufficiently large single crystals are not available. Basically, a high precision diffractometer and a monochromatic X-ray beam, typically Cu K_α radiation (λ = 1.5404 Å) is used in an angular dispersive instrument. Detailed descriptions of PXRD can be found in elementary text books.[49,50]

PXRD combined with Rietveld refinement (see Chapter 1.4.4), especially when using powerful synchrotron X-ray beam, can reveal small details in the 3-D microporous structures of zeolites including the detailed structural or atomic parameters: fractional atomic coordinates, site occupancy, and atomic displacement or temperature factor. Although specialised, synchrotron powder X-ray diffraction (SXRD) is a well-established technique and provides higher resolution data in general (see Chapter 1.4.6). The methodology is described in detail by Cox (1992), Cockcroft & Fitch (2008) and Wilmott (2011).[51–53]

In the next section, the structural characterisation of zeolites using PXRD will be discussed in detail.

1.4 Structural Characterisation

The acidic properties are not the full story of zeolite chemistry; the structural properties of zeolites complete the remainder of the story. The pore shape and size determine which molecules can enter the zeolitic frameworks, and how the pore hinders the product distribution in catalysis reactions. The traditional characterisation techniques described in Chapter 1.3, however, do not provide sufficient structural information of the BAS, and their corresponding structural chemistry in zeolites.

Classically, shape and size selectivity is understood to be caused by mass transfer and/or transition state effects.[54] The former simply circumvents the formation or diffusion of 'over-sized' products by the rigid zeolite framework, acting as a molecular sieve. Whereas the latter is caused by the confined space within the zeolite framework that influences the formation of certain transition state species. The sheer difference between the framework structure of the zeolites may provide information on how dominant is one effect.[54] Herein, this thesis employs PXRD to systematically understand the structural properties of zeolites in terms of molecular interactions at an atomistic level.

PXRD has long been regarded as an indispensable crystallographic technique in studying the structure of zeolites. The most basic use of PXRD is the 'fingerprint' phase identification; different zeolites produce different PXRD patterns, see Figure 1.6.[12] As early as the 1970s, crystallographers started to use the Rietveld method to solve and refine the fractional atomic coordinates (*x, y, z*), occupancy, and atomic displacement of the framework atoms of zeolites.[55] A notable example is Gallezot et al.

who in 1974 published the crystal structure of dealuminated H-Y zeolite, and revealed that the dealumination process does not create holes within the zeolite structure.[56]

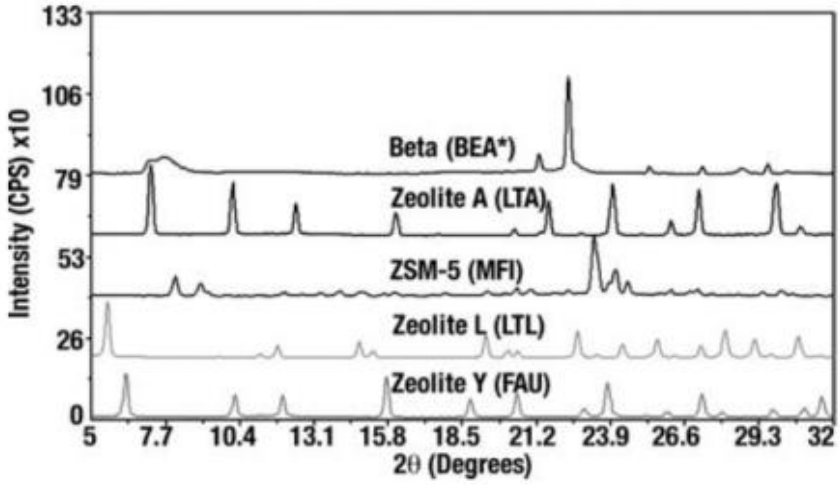

Figure 1.6. The powder X-ray diffraction (PXRD) patterns of five different commercially available zeolites. Different PXRD patterns are observed using Cu X-ray radiation (λ = 1.5404 Å) – 'fingerprint' phase identification.[12]

In addition to the crystal structure, other information could be obtained from PXRD by refinements, e.g., the topology, 'apparent' crystal size, strain or stress, extent of heteroatom substitution, crystallinity including lattice imperfections such as stacking faults, dislocation and atomic species disorder, etc.[12] As the work in this thesis employed SXRD as the primary characterisation technique, the following sub-sections discuss the background of PXRD and synchrotron radiation, as well as the general process for structure solution and structure refinement.

1.4.1 Background

The diffraction technique originates from the discovery of William Lawrence Bragg and his father William Henry Bragg in 1912, that a crystalline material generates unique patterns of diffracted X-ray, distributed according to the Bragg's law.[57] In short, Bragg's law has to be satisfied for diffraction to occur, where intense peaks of diffracted X-rays are detected at certain X-ray wavelengths and incident radiation angles (θ). Of course, Bragg's law also applies to electron diffraction and neutron diffraction (ND). Bragg peaks are observed when the scattered X-ray beams constructively interfere (where n is an integer). The Bragg's law can be described by the equation below, and can be understood through Figure 1.7.

$$2d\sin\theta = n\lambda$$

where d is the inter-planar distance,

θ is the scattering angle,

n is an integer, and

λ is the wavelength of the incident X-ray.

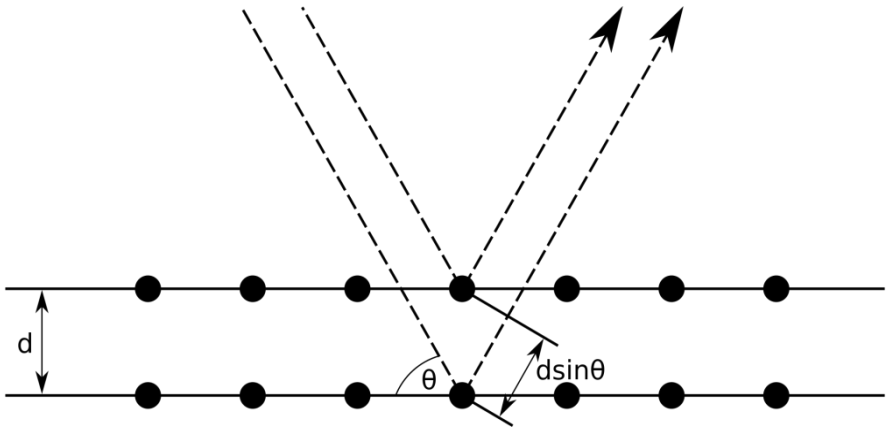

Figure 1.7. Schematic of a beam satisfying the Bragg's law.

In principle, irradiated X-rays are scattered by the electrons surrounding an atom. At low 2θ angles, the scattering factor for an atom is almost proportional to the number of electrons. Therefore, light atoms are weak X-ray scatterers, whereas heavy atoms are strong X-ray scatterers. On the other hand, at high 2θ angles, the scattering factor decreases rapidly due to the partial interference of X-rays away from the incident angle of the beam. Thus, there is a general decrease over the Bragg peak intensity (see Figure 1.8 for the angular dependence of X-ray scattering factors).

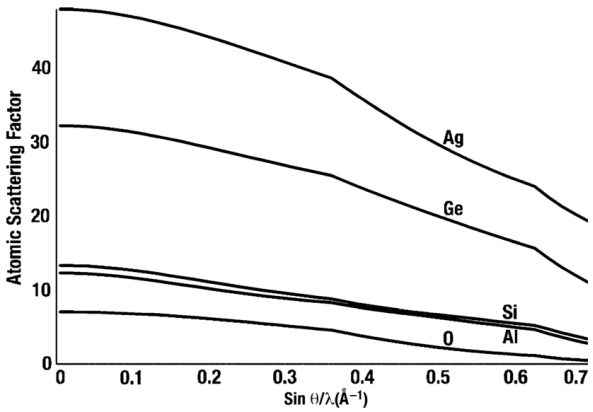

Figure 1.8. The angular dependence of X-ray scattering factors of various species. The curves were created from data in the International Tables for Crystallography.[12]

Indeed, both single-crystal XRD and PXRD can be used to study the structure of zeolites. When studying zeolite chemistry, PXRD is more commonly used due to its superiority in vast number of particle sampling (true representation of bulk behaviour) when the specimen is subjected to non-ambient or *operando* conditions. But a major disadvantage of PXRD is the overlap of Bragg peaks, which prevents the most accurate determination of the structure. Here the use of high resolution SXPD (to improve peak separation) has mitigate to some extend the issue.

Later in 1977, a whole-pattern refinement method was developed by Hugo M. Rietveld, the Rietveld refinement. It can independently calculate these overlapping peaks, which allows a more accurate determination of the crystal structure.[55,58]

1.4.2 Indexing

The most basic use of PXRD in zeolites is structural identification and impurity determination. The first step to understanding an unknown diffraction pattern is to 'index' the Bragg peaks as these can be assigned to their corresponding Miller *hkl* indices according to the space group symmetry of the structure. Herein, an investigator can extrapolate the lattice settings (e.g., cubic or monoclinic, etc.) and the space groups of the zeolite samples. However, as the zeolite structure has been determined in the past[8], the use of 'indexing' technique was not required in this thesis, the general procedure and theory will not be discussed.

1.4.3 Structure Solution – Le Bail Method

After 'indexing' that reveals the lattice setting and space group of a zeolite sample, an investigator can then perform 'structure solution' to determine the crystallographic parameters, such as the lattice strain/stress, apparent crystalline size and lattice parameters. To solve the zeolite structure, methods were reported in the past, such as the Pawley method, direct space method, Monte Carlo method, Patterson method, Le Bail method and multiple wavelengths phasing.[59–61]

In this thesis, the Le Bail method is used to reveal the crystallographic parameters by 'structure solution' of the zeolite samples. Since atomic parameters are not required in the Le Bail refinement, the useful crystallographic parameters can be easily obtained. It uses a least-squares algorithm over the whole diffraction pattern, where the background, peak shape function parameters, and lattice parameters can be refined together (provided there are sufficient experimental observables). A significant advantage is the input of instrumental parameters is not compulsory, where an analytic peak shape function can be used instead. As the Le Bail method is a whole pattern refinement technique, even the overlapped peaks can be calculated during the refinement process.

1.4.4 Structure Refinement - Rietveld Refinement

After 'structure solution', the next procedure is 'structure refinement' that refines the atomic parameters of a crystal structure. The most commonly used structure refinement method is called the Rietveld refinement, which is the basis of this thesis. The Rietveld refinement was devised by Hugo M. Rietveld; it is a whole-pattern fitting method using a non-linear least-squares procedure.[55] The non-linear least-squares procedure minimises the quantity based on the calculated peak intensity and observed peak intensity, with applied weighting statistics. The three contributors of the Bragg peaks are: sample lattice, diffraction optic effects, and instrumental effects. The Bragg peak intensity, I_{hkl}, is calculated as:

$$I_{hkl} = s\Sigma_{hkl} Lm_{hkl}|F_{hkl}|^2\varphi(2\theta_i-2\theta_{hkl})P_{hkl}A+I_{bi}$$

where s is the overall scale factor,

hkl represents the Miller plane indices,

L refers to the Lorentz-polarisation factors,

m_{hkl} is the multiplicity associated with the hkl plane,

F_{hkl} is the structure factor for the Bragg peak of the hkl plane,

$\varphi(2\theta_i-2\theta_{hkl})$ is the profile function, where $2\theta_i$ is corrected for 2θ zero error,

P_{hkl} is the preferred orientation function,

A is the absorption factor, and

I_{bi} is the background scattering intensity at the i^{th} step.

The structure factor (F_{hkl}) of a unit cell describes the Bragg peak of the *hkl* plane which contains the structural information:

$$F_{hkl} = \Sigma f_j g_j [exp\text{-}2\pi i(hx_j+ky_j+lz_j)] exp(-B_j sin2\theta/\lambda^2)$$

where f_j is the scattering factor of the atom *j*,

g_j is the site occupancy factor (SOF),

x_j, y_j, and z_j are the fractional atomic coordinates, and

B_j is a measure of the root-mean-square amplitude of atomic vibration.

As seen, multiplicity (m_{hkl}) is a factor that contributes to the Bragg peak intensity. Multiplicity arises from the sets of *hkl* planes in a crystal, which have identical d-spacing and $|F|^2$ values (due to symmetry). For example, in a cubic lattice $m_{100} = 6$, whereas $m_{111} = 8$. Therefore, the Bragg peak intensity is calculated including the multiplicity of the corresponding *hkl* plane. In addition, some planes overlap but possess different structure factors. For example, in a cubic lattice the 511 and 333 reflections possess identical lattice *d*-spacing. As the Rietveld refinement is a whole-pattern fitting technique that involves all the structural parameters, when the peak intensity is calculated, the overlapped Bragg peaks can be resolved.

The Rietveld refinement allows simultaneous refinements (and adjustments) of structural parameters, e.g., peak profile, unit cell, background, etc. Thus, the least-square algorithm allows an improvement of the structural model, which is continuously fed back during the course of the refinement.[55] By using the derivatives of the parameters in the least-squares minimisation equation with respect to zero, a set of non-linear equations can be obtained. By solving these derived non-linear equations using a $n \times n$ matrix, the solution is refined relative to the starting parameters,

until the solution ultimately converges.[55] Hence, the least-square refinement procedure ensures the global minimum of the parameters is met. In addition, a reasonable starting model is required; in this thesis, the initial H-ZSM-5 crystal structure is obtained from Heo et al.[9]

1.4.5 The Quality of Rietveld Refinement

Like other curve/peak fitting techniques, a set of R-factors can also be used to evaluate the quality and progress of the Rietveld refinement. But before judging the quality of the fit, the investigator should first study how close the fitting is between the observed and calculated PXRD pattern. This means the difference plots should always be first examined to identify any gross errors in the structural model. For a well-fitted PXRD pattern, the difference between the observed and calculated patterns should be small, and no specific peaks should be poorly fitted. If there is any major peak discrepancy, it may suggest the presence of any faults in the proposed model.

Next, the R-factors of the refinement can provide a more quantitative judgement over the quality of the fit, where the R-factor quantities are R_p, R_{wp}, R_{exp}, and χ^2 (a.k.a. goodness-of-fit):

$$R_p = \frac{\sum_i |I_o - I_c|}{\sum_i I_o}$$

$$R_{wp} = \sqrt{\frac{\sum_i w_i (I_o - I_c)^2}{\sum_i w_i I_o^2}}$$

$$R_{exp} = \sqrt{\frac{n - p}{\sum_i w_i I_o^2}}$$

$$\chi^2 = \frac{{R_{wp}}^2}{{R_{exp}}^2}$$

where n is the number of observables of the data,

p is the number of parameters of the refinement,

I_o is the experimental Bragg peak intensity,

I_c is the calculated Bragg peak intensity, and

w_i is the weighting coefficient at the i^{th} step ($={I_{o,ith}}^{-1/2}$).

From a statistical point of view, R_{wp} is the most significant as the numerator is the function being minimised. R_{exp} is the 'expected' R-factor when there are n observables and p parameters, which is the best possible value that the calculated R_{wp} value could possibly reach. For a general PXRD pattern, David[62] and Toby[63] have independently discussed the meanings of the fitting quantities of a Rietveld refinement. They proposed that adequate refinements generally have R_{wp} values below 12%, and χ^2 should approach 1 for a perfect refinement. Lutterotti and Scardi[64] have also critically commented on how to judge the R-factors. They suggested that, as the number of

peaks increases, it is more difficult to achieve low R_{wp} values. In general, for a highly symmetric structure that has few Bragg peaks, R_{wp} < 8% is considered acceptable. For a medium complex phase/structure, R_{wp} < 10% is good; for a complex phase/structure (i.e., monoclinic to triclinic), R_{wp} < 15% is acceptable.[64]

If the PXRD is performed using a synchrotron X-ray source, the R_{exp} values become less meaningful as the number of observables is much greater than that of a laboratory X-ray analogue. Note that the statistical precision increases due to better detection resolution (smaller 2θ step) and longer counting time. Both lead to a greater number of observables n, which lowers the R_{exp} value. Paradoxically, an improved statistical precision will in general increase the difference between R_{exp} and R_{wp}, eventually increasing χ^2.[59]

This means that for SXRD, the χ^2 value should not be the major quantities in studying the quality of a Rietveld refinement. Thus, the quality should be predominantly judged by how close the fitting is between the observed and calculated patterns, then by the R_{wp} value.

Finally, and equally importantly, the chemistry of the atomic parameters must be reasonable, which includes the bond distances, bond angles, and SOF values, etc. The refined result would still make no sense without a sensible and reasonable final crystal structure, even if the R_{wp} value is extremely low.

1.4.6 Synchrotron Powder X-ray Diffraction (SXRD)

However, as the incidental effects due to the very close lattice parameters that may lead to severe peak overlap, a high-quality and well-aligned instrument with high-resolution data is necessary for the Rietveld refinement work. Owing to the advancement of the synchrotron X-ray facilities around the globe, the PXRD pattern using synchrotron X-ray radiation can achieve higher peak resolution due to better instrumentation.

Synchrotron X-ray beams are generated by a large particle accelerator where very fast electrons (approaching the speed of light) accelerated in magnetic lattices such as bending magnets and insertion devices (undulators and wigglers).[53] There are powerful X-ray sources, in particular at today's 3rd generation synchrotron facilities such as Diamond Light Source (UK), European Synchrotron Radiation Facility (France), Advanced Photon Source (USA) and SPring-8 (Japan). Figure 1.9 is a schematic representation of a synchrotron facility. By harnessing the power of the synchrotron X-ray beams, purposely built beamlines (tangential to the main storage ring) are used to probe the minute details of material.

By taking advantage of the unique properties of synchrotron beam listed below, SXRD is known to be outstanding when comparing with the laboratory analogues.[49,52,53]

- High brightness (intense and tight collimation) means: (i) smaller angular divergence of the beam, hence high angular resolution data can be obtained, and (ii) deep probing of structural details with high contrast (high signal-to-noise ratio) data for the detection of small features,
- Horizontally polarised, which reduces the fall in intensity as a function of 2θ,
- Tuneable X-ray wavelength, i.e., the X-ray absorption problems of certain atoms can be avoided, which reduces sample fluorescence that causes high background,
- Large or spacious instrument for sample environments.

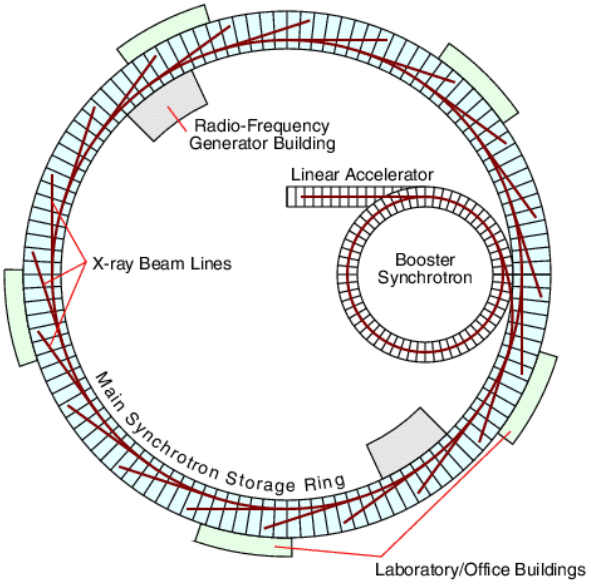

Figure 1.9. Schematic of a synchrotron X-ray facility.[53,65,66]

Due to the above, higher resolution of data can be obtained with relative short collection time using customised sample environments (see Chapter 2). When SXRD is employed in zeolite studies, it is mainly applied for the following purposes[53]:

- Investigation of new zeolite materials where high brightness instrument can accurately determine the structures,
- Extreme temperature and/or pressure study, which cannot be done using a laboratory diffractometer,
- *In situ*/*operando* study, technologically permissible to develop dedicated sample environments,
- Stress/strain study, using detailed peak profile analysis to high precision data which have negligible or small instrumental contributions.

To achieve the objective, it was necessary to study the behaviour of the zeolite ZSM-5 samples by performing *in situ*/*operando* SXRD experiments (to be described in Chapters 4 and 6).

1.4.7 SXRD or Neutron Diffraction (ND)?

Unlike X-ray, neutrons are scattered by the nucleus (a point) rather than from the electrons (diffused). The variation of the neutron scattering factors (scattering lengths) behaves differently from that of the X-ray analogues. They depend on the properties of the nucleus; hence different isotopes have different scattering factors. The presence of positive and negative scattering factors makes ND a handy tool in identifying different species from the Fourier contrast maps.

All in all, the most important use of zeolites is as catalysts for the petrochemical industry, which involves small organic molecules interacting with the BAS within their microporous channels. Thus, a reliable experimental method is needed to reveal the atomic arrangement of the adsorbates about the BAS. This may guide the rational design of new zeolite systems. Previous attempts have been made using ND or SXRD or a combination of the two to observe the presence of organic molecules in various zeolites. Previous work, notably by Czjzek, Fitch and Vogt, have located large organic molecules (e.g., benzene, aniline, and pyridine) in H-Y and H-ZSM-5 zeolites using ND in the early 1990s.[67,68] Furthermore, as ND is sensitive to hydrogen atoms, the BAS (H/D) location has been directly determined in highly symmetric H-Y zeolite.[69] But possibly due to the lower angular resolution in ND, further elucidation of the interactions between small organic adsorbates and BAS seems to be limited.

However, while ND is sensitive to light elements, it is difficult to study the catalysis chemistry in zeolites using ND. In general, when compared with SXRD, ND shows lower resolution, requires large sample sizes, has a low flux and small cross section.

Also, the complex ND instrumentation leads to limited availability and difficulties in carrying out *in situ* or *operando* catalysis experiments.

In contrast, the recent dramatic improvement of synchrotron sources and the use of modern instrumentation has allowed SXRD to determine the structure of various zeolites[65,70,71], as well as the positions and occupancies of Na^+, K^+, and Cs^+ ions in zeolites A and H-ZSM-5 with high precision.[72,73] More recently, SXRD has been used to establish the adsorption interactions of CO_2 and SO_2 in MOFs.[74] Thus, it is anticipated that not only the interaction between various organic molecules and the zeolite framework can be revealed, but also a mechanistic study of a carefully selected catalysis reaction is technically feasible and practical.

1.5 Theoretical Studies

Aside from the above mentioned experimental techniques, significant progress was made using theoretical computational modelling. Some common modelling techniques include density functional theory (DFT), quantum mechanics/molecular mechanics (QM/MM), QM-pot, and our own N-layered integrated molecular orbital and molecular mechanics (ONIOM)) for long-range zeolite–guest interactions, and for describing acid sites and their adsorption of molecular species at the quantum mechanical level.[39,75–80] Li et al. have studied the distribution of Al and Brønsted acid sites in MCM-22.[80] Redondo and Hay have determined that the most stable sites of the BAS oriented towards the major pores of the ZSM-5 lattice, using semi-empirical QM calculations.[81] Sillar and Burk[39], and Lomratsiri et al.[79] have calculated the properties of BAS of ZSM-5 using the ONIOM method. By the QM/MM method, de Vries et al. have studied the zeolite structure and reactivity.[77] Li et al. predicted the location and dribution Al sitting in a silicon-rich zeolite framework.[82] And there are many more examples where researches studied the properties of zeolites using various theoretical techniques.

In addition to quantum calculations, force-field calculations have also been employed widely in the study of molecular behaviour in zeolites. Van der Mynsbrugge et al.[83] and Bai et al.[84] have studied molecular adsorption behaviour in H-ZSM-5 supported by force-field calculations.

1.6 Aim and Objectives

The aim of this thesis is to provide understanding of the catalysis chemistry in zeolites from molecular and structural perspectives, via the study of H-ZSM-5 as one of the most commonly used zeolites. Attempts to determine the structures of organic species in microporous materials by SXRD were carried out. By conducting careful studies of the interactions between organic adsorbates and zeolite framework using SXRD and Rietveld refinement, their corresponding catalysis chemistry are systematically studied.

The objective of this thesis is to systematically study the zeolite catalysis chemistry in the following manner: (i) to reveal the location of the BAS in H-ZSM-5, (ii) to study the acid-base interactions of the BAS with various functional molecular species, (iii) to study the ammonia storage potential, (iv) to design a novel catalytic system, and (v) to investigate the mechanism and intermediate species of industrially important catalysis reactions.

1.7 Thesis Overview

This thesis consists of seven chapters. Chapters 3 to 6 inclusive, detail the research performed during my study for this D.Phil. degree.

Chapter 1 introduces the background of zeolites and their active acid sites during catalysis reactions, and reviews some up-to-date characterisation techniques of zeolites.

Chapter 2 details the experimental and characterisation techniques used.

Chapter 3 locates the BAS in H-ZSM-5, and elucidates their interactions with adsorbed functional molecular species using SXRD, supported with force-field calculations.

Chapter 4 studies the ammonia storage potential of H-ZSM-5 from the structural perspective. In addition, the ammonia sorption kinetics at specific adsorption sites is discussed using temperature programmed SXRD and TGA.

Chapter 5 reports a novel catalytic conversion of biomass-derived furans and alcohol to aromatics over zeolites. The key facilitating step is studied accordingly by experimental and theoretical techniques.

Chapter 6 studies the mechanistic of the industrially important methanol conversion process, by *operando* SXRD and theoretical calculations.

Chapter 7 concludes and outlooks the impact of the work presented.

1.8 References

(1) Jiang, J.; Yun, Y.; Zou, X.; Jorda, J. L.; Corma, A. *Chem. Sci.* **2015**, *6* (1), 480–485.

(2) Strohmaier, K. G.; Corma, A.; Diaz, M. J.; Rey, F.; Dorset, D. L.; Soled, S. L. Google Patents September 10, 2013.

(3) Stöcker, M. *Microporous Mesoporous Mater.* **1999**, *29* (1–2), 3–48.

(4) Liang, J.; Li, H.; Zhao, S.; Guo, W.; Wang, R.; Ying, M. *Appl. Catal.* **1990**, *64*, 31–40.

(5) Lai, Z. P.; Bonilla, G.; Diaz, I.; Nery, J. G.; Sujaoti, K.; Amat, M. A.; Kokkoli, E.; Terasaki, O.; Thompson, R. W.; Tsapatsis, M.; Vlachos, D. G. *Science* **2003**, *300* (5618), 456–460.

(6) Egeblad, K.; Christensen, C. H.; Kustova, M.; Christensen, C. H. *Chem. Mater.* **2008**, *20* (3), 946–960.

(7) Weitkamp, J. *Solid State Ionics* **2000**, *131* (1), 175–188.

(8) Van Koningsveld, H. *Acta Crystallogr. Sect. B Struct. Sci.* **1990**, *46* (6), 731–735.

(9) Heo, N. H.; Kim, C. W.; Kwon, H. J.; Kim, G. H.; Kim, S. H.; Hong, S. B.; Seff, K. *J. Phys. Chem. C* **2009**, *113* (46), 19937–19956.

(10) Van Speybroeck, V.; Hemelsoet, K.; Joos, L.; Waroquier, M.; Bell, R. G.; Catlow, C. R. A. *Chem. Soc. Rev.* **2015**, *44* (20), 7044–7111.

(11) IEA Statistics © OECD/IEA 2014. Fossil fuel energy consumption (% of total) http://data.worldbank.org/indicator/EG.USE.COMM.FO.ZS.

(12) Chester, W.; Derouane, E. G. *Zeolite Characterization and Catalysis - A Tutorial*; Springer.

(13) Tian, P.; Wei, Y.; Ye, M.; Liu, Z. *ACS Catal.* **2015**, *5* (3), 1922–1938.

(14) Fellah, M. F.; Onal, I. *Catal. Today* **2011**, *171* (1), 52–59.

(15) Beznis, N. V; Weckhuysen, B. M.; Bitter, J. H. *Catal. Letters* **2010**, *138* (1–2), 14–22.

(16) Woertink, J. S.; Smeets, P. J.; Groothaert, M. H.; Vance, M. A.; Sels, B. F.; Schoonheydt, R. A.; Solomon, E. I. *Proc. Natl. Acad. Sci.* **2009**, *106* (45), 18908–18913.

(17) Kosinov, N.; Gascon, J.; Kapteijn, F.; Hensen, E. J. M. *J. Memb. Sci.* **2016**, *499*, 65–79.

(18) van den Bergh, J.; Gücüyener, C.; Gascon, J.; Kapteijn, F. *Chem. Eng. J.* **2011**, *166* (1), 368–377.

(19) Nam, G.; Jeong, B.; Kang, S.; Lee, B.; Choi, D. *J. Chem. Eng. Data* **2005**, *61*, 72–76.

(20) Venna, S. R.; Carreon, M. A. *J. Am. Chem. Soc.* **2009**, *132* (1), 76–78.

(21) Weitkamp, J.; Fritz, M.; Ernst, S. *Int. J. Hydrogen Energy* **1995**, *20* (12), 967–970.

(22) Rosi, N. L.; Eckert, J.; Eddaoudi, M.; Vodak, D. T.; Kim, J.; Keeffe, M.; Yaghi, O. M. *Science* **2003**, *300* (5622), 1127–1129.

(23) Yang, Z.; Xia, Y.; Sun, X.; Mokaya, R. *J. Phys. Chem. B* **2006**, *110* (37), 18424–18431.

(24) Yang, Z.; Xia, Y.; Mokaya, R. *J. Am. Chem. Soc.* **2007**, *129* (6), 1673–1679.

(25) Wu, H.; Zhou, W.; Yildirim, T. **2007**, *129* (17), 5314–5315.

(26) Helminen, J.; Helenius, J.; Paatero, E.; Turunen, I. *J. Chem. Eng. Data* **2001**, *46* (2), 391–399.

(27) Doonan, C. J.; Tranchemontagne, D. J.; Glover, T. G.; Hunt, J. R.; Yaghi, O. M. *Nat. Chem.* **2010**, *2* (3), 235–238.

(28) Britt, D.; Tranchemontagne, D.; Yaghi, O. M. *Proc. Natl. Acad. Sci.* **2008**, *105* (33), 11623–11627.

(29) O'Malley, A. J.; Hitchcock, I.; Sarwar, M.; Silverwood, I. P.; Hindocha, S.; Catlow, C. R. A.; York, A. P. E.; Collier, P. J. *Phys. Chem. Chem. Phys.* **2016**, *18* (26), 17159–17168.

(30) Haag, W. O.; Lago, R. M.; Weisz, P. B. *Nature* **1984**, *309* (5969), 589–591.

(31) Gies, H.; Marker, B. *Zeolites* **1992**, *12* (1), 42–49.

(32) Schwieger, W.; Bergk, K. H.; Hunger, D.; Pfeifer, H. In *Zeolite Synthesis, ACS symposium series, Washington, DC*; 1989; pp 274–290.

(33) Lok, B. M.; Cannan, T.; Messina, C. A. *Zeolites* **1983**, *3* (4), 282–291.

(34) Occelli, M. L.; Robson, H. E. *Zeolite synthesis*; American Chemical Society, 1989.

(35) Vispute, T. P.; Zhang, H.; Sanna, A.; Xiao, R.; Huber, G. W. *Science* **2010**, *330* (6008), 1222–1227.

(36) Young, L. B.; Butter, S. A.; Kaeding W Weding. *J. Catal.* **1982**, *76* (2), 418–432.

(37) Fujita, H.; Kanougi, T.; Atoguchi, T. *Appl. Catal. A Gen.* **2006**, *313* (2), 160–166.

(38) Dědeček, J.; Sobalík, Z.; Wichterlová, B. *Catal. Rev.* **2012**, *54* (2), 135–223.

(39) Sillar, K.; Burk, P. *J. Mol. Struct.* **2002**, *589–590*, 281–290.

(40) Derouane, E. G.; Védrine, J. C.; Pinto, R. R.; Borges, P. M.; Costa, L.; Lemos, M. a. N. D. a.; Lemos, F.; Ribeiro, F. R. *Catal. Rev.* **2013**, *55* (4), 454–515.

(41) Kondo, J. N.; Nishitani, R.; Yoda, E.; Yokoi, T.; Tatsumi, T.; Domen, K. *Phys. Chem. Chem. Phys.* **2010**, *12* (37), 11576–11586.

(42) Li, S.; Zheng, A.; Su, Y.; Zhang, H.; Chen, L.; Yang, J.; Ye, C.; Deng, F. *J. Am. Chem. Soc.* **2007**, *129* (12), 11161–11171.

(43) Jin, F.; Li, Y. *Catal. Today* **2009**, *145* (1–2), 101–107.

(44) Maache, M.; Janin, A.; Lavalley, J. C.; Joly, J. F.; Benazzi, E. *Zeolites* **1993**, *13* (6), 419–426.

(45) Buzzoni, R.; Bordiga, S.; Ricchiardi, G.; Lamberti, C.; Zecchina, a.; Bellussi, G. *Langmuir* **1996**, *12* (4), 930–940.

(46) Kubelkova, L.; Kotrla, J.; Florian, J. *J. Phys. Chem.* **1995**, *99* (25), 10285–10293.

(47) Salin, I. M.; Seferis, J. C. *J. Appl. Polym. Sci.* **1993**, *47* (5), 847–856.

(48) Flynn, J. H.; Wall, L. A. *J. Polym. Sci. Part C Polym. Lett.* **1966**, *4* (5), 323–328.

(49) Cullity, B. D.; Stock, S. R. *Rading, MA Addison-Wesley* **1978**.

(50) Dinnebier, R. E.; Billinge, S. J. L. *Powder Diffraction - Theory and Practice*; 2008.

(51) Coppens, P.; Cox, D.; Vlieg, E.; Robinson, I. K. *Synchrotron radiation crystallography*; Academic Press London, 1992.

(52) Cockcroft, J. K.; Fitch, A. N. In *Powder Diffraction*; 2008; pp 20–57.

(53) Willmott, P. *An introduction to synchrotron radiation: techniques and applications*; John Wiley & Sons, 2011.

(54) Jae, J.; Tompsett, G. A.; Foster, A. J.; Hammond, K. D.; Auerbach, S. M.; Lobo, R. F.; Huber, G. W. *J. Catal.* **2011**, *279* (2), 257–268.

(55) Young, R. A. *The Rietveld Method* **1993**, *5*, 1–38.

(56) Gallezot, P.; Beaumont, R.; Barthomeuf, D. *J. Phys. Chem.* **1974**, *78* (15), 1550–1553.

(57) Bragg, W. L. In *Proceedings of the Royal Society of London A: Mathematical, Physical and Engineering Sciences*; The Royal Society, 1913; Vol. 89, pp 248–277.

(58) Rietveld, H. M. *The Rietveld Method*; Oxford University Press, 1993.

(59) David, W. I. F. *Structure determination from powder diffraction data*; Oxford University Press on Demand, 2002; Vol. 13.

(60) Le Bail, A.; Duroy, H.; Fourquet, J. L. *Mater. Res. Bull.* **1988**, *23* (3), 447–452.

(61) Le Bail, A. *J. Non. Cryst. Solids* **1995**, *183* (1–2), 39–42.

(62) David, W. I. F. I. F. *J. Res. Natl. Inst. Stand. Technol.* **2004**, *109* (1), 107.

(63) Coleman, J. N.; Lotya, M.; O'Neill, A.; Bergin, S. D.; King, P. J.; Khan, U.; Young, K.; Gaucher, A.; De, S.; Smith, R. J.; Shvets, I. V; Arora, S. K.; Stanton, G.; Kim, H.-Y.; Lee, K.; Kim, G. T.; Duesberg, G. S.; Hallam, T.; Boland, J. J.; Wang, J. J.; Donegan, J. F.; Grunlan, J. C.; Moriarty, G.; Shmeliov, A.; Nicholls, R. J.; Perkins, J. M.; Grieveson, E. M.; Theuwissen, K.; McComb, D. W.; Nellist, P. D.; Nicolosi, V. *Science* **2011**, *331* (6017), 568–571.

(64) Lutterotti, L.; Scardi, P. *J. Appl. Crystallogr.* **1990**, *23* (4), 246–252.

(65) Thompson, S. P.; Parker, J. E.; Marchal, J.; Potter, J.; Birt, A.; Yuan, F.; Fearn, R. D.; Lennie, A. R.; Street, S. R.; Tang, C. C. *J. Synchrotron Radiat.* **2011**, *18* (4), 637–648.

(66) Margaritondo, G. *Introduction to synchrotron radiation*; Oxford University Press, USA, 1988.

(67) Fitch, A. N.; Jobic, H.; Renouprezb, A. *Chem. Commun.* **1985**, No. 284, 284–286.

(68) Goyal, R.; Fitch, A. N.; Jobic, H. *J. Chem. Soc. Chem. Commun.* **1990**, No. 17, 1152.

(69) Czjzek, M.; Jobic, H.; Fitch, A. N.; Vogt, T. *J. Phys. Chem.* **1992**, *96* (1), 1535–1540.

(70) Tartoni, N.; Thompson, S. P.; Tang, C. C.; Willis, B. L.; Derbyshire, G. E.; Wright, A. G.; Jaye, S. C.; Homer, J. M.; Pizzey, J. D.; Bell, A. M. T. *J. Synchrotron Radiat.* **2008**, *15* (Pt 1), 43–49.

(71) Parker, J. E.; Thompson, S. P.; Cobb, T. M.; Yuan, F.; Potter, J.; Lennie, A. R.; Alexander, S.; Tighe, C. J.; Darr, J. a.; Cockcroft, J. C.; Tang, C. C. *J. Appl. Crystallogr.* **2011**, *44* (1), 102–110.

(72) Mentzen, B. F. *J. Phys. Chem. C* **2007**, *111* (51), 18932–18941.

(73) Liu, Q.; Mace, A.; Bacsik, Z.; Sun, J.; Laaksonen, A.; Hedin, N. *Chem. Commun.* **2010**, *46* (25), 4502–4504.

(74) Yang, S.; Sun, J.; Ramirez-Cuesta, A. J.; Callear, S. K.; David, W. I. F.; Anderson, D. P.; Newby, R.; Blake, A. J.; Parker, J. E.; Tang, C. C.; Schröder, M. *Nat. Chem.* **2012**, *4* (11), 887–894.

(75) Dunne, J. A.; Rao, M.; Sircar, S.; Gorte, R. J.; Myers, A. L. *Langmuir* **1996**, *12* (24), 5896–5904.

(76) Solans-Monfort, X.; Sodupe, M.; Branchadell, V.; Sauer, J.; Orlando, R.; Ugliengo, P. *J. Phys. Chem. B* **2005**, *109* (8), 3539–3545.

(77) de Vries, A. H.; Sherwood, P.; Collins, S. J.; Rigby, A. M.; Rigutto, M.; Kramer, G. J. *J. Phys. Chem. B* **1999**, *103* (29), 6133–6141.

(78) Koppel, I. A.; Burk, P.; Koppel, I.; Leito, I.; Sonoda, T.; Mishima, M. *J. Am. Chem. Soc.* **2000**, *122* (21), 5114–5124.

(79) Lomratsiri, J.; Probst, M.; Limtrakul, J. *J. Mol. Graph. Model.* **2006**, *25*, 219–225.

(80) Li, Y.; Guo, W.; Fan, W.; Yuan, S.; Li, J.; Wang, J.; Jiao, H.; Tatsumi, T. *J. Mol. Catal. A Chem.* **2011**, *338* (1–2), 24–32.

(81) Redondo, A.; Hay, P. J. *J. Phys. Chem.* **1993**, *97* (45), 11754–11761.

(82) Li, C.; Sklenak, S.; Sierka, M.; Sauer, J. *Angew. Chem. Int. Ed.* **2007**, 7286–7289.

(83) Van der Mynsbrugge, J.; Hemelsoet, K.; Vandichel, M.; Waroquier, M.; Van Speybroeck, V. *J. Phys. Chem. C* **2012**, *116* (9), 5499–5508.

(84) Bai, C.; Liu, L.; Sun, H. *J. Phys. Chem. C* **2012**, *116* (12), 7029–7039.

Chapter 2. Materials, Methods and Experimental Techniques

The procedures of the experimental and theoretical studies used in this thesis are provided in this chapter.

2.1 Zeolite Samples

All the zeolites used in this thesis are commercial samples obtained from SRIFT-SINOPEC, China.[1] The samples were pretreated with 0.1 M hydrochloric acid overnight for H^+-exchange to remove NH_4^+ or Na^+ residues from synthesis. The sample was first calcined in air at a ramp rate of 1 °C min^{-1} to 480 °C. Then, the sample was cooled and stored in dry air for further use.

2.2 Sample Preparation for SXRD Measurements

The preparation details for zeolite adsorption study are described in this section. All the specific experimental/preparation methods will be individually described in the corresponding chapters in this thesis.

For pyridine adsorption

The pretreated H-ZSM-5 was loaded into a 0.7 mm (diameter) borosilicate glass capillary. The sample tube was connected to the gas-cell developed by Parker et al.[2] and then repeatedly evacuated-heated to 300 °C for 2 hours, to remove any residual water before pyridine adsorption. Next, the sample was reacted with vaporised anhydrous pyridine (Sigma Aldrich, Germany) in the gas-cell for 30 minutes. The capillary was cooled, cut and sealed for the SXRD measurements.

For ammonia adsorption

Same procedure as described for pyridine adsorption was employed. Anhydrous ammonia (Sigma Aldrich, Germany) was used.

For methanol adsorption

Same procedure as described for pyridine adsorption was employed. Anhydrous methanol (Sigma Aldrich, Germany) was used.

For ethanol & dimethylfuran (DMF) study

The zeolite sample was first treated under vacuum at 200 °C for 2 hours before adsorption with ethanol and/or DMF vapour. For pure ethanol or DMF uptake experiment, a saturated vapour pressure of adsorbate was used. For the equimolar ethanol/DMF uptake experiment, an equimolar mixture of ethanol/DMF was used. The total number of mole of ethanol/DMF introduced to the reactor chamber containing the zeolite was set at 75% of the total number of BAS.

Isothermal Testing – Carbon Deposition

The H-ZSM-5 sample was loaded in a 250 mL round bottom flask reactor at 200 °C, and connected to a flowing stream of methanol vapour under a N_2 flow rate of 2 mL min^{-1} at 1 atmosphere via a methanol saturator at room temperature.

Operando SXRD High-Pressure Gas-cell

A capillary high-pressure gas-cell was specifically designed for the methanol dehydration reaction in the H-ZSM-5 sample under *operando* SXRD in a controllable manner (see Figure 2.1). The stainless-steel capillary cell support holder was strong and rigid enough to ensure the alignment of the capillary for low and high temperature experiments. A both-way open-ended borosilicate capillary (diameter of

0.7 mm) was mounted by two brass capillary holders and was glued using Araldite; over the reaction temperature and pressure (up to 10 bar), no gas leakage was detected. Within the both-way open-ended capillary, the H-ZSM-5 sample was sandwiched between two pieces of quartz wool in the capillary to prevent sample dislocation. One end of the capillary was connected to a gas inlet end that received anhydrous methanol vapour from a liquid saturator kept at room temperature with He carrier gas (flow rate = 2 mL min^{-1}). The vapour pressure of methanol and the flow of He carrier gas were carefully calibrated to ensure a reasonable amount of methanol vapour reaching the sample. The other end was connected to a quadrupole mass spectrometer (MS) that analysed the gas composition on-line with simultaneous SXRD data collection. In addition, the dead volume between the MS and the reactor cell was kept minimal under a slow flow rate of He within 30 sec time delay. A hot-air blower was mounted at 5 mm from the capillary for heating. The temperature of the hot-air blower had been calibrated using a high-quality standard Pt powder sample. A separate fan was mounted 150 mm from the hot-air blower to reduce the heat conducted to the detectors. In general, SXRD measurements that are performed using capillary sample holders requires high-speed spinning to allow an optimal measurement statistic. However, it was technically extremely difficult to achieve spinning with the current set-up. Therefore, a constant capillary rocking generated by the sample stage holder was employed to reduce the loss in data quality.

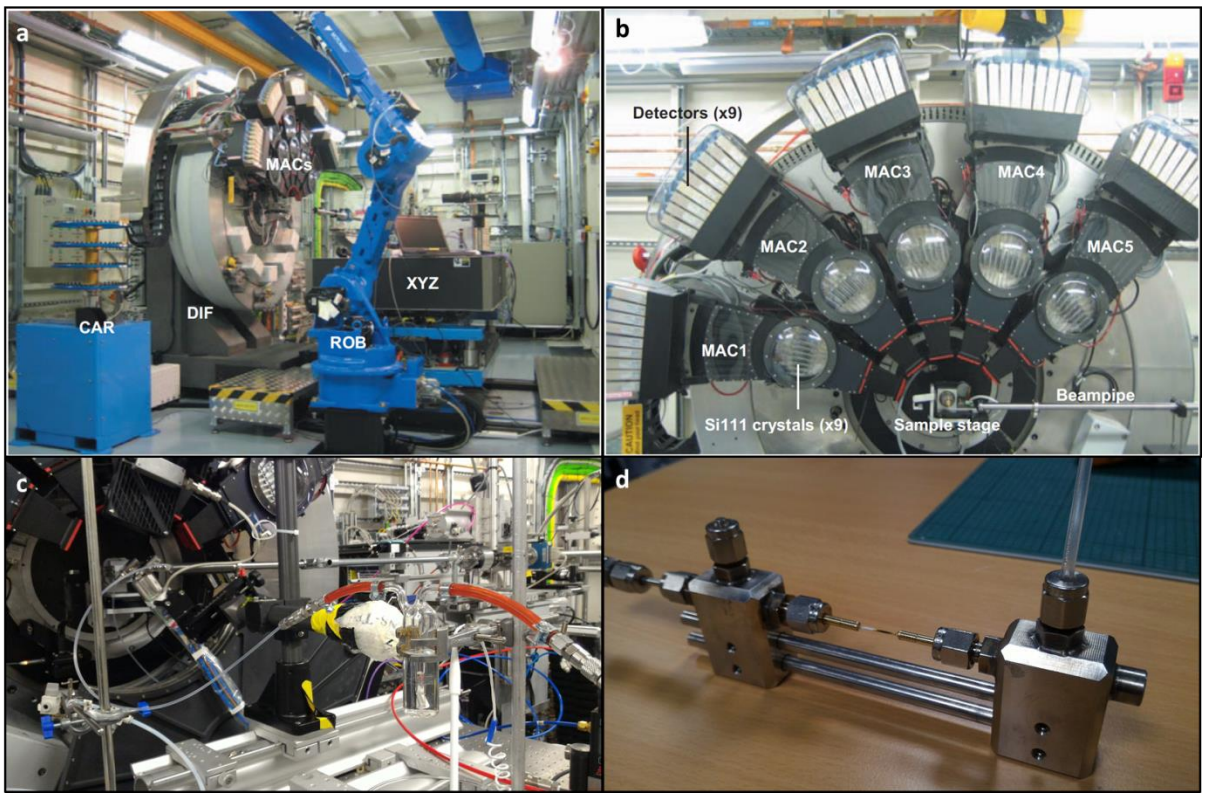

Figure 2.1. (**a,b**) 5 arms (x9) multiple-analyser crystals (MAC) detectors of SXRD diffractometer (DIF) with carousal auto-sampler and a capillary sample stage at beamline I11, Diamond Light Source, UK, for high-resolution SXRD measurements.[3,4] (**c**) The *operando* SXRD system with one end of the both-way open-ended capillary (diameter of 0.7 mm) connected to inlet methanol vapour, with the other end connected to the mass spectrometer for on-line gas analysis. The hot-air blower is also in place. (**d**) The high-pressure *operando* gas-cell with stainless-steel support and air-tight brass holders that ensure good capillary alignment and no gas leakage.

2.3 Catalytic Conversion of 2,5-Dimethylfuran and Ethanol

In a typical experiment, 15 mL DMF (99% Sigma-Aldrich), 8.2 mL of ethanol (99.5% Sigma-Aldrich) and 0.4 g of zeolite were used over a temperature range of 200 to 300 °C and 1.0 mL of tridecane as an internal standard. The reaction vessel was flushed with inert N_2. In addition, the solid residue was filtered and washed with acetone and dried overnight (80 °C). The solid residue was then analysed by TGA by heating at 10 °C min^{-1} from room temperature to 900 °C under air, to determine the coke content for the carbon balance. The conversion was expressed in term of the molar conversion of DMF and carbon balance was achieved at the minimum of 90-95%. After reaction, the autoclave was cooled down to –60 °C by a dry ice/acetone bath. The liquid products were identified and quantified by 5977A Series GC/MSD System, whereas the gas products (CO, CO_2, CH_4) analysed by Perkin Elmer Autosystem XL Arnel Gas phase GC-FID-Methanator, in which C_2H_4 was assumed to be mainly produced from ethanol.

2.4 Characterisation Techniques

The details of the characterisation techniques in thesis are provided in this section.

2.4.1 SXRD and Rietveld refinement

All the SXRD data were collected at Beamline I11, Diamond Light Source, UK.[3] The energy of the incident X-ray flux was set at 15 keV. The wavelength and the 2θ-zero point were refined using a diffraction pattern obtained from a high-quality Si powder (SRM640c). The high-resolution SXRD data were obtained from the zeolite samples using the multiple-analyser crystals (MAC) detectors. The patterns were collected in the 2θ range of 0-150° with 0.001° data binning. Each MAC pattern was collected for an hour for good statistics. In total, there are 4190 *hkl* reflections measured within the 2θ refinement region of 3-55°, of which at least 300 independent *hkl* reflections are observed. From a mathematical perspective, the number of variables, *p*, should not exceed the number of observables, *n*. In the Rietveld refinements performed in this work, the number of structural parameters has not exceeded 190.

The crystallographic parameters were refined using the Le Bail method, whereas the atomic parameters were refined using the Rietveld refinement method, both using the TOPAS software. The starting coordinates used were based on the H-ZSM-5 zeolite model by Heo et al. for sample refinement.[5] The background curve was fitted by a Chebyshev polynomial with an average of 20 coefficients. The Thompson-Cox-Hastings pseudo-Voigt peak function proposed by Thompson et al. was applied.[6] The scale factor and lattice parameters were allowed to vary for all the histograms.

The final refined atomic parameters for each data histogram were carried out using the Rietveld method with the fractional atomic coordinates (*x, y, z*), SOF and isotropic displacement factors (B_{eq}) for all the atoms.

(i) *Framework atoms*

In principle, upon organic molecule adsorption, the positions of the framework atoms may change slightly – a small deviation from the model by Heo et al.[5] Therefore, prior to the refinement of the entire structure with guest molecules, the framework atoms were first refined to avoid a miscalculation of the structure. As the guest molecules do not consist of any heavy atoms, it is reasonable to assume the guest molecules only minimally contribute to the low 2θ angle reflections. Thus, the fractional coordinates and the B_{eq} values of the framework atoms (Si and O) were first independently refined over the 2θ range of 30-55°.

(ii) *Fourier analysis*

Over the 2θ range of 3-55°, the Fourier analysis (electron contrast map) was used to identify the positions with the highest remaining electron density in the framework, once the positions of the framework atoms have been refined. For example, in the case of ammonia pre-adsorbed in H-ZSM-5, the (approximate) positions of the N atoms can be determined.

(iii) *Inclusion of guest molecules*

Based on the Fourier analysis, a Monte Carlo-based simulated annealing technique was used to locate the positions of the guest molecules in the H-ZSM-5. The guest

molecules were described by rigid body Z-matrices. During the refining process, the fractional atomic coordinates of the framework atoms were fixed.

Taking the H-ZSM-5 pre-adsorbed with methanol sample as an example, it was refined using four rigid body Z-matrices that describe methanol molecules at fixed bond distances and angles. The rigid body Z-matrices were first applied to be simulated annealed using the Rietveld method (while the fractional atomic coordinates of the framework atoms kept fixed). The SOF of two of these four rigid body Z-matrices approached zero. Thus, the annealing technique ensures the correct number of guest molecule sites.

After identifying the number and location of the guest molecules, the SOF and B_{eq} were first separately refined. Then, all the relevant parameters were all relaxed to be refined by simulated annealing repeatedly, to ensure the global minimum has been reached. In general, the global minimum is indicated by the lowest R_{wp} and χ^2 values.

However, in some cases, the derived crystal structures did not make much chemical sense, e.g., the guest molecules are located far too close from the framework. This required a closer check of the parameters before repeating refinement procedure. Ultimately, several criteria were met to ensure high quality and reliability of refinement, namely, (i) the global minimum has been reached, (ii) the derived crystal structure fits chemical sense, (iii) reasonable systematic error values for all the refined parameters, and (iv) reasonable SOF and B_{eq} values.

The B_{eq} values of the framework T and O atoms are constrained in the following ways: (i) all the T atoms share the same value, and the O atoms share the same value, (ii) the

B_{eq} of the H atoms of the adsorbed species are set 1.3 times that of the parent C/N/O atom, and (iii) the B_{eq} values of 'carbon' were all fixed to 8 Å^2.[7]

To determine the number of guest molecule to be included in the model, the procedure is described as follows (taking ammonia as an example):

The rigid body matrix describing ammonia molecule was added into H-ZSM-5 progressively (N1, N2, N3, N4…). The R-factors (R_{wp}, χ^2) were used to gauge the quality of the Rietveld refinement. When the number of ammonia molecule increased, R_{wp} decreased. This indicates the approaching of the global minimum of the Rietveld refinement procedure. Judging by the chemistry of the intermolecular distances between the ammonia molecules in the derived crystal models, the total number of rigid body matrices can be concluded. In the case of H-ZSM-5 pre-adsorbed with ammonia measured at 25 °C, the best-fit was concluded to contain four ammonia sites per unit cell.

2.4.2 Force-field Modelling Optimisation

Force-field modelling optimisation is a functional form of calculation with the potential energy of atoms based on molecular mechanics. It includes bonding and non-bonding energy functions, with both covalent and non-covalent contributions. The parameters of the energy functions were derived from experimental work and QM calculations.

In Chapters 3 and 4, the force-field modelling optimisation was used to verify the accuracy of the initially derived models, by comparing the interatomic bond distances and bond angles. The pyridine positions were modelled using the corresponding force-field atomic potential energies and compared to the Rietveld derived crystal structures. The framework energy for the zeolite adsorbed with pyridine was calculated using the Forcite modules in Materials Studio v6.0 in collaboration with Dr Qu Jin (Tsang group, Oxford). The zeolite framework was calculated in a pure SiO_2 form, with Al at the T6 site. The force-field of COMPASS27 was used with parameters of o2z (for O), si4z (for Si), al4z (for Al), h1 (for H), c3a (for C), and n2a (for N). The Smart algorithm, by calculating the potential energy overlaps, was used to optimise the geometry and lattice parameters at high quality.[8–10]

2.4.3 Theoretical Calculation – Reaction Energetics

The *ab initio* electronic structure calculations were performed to study p-xylene formation from ethanol and DMF over the BAS in zeolites. The detailed reaction energetics were calculated at the M06-2X/6-311+G(d,p)[11] level of theory, as implemented in the Gaussian 09 package in collaboration with Dr Giannis Mpourmpakis (University of Pittsburgh, USA).[12] The BAS has been modelled as a point proton site in our calculations. The identical computational approach has been shown to be effective in calculating the reaction energetics in the production of p-xylene via cycloaddition between ethylene and DMF.[13] The reaction pathways were first mapped by scanning the potential energy surface (PES) along the reaction coordinate. The energy maximum found along each reaction coordinate was relaxed to a saddle point to locate the actual transition state. All transition states and local minima were obtained by full optimisations and verified by vibrational frequency and Intrinsic Reaction Coordinate (IRC) calculations.[14] In addition, the proton affinities (PA) of all relevant reaction species were calculated at the CBS-QB3[15] level of theory, chosen for its accuracy in calculating the gas-phase thermos-chemistries, as reported by Kostestkyy et al.[16] The PA values were used to quantify the thermodynamic preference of the different species to bind the acidic proton and it is calculated according to the equation below:

$$PA = E_{molecule+H^+} - E_{molecule}$$

where $E_{molecule+H^+}$ and $E_{molecule}$ are the total electronic energies of the protonated and neutral species, respectively, as the electronic energy of a proton is zero.

2.4.4 Theoretical Calculation – Binding Energies Estimation

This ONIOM calculation was performed in collaboration with Dr Giannis Mpourmpakis (University of Pittsburgh, USA). To investigate the adsorption behaviour of ethanol, DMF and ethylene in the pores of the zeolite samples, we used the ONIOM method that was first developed by Morokuma et al.[17] It is a hybrid method that can be applied to large systems using multiple levels of theory. The ONIOM3 (three-layer) method was used for these calculations, applying MM (UFF) calculation for the Low-Level calculations, Semi-Empirical (PM6) calculation for the Intermediate-Model, and QM (hybrid density functional, M06-2X/6-311+G(d,p)) calculation by Truhlar and Zhao for the high-level system.[11,18,19]

The atoms in the Low- and Intermediate-layers were kept frozen in their crystallographic positions, while the High-Level atoms were allowed to relax during geometry optimisations. The gas phase electronic binding energies of the adsorbates were calculated using the following equation:

$$Binding\ energy = E_{ONION3,ads} - E_{ONION3,zeolite} - E_{adsorbate}$$

where $E_{ONION3,ads}$ and $E_{ONION3,zeolite}$ are the energies of the adsorbate species in the zeolite and the empty zeolite pore system, respectively, and $E_{adsorbate}$ is the (high-level) electronic energy of the adsorbates.

2.4.5 Theoretical Calculation – Reaction Profile Calculation

The periodic 3-D H-ZSM-5 zeolite structure of $Si_{96}O_{192}$ with experimental lattice parameters of 20.022×19.899×13.383 $Å^3$ was used to explore the reaction mechanisms in collaboration with Dr Donghai Mei (PNNL, USA). Consistent with the experiments,

the H-ZSM-5 zeolite with the Si/Al ratio of 23 was modelled by replacing four Si atoms at the T6 sites with Al atoms in one unit cell. The resulting negative charges were compensated by adding four H atoms at the O atoms shown in Figure 6.5, forming the BAS, i.e., Si–O(H)–Al of the H-ZSM-5 framework.

In Chapter 6, the DFT theoretical calculations were performed using the CP2K code.[20] The core electrons were represented with norm-conserving Goedecker-Teter-Hutter pseudo-potentials[21–23], and the valence electron wave function was expanded in a double-zeta basis set with polarisation functions[24] along with an auxiliary plane wave basis set with an energy cut-off of 360 eV. The generalised gradient approximation exchange-correlation functional of Perdew, Burke, and Enzerhof was used.[25] The test calculations showed that the total energy change of the reactive system was negligible (<0.01 eV) when the maximum force convergence criteria of 0.001 Hartree/Bohr was used. Each reaction state configuration was optimised with the Broyden-Fletcher-Goldfarb-Shanno algorithm with SCF convergence criteria of 1.0×10^{-8} au. To compensate the long-range van der Waals dispersion interaction between methanol molecules and the zeolite framework, the DFT-D3 scheme[26] with an empirical damped potential term was added into the energies obtained from exchange-correlation functional in all the calculations. The transition states of elementary steps were located using the Climbing Image Nudged Elastic Bands method[27,28] with seven intermediate images along the reaction pathway between the initial and final states.

2.4.6 Theoretical Calculation – Interatomic Distance Estimation

The dynamic behaviour of methanol molecules was investigated using *ab initio* molecular dynamics (AIMD) simulations in collaboration with Dr Donghai Mei (PNNL, USA). The AIMD simulations were performed in the canonical ensemble (NVT) with Nose-Hoover thermostat[29,30] at six different temperatures between the range of 298 - 523 K for a long time period of 15 ps. The time step of 0.5 fs was used in all AIMD simulations. In this case, the H-ZSM-5 zeolite (Si/Al = 95) with three methanol molecules around the T6 site shown in Figure 6.5 was used. The radial pair distribution functions, *g(r)*, between O_m with O5 and O18 adjacent to the Al (T6) atom were calculated using the AIMD trajectories of the final 10,000 steps.

For the zeolite acid-catalysed reaction, the confinement and steric hindrance strongly affect the stabilities of reaction intermediates and transition states.[31–35] To account for the entropic contribution and zero-point energy corrections, Gibbs free reaction energies (ΔG) and Free energy of activation ($\Delta G^{\neq}$) along the associative and reaction mechanisms leading to the formation of DME were calculated using standard thermodynamic method.[36–38]

2.4.7 FT-IR Spectroscopy

The FT-IR measurements were provided by SRIFT-Sinopec, China. For the FT-IR measurements, a self-supported wafer placed in an IR cell was pretreated in vacuum at 400 °C for 2 h. The samples were exposed to 1 Torr of pyridine at 50 °C for 10 min, followed by outgassing at 50, 100, 200, 300 and 400 °C for 5 min, respectively (ramping rate of 10 °C min^{-1}). The FT-IR spectra from 400 to 4000 cm^{-1} were recorded on a Nicolet 5700 FT-IR instrument.

2.4.8 TGA

The TGA measurements of adsorbed pyridine zeolite sample were performed in air (60 cm^3 min^{-1}) up to 600 °C using TA Instruments TGA Q50 at 1 °C min^{-1}.

For the desorption of adsorbed pyridine molecules from H-ZSM-5 (diffusion controlled, 1st order process), the rate constants were calculated using the 1st order rate Arrhenius equation by originally developed by Rouquerol[39] and later improved by Paulik and Paulik[40]:

$$d\alpha/_{dt} = Ae^{\frac{E_{des}}{RT}}(1-\alpha)^n$$

By taking natural log yields:

$$\ln\left(\frac{d\alpha}{dt}\right) = \ln A - \left(\frac{E_{des}}{RT}\right) + \ln(1-\alpha)^n$$

$$\ln\left(\frac{1}{(1-\alpha)^n}\right) = -\frac{E_{des}}{RT} + lnA - \ln\left(\frac{d\alpha}{dt}\right)$$

where α is the fraction of dissociation E_{des} is the activation energy, R is the gas constant (=8.314 J mol^{-1} K^{-1}), T is the reaction temperature (in Kelvin), n is the order of reaction, and A is the Arrhenius pre-exponential factor.

For the desorption of ammonia (1st order process), the desorption activation energies were estimated by the modified Arrhenius equation in the stretched exponential form below at five different temperature ramping rates:[41,42]

$$2lnT_m - ln\beta = \frac{E_{des}}{RT_m} + ln\frac{E_{des}}{AR}$$

where T_m is the peak desorption temperature at a specific β, β is the temperature ramping rate, E_{des} is the desorption energy and A is a numerical constant. Plotting ($2lnT_m - ln\beta$) versus $1/T_m$ for a series of β values allows the estimation of E_{des}.

2.4.9 ^{27}Al ssNMR – Aluminium Environment

All the ssNMR measurements were performed on 400WB AVANCE III Spectrometer at room temperature in collaboration with Dr Lin Ye (Fudan University, China). The pretreatment was carried out at 300 °C for 2 h under vacuum (10^{-1} Pa). According to the electron density difference between four- and six-coordinate Al, ^{27}Al ssNMR was used to study the coordination of Al in H-ZSM-5.[43] For the ^{27}Al ssNMR measurement, the ^{27}Al ssNMR spectrum was obtained at the Larmor frequency of 104.34 MHz. The one pulse sequence was adopted, with a 10° pulse, a delay time of 0.4 s and a scanning number of 8000. The chemical shift was referenced to 1 M $AlCl_3$ aqueous solution.

2.4.10 ^{31}P ssNMR – Acid Sites Determination

The Brønsted acidic properties of were characterised using ^{31}P ssNMR (high-powered decoupling) with probing TMP. For the ^{31}P MAS ssNMR measurement, the sample was

introduced into a glass tube, which was then connected to a vacuum system. The pretreatment was carried out at 300 °C for 2 h under vacuum (10^{-1} Pa). After exposing the sample to TMP vapour at room temperature, the glass tube was then isolated and immersed in liquid nitrogen. Then the content of the glass tube was transferred to a glove box. Under dry nitrogen, the sample was packed into a 4 mm ZrO_2 rotor and closed with Kel-F lids. ^{31}P NMR spectra were acquired at a resonance frequency of 161.9 MHz, using 30° pulses with a recycle delay of 15 s at a speed of 12 kHz. $NH_4H_2PO_4$ was used as a standard sample for chemical shift reference and the external intensity standard to quantify the signal in the ^{31}P ssNMR spectra. The error between the amount of BAS that calculated from the ^{27}Al and ^{31}P ssNMR measurements can be explained by the systemic errors in the measurements of peak area and sample weight.

2.4.11 ^{1}H-^{15}N ssNMR - Pyridine Adsorption

After adsorption of pyridine at room temperature, the glass tube was immersed in liquid nitrogen and switched off. Then the glass tube was transferred to a glove box. Under dry nitrogen condition, the sample was compacted into a 4 mm ZrO_2 rotor and closed with Kel-F lids. Cross coupling ^{1}H-^{15}N ssNMR spectra were obtained at a MAS speed of 6 kHz with proton pulse duration of 2.8 μs, a contact time of 2 ms, a recycle delay of 3 s and several transients of 1000.

2.4.12 Scanning Electron Microscopy (SEM)

SEM provides the surface information of a sample. In this thesis, SEM is employed as a supporting technique to show the crystal size and size distribution of the zeolite samples.

SEM first focuses electron beams that are controlled by coils over a defined area of the sample surface (see Figure 2.2). The electrons interact (mainly via reflection) with the surface, then are captured by appropriate detectors in the microscope.[44] After coating the zeolite samples with a thin layer of gold (to create/ensure a conducting surface), the morphologies were observed using a Philips XL30 FEG SEM equipped with an EDAX energy dispersive X-ray spectrometer (EDS) (Oxford ISIS-Energy) in SRIFT-Sinopec, China.

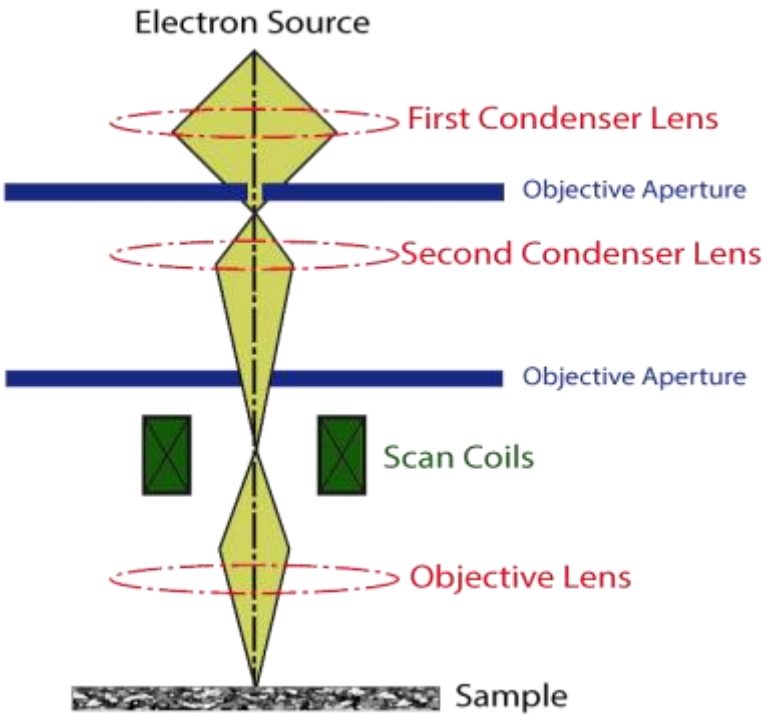

Figure 2.2. Schematic of a SEM microscope. The detectors are not shown.[44]

2.4.13 Transmission Electron Microscopy (TEM)

TEM works on a similar principle as a conventional optical microscopy. In TEM microscope (see Figure 2.3), a beam of electrons is 'transmitted' through an ultra-thin sample coated on a copper grid. The beam of electrons interacts with the electrons of the sample atoms when the beam is 'transmitted' through the sample. An image is therefore captured based on the electron-sample atom interactions from solid angle scattering.[45,46] The detectors in TEM capture the transmitted electrons; unlike in SEM, the detectors capture electrons from surface reflection. The intensity of the electron-sample interactions depends on the atomic number of the sample atoms: an atom with more electrons interacts with the electron beam more strongly, creating a darker area in the image, and *vice versa*.

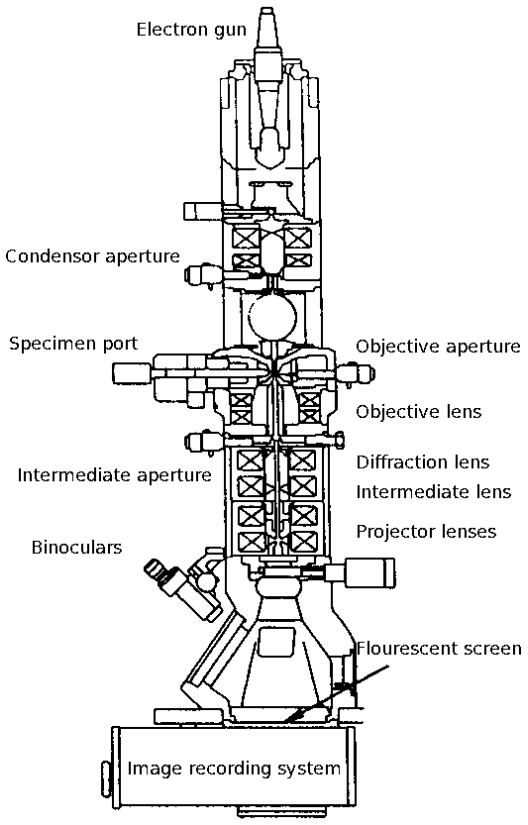

Figure 2.3. Schematic of a TEM microscope, with a fluorescent screen detector.[45]

In this thesis, TEM was measured by FEI TECNAI-20 with an accelerating voltage of 200 kV in SRIFT-Sinopec, China. The TEM specimen was prepared by dispersing the sample in ethanol and dropping onto a holey carbon film supported on a copper grid, then dried in air.

2.4.14 Inductive Coupled Plasma-Atomic Emission Spectroscopy (ICP-AES)

ICP-AES is an emission spectroscopic technique that first excites atoms and ions by ICP, then measures the electromagnetic radiation emitted from decaying by AES. Consequently, the characteristic emission energy by different excited atoms/ions can allow elemental identification.[47,48] ICP-AES provides quantitative elemental information of a sample, where the intensity of the emission shows the concentration of the corresponding element.

Once an aqueous sample (by solving zeolites in a known concentration of acid/alkali) is injected into the ICP-AES instrument, it is atomised into a mist-like cloud. This cloud is then thermally excited by ICP (argon) that has a temperature of close to 7,000 °C. The thermally excited electrons relax to the ground state, which emits an electromagnetic radiation that the energy is element specific.[49]

In this thesis, the ICP-AES data of the solid samples was measured by Hitachi P-4010/ICP-AES, provided by SRIFT-Sinopec, China.

2.4.15 BET Isotherm - Surface Area Measurement

The BET (named after Brunauer, Emmett and Teller) isotherm is a common technique used to estimate the surface area of a sample.[50] The technique is based on the Langmuir theory[51] for monolayer adsorption and with the same assumptions applying on multilayer adsorption, which assumed the layers with an exposed surface are in equilibrium with adsorbate species. This process is described by the following equation:

$$\frac{P}{V(P_0-P)} = \frac{1}{V_m C} + \frac{(C-1)P}{V_m C P_0}$$

where V refers to the volume of nitrogen gas adsorbed by the sample at pressure P, V_m is the volume by monolayer adsorption, P_o is the pressure with saturated adsorbate, and C is the BET constant that is a function of the heat of adsorption.

The N_2 sorption isotherms were obtained at -194 °C on a Micromeritics Tristar-3000 apparatus in collaboration with Dr Lin Ye (Fudan University, China). The samples were pretreated for 4 h under vacuum at 350 °C. The specific surface area was calculated using the BET method. The total pore volume was obtained by converting the amount adsorbed at a relative pressure of 0.995 to the volume of liquid nitrogen. The microporous surface area and volume were determined by the t-plot analysis of the adsorption branch of the isotherm. The pore size distributions of the samples were analysed from the desorption branch of the isotherm by the BJH method.[52]

2.4.16 Gas Chromatography-Mass Spectrometry (GC-MS)

GC-MS is a combined tool (GC with MS) for a conclusive proof of chemical identity, despite some limitations. Indeed, GC or MS on its own is not sufficient for a reliable identification of specific compounds. As shown in Figure 2.4, the first part, GC, is effective in the separation of molecules from a mixture using a capillary column, due to the molecular difference in interacting with the stationary phase of the column. Different molecules have different retention times in the capillary, before being eluted. This allows the second part, MS, to separately identify the eluted molecules, where the MS ionises and breaks the molecules into ionised fragments for the determination of the charge-to-mass ratio.[53]

In this thesis, GC-MS was used to identify liquid products from the catalytic conversion of DMF and ethanol, in collaboration with Ivo F. Teixeira (Tsang group, Oxford), using Agilent 6890 and Agilent MSD 5973 (N) calibrated with pure standards.[54]

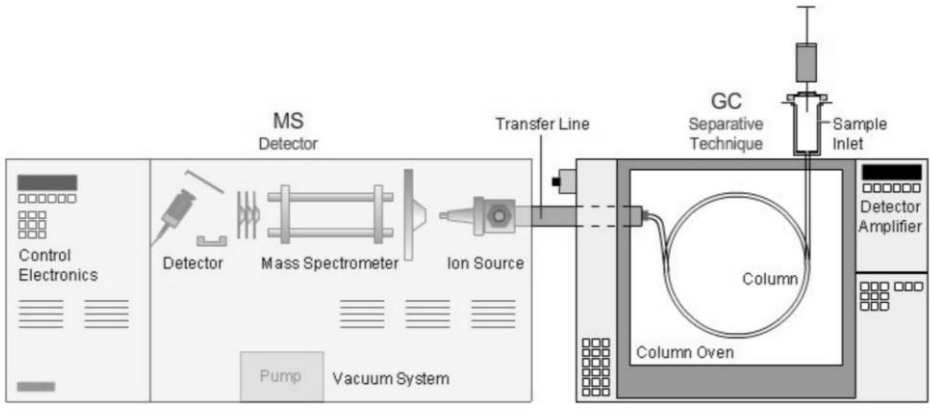

Figure 2.4. Schematic of a GC-MS instrument.[53]

2.4.17 Gas Chromatography (GC)

The components in the gaseous mixture are separated based on the difference in vapour pressure between the mobile phase (helium as an inert carrier gas) and the gaseous analyte. In this thesis, the gaseous products were analysed by Perkin Elmer Autosystem XL Arnel Gas Phase GC-FID-Methanator to reveal the concentrations of CO, CH_4, CO_2, and other gases in collaboration with Ivo F. Teixeira (Tsang group, Oxford).[55,56]

The GC instrument in this part is slightly different from the part in GC-MS, which also contains a methanator and a flame ionisation detector (FID). The methanator is a device made by nickel, converting the carbon-containing gaseous compounds into methane after the gaseous compounds have eluted from the column. Then the FID measures the quantity of methane from the methanator at a given time.[57]

2.5 References

(1) Argauer, R. J.; Landolt, G. R. Google Patents November 14, 1972.

(2) Parker, J. E.; Thompson, S. P.; Cobb, T. M.; Yuan, F.; Potter, J.; Lennie, A. R.; Alexander, S.; Tighe, C. J.; Darr, J. a.; Cockcroft, J. C.; Tang, C. C. *J. Appl. Crystallogr.* **2011**, *44* (1), 102–110.

(3) Thompson, S. P.; Parker, J. E.; Marchal, J.; Potter, J.; Birt, A.; Yuan, F.; Fearn, R. D.; Lennie, A. R.; Street, S. R.; Tang, C. C. *J. Synchrotron Radiat.* **2011**, *18* (4), 637–648.

(4) Thompson, S. P.; Parker, J. E.; Potter, J.; Hill, T. P.; Birt, A.; Cobb, T. M.; Yuan, F.; Tang, C. C. *Rev. Sci. Instrum.* **2009**, *80* (7).

(5) Heo, N. H.; Kim, C. W.; Kwon, H. J.; Kim, G. H.; Kim, S. H.; Hong, S. B.; Seff, K. *J. Phys. Chem. C* **2009**, *113* (46), 19937–19956.

(6) Thompson, P.; Cox, D. E.; Hastings, J. B. *J. Appl. Crystallogr.* **1987**, *20* (2), 79–83.

(7) Geologicalsciences, D.; Austin, U. T.; Downs, R. T.; Gibbs, G. V; Boisen, M. B.; Birch, J. B. **1995**, *80*, 680–690.

(8) Sun, H.; Ren, P.; Fried, J. R. *Comput. Theor. Polym. Sci.* **1998**, *8* (1–2), 229–246.

(9) Sun, H. *J. Phys. Chem.* **1998**, *5647* (98), 7338–7364.

(10) Rigby, D.; Sun, H.; Eichinger, B. E. *Polym. Int.* **1997**, *44* (October), 311–330.

(11) Zhao, Y.; Truhlar, D. G. *Theor. Chem. Acc.* **2008**, *120* (1–3), 215–241.

(12) Gaussian09, R. A. *Inc., Wallingford CT* **2009**.

(13) Nikbin, N.; Do, P. T.; Caratzoulas, S.; Lobo, R. F.; Dauenhauer, P. J.; Vlachos, D. G. *J. Catal.* **2013**, *297*, 35–43.

(14) Hratchian, H. P.; Schlegel, H. B. *J. Chem. Phys.* **2004**, *120* (21), 9918–9924.

(15) Montgomery Jr, J. A.; Frisch, M. J.; Ochterski, J. W.; Petersson, G. A. *J. Chem. Phys.* **1999**, *110* (6), 2822–2827.

(16) Kostestkyy, P.; Maheswari, J. P.; Mpourmpakis, G. *J. Phys. Chem. C* **2015**, *119* (28), 16139–16147.

(17) Morokuma, K.; Froese, R. D.; Dapprich, S.; Komaromi, I.; Khoroshun, D.; Byun, S.; Musaev, D. G.; Emerson, C. L. In *Abstracts of Papers of the American Chemical Society*; Amer Chemical Soc 1155 16th St, NW, Washington, DC 20036 USA, 1998; Vol. 215, pp U218–U218.

(18) Stewart, J. J. P. *J. Mol. Model.* **2007**, *13* (12), 1173–1213.

(19) Rappé, A. K.; Casewit, C. J.; Colwell, K. S.; Goddard III, W. A.; Skiff, W. M. *J. Am. Chem. Soc.* **1992**, *114* (25), 10024–10035.

(20) VandeVondele, J.; Krack, M.; Mohamed, F.; Parrinello, M.; Chassaing, T.; Hutter, J. *Comput. Phys. Commun.* **2005**, *167* (2), 103–128.

(21) Goedecker, S.; Teter, M.; Hutter, J. *Phys. Rev. B* **1996**, *54* (3), 1703.

(22) Hartwigsen, C.; Gœdecker, S.; Hutter, J. *Phys. Rev. B* **1998**, *58* (7), 3641.

(23) Krack, M.; Parrinello, M. *Phys. Chem. Chem. Phys.* **2000**, *2* (10), 2105–2112.

(24) VandeVondele, J.; Hutter, J. *J. Chem. Phys.* **2007**, *127* (11), 114105.

(25) Perdew, J. P.; Burke, K.; Ernzerhof, M. *Phys. Rev. Lett.* **1996**, *77* (18), 3865.

(26) Grimme, S.; Antony, J.; Ehrlich, S.; Krieg, H. *J. Chem. Phys.* **2010**, *132* (15), 154104.

(27) Henkelman, G.; Uberuaga, B. P.; Jónsson, H. *J. Chem. Phys.* **2000**, *113* (22), 9901–9904.

(28) Mills, G.; Jónsson, H.; Schenter, G. K. *Surf. Sci.* **1995**, *324* (2), 305–337.

(29) Nosé, S. *J. Chem. Phys.* **1984**, *81* (1), 511–519.

(30) Bussi, G.; Donadio, D.; Parrinello, M. *J. Chem. Phys.* **2007**, *126* (1), 14101.

(31) Bhan, A.; Gounder, R.; Macht, J.; Iglesia, E. *J. Catal.* **2008**, *253* (1), 221–224.

(32) Gounder, R.; Iglesia, E. *J. Am. Chem. Soc.* **2009**, *131* (5), 1958–1971.

(33) Gounder, R.; Iglesia, E. *Acc. Chem. Res.* **2011**, *45* (2), 229–238.

(34) Jones, A. J.; Iglesia, E. *Angew. Chem. Int. Ed.* **2014**, *53* (45), 12177–12181.

(35) Jones, A. J.; Zones, S. I.; Iglesia, E. *J. Phys. Chem. C* **2014**, *118* (31), 17787–17800.

(36) Song, W.; Liu, Y.; Baráth, E.; Wang, L. L.; Zhao, C.; Mei, D.; Lercher, J. A. *ACS Catal.* **2016**, *6* (2), 878–889.

(37) Zhi, Y.; Shi, H.; Mu, L.; Liu, Y.; Mei, D.; Camaioni, D. M.; Lercher, J. A. *J. Am. Chem. Soc.* **2015**, *137* (50), 15781–15794.

(38) Mei, D.; Lercher, J. A. *AIChE J.* **2017**, *63* (1), 172–184.

(39) Rouquerol, J. *Bull. Soc. Chim. Fr.* **1964**, *1*, 31–39.

(40) Paulik, J.; Paulik, F. *Anal. Chim. Acta* **1971**, *56* (2), 328–331.

(41) Corma, A.; Forn, V.; Melo, F. V. *Zeolites* **1987**, *7*, 559–563.

(42) Lonyi, F.; Valyon, J. *Microporous Mesoporous Mater.* **2001**, *47* (2–3), 293–301.

(43) Chu, Y.; Yu, Z.; Zheng, A.; Fang, H.; Zhang, H.; Huang, S. J.; Liu, S. Bin; Deng, F. *J. Phys. Chem. C* **2011**, *115* (15), 7660–7667.

(44) Oatley, C. W.; Nixon, W. C.; Pease, R. F. W. *Adv. Electron. Electron Phys.* **1966**, *21*, 181–247.

(45) Williams, D. B.; Carter, C. B. In *Transmission electron microscopy*; Springer, 1996; pp 3–17.

(46) Blake, A. J.; Clegg, W. *Crystal Structure Analysis: Principles and Practice*; Oxford University Press, 2009; Vol. 13.

(47) Mermet, J. M. *J. Anal. At. Spectrom.* **2005**, *20* (1), 11–16.

(48) Stefansson, A.; Gunnarsson, I.; Giroud, N. *Anal. Chim. Acta* **2007**, *582* (1), 69–74.

(49) Skujins, S. *A short Guid. to Vista Ser. ICP-AES Oper. Varian Int. AG, Zug, Version* **1998**, *1*.

(50) Brunauer, S.; Emmett, P. H.; Teller, E. *J. Am. Chem. Soc.* **1938**, *60* (2), 309–319.

(51) Langmuir, I. *J. Am. Chem. Soc.* **1918**, *40* (9), 1361–1403.

(52) Suzuki, T.; Okuhara, T. *Microporous Mesoporous Mater.* **2001**, *43* (1), 83–89.

(53) Hussain, S. Z.; Maqbool, K. *Int. J. Curr. Sci.* **2014**, *13*, 116–126.

(54) Kreissl, H. T.; Nakagawa, K.; Peng, Y.-K.; Koito, Y.; Zheng, J.; Tsang, S. C. E. *J. Catal.* **2016**, *338*, 329–339.

(55) Liao, F.; Woon, T.; Lo, B.; Sexton, D.; Qu, J.; Wu, C.; Chi, S.; Tsang, E. *Catal. Sci. Technol.* **2015**, *5*, 887–896.

(56) Wu, C.-T.; Yu, K. M. K.; Liao, F.; Young, N.; Nellist, P.; Dent, A.; Kroner, A.; Tsang, S. C. E. *Nat. Commun.* **2012**, *3*, 1050.

(57) Adams, R. P. *Quadrupole mass Spectrosc.* **2001**.

Chapter 3. Elucidation of Adsorbate Structures and Interactions on Brønsted Acid Sites in H-ZSM-5 by Synchrotron Powder X-ray Diffraction

This chapter investigates a microporous H-ZSM-5 that hosts pyridine, methanol and ammonia as guest molecules for the elucidation of their adsorption geometries and interactions with the BAS by SXRD and Rietveld refinement. By carefully studying the interatomic distances and angles, the locations of the BAS are *for the first time* identified at the framework T6 and O18 sites in this given synthesised H-ZSM-5 of Si/Al ratio of 20.4.

The work in this chapter was published in Angewandte Chemie International Edition as a back cover, 'Elucidation of Adsorbate Structures and Interactions on Brønsted Acid Sites in H-ZSM-5 by Synchrotron X-ray Powder Diffraction' by **Lo, B. T. W.,** Ye, L., et al. with equal contribution.

A Journal of the Gesellschaft Deutscher Chemiker

Angewandte Chemie

GDCh

International Edition

www.angewandte.org

2016–55/20

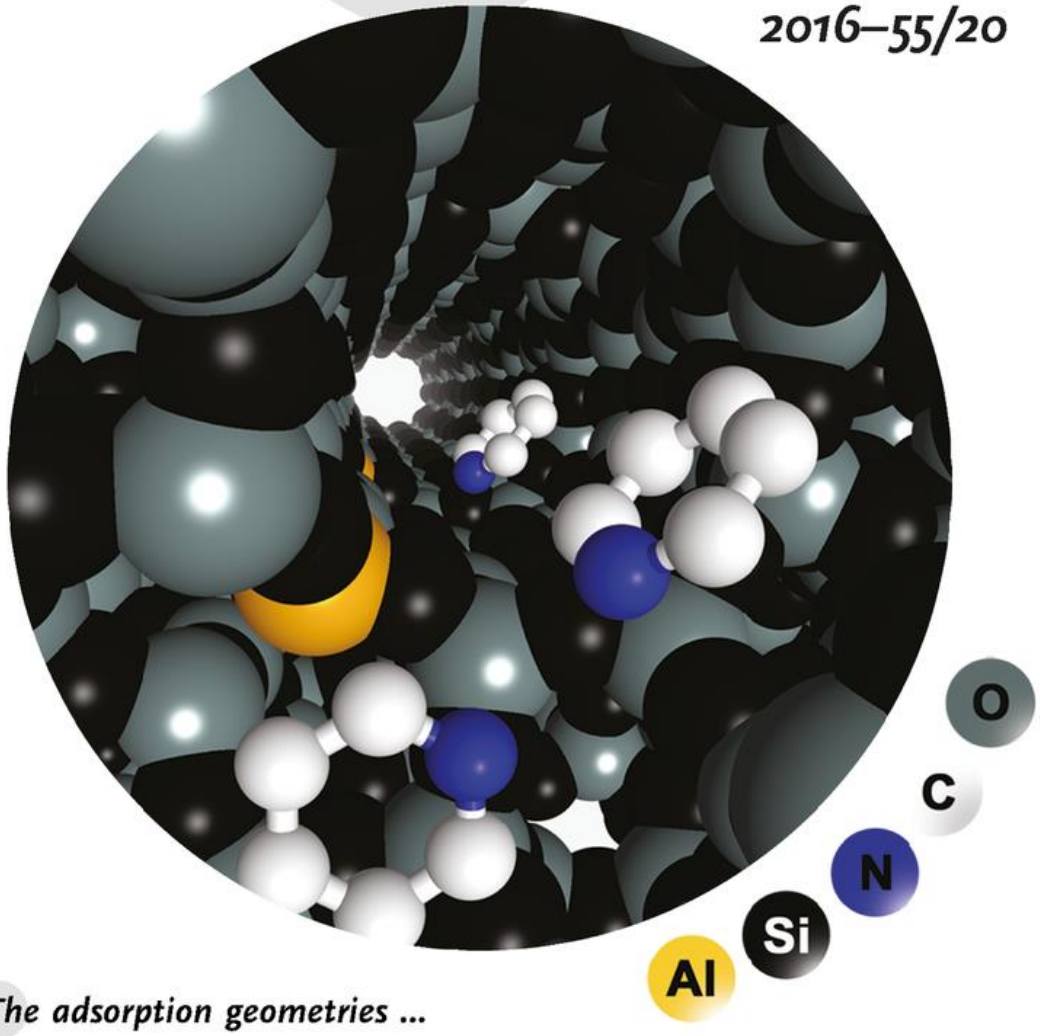

The adsorption geometries ...

... and interactions of pyridine molecules with the Brønsted acid sites of microporous zeolite H-ZSM-5 were studied. In their Communication on page 5981 ff. S. C. E. Tsang et al. report on the adsorption of pyridine molecules in H-ZSM-5. The image was generated by an in situ synchrotron X-ray diffraction technique combined with Rietveld refinement, which is based on the slight but significant alternation in scattering parameters of framework atoms modified by the pyridine molecules.

WILEY-VCH

3.1 Introduction

Traditionally, adsorbates containing light elements such as C, N and O are difficult to be located by X-ray techniques, as X-ray only 'sees' electrons. However, such adsorbates can give rise to a slight but significant alteration in the scattering parameters of the framework atoms in close proximity. In this way, Brønsted basic molecules such as pyridine, methanol, and ammonia (C_5H_5N, CH_3OH and NH_3) can act as chemical probes for the BAS in zeolites. By using modern SXRD instrumentation combined with Rietveld refinement, the acid-base interactions can be revealed. It clearly suggests the intrinsic acidity is not the only parameter that influences catalytic performance, but the effect of the zeolite framework should also be considered.[1] To achieve stereo-specificity like in enzyme systems, the tertiary structure of the adsorbate molecules will determine the spatial conformation, as well as the nature of H-bonding about the zeolite framework.

3.2 Conventional Characterisation for the Fresh H-ZSM-5 Sample

The fresh H-ZSM-5 sample was characterised extensively using conventional techniques. In short summary, the fresh H-ZSM-5 sample is uniform, highly crystalline, and possesses predominantly only one type of Al (and hence BAS) within the framework. As determined by ICP-AES and ssNMR, the structural formula of the H-ZSM-5 is $H_{4.48}Al_{4.48}Si_{91.52}O_{192}$; hence each asymmetric unit (4 asymmetric units per unit cell) possesses about 1 Al site.

3.2.1 SEM, TEM and BET

The SEM and TEM images (see Figure 3.1) clearly show a uniform distribution of crystal that has a mean particle size of *ca.* 2 μm × 1 μm × 1 μm. The uniform, micron particle size and high quality crystallinity ensure an accurate and reliable Rietveld refinement of the corresponding SXRD data. As measured by BET isotherm, the H-ZSM-5 particles has a surface area of 330 m^2 g^{-1}. The calculated micropore volume (see Figure 3.2) is 0.179 cm^3 g^{-1}, which falls in the range of a typical MFI structure.

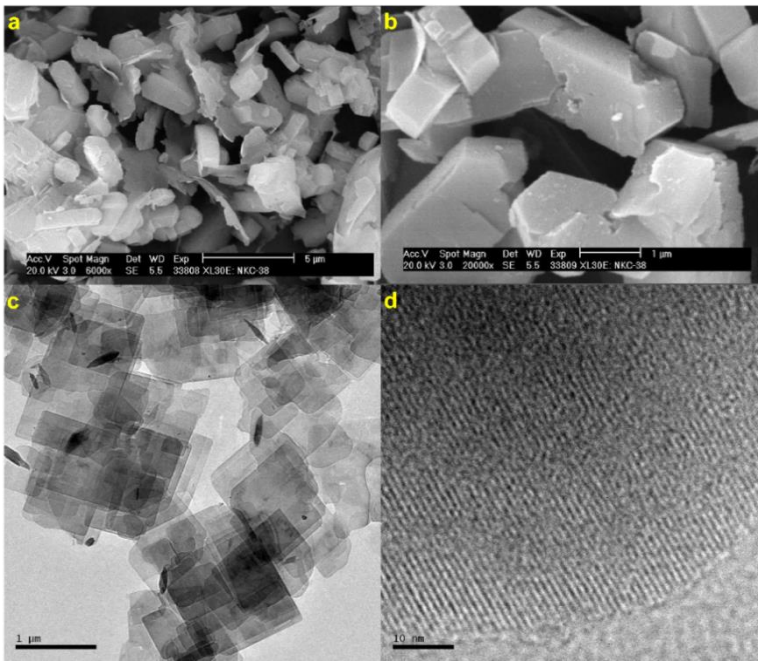

Figure 3.1. SEM and TEM images, showing the particle size and the crystallinity of the crystals: (**a**) SEM (×6000), (**b**) SEM (×20000), (**c**) TEM, and (**d**) high-resolution TEM.

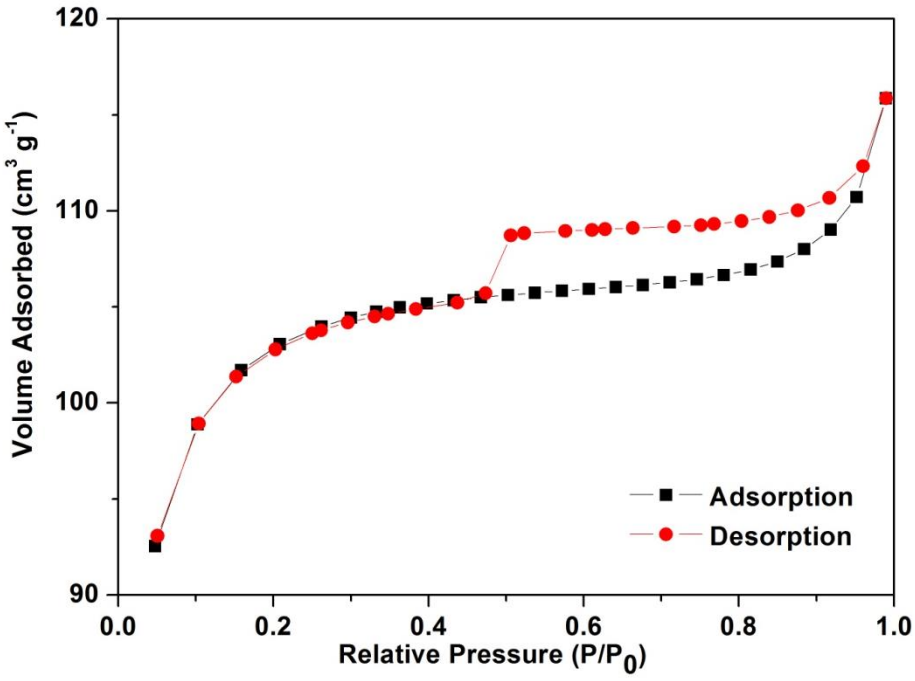

Figure 3.2. N_2 sorption isotherm of H-ZSM-5.

3.2.2 ^{27}Al ssNMR Spectroscopy

The ^{27}Al ssNMR measurement was performed on the H-ZSM-5 sample to determine the Al quantity and environment. There are three peaks observed in the ^{27}Al ssNMR spectrum (see Figure 3.3): (i) a sharp peak at 56 ppm, which is assigned to framework-Al, (ii) a small peak at 1 ppm, which is assigned to EFAl, and (iii) a spinning sideband at -36 ppm. Based on the integrated peak area between (i) and (ii), the quantity ratio between framework-Al and EFAL is 17:1. In addition, assuming all framework-Al are exposed on the inner surface, the amount of BAS is calculated to be 0.78 mmol g^{-1}.

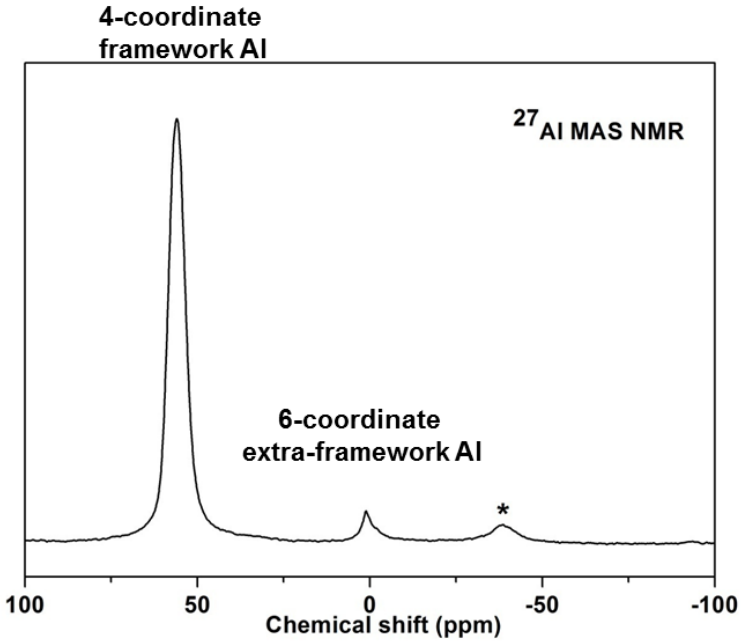

Figure 3.3. ^{27}Al ssNMR spectrum of H-ZSM-5 measured at room temperature, showing a sharp peak at 56 ppm and a small peak at 1 ppm. The asterisk denotes the spinning sideband. This indicates most Al atoms are located at one specific T-site.[2]

3.2.3 ^{31}P ssNMR Spectroscopy

After studying the Al environments, the types and quantity of BAS will be revealed using ^{31}P ssNMR with probing TMP. In the ^{31}P ssNMR spectrum (see Figure 3.4), there is only one sharp and symmetrical peak at -4 ppm, which manifests only one type of BAS in the sample.[3] As the acidity of H-ZSM-5 is relative to ∠Al-O-Si, the proton of the BAS should reside on the same framework O atom. Together with the ICP-AES characterisation, the chemical formula of this H-ZSM-5 sample can be written as $H_{4.48}Al_{4.48}Si_{91.52}O_{192}$ (which corresponds to the actual number of BAS). The amount of BAS is determined to be 0.76 mmol g^{-1}. Consistent with the ^{27}Al ssNMR result, there is almost only one type of BAS in the H-ZSM-5 sample.

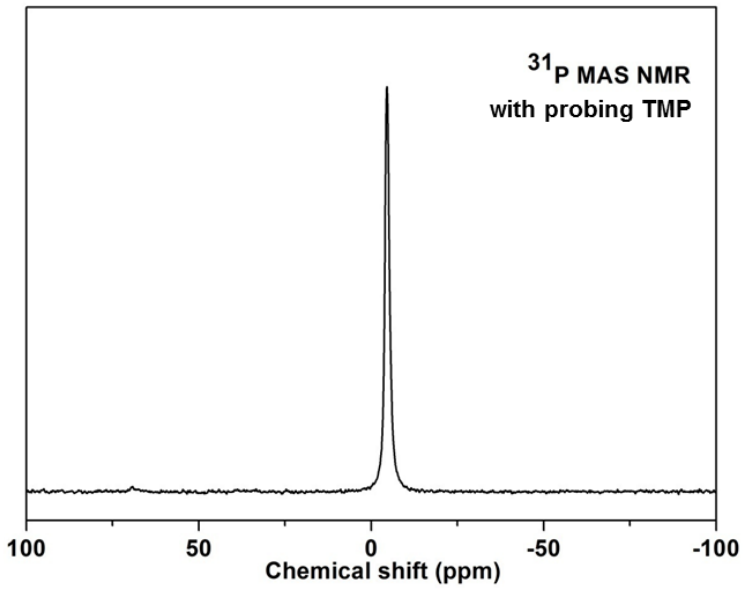

Figure 3.4. ^{31}P ssNMR spectrum of H-ZSM-5 with probing TMP, showing a nearly symmetrical peak at -4 ppm at room temperature. The asterisk denotes the spinning sideband. This indicates the Al distribution is uniform.[2]

3.2.4 SXRD

The crystal structure of H-ZSM-5 is generated from the SXRD pattern (see Figure 3.5) showing several unit cells in Figure 3.6. The crystal structure of H-ZSM-5 has a space group of *Pnma* (8 equivalent positions). This means a unit cell can be viewed as four asymmetric units, each possessing a symmetry mirror plane in between that is perpendicular to [010] (as shown in Figure 3.6). Provided the distribution of Al is uniform as determined by ^{31}P ssNMR with probing TMP, this means each asymmetric unit contains about 1 Al site.

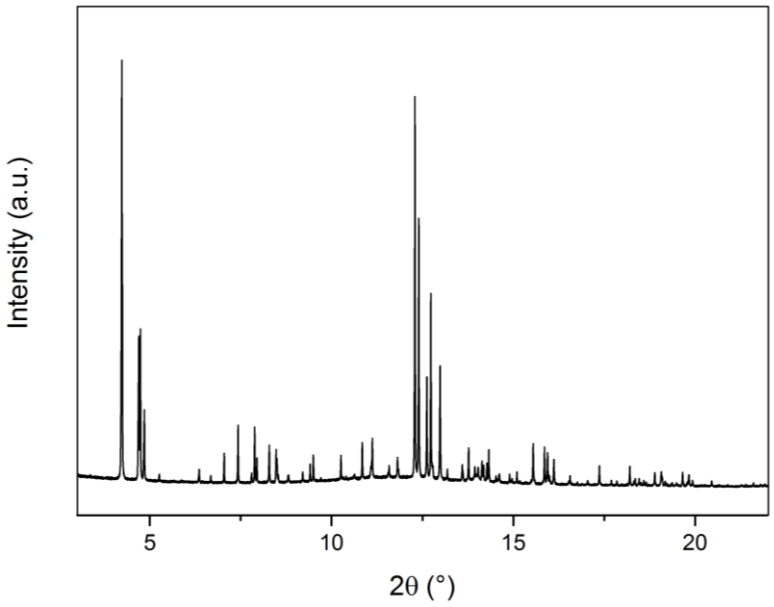

Figure 3.5. SXRD pattern of the fresh H-ZSM-5 sample, the sharp and symmetric peaks suggest high sample crystallinity and large particle size.

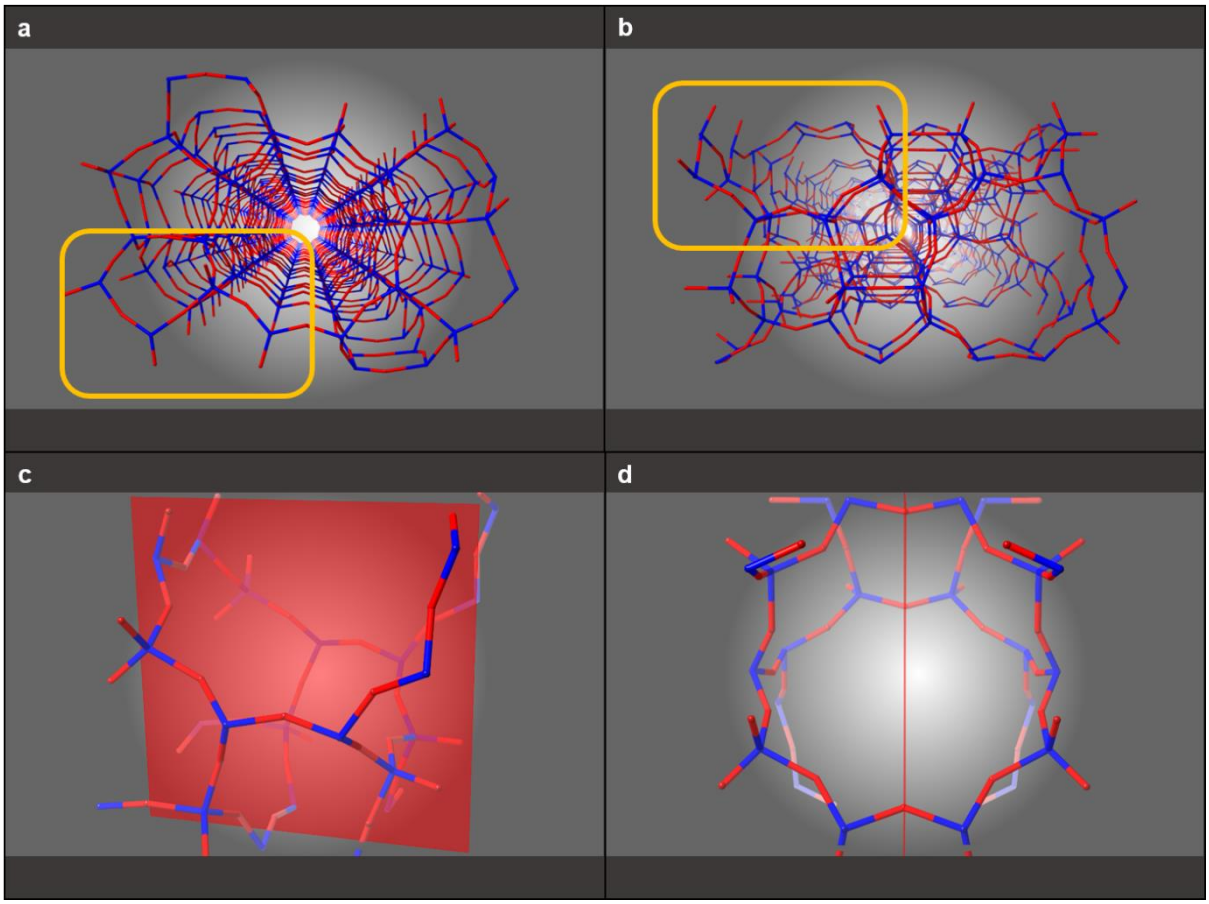

Figure 3.6. Published crystal structures of H-ZSM-5 by Heo et al.[4], showing several unit cells viewing from the (**a**) [010] (straight channel) and (**b**) [100] directions (sinusoidal channel), and one asymmetric unit viewing from the (**c**) [010] and (**d**) [100] directions, possessing a symmetry mirror plane in between which is perpendicular to [010] as shown in red. Atoms are represented in ball/sticks: blue = Si/Al and red = O.

3.3 Results and Discussion

In this section, H-ZSM-5 pre-adsorbed with probing pyridine is used as the primary example, alongside methanol and ammonia, to elucidate the adsorbate-framework interactions at an atomistic level.

3.3.1 TGA

From the TGA (blue curve in Figure 3.7(a)) with pre-adsorbed pyridine, the desorption process of pyridine is under a diffusion controlled regime with typical low desorption temperatures below 380 °C. From weight calibration, 6.02(1) pyridine molecules were desorbed from room temperature to 600 °C with no evidence of further desorption of pyridine beyond (due to the levelling of the thermal baseline). This corresponds to 1.50 pyridine molecules per BAS. From the integrated peak area of the differential data (black curve in Figure 3.7(a)), the sample contains 1.00 strongly bound and 0.50 less strongly bound pyridine molecules per BAS. One pyridine desorbs at a lower temperature, while the other at a higher temperature, giving a roughly 1:2 molecular ratio (see Figure 3.7(b)). Therefore, this implies the co-existence of two distinct pyridine behaviours per BAS, a monomeric interaction ($PyrH^+$) and a dimeric interaction ($[PyrH\cdots Pyr]^+$). It is well known that the BAS in H-ZSM-5 are strongly acidic, which can readily protonate most basic organic adsorbates.[15] Thus, in the dimeric form, the second pyridine molecule is held by the primary protonated pyridinium ion through a weaker H-bonding interaction. The second pyridine is hence expected to be less strongly adsorbed than any protonated (first) pyridinium ion.

The apparent pyridine desorption energies (E_{des}) for the two pyridine desorption profiles are estimated by the 1st order linear plots derived from the TGA traces (see

Figure 3.8). They correspond to 23.31(3) kJ mol^{-1} and 39.94(5) kJ mol^{-1}. The low activation energies reflect typical diffusion limitations due to the micro-porosity of the H-ZSM-5.[5]

Similarly, from the TGA experiments of H-ZSM-5 independently pre-adsorbed with methanol and ammonia as displayed in Figure 3.9, two different forms of methanol interactions and three different forms of ammonia interactions are identified.

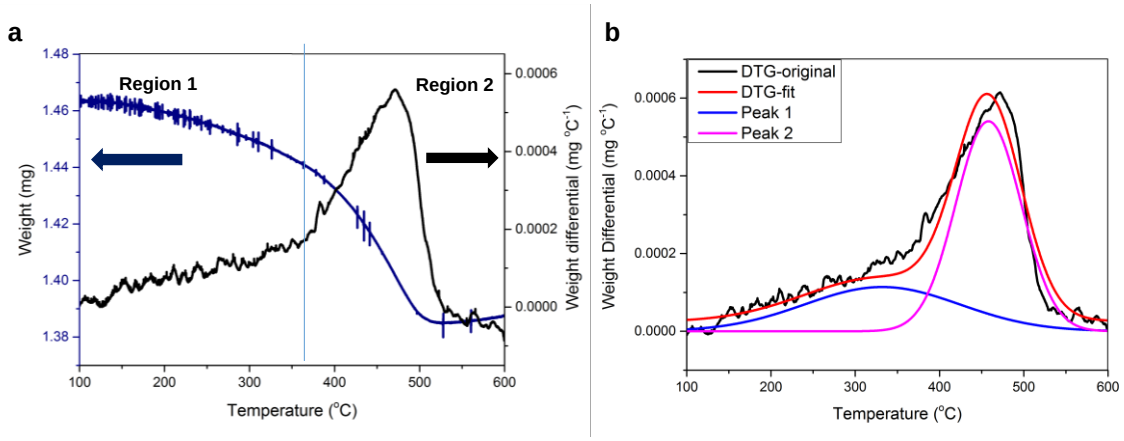

Figure 3.7. TGA of H-ZSM-5 sample pre-adsorbed with pyridine. (**a**) TGA and its corresponding differential curve measured at 1 °C min^{-1}, and (**b**) the peak fit of the differential curve with Peak 1 at 332 °C and Peak 2 at 458 °C, giving an area ratio of about 1:2.

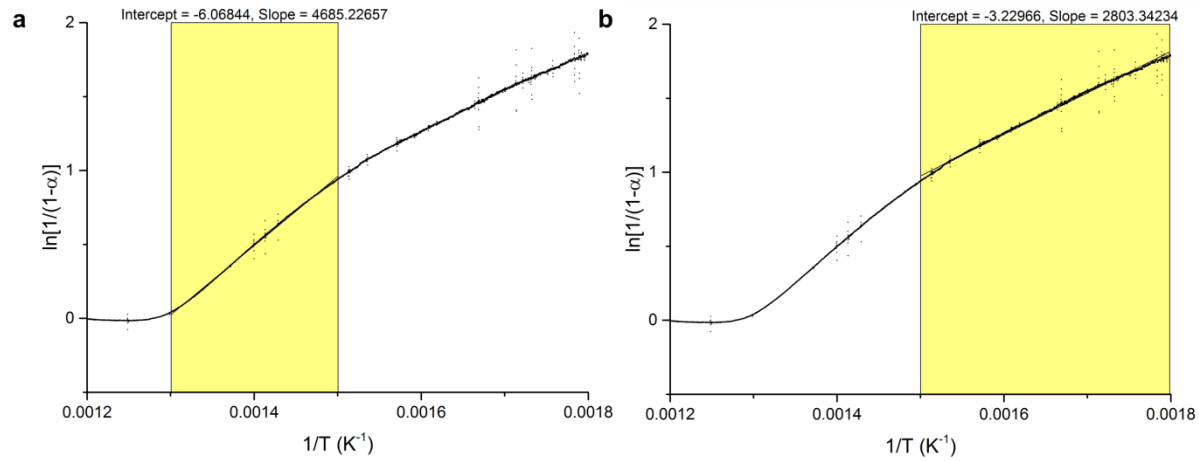

Figure 3.8. Activation energies derived from the TGA traces. (**a**) Above 380 °C, corresponds to E_{des} of 38.94(5) kJ mol^{-1}, and (**b**) below 380 °C, corresponds to E_{des} of 23.31(3) kJ mol^{-1}. Note that α is the fraction of desorption of pyridine.

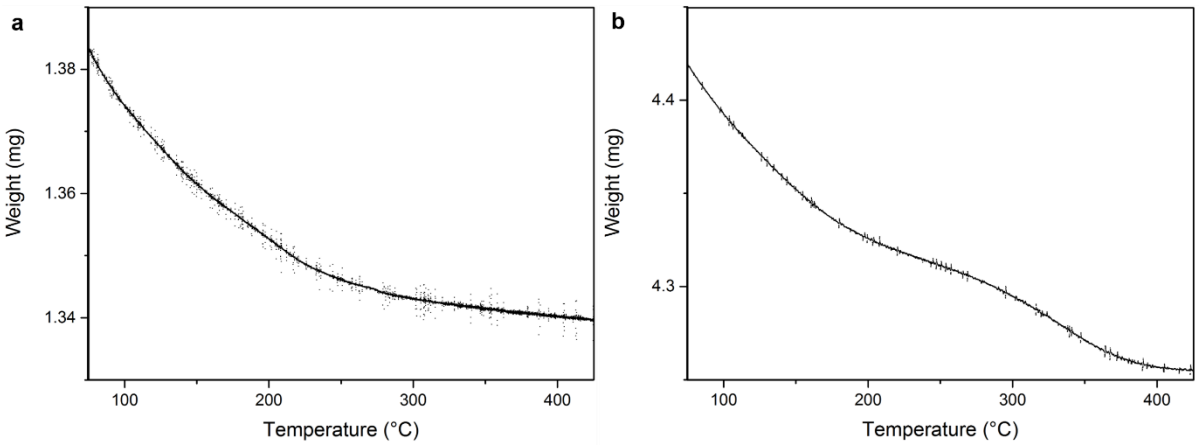

Figure 3.9. TGA of H-ZSM-5 pre-adsorbed with (**a**) ammonia and (**b**) methanol, at 1 °C min^{-1}.

3.3.2 *In situ* FT-IR Spectroscopy

FT-IR is widely used to study the interactions between pyridine and zeolite acid sites.[6,7] The *in situ* FT-IR spectra of the H-ZSM-5 samples pre-adsorbed with pyridine at increasing temperatures are displayed in Figure 3.10. The peak at 1540 cm^{-1} is generally ascribed to C-C stretching modes of the protonated pyridinium ion.[6]

The existence of pyridine dimer in zeolites is well studied, despite an absence of a characteristic peak in FT-IR. The peak at 1450-1490 cm^{-1} arises from the C-C stretches of the weakly coordinated pyridine complex. The peak can be caused by either physisorbed pyridine or by the secondary pyridine in $[PyrH\cdots Pyr]^+$. But it is highly unlikely to be caused by physisorbed pyridine, as this peak still exists at the 100 °C measurement. Upon elevated temperatures, the change in the ratio of the peak intensity of 1540 to 1450 cm^{-1} signifies the decomposition of $[PyrH\cdots Pyr]^+$ to $[PyrH]^+$.[6,7]

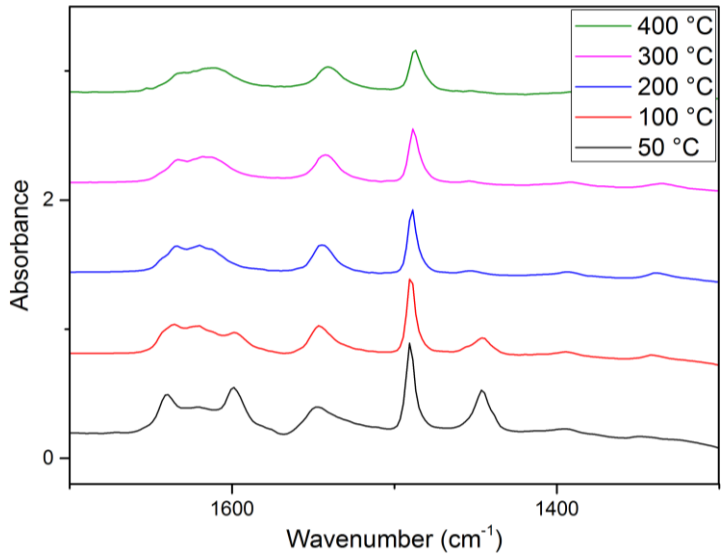

Figure 3.10. FT-IR spectra of H-ZSM-5 pre-adsorbed with pyridine at increasing temperature. The peaks at 1450, 1490 and 1540 cm^{-1} are ascribed to the acid-base interactions of pyridine with the H-ZSM-5 framework.

3.3.3 ^{1}H-^{15}N ssNMR Spectroscopy

Aside from FT-IR and TGA, we also employed ^{1}H-^{15}N cross polarisation ssNMR spectroscopy to qualitatively differentiate various pyridine adsorption structures in the H-ZSM-5. From the ^{1}H-^{15}N ssNMR spectrum (see Figure 3.11), two peaks are identified at -92.8 ppm (broad peak) and -176.0 ppm (sharp peak). The former broad peak can be attributed to a ^{15}N-pyridine molecule with a long-range coupling with H^{+}, which implies the formation of $[PyrH\cdots Pyr]^{+}$.[8,9] Whereas the latter sharp peak matches with the typical literature peak value of pyridinium ion ($PyrH^{+}$) with a stronger ^{1}H-^{15}N coupling for the greater downshift in the chemical shift of the ^{15}N of pyridine.[10]

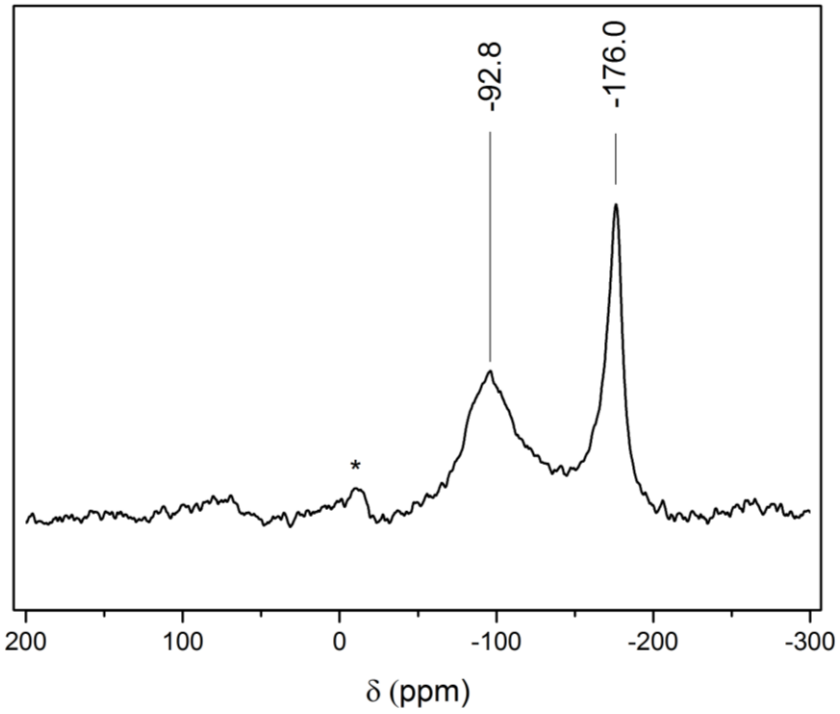

Figure 3.11. ^{1}H-^{15}N cross coupling ssNMR spectrum of H-ZSM-5 pre-adsorbed with pyridine, showing two types of pyridine interactions within the H-ZSM-5 framework at room temperature as indicated. The asterisk denotes the spinning sideband.

3.3.4 SXRD

The typical characterisation techniques, namely TGA, FT-IR and ssNMR, have provided the global information between the zeolite framework and adsorbate molecules. However, the local environment (i.e., where the atomic positions of the probe molecule locate about the BAS) has not been revealed. In this section, we employed SXRD with Rietveld refinement to study the statistical average atomic positions of these adsorbates in the H-ZSM-5.

The SXRD patterns and the corresponding Rietveld derived crystal structures of H-ZSM-5 pre-adsorbed with pyridine, methanol, and ammonia are summarised in Figure 3.12. In addition, from the Fourier contrast map of H-ZSM-5 pre-adsorbed with ammonia as displayed in Figure 3.13, the electron density clearly resides along the channels (see Table 3.1 for the electron contrast optimisation during the refinement process and Table 3.2 for the summary of the lowest R-factors from various attempts of the Rietveld refinement with different number of ammonia species). Note that the SXRD patterns of H-ZSM-5 pre-adsorbed with pyridine and methanol were also treated similarly.

Upon adsorption, the parent structure of the H-ZSM-5 zeolite is not altered with the lattice parameters maintained (see Table 3.3). However, the observable change in Bragg peak intensity in the low 2θ region indicates the presence of adsorbate molecules in the host H-ZSM-5.

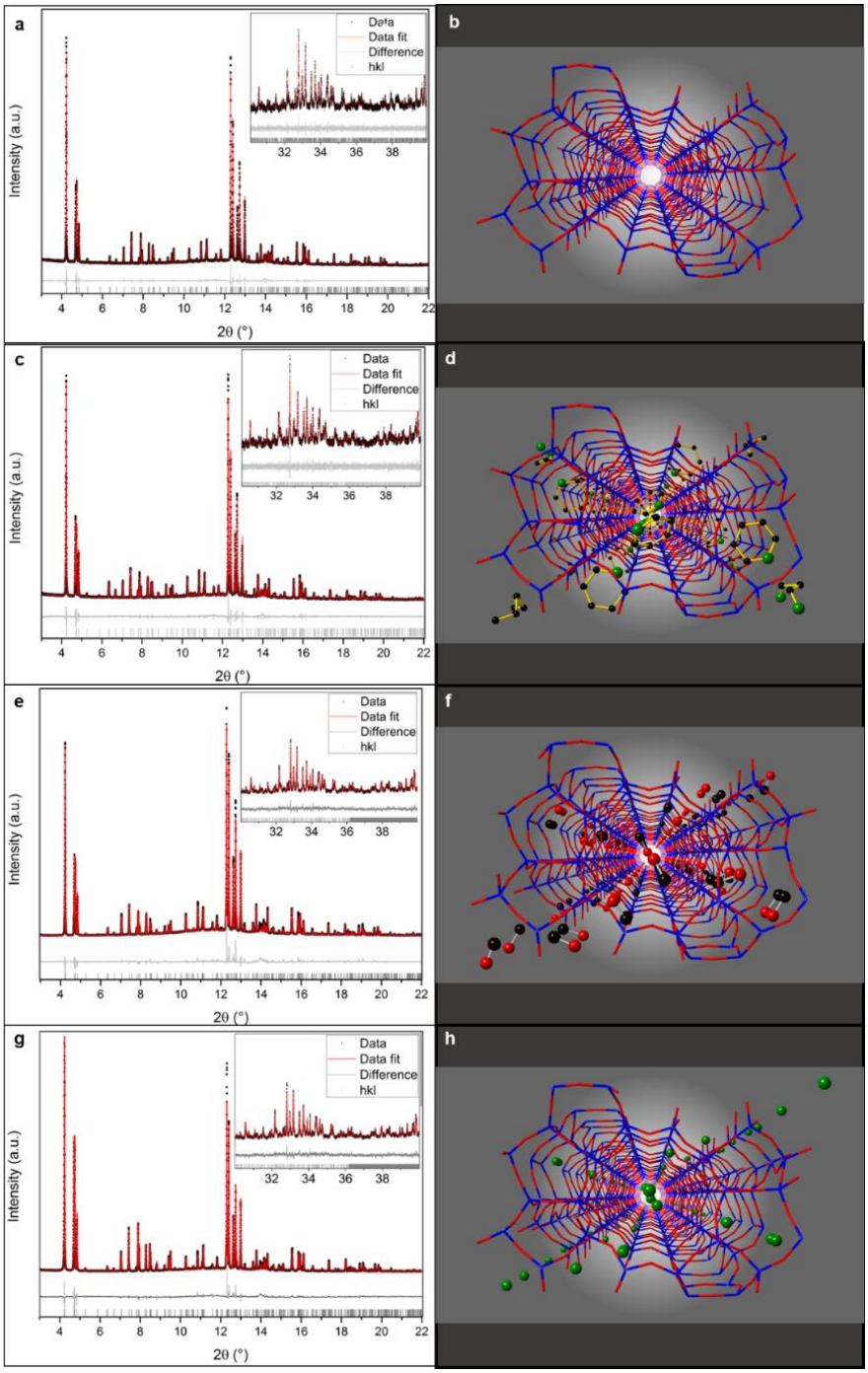

Figure 3.12. Rietveld refinements of the SXRD patterns of H-ZSM-5, measured at 25 °C, (**a**) dehydrated, pre-adsorbed with (**c**) pyridine, (**e**) methanol, and (**g**) ammonia. Their Rietveld derived atomic parameters of the SXRD data are summarised in Appendix Tables A3.1-A3.3, and the corresponding derived crystal structures are displayed in (**b**) dehydrated, pre-adsorbed with (**d**) pyridine, (**f**) methanol, (**h**) ammonia from the [010] direction (straight channel view). Atoms are represented in ball/sticks: blue = Si/Al, red = O, green = N, black = C. No hydrogens are plotted for clarity.

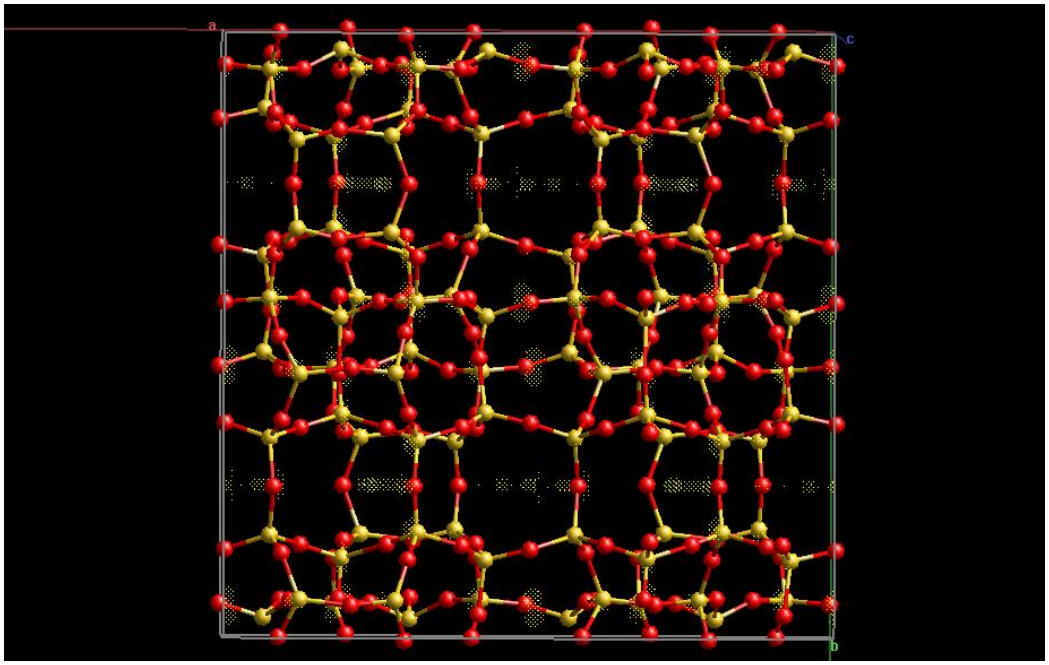

Figure 3.13. Fourier contrast map of H-ZSM-5 pre-adsorbed with ammonia measured at 25 °C. The electron density clearly resides along the channels.

Table 3.1. The electron contrast between H-ZSM-5 pre-adsorbed with ammonia and dehydrated H-ZSM-5.

	Rho	***x***	***y***	***z***
1	2.873	0.2007	0.2500	0.9004
2	2.295	0.0588	0.7500	0.0710
3	2.232	0.0711	0.2500	0.8395
4	2.212	0.0147	0.0499	0.4483
5	1.791	0.2031	0.1634	0.4005
6	1.707	0.1007	0.0435	0.9859
7	1.658	0.1212	0.5445	0.2522
8	1.573	0.0978	0.1325	0.0743
9	1.566	0.0269	0.2500	0.7117
10	1.493	0.0715	0.6077	0.1082

Rho refers to the calculated electron density.

Table 3.2. Summary of the lowest R-factors from various Rietveld refinement attempts of H-ZSM-5 pre-adsorbed with ammonia measured at 25 °C (with the number ammonia sites underlined).

Samples	R_{wp}	R_p	R_{exp}	χ^2
H-ZSM-5 with $\underline{1}NH_3$	13.541	10.784	3.441	3.935
H-ZSM-5 with $\underline{2}NH_3$	12.775	10.190	3.441	3.713
H-ZSM-5 with $\underline{3}NH_3$	10.984	8.709	3.441	3.192
H-ZSM-5 with $\underline{4}NH_3$	9.655	7.499	3.440	2.806
H-ZSM-5 with $\underline{5}NH_3$	9.648	7.529	3.440	2.804

Table 3.3. Crystallographic parameters of the H-ZSM-5 samples measured at 25 °C, dehydrated, pre-adsorbed with pyridine, methanol, and ammonia.

Samples	**H-ZSM-5 (dehydrated)**	**H-ZSM-5 (pyridine)**	**H-ZSM-5 (methanol)**	**H-ZSM-5 (ammonia)**
Chemical formula	$H_{4.48}Al_{4.48}Si_{91.52}O_{192}$	$H_{4.48}Al_{4.48}Si_{91.52}O_{192}$. nC_5H_5N	$H_{4.48}Al_{4.48}Si_{91.52}O_{192}$. nCH_3OH	$H_{4.48}Al_{4.48}Si_{91.52}O_{192}$. nNH_3
Temperature (°C)	25(2)	25(2)	25(2)	25(2)
Wavelength (Å)	0.825634(2)	0.825634(2)	0.825771(4)	0.826617(4)
X-ray source	Synchrotron	Synchrotron	Synchrotron	Synchrotron
2θ -zero point (°)	-0.002500(10)	-0.002500(10)	-0.001932(10)	0.000254(10)
Space group	*Pnma*	*Pnma*	*Pnma*	*Pnma*
Crystal system	Orthorhombic	Orthorhombic	Orthorhombic	Orthorhombic
a (Å)	20.13675(3)	20.14034(4)	20.14167(4)	20.11343(4)
b (Å)	19.95928(3)	19.92144(4)	19.95348(4)	19.94445(4)
c (Å)	13.43725(2)	13.43087(3)	13.43055(4)	13.43221(3)
V (Å^3)	5400.63(2)	5388.80(2)	5397.69(2)	5388.35(2)
2θ range for refinement (°)	3-55	3-55	3-55	3-55
Detector	MAC	MAC	MAC	MAC
Number of parameters	36	150	156	156
Number of *hkl*s	4190	4190	4190	4190
Refinement methods	Le Bail	Rietveld	Rietveld	Rietveld
$R_{wp}/R_p/R_{exp}$ (%)	6.621/5.077/4.958	8.461/6.377/4.822	9.005/6.977/5.258	7.542/5.860/3.436
χ^2	1.335	1.755	1.712	2.195

Although the uncertainty observed in the atomic positions of these adsorbed molecules are higher than the rigid framework atoms (O, Si) due to their intrinsic higher degrees of freedom and higher isotropic temperature factors, B_{eq} (see Tables A3.1-A3.3 in Appendix for the detailed atomic parameters). The low R_{wp} and χ^2 values with the closely fitted diffraction patterns suggest good quality of Rietveld refinements. It also reflects the high reliability of the atomic positions and angles.

From the Rietveld derived crystal structures (see Figures 3.12 and 3.14), all three primary adsorbates (Pyridine 1, Methanol 1 and Ammonia 1) are found to locate in the sinusoidal-straight cross-channel region of the H-ZSM-5 framework. This agrees with the earlier postulations from spectroscopic and modelling characterisations, that the BAS are likely to be located in the cross-channel region.[11] As H atoms cannot easily identified by SXRD, a simple way to gauge the location of the BAS is by examining the interatomic distances and angles between the framework O atoms and the lone pair electrons donor of the probe molecules (i.e., Pyridine 1 (N), Methanol 1 (O) or Ammonia 1 (N)). As seen in Figure 3.14, the shortest comparable interatomic distances are adsorbate-O5 and -O18 in all the three cases. We can therefore identify the Al site at T6 which is sandwiched between O5 and O18 in the H-ZSM-5. Note that there are four equivalent O atoms of T6, with O5 and O18 directed to the channel surface.[12]

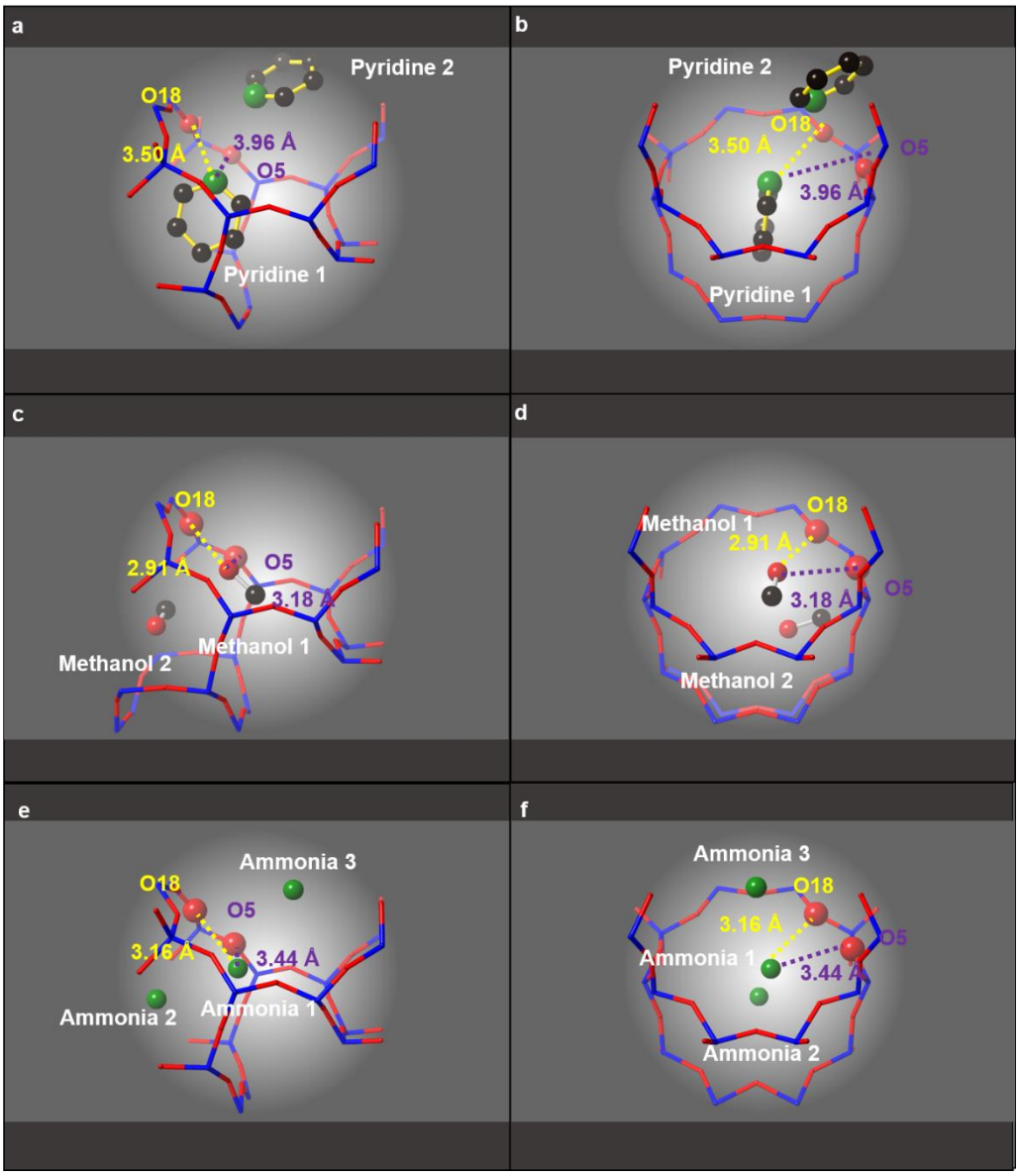

Figure 3.14. The Rietveld derived crystal structures showing one asymmetric unit, from the Rietveld refinements of the corresponding SXRD data: (**a**) pyridine, (**c**) methanol, and (**e**) ammonia with the unit cell from the [010] direction (straight channel view); (**b**) pyridine, (**d**) methanol, and (**f**) ammonia with the unit cell from the [100] direction (sinusoidal channel view). Atoms are represented in ball/sticks: blue = Si/Al, red = O, green = N, black = C. No hydrogens are plotted for clarity.

The strongly acidic nature of the bridging O18(H) between Al and Si in O5-T6(Al)-O18 of H-ZSM-5 can easily protonate the basic adsorbate molecules to form protonated cations. For each adsorbate, there are more than one adsorbed molecules observed in the channels. The adsorbed molecules are less strongly bound as observed by lower desorption temperatures in TGA (see Figures 3.7 and 3.9). As seen in the derived crystal structure of H-ZSM-5 pre-adsorbed with methanol, there is one additional methanol (Methanol 2) in the sinusoidal channel. It is linked to the protonated Methanol 1 via H-bonding (Figures 3.12(f) and 3.14(c,d)). For ammonia (Figures 3.12(h) and 3.14(e,f)), there are three additional ammonia molecules connected through an H-bonding network to the protonated Ammonia 1, with Ammonia 2 in the sinusoidal channel, and Ammonia 3 and 4 in the straight channel. Thus, the common features appear to originate from the protonation of the adsorbate molecules by the BAS. The protonated chemisorbed species resides in the cross-channel region, and links with additional adsorbates via weak H-bonds.

However, while the second methanol and ammonia[13] resides preferentially in the sinusoidal channel, the second pyridine (Pyridine 2) locates in the less sterically hindered straight channel (see Figures 3.12(d) and 3.14(a,b)). Despite the anticipated equal charge density of O5 and O18 (of O5-T6-O18), $N_{Pyridine1}$-O5 is considerably longer than $N_{Pyrindine1}$-O18 (cf. 3.96(5) and 3.50(4) Å). Also, the derived interatomic distances of $N_{Pyridine1}$–O18 (3.50(4) Å) and $N_{Pyridine2}$–O18 (3.72(4) Å) correspond well with the general distance of electrostatic interaction between -NH^+ (Pyridine-H^+) and the negatively charged framework O18. Thus, the steric factor of the bulky pyridine molecules therefore clearly plays an important role in the actual adsorption geometry. Pyridine 1 that is in the more hindered sinusoidal channel experiences more steric

repulsion, whereas Pyridine 2 that is in the straight channel is less sterically repelled. This leads to the difference in interatomic distances (also see force-field modelling optimisation in the Chapter 3.3.6).

Acid-base properties from the Rietveld derived interatomic distances

It is believed that the basicity of the adsorbate molecules can affect the interatomic distances between the acid-base adducts. From Figure 3.14, the shortest interatomic distances of different probe molecules are comparable, which range within 2.9-3.5 Å. Considering the presence of a 'bridging' proton between the strongest adsorption site (site 1) and O18 atom, these 2.9-3.5 Å interatomic distances match well with the expected interatomic distances of acid-base adducts within experimental errors.

In fact, the BAS of zeolites are generally considered to be 'solid acids', because the acid-base properties in zeolites do not require the participation of 'water'. As mentioned earlier, a base molecule is protonated when it interacts with a BAS, then subsequently form an acid-base adduct. It is noted that upon protonation, a strong base becomes a weak conjugate acid, and *vice versa*. Therefore, according to the PA of pyridine (924 kJ mol^{-1}), ammonia (854 kJ mol^{-1}) and methanol (761 kJ mol^{-1}),[14] pyridine forms the weakest conjugate acid and interacts the least strongly with the framework conjugate base. This is consistent with the derived interatomic distances: $N_{Pyridine1}$-O18 = 3.50(3) Å > $N_{Ammonia1}$-O18 = 3.16(4) Å > O_{MeOH1}-O18 = 2.91(4) Å.

In short, the derived interatomic distances can reflect the strength of the acid-base adducts: the longer is the distance, the weaker is the acid-base interaction, the more readily is the desorption.

3.3.5 Temperature programmed SXRD

We notice a significant mismatch between the SOF of Pyridine 1 (0.239) and Pyridine 2 (0.505) from SXRD. It suggests the co-existence of a dimer ($[PyrH\cdots Pyr]^+$) and a monomer ($PyrH^+$) at 25 °C, which agrees with our earlier deduction from the TGA experiment (see Chapter 3.3.1). To differentiate the monomer from the dimer, a temperature programmed SXRD experiment was performed (see Figure 3.15). Despite a greater thermal vibration motion at high temperatures, the $N_{prydine1}$-O18 and $N_{Pyridine2}$-O18 interatomic distances remain almost unchanged within experimental error from 25 to 200 °C (see Table 3.4).

Upon heating from 25 to 100 °C, the SOF value of Pyridine 2 sharply decreases from 0.505 to 0.320 (see Table 3.4). Then, the SOF values of both Pyridine 1 & 2 decrease steadily. This means some of Pyridine 2 preferentially desorbs upon heating to 100 °C. From the TGA experiment (see Figure 3.7), the estimated desorption energy (E_{des}, Figure 3.8) is 24.93 kJ mol^{-1}, which implies Pyridine 2 in the dimer form desorbs more easily. This would leave behind only the two monomer forms at *ca*. 200 °C before their final desorption at higher temperatures (E_{des} = 39.85 kJ mol^{-1}, Figure 3.8). Interestingly, the SOF values of the two pyridine sites are comparable at 200 °C, which may imply a thermal equilibrium is achieved between these two sites. Taking the entropy factor of the molecule in the adsorption site into consideration, Pyridine 2 that is in the less sterically hindered straight channel is likely to be the kinetic intermediate site before the filling or emptying of other sites.

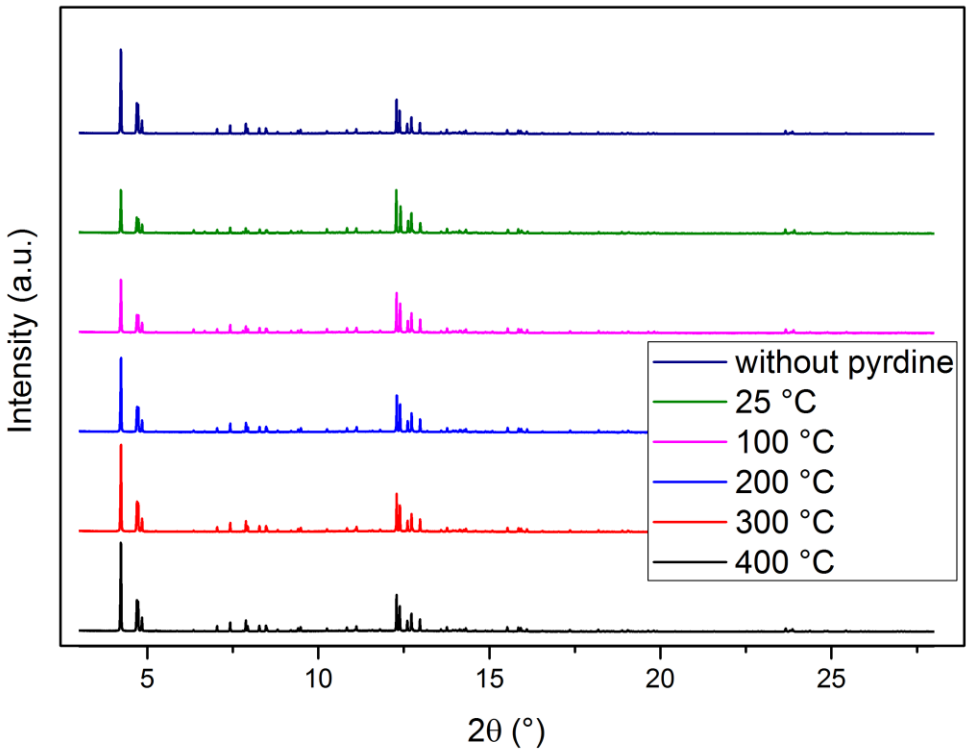

Figure 3.15. Temperature programmed SXRD patterns of the H-ZSM-5 samples pre-adsorbed with pyridine at various temperatures. Upon adsorption of pyridine, the increase in Bragg peak intensity at the low 2θ region indicates pyridine desorption from the host H-ZSM-5.

Table 3.4. Table displaying H-ZSM-5 pre-adsorbed with pyridine at various temperatures, SOF values, N1-O18, N2-O18, and N1-N2 interatomic distances. It is noted that the total SOF value from temperature programmed SXRD is noticeably different from that deduced from the TGA measurement at various prolonged stepwise temperatures.

Temperature (°C)	**25**	**100**	**200**	**300**	**400**
SOF (Pyr1)	0.239(2)	0.230(2)	0.253(2)	0.187(4)	0.137(3)
SOF (Pyr2)	0.505(2)	0.320(2)	0.217(2)	0.084(4)	0.067(3)
N1-O18 (Å)	3.50(4)	3.51(5)	3.47(4)	3.51(5)	3.71(5)
N2-O18 (Å)	3.72(3)	3.76(3)	3.76(6)	3.83(6)	4.40(7)
N1-N2 (Å)	3.61(6)	3.41(6)	3.39(6)	-	-
R_{wp} (%)	8.461	8.185	7.721	7.371	7.486
χ^2	1.755	1.695	1.601	1.524	1.544

3.3.6 Force-field Modelling Optimisation

To verify the Rietveld derived crystal structures (see Figure 3.16), the pyridine positions in H-ZSM-5 were modelled using the corresponding force-field atomic potential energies. As shown in the SXRD derived crystal structure with pre-adsorbed pyridine at 25 °C (see Figure 3.16(a) and Table 3.5), N1-O18 corresponds to 3.50(4) Å with ∠X1-N1-O18 of 102.2(16)°; N2-O18 corresponds to 3.72(4) Å with ∠X2-N2-O18 of 136.4(16)° (where X1 and X2 refer to the centre of the pyridine molecule). The best-fit calculation was based on the protonation of Pyridine 1 which connects Pyridine 2 through an H-bonding interaction (see Figure 3.16(b)). The calculated N1-O18 of 3.33 Å with ∠X1-N1-O18 of 113.6° and N2-O18 of 3.80 Å with ∠X2-N2-O18 of 143.0° are in good agreement with the SXRD data. Although this simple calculation could be improved by more rigorous QM calculations, the small discrepancies (*ca*. 10% longer interatomic distances of the derived crystal structure at 25 °C) could be accounted for by the difference in the thermal vibration factors between the experimental and theoretical approaches. The values for the calculated N1-O18 distances of Pyridine 1 monomer presented in Figure 3.16(d) and the N2-O18 of Pyridine 2 monomer (see Figure 3.16(f)) remain almost unchanged as those in the dimer model. This suggests the weak H-bonding in the dimer model seems to affect the interatomic angle and orientation slightly, but has limited effect on the N-O interatomic distances.

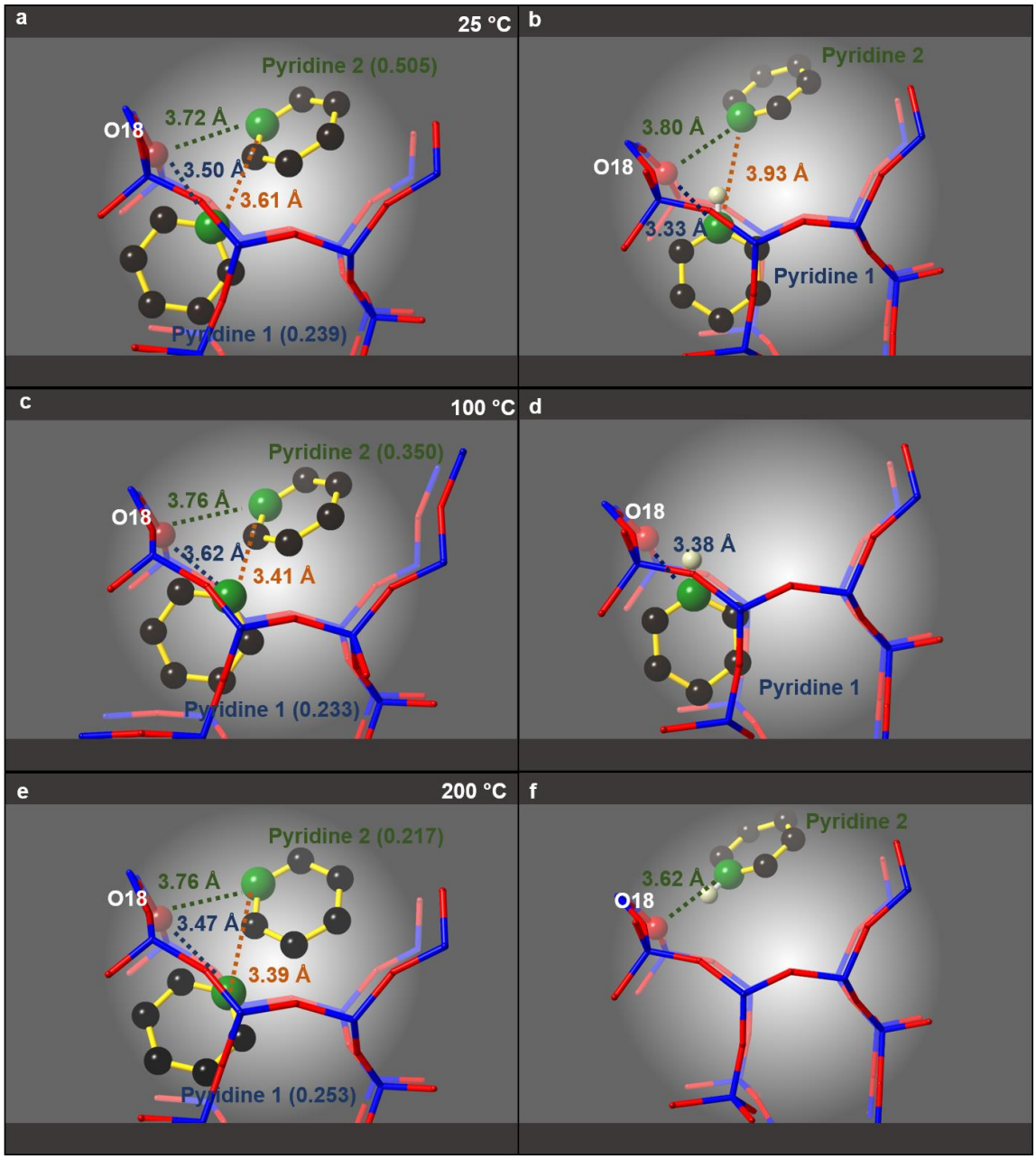

Figure 3.16. (**a**, **c**, **e**) Rietveld derived crystal structures of H-ZSM-5 pre-adsorbed with pyridine molecules from 25 °C to 200 °C, and the force-field modelling optimised crystal structures of (**b**) pyridine dimer ($[PyrH\cdots Pyr]^+$); (**d**) Pyridine 1 monomer in the cross-channel; (**f**) Pyridine 2 monomer in the straight channel. There is no significant difference between the N1-O18 distances, but slight variations in the bond angles and molecular orientation, see Table 3.5. Atoms are represented in balls/sticks: blue = Si/Al, red = O, green = N, black = C, and light yellow = H. The values in brackets refer to SOF. Some hydrogens are omitted for clarity.

Table 3.5. Comparison of Rietveld refinement of SXRD and force-field modelling optimisation of H-ZSM-5 pre-adsorbed with pyridine. Selected bond lengths and bond angles from the Rietveld refinement of the SXRD data measured at 25 °C and force-field optimisation data are shown. All interatomic distances and angles are measured by the CrystalMaker software. X1 and X2 refer to the centre of the corresponding pyridine.

Bond lengths (Å)	**From SXRD - Rietveld**	**From force-field modelling**	**Bond angles (°)**	**From SXRD - Rietveld**	**From force-field modelling**
N1-O5	3.96(4)	3.86	∠X1-N1-O5	100.0(16)	105.2
N1-O18	3.50(3)	3.34	∠X1-N1-O18	102.2(16)	126.6
N2-O5	3.53(3)	3.61	∠X2-N2-O5	126.9(16)	110.3
N2-O18	3.27(3)	3.08	∠X2-N2-O18	136.4(16)	143.0

3.4 Conclusions

In short summary, the atomic positions and angles of the small C-, O-, N-containing molecules, namely, pyridine, methanol and ammonia, adsorbed on the H-ZSM-5 have been determined. More importantly, the locations of the BAS have been successfully identified, with the substituted Al at the T6 site and the proton on the O18 site. The strength of the acid-base interactions has been further elucidated by studying their corresponding interatomic distances between the BAS and probe molecules. However, to characterise the H positions to further elucidate the structures of the adsorbed ammonia molecules within H-ZSM-5, ND (neutron diffraction) experiments should be carried out.

This is proven to be a unique and reliable way to reveal the locations of the BAS and Al sites, as well as the adsorbate structure in zeolites. Supported by theoretical calculations, high-resolution SXRD combined with Rietveld refinement can now offer a unique and reliable way to determine adsorbate structures and their interactions with the interior acid sites for further exploration of zeolite chemistry.

3.5 References

(1) Lomratsiri, J.; Probst, M.; Limtrakul, J. *J. Mol. Graph. Model.* **2006**, *25*, 219–225.

(2) Li, C.; Sklenak, S.; Sierka, M.; Sauer, J. *Angew. Chem. Int. Ed.* **2007**, 7286–7289.

(3) Chu, Y.; Yu, Z.; Zheng, A.; Fang, H.; Zhang, H.; Huang, S. J.; Liu, S. Bin; Deng, F. *J. Phys. Chem. C* **2011**, *115* (15), 7660–7667.

(4) Heo, N. H.; Kim, C. W.; Kwon, H. J.; Kim, G. H.; Kim, S. H.; Hong, S. B.; Seff, K. *J. Phys. Chem. C* **2009**, *113* (46), 19937–19956.

(5) Logan, S. R. *Trans. Faraday Soc.* **1967**, *63*, 1712–1719.

(6) Jin, F.; Li, Y. *Catal. Today* **2009**, *145* (1–2), 101–107.

(7) Buzzoni, R.; Bordiga, S.; Ricchiardi, G.; Lamberti, C.; Zecchina, a.; Bellussi, G. *Langmuir* **1996**, *12* (4), 930–940.

(8) Michel, D.; Germanus, A.; Pfeifer, H. *J. Chem. Soc. Faraday Trans. 1* **1982**, *78* (1), 237.

(9) Ukrainczyk, L.; Smith, K. *Environ. Sci. Technol.* **1996**, *30* (11), 3167–3176.

(10) Shenderovich, I. G.; Buntkowsky, G.; Schreiber, A.; Gedat, E.; Sharif, S.; Albrecht, J.; Golubev, N. S.; Findenegg, G. H.; Limbach, H. *J. Phys. Chem. B* **2003**, *107* (43), 11924–11939.

(11) Dědeček, J.; Sobalík, Z.; Wichterlová, B. *Catal. Rev.* **2012**, *54* (2), 135–223.

(12) Jones, A. J.; Iglesia, E. *ACS Catal.* **2015**, 5741–5755.

(13) Ye, L.; Lo, B. T. W.; Qu, J.; Wilkinson, I.; Hughes, T.; Murray, C. A.; Tang, C. C.; Tsang, S. C. E. *Chem. Commun.* **2016**, *52* (16), 3422–3425.

(14) Billo, E. J. *J. Chem. Educ.* **1985**, *62* (4), A137.

Chapter 4. Probing Atomic Positions in Ammonia Storage in H-ZSM-5

In this chapter, the storage capability and sorption kinetics in H-ZSM-5 are reported based on our structural findings. Some of the data particularly the evaluation of sorption kinetics were acquired in collaboration with Dr Lin Ye of our group.

The work in this chapter was published in Chemical Communications 52, 3422–3425 (2016), 'Probing atomic positions of adsorbed ammonia molecules in zeolite', by Ye, L., **Lo, B. T. W.**, et al. with equal contribution.

4.1 Introduction

The catalytic production of ammonia from nitrogen and hydrogen by the Haber–Bosch process is the second largest industrial chemical manufacturing process in global trade. The main drivers are for the agricultural sector as fertiliser and for industrially diverse applications as an enabling chemical.[1,2] Furthermore, ammonia is a possible carbon-free fuel candidate. This offers an exciting potential for ammonia to be used as an energy storage with better energy density factors than liquid hydrogen.[3,4] An established logistics chain for worldwide trading and transportation of ammonia already exists.

Compressed liquefied ammonia is a current solution for ammonia storage and transportation, but it is not for long term applications because of ammonia toxicity and corrosiveness. Indeed, the choice, cost, weight and design of container, and the associated health and safety issues will reduce the attractiveness of using liquefied ammonia as a fuel for small vehicles. Recently, zeolites[3] , porous COFs[4] and MOFs[5] have been used to store ammonia reversibly. These materials show great storage performance by using the LAS or BAS to interact with ammonia. They may also be used to store ammonia as a selective reductant for deNOx for both stationary and mobile applications.[6–8] At the ammonia release step, some ammonia could be released under low energy input conditions, but some may need high temperature with no rationalisation. Meanwhile, the highest ammonia uptake (15 mmol g^{-1}) achieved to date is still not satisfactory for industrial requirements. Thus, elucidating the fundamental interactions between the adsorbed ammonia and porous frameworks is critical for improved storage.

In the case of ammonia storage over porous materials, NH_3-TPD (temperature programmed desorption) is widely used to characterise the amount and strength of ammonia adsorption crudely. In zeolite materials, by combining NH_3-IR and theoretical calculations, the formation of $NH_4^+ \cdot nNH_3$ ($n \geq 1$) has been determined, when NH_3/Al used was greater than 1.[9,10] However, these measurements can neither provide the atomic information of the adsorbates nor reflect the nature of interactions. In zeolites, the BAS can form strong acid-base adducts with ammonia molecules;[11,12] also, the small cavity within the zeolite framework allows ammonia–ammonia interactions at high loading of ammonia uptake.[13,14]

In this chapter, based on the BAS identification in H-ZSM-5 from Chapter 3, the understanding of the internal topology of porous structures and molecular adsorbates at an atomic level is revealed. This may lead to a rational design of highly selective adsorbents and catalysts. By using temperature programmed *S*XRD combined with Rietveld refinement, together with TGA and force-field modelling optimisation, the bonding geometries of the adsorbed ammonia about the internal surface of BAS are probed within experimental error.

4.2 Results and Discussion

In this section, a series of characterisation techniques are employed to investigate the ammonia-framework and ammonia-ammonia interactions in H-ZSM-5.

4.2.1 SXRD

From the SXRD patterns of H-ZSM-5 before and after adsorption, (as discussed in Chapter 3.3.4), the crystal structure of the H-ZSM-5 framework remains unchanged upon the adsorption of ammonia.

From the Rietveld derived crystal structure (see Figure 4.1, measured at 25 °C), there are three ammonia species along the sinusoidal channel and one ammonia deep in the straight channel. As determined by the interatomic distances in Chapter 3.3.4, Ammonia 1 has the shortest interatomic distance with the framework O18 atom ($N_{Ammonia1}$–O18 = 3.16(3) Å). This first ammonia acts as a Brønsted base that accepts the proton from the BAS to form an NH_4^+ ion. Meanwhile, the derived interatomic distances among the four adsorbed ammonia molecules are $N_{Ammonia2}$–$N_{Ammonia1}$ = 3.43(8) Å, $N_{Ammonia3}$–$N_{Ammonia1}$ = 3.84(8) Å and $N_{Ammonia4}$–$N_{Ammonia3}$ = 4.36(9) Å. The former two fall in the range of typical H-bonding interactions and geometries of (N–H···N) with medium strength as displayed in Table 4.1. Whereas, the latter shows almost no formal bonding interaction between Ammonia 3 & 4. Therefore, Ammonia 4 is likely to have arisen from physisorption in the straight channel through weak interaction with the internal framework surface.

Table 4.1. The guiding values of "strong", "moderate" and "weak" hydrogen bonds.[15]

	Strong	**Moderate**	**Weak**
Type of interaction	Strongly covalent	Mostly electrostatic	Electrostatic/ dispersive
Bond lengths B-H (Å)	1.2 – 1.5	ca. 1.0	ca. 1.0
Bond lengths H···A (Å)	1.2 – 1.5	1.5 – 2.2	> 2.2
Bond lengths B·····A (Å)	2.2 – 2.5	2.5 – 3.2	3.2 – 4.0
Bond energy (kJ mol^{-1})	63 – 167	16 – 63	< 16
Bond angles (°)	170 – 180	> 130	> 90

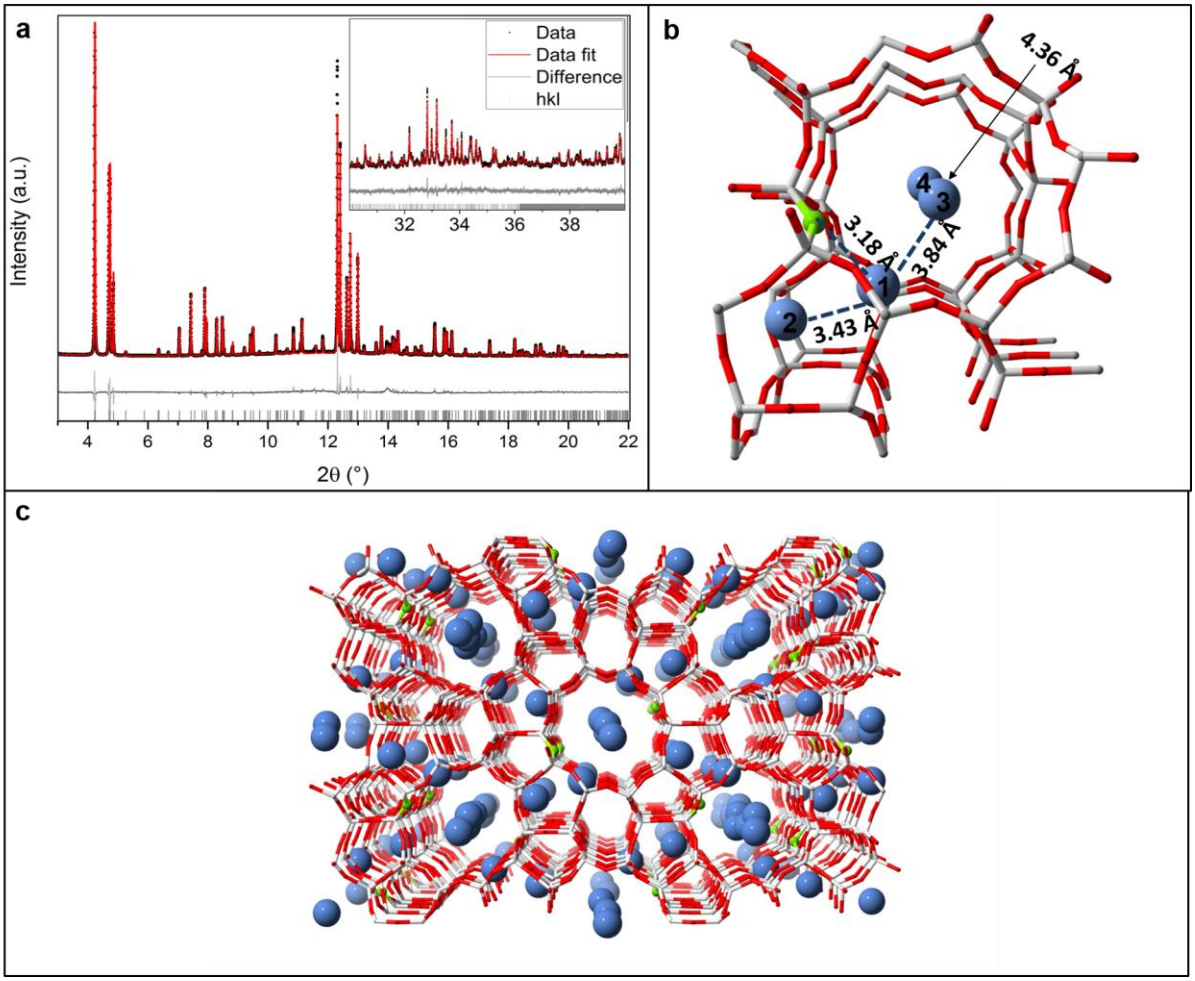

Figure 4.1. (**a**) Rietveld refinement profile of the SXRD pattern of H-ZSM-5 pre-adsorbed with ammonia, measured at 25 °C, and its corresponding Rietveld derived crystal structures, viewed from the [010] direction showing (**b**) an asymmetric unit, and (**c**) several unit cells. There are four ammonia molecules per asymmetric unit: Ammonia 1-3 in the sinusoidal channel and Ammonia 4 in the straight channel. Atoms are represented in ball/sticks: white = Si/Al, red = O, light green = O18, blue = N. No hydrogens are plotted for clarity.

4.2.2 Force-field modelling optimisation

To verify the atomic positions of the adsorbed ammonia species, a force-field modelling optimisation has been performed (see Figure 4.2 and Table 4.2). The optimisation result is consistent with the Rietveld refinement result in terms of ammonia location; three ammonia species along the sinusoidal channel and one ammonia species in the straight channel. There is however a slight deviation in the interatomic distances between the adsorbed ammonia molecules and BAS at 25 °C from the Rietveld refinement analogues. It is likely due to the absence of thermal factors in the theoretical calculations and the selected part of a unit cell in the theoretical calculations. Despite the force-field modelling optimisation agrees with the atomic information of H-ZSM-5 pre-adsorbed with pyridine in Chapter 3, the optimisation of ammonia seems less promising in terms of atomic coordinates.

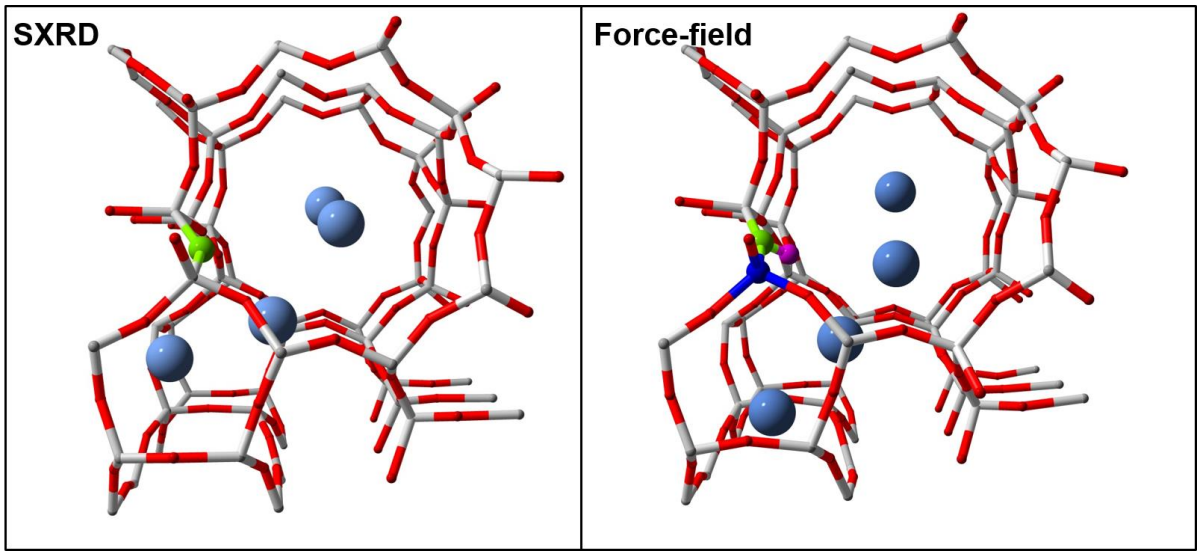

Figure 4.2. Comparison between the Rietveld derived crystal structure from SXRD and force-field modelling optimisation, showing one asymmetric unit. The preliminary calculation result is consistent with the Rietveld refinement result, apart from a slight deviation in the interatomic distances. The same colour scheme is applied as Figure 4.1.

Table 4.2. Force-field modelling optimisation of H-ZSM-5 pre-adsorbed with ammonia, comparing the interatomic distances and the atomic coordinates with the Rietveld derived crystal structure.

Interatomic distance (Å)	**SXRD (N···H···O)**	**Force-field (N···H···O)**	***x*** **(SXRD/Force-field)**	***y*** **(SXRD/Force-field)**	***z*** **(SXRD/Force-field)**
N1-O18	3.18(3)	4.49	-0.5336/-0.4694	-0.4580/-0.7020	0.2708/0.0160
N2-N1	3.43(8)	2.74	-0.8939/-0.0537	-0.7836/-0.8072	0.1300/0.0271
N3-N1	3.84(9)	2.62	-0.5007/-0.6952	-0.0504/-0.0414	0.5839/0.8331
N4-N3	4.36(9)	3.03	-0.6987/-0.7382	-0.9195/-0.9599	0.9582/0.8195

4.2.3 TGA

To understand the ammonia sorption properties of H-ZSM-5, TGA was used to reveal the ammonia desorption kinetics from H-ZSM-5.

The TGA data of H-ZSM-5 pre-adsorbed with ammonia were collected up to 600 °C in air at ramping rates of 1, 7.5, 10, 15 and 20 °C min^{-1} (see Figures 4.3 and 4.4). From calibration, 5.06% in weight loss was observed upon heating from 25 to 400 °C, which is equivalent to a total ammonia storage capacity of H-ZSM-5 of 3.13 mmol g^{-1} (equivalent to 18 ammonia molecules per unit cell, see Table 4.3). According to the modified Arrhenius plot (see Figure 4.5, as described in Chapter 2.4.8), the estimated ammonia desorption energies, E_{des}, from H-ZSM-5 correspond to 6.81(6), 21.3(1), and 62.5(2) kJ mol^{-1}. Referring to the strength of H-bonding (see Table 4.1), the E_{des} of 62.5 kJ mol^{-1} falls in the range of "Moderate" to "Strong" H-bonding. Note that the ∠O-H···N hence should be almost linear. Whereas, the first two E_{des} values, 6.81(2) and 21.3(1) kJ mol^{-1}, are noticeably smaller than the case in pyridine (see Chapter 3.3.1, c.f. 24.93(3) and 39.85(4) kJ mol^{-1}). This is due to the smaller ammonia molecules are much less sterically hindered from the desorption process from the zeolite confined channels.

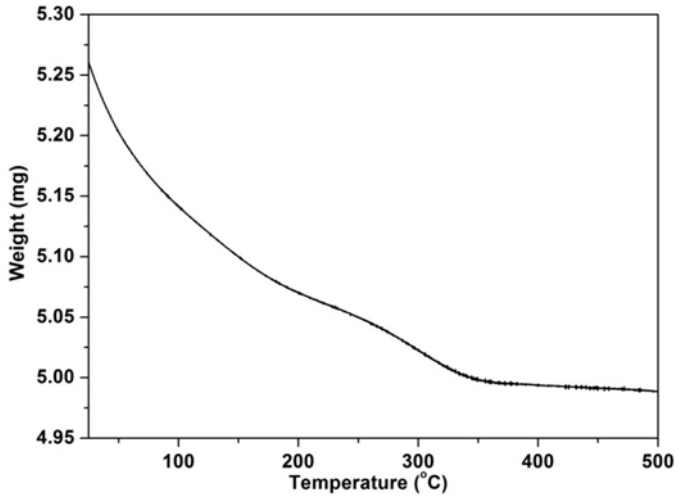

Figure 4.3. TGA of H-ZSM-5 pre-adsorbed with ammonia measured at 1 °C min^{-1}, 5.06% in weight loss was observed from 25 to 400 °C. The total ammonia storage capacity of H-ZSM-5 is 3.13 mmol g^{-1} (18 ammonia molecules per unit cell).

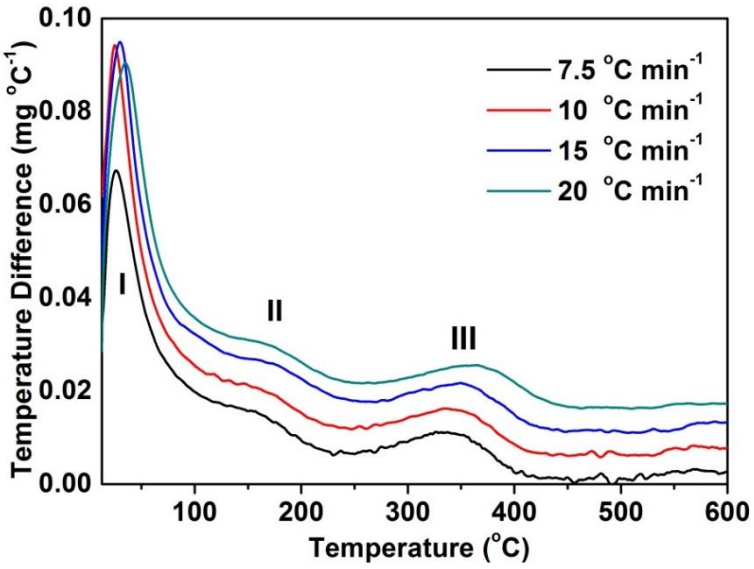

Figure 4.4. Difference TGA of H-ZSM-5 pre-adsorbed with ammonia, measured at 7.5, 10, 15, and 20 °C min^{-1}.

Table 4.3. Comparison of residual ammonia molecules per unit cell at various temperatures between TGA and Rietveld refinements.

Temperature (°C)	#Ammonia/unit cell from TGA	#Ammonia/unit cell from Rietveld refinements*
25	18.0	18.0
100	10.0	9.36
200	5.23	5.44
300	1.97	2.00
400	0	0

*The number of ammonia molecules from Rietveld refinements is calculated from the sum of the derived SOF values of the ammonia sites, taking symmetry into account.

Table 4.4. The peak temperatures of ammonia desorption from H-ZSM-5 at different temperature ramping rates. The desorption energies, E_{des}, are estimated from the modified Arrhenius plot in Figure 4.5.

Ramping rate (°C min^{-1})	7.5	10	15	20	E_{des} (kJ mol^{-1})
T_I (°C)	22	25	30	34	6.81(6)
T_{II} (°C)	134	142	156	170	21.3(1)
T_{III} (°C)	330	338	354	369	62.5(2)

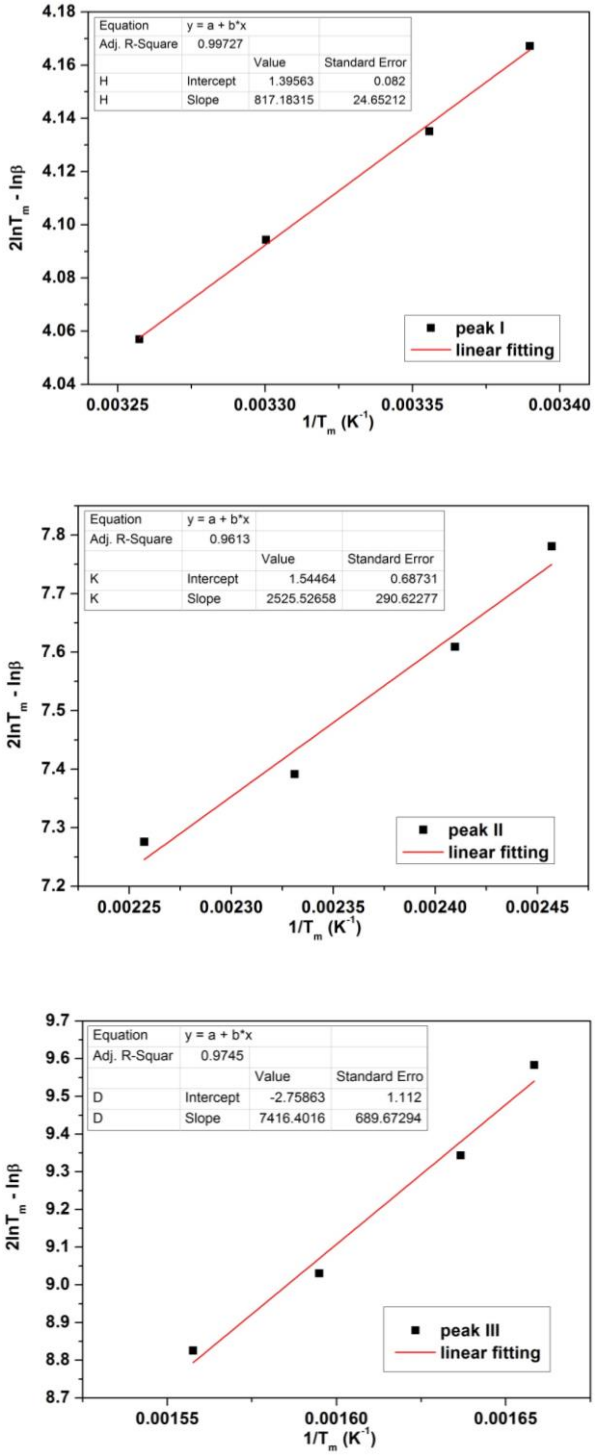

Figure 4.5. E_{des} estimation from the modified Arrhenius plots. Linear fitting of the peak temperature of three types of desorption measured at different temperature ramping rates. The R^2 values are 0.997 (top, peak I), 0.961 (middle, peak II) and 0.974 (bottom, peak III).

4.2.4 Temperature programmed SXRD

As mentioned in Chapter 3, conventional techniques only detect the global picture of the ammonia desorption process. In this section, temperature programmed SXRD was employed to directly 'visualise' the ammonia desorption process from the H-ZSM-5 sample.

The temperature programmed SXRD patterns are displayed in Figure 4.6. Upon elevated temperatures, the Bragg peak intensity significantly increases in the low 2θ region. This signifies ammonia desorption from H-ZSM-5 (see Table A4.1 for the detailed crystallographic parameters). From the Rietveld derived crystal structures (see Figure 4.7), at elevated temperatures (i) the interatomic distances between ammonia–BAS and ammonia–ammonia both increase, and (ii) the number of residual ammonia molecules decreases. At 200 °C, nearly all physisorbed ammonia and intermolecular H-bonding connected ammonia are readily desorbed from H-ZSM-5. To release the remaining strongly bound BAS adduct NH_4^+ species with the framework, a higher energy input is needed. Interestingly, the TGA and temperature programmed SXRD experiments have shown an excellent match for the number of residual ammonia molecules in the H-ZSM-5 at various desorption temperatures (25, 100, 200, 300, and 400 °C, as seen in Table 4.3).

As determined by TGA, the estimated E_{des} for ammonia desorption from H-ZSM-5 are 6.81(6), 21.3(1), and 62.5(2) kJ mol^{-1}. They correspond well with the expected activation barriers from the interatomic distances derived from the temperature programmed SXRD measurements: for very weak interactions (N–H···O), H-bonded (N–H···N), and strong Brønsted acid–base adduct (O···$^+$H-N) (see Table 4.5).[15] We acknowledge these

interatomic distances may not be referenced directly, especially for the immediate desorption of weakly bound molecules under 50 kJ mol^{-1}, and the possible water molecule contamination that could introduce small errors. Nonetheless, the TGA and temperature programmed SXRD results agree well with each other.

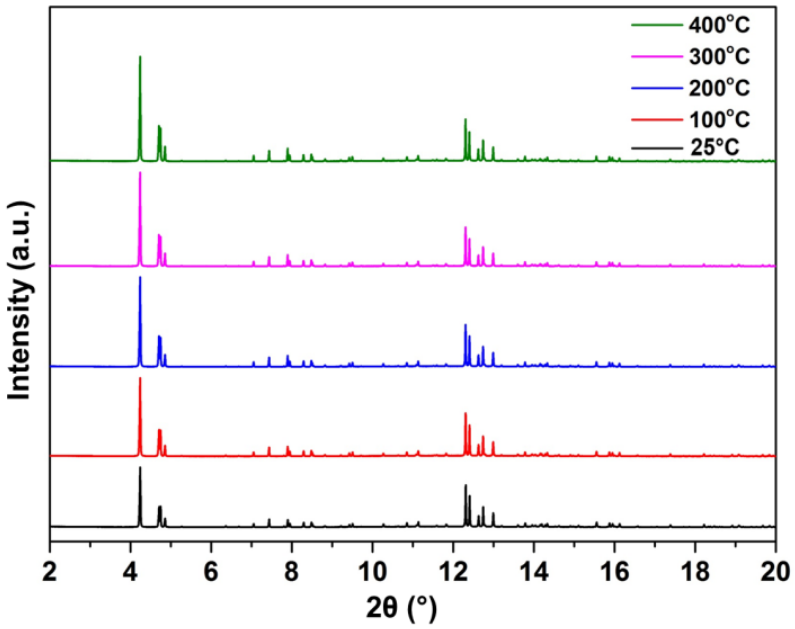

Figure 4.6. Temperature programmed SXRD patterns of ammonia desorption from the H-ZSM-5, measured at 25, 100, 200, 300, and 400 °C.

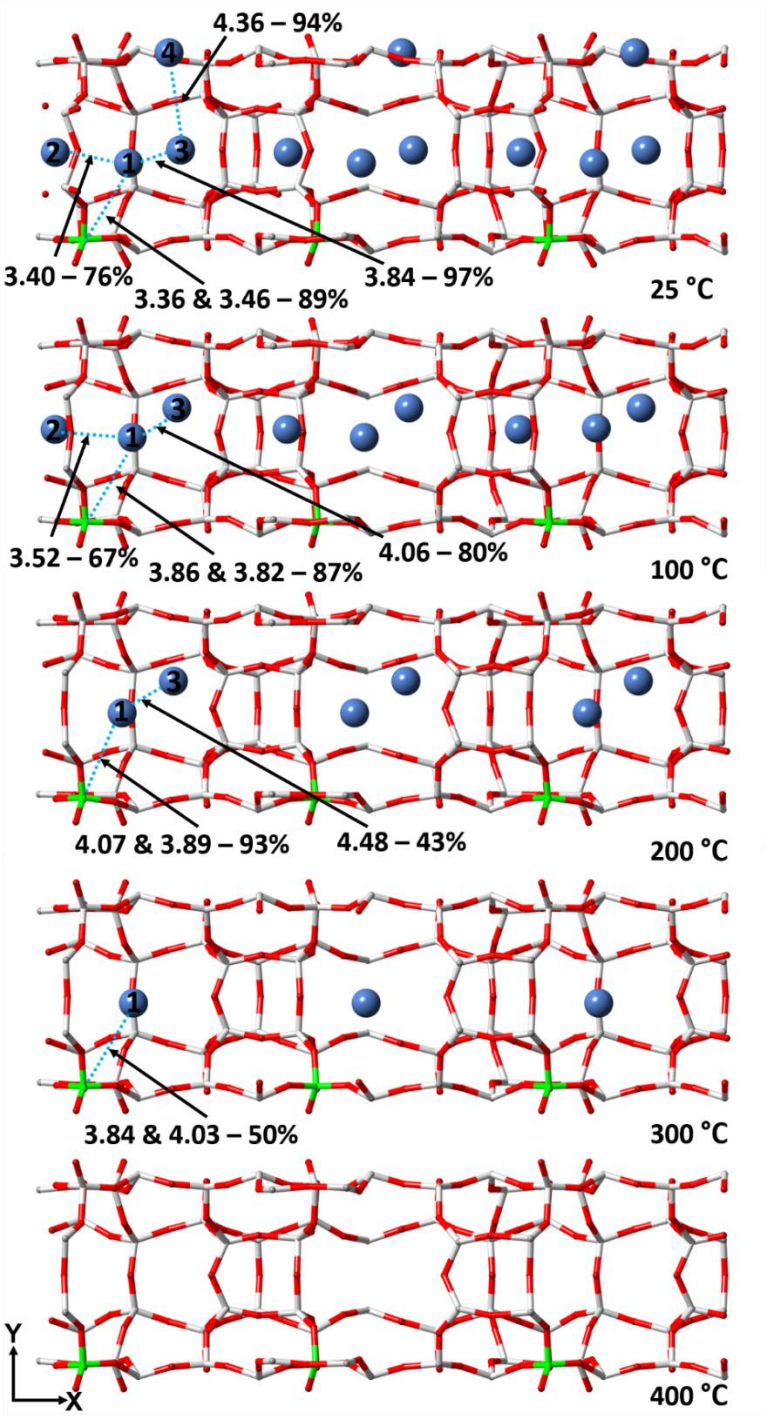

Figure 4.7. Rietveld derived crystal structures of temperature programmed SXRD measurements of H-ZSM-5 pre-adsorbed with ammonia. The numerical values represent the interatomic distances, whereas the percentage values correspond to the SOF values of the corresponding site. The same colour scheme as Figure 4.1 is applied. (See Figures A4.1-A4.4 and Tables A4.2-A4.5 in Appendix for the corresponding Rietveld refinement profiles and detailed atomic parameters.)

Table 4.5. Summary of the Rietveld refinement results of the temperature programmed SXRD of H-ZSM-5 pre-adsorbed with ammonia, showing the derived interatomic distances and the SOF values of the ammonia sites.

Temperature (°C)	**25**	**100**	**200**	**300**	**400**
SOF (Ammonia1)	0.89(1)	0.87(1)	0.93(1)	0.50(1)	-
SOF (Ammonia2)	0.76(1)	0.67(1)	-	-	-
SOF (Ammonia3)	0.97(1)	0.80(1)	0.43(1)	-	-
SOF (Ammonia4)	0.94(1)	-	-	-	-
N1-O18 (Å)	3.18(3)	3.82(4)	3.89(4)	4.03(4)	-
N1-O5 (Å)	3.44(4)	3.86(4)	4.07(4)	3.84(4)	-
N2-N1 (Å)	3.43(4)	3.52(5)	-	-	-
N3-N1 (Å)	3.84(6)	4.06(6)	4.48 (5)	-	-
N4-N3 (Å)	4.36(9)	-	-	-	-

4.3 Conclusions

In conclusion, ammonia storage in H-ZSM-5 is clearly originated from strong acid-base interactions between BAS and ammonia (by first forming a chemisorbed NH_4^+ species (O···$^+$HN)). Due to the confinement effect by the framework structure of H-ZSM-5, there are only two other ammonia molecules interacting with the first NH_4^+ species through its unused H moieties to form typical H-bonds (N–H···N) along the sinusoidal channel. At 25 °C, an additional ammonia molecule is weakly adsorbed on the internal surface of the H-ZSM-5 deep in the straight channel through N–H···O. At elevated desorption temperatures, ammonia molecules with different sorption strengths desorb accordingly. It results in three desorption peaks from the differential of the TGA measurements. We believe such atomic coordination analysis unprecedentedly achieved in the present case could provide fundamental rationalisation, as to why multiple release stages are frequently observed in many reported ammonia storage materials in the forms of physisorption, intermolecular H-bonding, acid–base adducts, etc.

As far as ammonia storage is concerned, large fractions of ammonia characterised with physisorption and H-bonding interactions could be made available by relatively low energy input/output, if they are stored in materials with large voids/channel dimensions. To render the strongly bound ammonia available for recyclable ammonia storage, a much higher energy input would be required. However, a greater number of BAS in the material synthesis is essential to hold the first adsorption layer of ammonia before more ammonia molecules are taken up through the H-bonding network.

Meanwhile, tuning the acidity of the BAS and their spatial arrangement could be feasible to reduce the energy cost of the desorption process.

4.4 References

(1) Stoll, R. E.; Von Linde, F. *Hydrocarb. Process* **2000**, *79* (12), 42–46.

(2) Erisman, J. W.; Sutton, M. A.; Galloway, J.; Klimont, Z.; Winiwarter, W. *Nat. Geosci.* **2008**, *1* (10), 636–639.

(3) Helminen, J.; Helenius, J.; Paatero, E.; Turunen, I. *J. Chem. Eng. Data* **2001**, *46* (2), 391–399.

(4) Doonan, C. J.; Tranchemontagne, D. J.; Glover, T. G.; Hunt, J. R.; Yaghi, O. M. *Nat. Chem.* **2010**, *2* (3), 235–238.

(5) Britt, D.; Tranchemontagne, D.; Yaghi, O. M. *Proc. Natl. Acad. Sci.* **2008**, *105* (33), 11623–11627.

(6) Ma, A.-Z.; Grünert, W. *Chem. Commun.* **1999**, No. 1, 71–72.

(7) Long, R. Q.; Yang, R. T. *Catal. Letters* **2002**, *78* (1–4), 353–357.

(8) Schwidder, M.; Kumar, M. S.; Klementiev, K.; Pohl, M. M.; Brückner, A.; Grünert, W. *J. Catal.* **2005**, *231* (2), 314–330.

(9) Lonyi, F.; Valyon, J. *Microporous Mesoporous Mater.* **2001**, *47* (2–3), 293–301.

(10) Zecchina, A.; Marchese, L.; Bordiga, S.; Paze, C.; Gianotti, E. *J. Phys. Chem. B* **1997**, *101* (48), 10128–10135.

(11) Woolery, G. L.; Kuehl, G. H.; Timken, H. C.; Chester, A. W.; Vartuli, J. C. *Zeolites* **1997**, *2449* (97), 288–296.

(12) Kokotailo, G. T.; Lawton, S. L.; Olson, D. H. *Nature* **1978**, *272*, 437–438.

(13) Redondo, A.; Hay, P. J. *J. Phys. Chem.* **1993**, *97* (45), 11754–11761.

(14) Kyrlidis, A.; Cook, S. J.; Charkraborty, A. K.; Bell, A. T.; Theodorou, D. N. *J. Phys. Chem. C* **1995**, *99* (5), 1505–1515.

(15) Steiner, T. *Angew. Chem. Int. Ed.* **2002**, *41* (1), 48–76.

Chapter 5. From Biomass-Derived Furans to Aromatics with Ethanol

Based on the structural understanding of the BAS of H-ZSM-5, this chapter reports the rational design of a novel biomass conversion reaction from biomass-derived furan and ethanol to aromatics. The use of liquid ethanol instead of high-pressure gaseous ethylene as the source of dienophile in this one-pot synthesis makes the aromatics production much simpler and renewable. The key step in facilitating the reaction is accordingly studied by experimental and theoretical techniques. Some of the data particularly the evaluation of catalytic performances was acquired in collaboration with Mr Ivo Teixeira of our group.

The work in this chapter was published in Angewandte Chemie International Edition as an inside back cover, 'From Biomass-Derived Furans to Aromatics with Ethanol over Zeolite' by Teixeira, I. F., **Lo, B. T. W.,** et al. with equal contribution.

A Journal of the Gesellschaft Deutscher Chemiker

Angewandte International Edition Chemie

GDCh

www.angewandte.org

2016–55/42

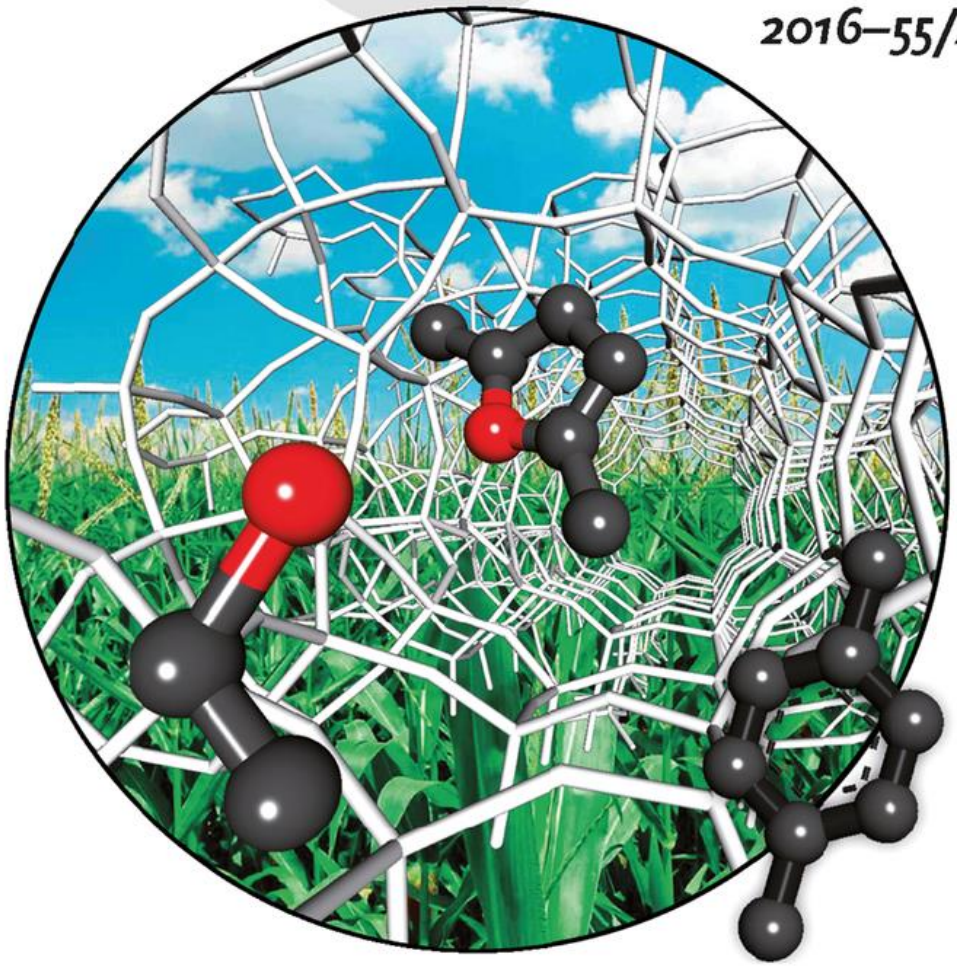

Liquid lunch anyone?

Ethylene produced in situ from ethanol dehydration over zeolite is used for the catalytic conversion of biomass-derived furans into aromatic compounds by Diels–Alder cycloaddition. In their Communication on page 13061 ff., G. Mpourmpakis, S. C. E. Tsang et al. describe a rapid and renewable one-pot synthesis of aromatic compounds using liquid ethanol as a source of dienophile instead of pressurized ethylene gas.

WILEY-VCH

5.1 Introduction

Non-renewable fossil fuels are of great importance for the current energy and chemicals provision for the society.[1–3] The CO_2 and related problems from the consumption of these fuels have evidently associated with global warming and climate change.[1–3] Therefore, a CO_2-neutral solution has attracted substantial attention, such as solar power and biomass conversion are possible candidates.[4] Lignocellulose is one of the most common biomass materials available around the globe.[5,6] It can readily be converted into valuable platform chemicals, including furfuryl alcohol and 2,5-dimethylfuran (DMF).[7,8] Some of these platform chemicals contain a furan group; the presence of the furan group makes it available to be further converted into various aromatic products, via Diels-Alder (DA) and dehydration reactions. These conversions have been investigated over a range of zeolite catalysts, using ethylene or propylene as the co-substrate.[9–11]

To avoid the handling of high-pressure ethylene/propylene gas, we present a novel catalytic conversion of biomass-derived DMF and ethanol to aromatics (mainly p-xylene) over zeolite catalysts. From our experimental and theoretical studies, ethanol first dehydrates to form ethylene; the *in situ* produced ethylene (dienophile) then reacts with DMF (diene) via the DA reaction. The use of liquid ethanol instead of high-pressure ethylene for the DA reaction makes the entire 'one-pot' process much simpler and safer to handle, and more importantly, completely renewable. Under the optimised reaction conditions, much higher reaction rates are observed. The rate promotion is investigated using both experimental and theoretical approaches, that a preferential protonation of ethanol over DMF leads to a lower activation barrier. The

preferential protonation of ethanol is believed to be the key step facilitating the DA and cycloadduct dehydration reactions in zeolite catalysts.

5.2 Catalytic Performance

The catalytic conversion of ethanol and DMF (ethanol/DMF) was first compared against ethylene/DMF under comparable reaction conditions as reported by Mpourmpakis et al.[12] High catalytic activities (> 80% conversion) are observed over all zeolite samples (H-USY and H-ZSM-5 with different Si/Al ratio, see Table 5.1). H-USY (Si/Al = 6) shows the best catalytic performance, with the highest DMF conversion and aromatic selectivities. In general, the p-xylene selectivity is higher when H-USY is used as the catalyst.

Like that of ethylene/DMF[9,10], ethanol/DMF produces p-xylene as the main product (see Figure 5.1 and Scheme 5.1). This hints ethylene may be produced *in situ* from the dehydration of ethanol over the BAS in zeolites. The side products include 2,5-hexanedione (from DMF hydrolysis), alkylated aromatics, alkylated furans and coke. As displayed in Figure 5.2, the overall conversion (yield) of ethanol/DMF is also higher than that of ethylene/DMF (97% vs. 70%) over H-USY (Si/Al = 6). Note that the use of ethanol produces a small quantity of aromatics with oxygen-containing substituent groups. In addition, the reaction conditions were also optimised for a range of parameters, such as time, temperature and ethanol/DMF ratio (see Chapter 2.3).

We understand the same Si/Al ratio should be compared between H-USY and H-ZSM-5. But due to the difference in sample synthesis, a direct comparison is extremely difficult. In fact, H-USY (Si/Al = 6) and H-ZSM-5 (Si/Al = 19) are in the same regime in terms of BAS concentration (0.6 vs. 0.76 mmol g^{-1}, see Table 5.1). This suggests the

framework structure of H-USY may favour the specific geometric requirement for the DA reaction.

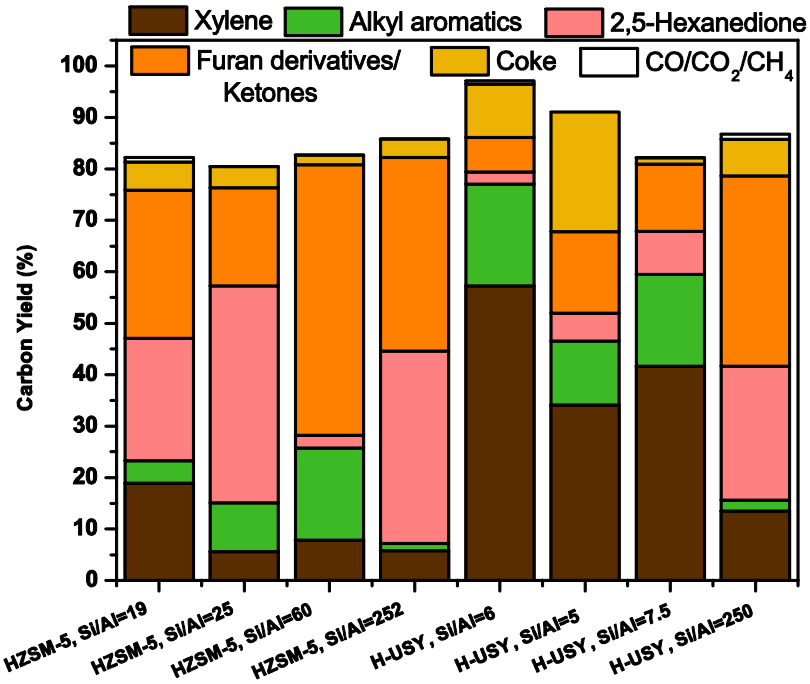

Figure 5.1. Product distribution for the catalytic conversion of 2,5-dimethylfuran (DMF) with ethanol over different zeolites.

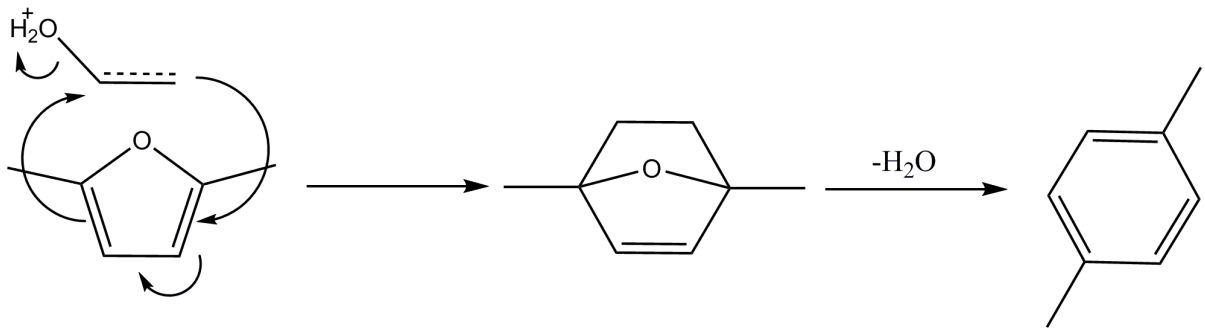

Scheme 5.1. Schematic for the catalytic production of p-xylene from DMF and ethanol.

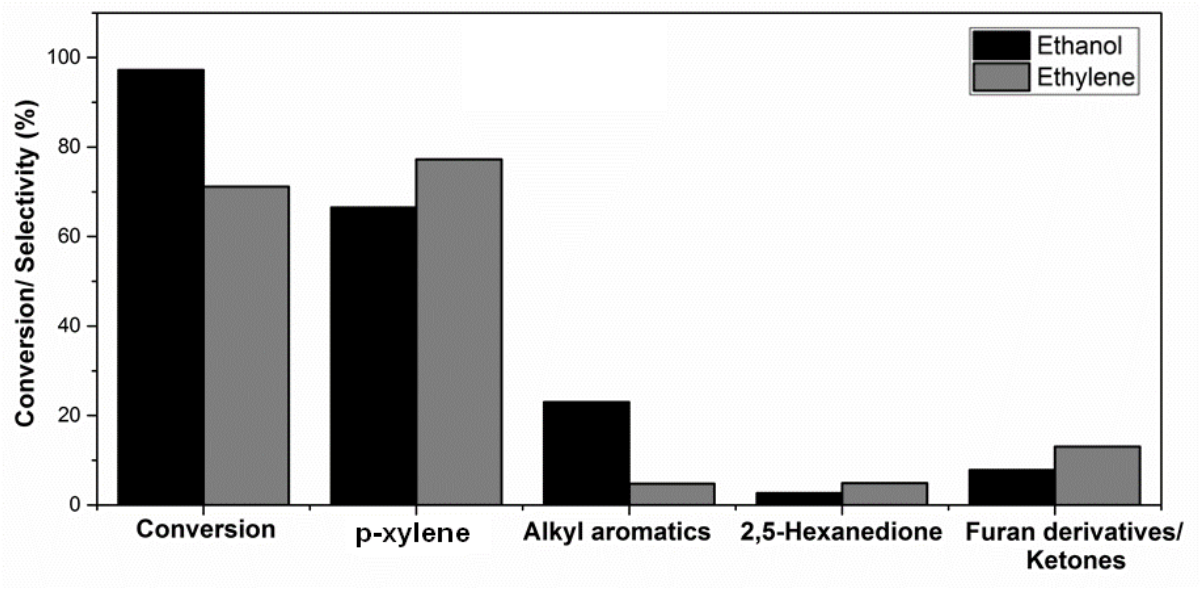

Figure 5.2. Catalytic performance of the conversion of ethanol/DMF and ethylene/DMF reactions over H-USY (Si/Al = 6). Reaction condition: temperature = 300 °C; substrate concentration: ethylene = 0.45 mol (40 bar), ethanol = 0.14 mol, and DMF = 0.14 mol.

Table 5.1. Acid site concentrations and surface area of the zeolite samples.

Zeolite Samples	**Si/Al**[i]	**BAS conc.**[ii] **(mmol g^{-1})**	**Surface Area**[iii] **(m^2 g^{-1})**	**Turnover frequency**[iv] **(10^2 h^{-1})**
H-ZSM-5	19	0.76	349	0.63
	25	0.31	311	1.50
	60	0.03	309	14.95
	252	-	329	-
H-USY	6	0.6	735	2.57
	5	1.1	650	0.23
	7.5	0.1	550	4.75
	250	0.1	620	5.02

[i] synthesis ratio

[ii] the values for H-ZSM-5 are estimated using the extinction coefficient method by Emeis[13]; the values for H-USY are provided by SRIFT-Sinopec

[iii] from BET

[iv] rate per mole of DMF to mole of products per BAS per hour

5.3 Kinetic Studies

When ethanol is used as the co-substrate instead of ethylene, the improvement in the catalytic conversion of DMF is significant. The initial conversion rate is improved by more than four times under the same reaction conditions over H-USY (Si/Al =6, 0.141 and 0.034 mol g_{cat}^{-1} h^{-1} for ethanol/DMF and ethylene/DMF).

The optimised substrate concentrations over the H-USY (Si/Al = 6) are DMF (0.14 mol) with ethanol (0.14 mol) or ethylene (40 bar, 0.45 mol). Interestingly, a higher reaction rate was however observed when ethanol was used as the dienophile (see Figures 5.3(a) & 5.4). Not to mention that less ethanol was used, the possible competing side reactions from ethanol should also lower the rate of reaction. Therefore, the kinetic difference may reveal important mechanistic details.

In addition, the apparent activation energy of ethanol/DMF is estimated to be 55.8(12) kJ mol^{-1} from the Arrhenius plot (see Figure 5.3(b)). It is notably lower than that of ethylene/DMF (*ca*. 100 kJ mol^{-1}, making a difference of *ca*. 44 kJ mol^{-1}).[9] Hence, the two reaction profiles could be substantially different.

In the next sections, the rate promotion will be extensively discussed by combing theoretical calculations and experimental techniques.

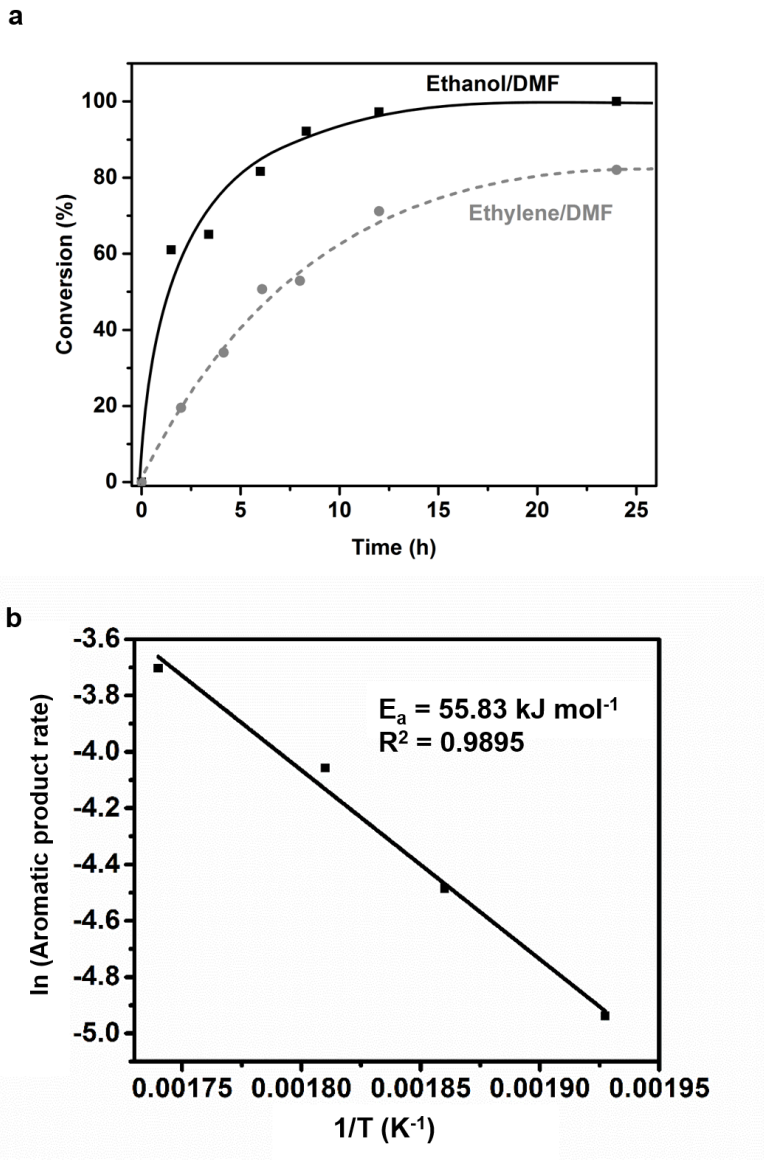

Figure 5.3. (**a**) Kinetic data derived for the catalytic conversion of ethanol/DMF and ethylene/DMF over H-USY (Si/Al = 6). (**b**) Arrhenius plot for the estimation of apparent activation energy of ethanol/DMF. Reaction condition: temperature = 300 °C; substrate concentration: ethylene = 0.45 mol (40 bar), ethanol = 0.14 mol, and DMF = 0.14 mol.

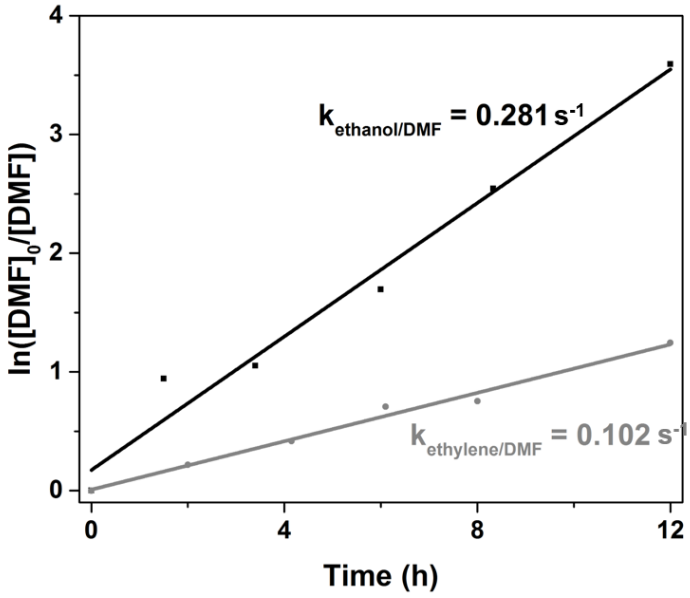

Figure 5.4. Rate constant derivation based on first order fitting. R^2 (ethanol/DMF) = 0.971, R^2 (ethylene/DMF) = 0.985.

5.4 Theoretical Calculations

In this section, the energy profiles of p-xylene formation from ethanol/DMF and ethylene/DMF, and the binding energies between the BAS and the adsorbates are calculated by theoretical calculations.

5.4.1 Reaction Energetics

The DFT - electronic structure methods were used to calculate the two energy profiles of the elementary steps of p-xylene formation from ethanol/DMF (green path) and ethylene/DMF (black path), as shown in Figure 5.5. The corresponding free energies, enthalpies and entropies of the elementary steps were also computed under our reaction conditions and summarised in Table 5.2. To express the computational energy representation (E-representation) landscapes of a catalytic cycle in term of experimental kinetics (k-representation), the energetic span model of Kozuch and Shaik was also summarised in Table 5.2.[14]

In ethylene/DMF (black), DMF is first protonated by the BAS (see Table 5.3 and Chapter 5.5 for the PA analysis). Therefore, either the DA reaction (via DA$^{\neq}$) or dehydration of the cycloadduct (via C–O$^{\neq}$ and C–H$^{\neq}$) should be the rate determining step. It is however difficult to judge between the two due to the similarity in energy barrier. It has recently reported that the rate determining step is BAS concentration dependent.[9,10] From the BAS concentration of our H-USY (Si/Al = 6) sample, it is believed the DA reaction should be rate-limiting as proposed by Williams et al.[9,10] Note that the ethylene/DMF route was originally studied by Caratzoulas et al. using the same approach.[9,15]

In the case of ethanol/DMF (green), there are a cascade of fundamental steps: ethanol will be first preferentially protonated instead of DMF by the BAS. The pronated ethanol is then followed by dehydration of the protonated ethanol (via E1 mechanism) to ethylene and hydronium ion (H_3O^+). The H_3O^+ then binds with the DMF through weak H-bonding (O-H‡). This weak interaction does not alter the electron density of the DMF as much as in the case of ethylene/DMF (where DMF is preferentially protonated). Hence, the HOMO-LUMO gap is narrowed (see Figure 5.6), which lowers the activation barrier for the rate-determining DA‡ state. Indeed, the calculated electronic stabilisation energy of ethanol/DMF (96.7 kJ mol^{-1}) is notably lower than that of ethylene/DMF (107.9 kJ mol^{-1}, see Table 5.3). In addition, the BAS with the H_3O^+ produced can further catalyse C-O cleavage (C-O‡) and C-H removal (C-H‡) via facilitated hydrogen transfer. This ultimately forms another water molecule. The catalytic cycle is completed by a final proton transfer, forming p-xylene and a proton.

From the overall Gibbs free energy, the calculated energetic span barriers are 115.1 kJ mol^{-1} for ethanol/DMF and 155.4 kJ mol^{-1} for ethylene/DMF, respectively. Surprisingly, the difference in energetic span barrier between the two routes, 40.3 kJ mol^{-1}, matches perfectly with the kinetic experimental observations (*ca*. 44 kJ mol^{-1}).

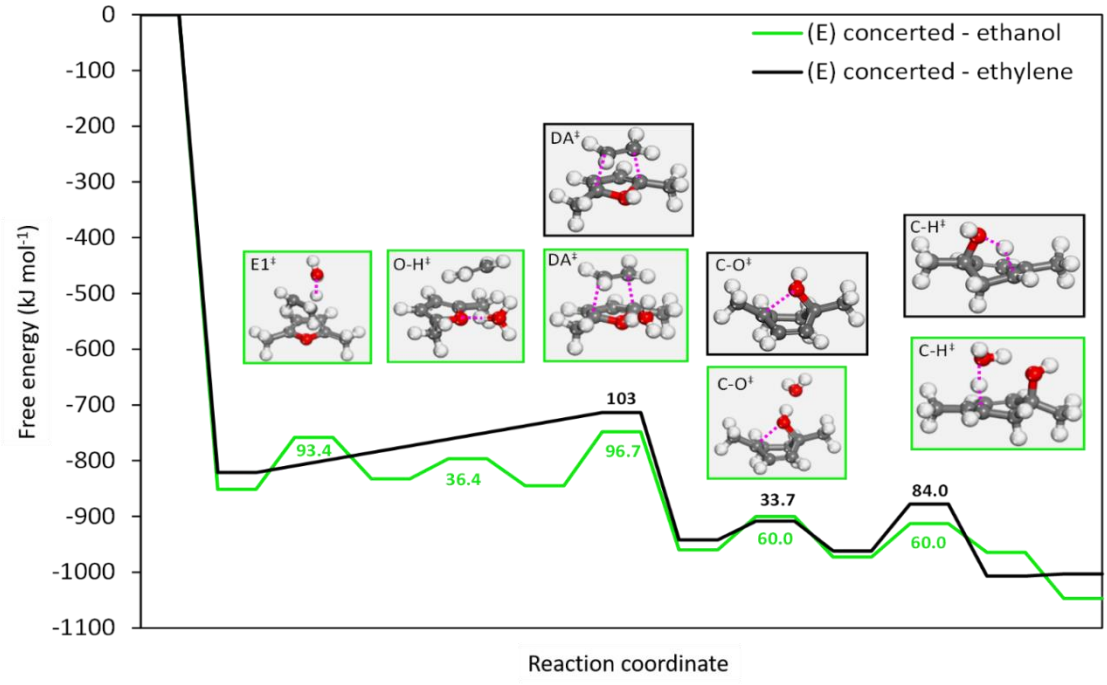

Figure 5.5. Calculated Gibbs free energy profiles for the catalytic conversion of ethanol/DMF (green) and ethylene/DMF (black), with the corresponding transition state geometries shown as insets.

Table 5.3. DFT calculated barriers for the elementary steps in the ethylene/DMF and ethanol/DMF routes at 300 °C.

Pathway	Elementary step	Enthalpy (kJ mol^{-1})	Entropy (J mol^{-1} K^{-1})	Total Gibbs free energy (kJ mol^{-1})	Electronic stabilisation energy (kJ mol^{-1})
Ethylene/DMF	DA‡	109.0	-63.2	145.2	107.9
	C-O‡	25.4	3.5	23.4	33.7
	C-H‡	69.9	-27.4	85.6	84.0
Ethanol/DMF	E1‡	77.6	10.5	71.6	93.3
	O-H‡	38.5	-15.4	47.3	36.4
	DA‡	96.3	-54.7	127.6	96.7
	C-O‡	53.6	11.6	46.9	59.9
	C-H‡	17.1	-28.5	33.5	59.9

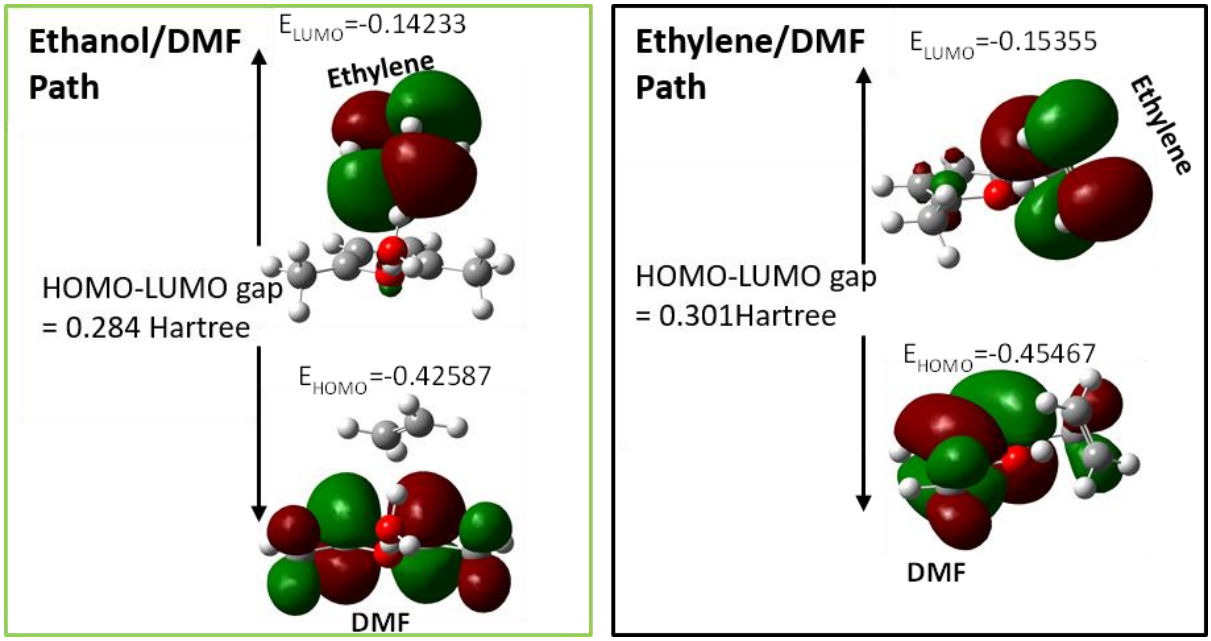

Figure 5.6. HOMO-LUMO orbital analysis at the initial state of the DA reaction of the ethanol/DMF and ethylene/DMF pathways.

Table 5.3. CBS-QB3 calculated gas phase proton affinities (PA) of reaction species. Note that negative values indicate exothermicity.

Reaction species	**Gas phase proton affinity (kJ mol^{-1})**
Ethylene	-677.3
Water	-682.2
DMF (C)	-732.3
p-xylene	-770.8
Ethanol	-779.1

5.4.2 Binding Energies Estimation

We further investigated the adsorption behaviour in zeolites using the ONIOM method. However, the H-USY structure is extremely highly symmetric (space group of *Fd-3m*). There are limitations in using the combined theoretical-experimental method to study the adsorbate structure in H-USY. Therefore, H-ZSM-5 (Si/Al = 19, space group of *Pnma*) was deliberately chosen based on our structural understanding. Figure 5.7(a) shows the ONIOM three-layer partitioning scheme. The corresponding ground state adsorption geometries are displayed in Figure 5.7(b)-(e). The ONIOM calculated binding energies for ethanol, ethylene and DMF are -70.1, -24.1 and +16.5 kJ mol^{-1}, respectively. It means that the adsorption of DMF is slightly endothermic, in contrast to the highly exothermic ethanol adsorption. This is perhaps caused by the steric hindrance of the bulky DMF when it is adsorbed onto the zeolite framework. Thus, the ONIOM calculation indicates that ethanol is more preferentially protonated by the BAS than DMF and ethylene.

Next, the preferential protonation will be experimentally verified by SXRD in this next section.

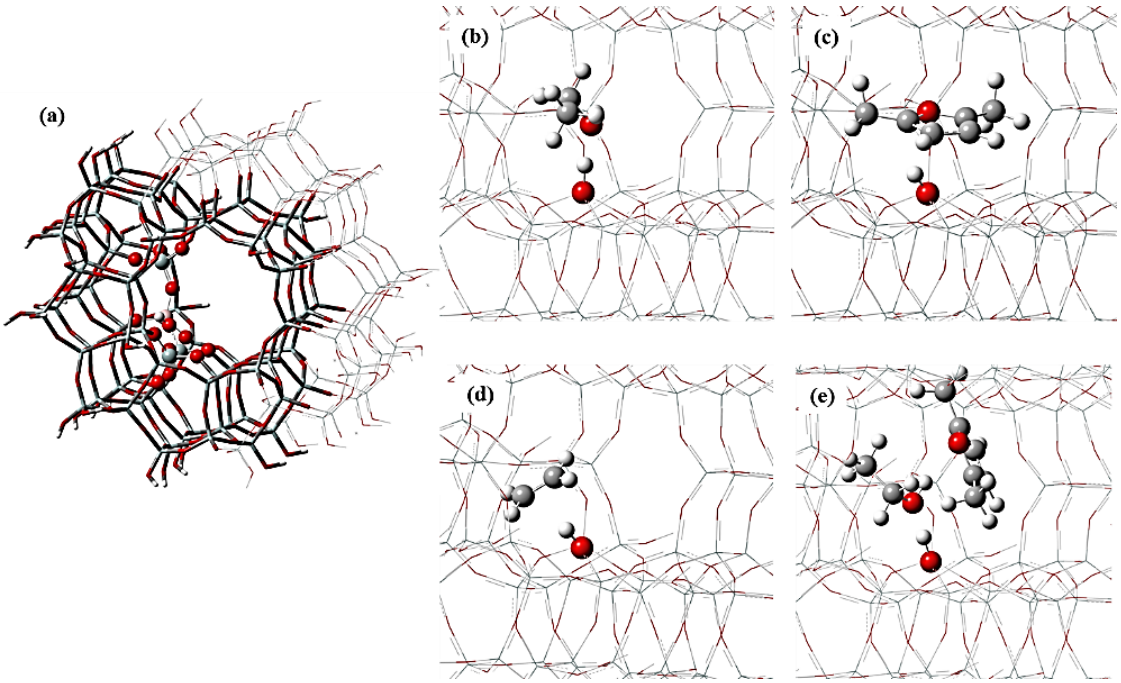

Figure 5.7. (**a**) ONIOM3 partitioning scheme applied on H-ZSM-5. (**b**)-(**e**) Ground state adsorption conformations of ethanol, DMF, ethylene, and ethanol-DMF dimer, respectively, on H-ZSM-5. The adsorbate molecules are shown in ball model: grey = C, white = H, and red = O. The zeolite framework is shown in line representation.

5.5 Experimental characterisation: SXRD

It has been demonstrated by DFT and ONIOM calculations that the rate promotion in the catalytic conversion of ethanol/DMF is partly due to the preferential protonation of the ethanol. When ethanol is protonated by the BAS in zeolites, the *in situ* production H_3O^+ stabilises the key $DA^‡$ transition states (see Figure 5.5). To experimentally verify the subtle change in terms of preferential protonation, we combined SXRD with Rietveld refinement to elucidate the adsorbate structures at an atomistic level. As displayed in Figure 5.8, the Rietveld refinement profiles and the corresponding crystal structures of H-ZSM-5 pre-adsorbed (a,b) independently with ethanol, (c,d) independently with DMF, and (e,f) with an equimolar mixture of ethanol and DMF. Also see Table 5.4 for the corresponding crystallographic parameters.

In the case of H-ZSM-5 **independently** pre-adsorbed with ethanol or DMF, the two primary adsorbates (labelled as EtOH 1 and DMF 1) locate in the sinusoidal-straight cross-channel region of the framework. From the shortest interatomic/intermolecular distances (like the interpretation in Chapter 3), the BAS selectively protonates the adsorbate molecules to form primary protonated adduct cations, followed by linking other adsorbate molecules via weak H-bonding interactions. By comparing the interatomic/intermolecular distances, it clearly shows the first protonated ethanol or DMF molecule locates in the cross-channel region. The interatomic distances between these primary acid-base adducts are 3.2±0.1 Å. Next, weakly adsorbed species are detected at > 4.0 Å from the framework O atoms.

However, when an **equimolar mixture** of ethanol and DMF is applied, ethanol is preferentially protonated by the BAS in the cross-channel region, then interacts with DMF via a weak intermolecular H-bonding. Thus, the DMF in the straight channel will be forced to interact with the $EtOH_2^+$ through a weak intermolecular H-bonding interaction, as depicted in Figure 5.5.

Excitingly, we have experimentally verified by SXRD the preferential protonation of ethanol in the case of ethanol/DMF. It agrees with our prediction based on the theoretical PA values of the adsorbate species (see Table 5.3; ethanol > DMF > water > ethylene). This is also consistent with the ideal proton flux for this reaction, as demonstrated by our DFT calculations.

In short, as ethanol is readily adsorbed on the BAS in zeolites, the subsequent rapid dehydration will produce high concentration of ethylene and H_3O^+. There are two rate promoting effects in the catalytic conversion of DMF, when ethanol is used instead of ethanol; (i) the H_3O^+ facilities the DA reaction by lowering the HOMO-LUMO gap, and (ii) the ethylene *in situ* produced has a higher local concentration than that of ethylene/DMF.

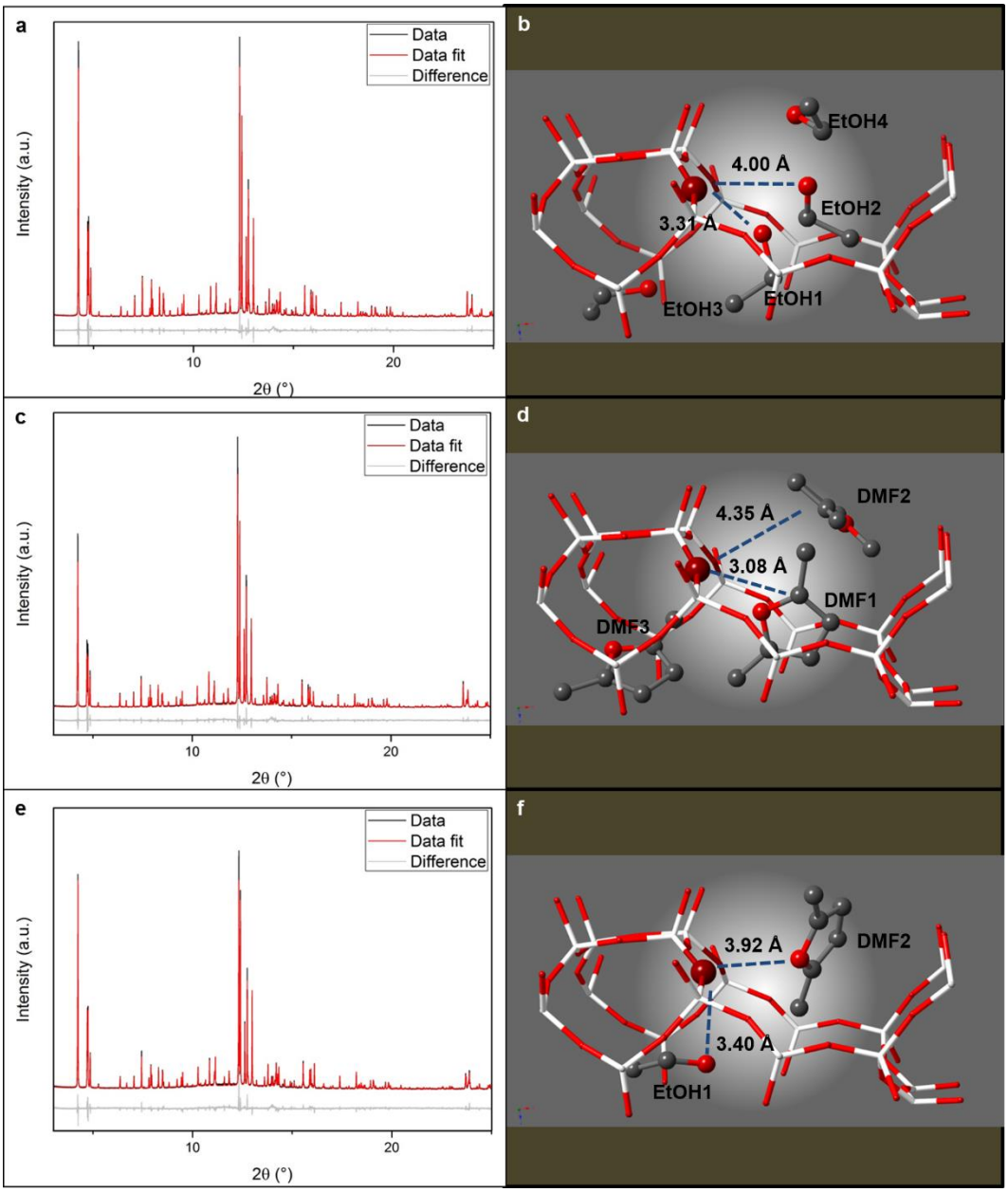

Figure 5.8. Rietveld refinement profiles of H-ZSM-5 pre-adsorbed with (**a**) ethanol, (**c**) DMF, and (**e**) ethanol/DMF at 25 °C, and the corresponding crystal structures viewing from the [010] direction are displayed; (**b**) ethanol, (**d**) DMF, (**f**) ethanol/DMF. Their crystallographic/atomic parameters from Rietveld refinement are summarised in Table 5.6 and Tables A5.1-A5.3 in Appendix. Atoms are represented in ball/sticks: white = Si/Al, red = O, black = C. No hydrogen atoms are plotted for clarity.

Table 5.4. Crystallographic parameters of the H-ZSM-5 samples measured at 25 °C, dehydrated, pre-adsorbed with ethanol, DMF, and an equimolar mixture of DMF and ethanol.

Samples	**H-ZSM-5 (dehydrated)**	**H-ZSM-5 (ethanol)**	**H-ZSM-5 (DMF)**	**H-ZSM-5 (DMF & ethanol)**
Chemical formula	$H_{4.48}Al_{4.48}Si_{91.52}O_{192}$	$H_{4.48}Al_{4.48}Si_{91.52}O_{192}$ -$n$$C_2H_5OH$	$H_{4.48}Al_{4.48}Si_{91.52}O_{192}$ -$n$$C_6H_8O$	$H_{4.48}Al_{4.48}Si_{91.52}O_{192}$ -$m$$C_6H_8O$.$n$$C_2H_5OH$
X-ray source	Synchrotron	Synchrotron	Synchrotron	Synchrotron
Wavelength (Å)	0.825634(2)	0.825850(2)	0.825850(2)	0.825850(2)
2θ -zero point (°)	-0.002500(10)	0.010275(10)	0.010275(10)	0.010275(10)
Space group	*Pnma*	*Pnma*	*Pnma*	*Pnma*
Crystal system	Orthorhombic	Orthorhombic	Orthorhombic	Orthorhombic
a (Å)	20.13675(3)	20.12191(3)	20.16651(4)	20.09515(4)
b (Å)	19.95928(3)	19.93057(3)	19.97710(4)	19.96020(4)
c (Å)	13.43725(2)	13.42604(2)	13.45305(3)	13.43518(3)
V (Å^3)	5400.631(22)	5384.394(15)	5419.812(19)	5388.893(22)
2θ range for refinement (°)	3-55	3-55	3-55	3-55
Detector	MAC	MAC	MAC	MAC
Number of parameters	36	170	161	153
Number of *hkl*s	4190	4190	4190	4190
Refinement methods	Le Bail	Rietveld	Rietveld	Rietveld
$R_{wp}/R_p/R_{exp}$ (%)	6.621/5.077/4.958	7.649/5.808/3.364	8.457/6.461/3.339	8.955/7.030/3.883
X^2	1.335	2.274	2.533	2.306

5.6 Conclusions

In summary, combining high-resolution SXRD, detailed kinetic measurements and quantum level calculations, we demonstrate that ethanol is a much superior co-substrate and dienophile than ethylene for the catalytic conversion of biomass-derived furan over zeolites. Not only the use of high-pressure gaseous ethylene is avoided, but the rate of reaction has also been remarkably increased. The DA reaction with different biomass-derived furans and dienophiles, including alkynes and alkenes in spatially defined zeolites may lead to tailored activity and stereochemistry. More importantly, the successful and rational design of the catalytic system in zeolites is encouraging. We believe the progressive advancement in biomass utilisation makes such renewable resource more valuable, and biomass will eventually play a major role in the future energy and chemicals provision.

5.7 References

(1) Brandt, A.; Gräsvik, J.; Hallett, J. P.; Welton, T. *Green Chem.* **2013**, *15* (3), 550–583.

(2) Xing, R.; Subrahmanyam, A. V; Olcay, H.; Qi, W.; van Walsum, G. P.; Pendse, H.; Huber, G. W. *Green Chem.* **2010**, *12* (11), 1933–1946.

(3) Ragauskas, A. J.; Williams, C. K.; Davison, B. H.; Britovsek, G.; Cairney, J.; Eckert, C. A.; Frederick Jr., W. J.; Hallett, J. P.; Leak, D. J.; Liotta, C. L.; Mielenz, J. R.; Murphy, R.; Templer, R.; Tschaplinski, T. *Science* **2006**, *311* (5760), 484–489.

(4) Román-Leshkov, Y.; Chheda, J. N.; Dumesic, J. A. *Science* **2006**, *312* (5782), 1933–1937.

(5) Alonso, D. M.; Wettstein, S. G.; Dumesic, J. A. *Chem. Soc. Rev.* **2012**, *41* (24), 8075–8098.

(6) Climent, M. J.; Corma, A.; Iborra, S. *Green Chem.* **2014**, *16* (2), 516–547.

(7) Luterbacher, J. S.; Alonso, D. M.; Dumesic, J. A. *Green Chem.* **2014**, *16* (12), 4816–4838.

(8) Zheng, A.; Zhao, Z.; Chang, S.; Huang, Z.; Zhao, K.; Wu, H.; Wang, X.; He, F.; Li, H. *Green Chem.* **2014**, *16* (5), 2580–2586.

(9) Williams, C. L.; Chang, C.-C.; Do, P.; Nikbin, N.; Caratzoulas, S.; Vlachos, D. G.; Lobo, R. F.; Fan, W.; Dauenhauer, P. J. *ACS Catal.* **2012**, *2* (6), 935–939.

(10) Williams, C. L.; Vinter, K. P.; Chang, C.-C.; Xiong, R.; Green, S. K.; Sandler, S. I.; Vlachos, D. G.; Fan, W.; Dauenhauer, P. J. *Catal. Sci. Technol.* **2016**, *6* (1), 178–187.

(11) Cheng, Y.-T.; Huber, G. W. *Green Chem.* **2012**, *14* (11), 3114–3125.

(12) Kostestkyy, P.; Maheswari, J. P.; Mpourmpakis, G. *J. Phys. Chem. C* **2015**, *119* (28), 16139–16147.

(13) Emeis, C. A. *J. Catal.* **1993**, *141* (2), 347–354.

(14) Kozuch, S.; Shaik, S. *Acc. Chem. Res.* **2010**, *44* (2), 101–110.

(15) Nikbin, N.; Do, P. T.; Caratzoulas, S.; Lobo, R. F.; Dauenhauer, P. J.; Vlachos, D. G. *J. Catal.* **2013**, *297*, 35–43.

Chapter 6. Identification of Activated Organic Adsorbates in H-ZSM-5 during Methanol Conversion by *Operando* Synchrotron Powder X-ray Diffraction

This chapter studies the mechanism of an industrially important catalytic process. By monitoring the catalytic conversion of methanol using *operando* SXRD in combination with theoretical calculations, we demonstrate *for the first time,* that the concerted associative mechanism is responsible for dimethyl ether production via an activated protonated methanol intermediate species over H-ZSM-5 in an early stage of the reaction at 200 °C. The minor contribution from the dissociative mechanism of the adsorbed methoxy intermediate species at the BAS, renders their accumulation during the late stage of the reaction. The accumulation of the methoxy species leads to a build-up of the 'hydrocarbon pool' and eventually to 'carbon' through C-C bond formation.

The work in this chapter was submitted, 'Identification of Activated Organic Adsorbates in H-ZSM-5 during Methanol Conversion by *Operando* Synchrotron Powder X-ray Diffraction' by **Lo, B. T. W.,** et al.

6.1 Introduction

Methanol becomes increasingly important as the building block for chemicals and energy carrier in 'methanol economy' according to George A. Olah, the Nobel laureate in Chemistry in 1994. It ultimately utilises renewable biomass sources to replace traditional fossil fuels.[1] Although methanol is currently produced from fossil fuels via the syn-gas route, it can also be produced from various biomass sources or from CO_2 reduction in carbon recycling.[1] Despite the fact that methanol can be directly combusted as a fuel, the general routes to convert methanol-to-hydrocarbons (MTH) have also recently been attracting more attention as an alternative pathway to crude-oil-derived hydrocarbons, such as commodity chemicals (olefins, MTO), aromatics (MTA) and high-grade gasoline (MTG), etc.[2,3] One of the most important technical problems is during methanol conversion, rapid catalyst deactivation and 'carbon' deposition commonly occur.[4] The successful practice of these processes is critically dependent on the catalyst nature and conditions used.

Although catalytic methanol conversion has been extensively investigated over various acidic catalysts, including zeolites and alumina,[5–7] the prevailing mechanism of how methanol is first activated and the fates of intermediates are still not fully understood. At low temperatures and high flow rate condition, methanol dehydration to dimethyl ether (DME) is known to take place favourably.[8] Consequently, although the reaction route leading to the formation of DME from methanol is still debateable, it is broadly believed that the organic intermediates as so-called 'hydrocarbon pools' (HCP) in zeolites are derived from DME and related species (as initially proposed by Dahl and Kolboe).[9–11] Briefly, there are two proposed mechanisms[12–15]: (i) the dissociative route:

methanol is protonated at a BAS, followed by dehydration generating surface methoxy species, which then reacts with another incoming methanol; (ii) the associative route: methanol first adsorbs onto a BAS. This 'activated' protonated species then combines with another methanol molecule, forming a dimer like species, subsequently followed by dehydration producing DME. Recent theoretical modelling efforts by Moses and Nørskov[15] (in H-ZSM-22), and Grabow et al.[16] (in H-ZSM-5) have suggested that the associative mechanism dominates at low temperature, while the dissociative mechanism prevails at high temperature. Based on comprehensive calculations, Grabow et al. have reported that the 'crossover' temperature between these two mechanisms is zeolite framework and acidity dependent, where the 'crossover' temperature in H-ZSM-5 is around 427 °C.[16] However, there is a general lack of experimental evidence, particularly at *in situ* or *operando* condition to verify one mechanism from the other. There is also a chance for the two reactions concurrently taking place, should their activation barriers are both overcome. In fact the methoxy species (CH_3-O_z, where O_z is a framework O atom adjacent to the Al site) has been previously identified by *ex situ* spectroscopic techniques such as ^{13}C ssNMR[17–19] and FT-IR[6,20,21], which is indicative of the dissociative mechanism. But there is no proof for the associative mechanism or hint for the hydrocarbon and carbon formations during methanol conversion in zeolites at specific experimental conditions.

From the previous chapters, by making use of the Bragg repeating zeolite porous templates as an alternative to the spectroscopic techniques, the interatomic distances and angles between organic adsorbates with the BAS in H-ZSM-5 have been measured within experimental errors.[22,23] Thus, we have built a high-pressure, low-dead-volume capillary reactor gas-cell using an on-line mass spectrometer (see details in Chapter 2.2)

to monitor the structure-activity relationship for catalytic studies under *operando* SXRD conditions.

In this chapter, it is demonstrated *for the first time*, that the direct observation of the activated protonated methanol species in H-ZSM-5. It locates on the BAS during the early stage at 200 °C, where a high activity for DME is prevalence. As the reaction progressed, only small residual activity for DME formation is observed in the late stage (over 10 h), largely due to catalyst deactivation. Our structure refinement shows that the methoxy species associated with poly-aromatic condensed 'carbon' in the macro-pore of H-ZSM-5 can be favourably detected at increasing quantity.

6.2 Results and Discussion

The experimental and theoretical work will be discussed accordingly for the mechanistic study of methanol conversion over H-ZSM-5.

6.2.1 Kinetic Analysis and Basic Characterisation

The H-ZSM-5 sample, containing one Al (one BAS) per asymmetric unit was deliberately chosen. The temperature programmed ramping at 10 °C min^{-1} for methanol conversion over H-ZSM-5 in the capillary reactor under a N_2 flow rate of 1 mL min^{-1} at 1 atmosphere via a methanol saturator (kept at RT) was first collected. The on-line mass spectra of methanol substrate and DME as the major product (traces of CO, HCHO and CH_4) were simultaneously monitored. As seen in Figure 6.1(a), the slight increase in the methanol concentration from 25 – 150 °C is due to a higher methanol vapour pressure from the warm-up of methanol saturator placed near the reactor. However, Figure 6.1(a) clearly shows an increasing DME concentration from 100 °C, with a corresponding fall in methanol indicative of the initial dehydration process. Figure 6.1(b) shows the corresponding intensity changes of the Bragg peaks at low 2θ angles. It is attributed to the decrease in adsorbed methanol occupancy and increase in thermal vibrations at higher temperatures. The apparent activation energy is estimated from the Arrhenius plot to be 40.3(18) kJ mol^{-1} (see Figure 6.2). This value of activation energy falls in the range of a diffusion control reaction as expected in a typical zeolite catalysis reaction. Also, the lattice of H-ZSM-5 slightly expands at higher temperatures (see Table 6.1 for the detailed crystallographic parameters).

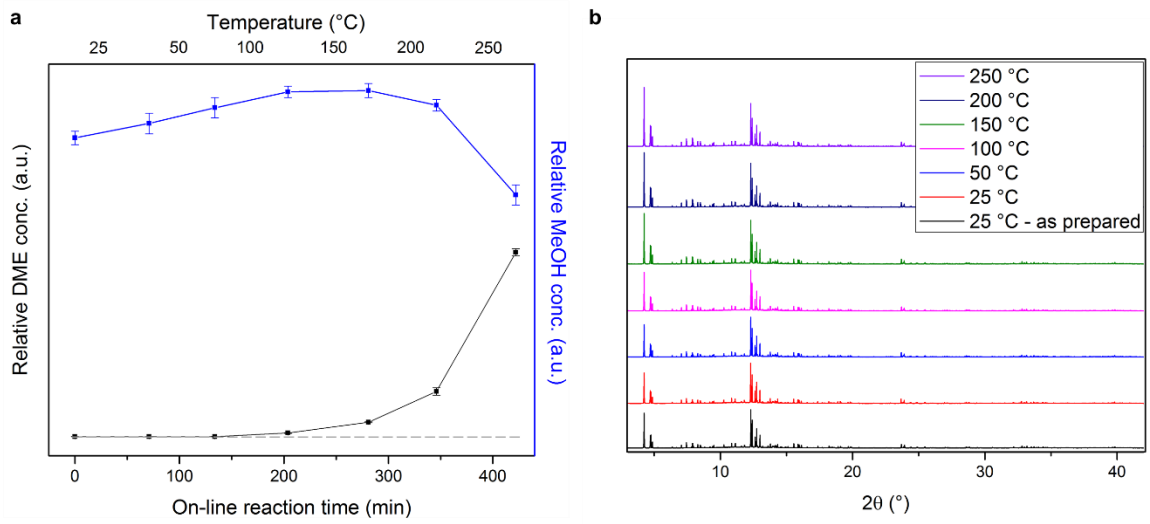

Figure 6.1. (**a**) On-line mass spectra showing the relative DME and methanol concentrations, and (**b**) *operando* SXRD patterns with a flowing stream of methanol vapour over H-ZSM-5 (25 to 250 °C).

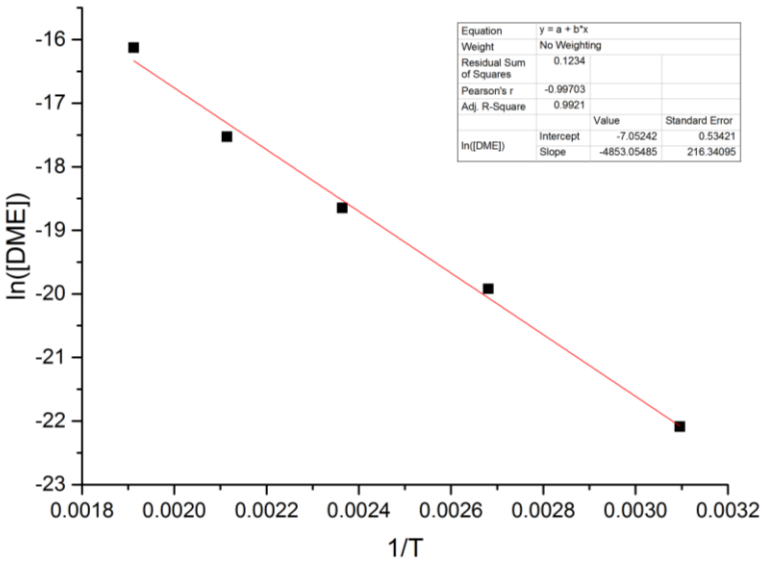

Figure 6.2. The apparent activation energy estimation from the Arrhenius plot.

Table 6.1. *Operando* SXRD crystallographic parameters of the H-ZSM-5 sample at various temperatures with a flowing stream of methanol vapour.

Temperature (°C)	**25(1)**	**50(1)**	**100(1)**	**150(1)**	**200(1)**	**250(1)**
X-ray source	Synchrotron	Synchrotron	Synchrotron	Synchrotron	Synchrotron	Synchrotron
Wavelength (Å)	0.826617(2)	0.826617(2)	0.826617(2)	0.826617(2)	0.826617(2)	0.826617(2)
2θ - zero point (°)	0.00025(1)	0.00025(1)	0.00025(1)	0.00025(1)	0.00025(1)	0.00025(1)
Space group	*Pnma*	*Pnma*	*Pnma*	*Pnma*	*Pnma*	*Pnma*
Crystal system	Orthorhombic	Orthorhombic	Orthorhombic	Orthorhombic	Orthorhombic	Orthorhombic
a (Å)	20.15846(3)	20.14305(3)	20.12853(3)	20.13284(3)	20.13535(3)	20.11817(4)
b (Å)	19.96164(3)	19.96386(3)	19.96378(3)	19.96097(3)	19.96414(3)	19.97811(3)
c (Å)	13.43443(3)	13.43133(3)	13.42803(3)	13.42818(2)	13.43113(2)	13.43698(3)
V (Å^3)	5405.959(17)	5401.181(16)	5395.940(16)	5396.396(13)	5399.189(14)	5400.634(18)
2θ range for refinement (°)	3-55	3-55	3-55	3-55	3-55	3-55
Detector	MAC	MAC	MAC	MAC	MAC	MAC
Number of parameters	168	168	168	168	168	168
Number of *hkl*s	4190	4190	4190	4190	4190	4190
Refinement methods	Rietveld	Rietveld	Rietveld	Rietveld	Rietveld	Rietveld
$R_{wp}/R_{exp}/R_p$ (%)	6.855/2.436/5.366	6.538/2.441/5.124	6.515/2.434/5.085	5.976/2.354/4.634	5.903/2.341/4.601	6.285/2.328/4.796
χ^2	2.814	2.679	2.676	2.629	2.522	2.700

R_{wp}: weighted profile; R_{exp}: expected; R_p: profile; χ^2: goodness-of-fit.

6.2.2 *Operando* SXRD

Figure 6.3 shows the selected Rietveld refinement profile of the SXRD of the H-ZSM-5 with a flowing stream of methanol vapour measured at 25 °C and the corresponding derived crystal structure in an asymmetric unit (the atomic parameters of the *operando* SXRD are summarised in Tables A6.1-A6.6 in Appendix). In general, the SXRD data have been refined well with three methanol molecules (rigid bodies, at all temperatures) producing acceptable R_{wp} and excellent data fittings. In all the Rietveld derived structures, three MeOH species are observed in the H-ZSM-5 per asymmetric unit. We acknowledge the increase in thermal motion of the adsorbed species at higher temperatures. Therefore, the more rigid framework O atoms with less disorder are chosen as the crystallographic pointers in measuring their interatomic distances with the O atom of the most strongly bound methanol species. Clearly, the BAS in the sinusoidal-straight cross-channel region attracts the MeOH1 molecule, giving O18-O_{MeOH1} = 3.80(4) Å and O5-O_{MeOH1} = 3.85(4) Å as the closest distances. This implies that this species is directly protonated, forming a nearly bidentate mode with the two framework O atoms. Also, other adsorbed species can be identified and resolved by SXRD under reaction conditions. The slightly uneven negative charge distribution on O5 (smaller) and O18 (larger) adjacent to Al is due to the steric characteristics of H-ZSM-5 that slightly distorts the bidentate morphology.[24]

Comparing to our previous study in Chapter 3 under a static *ex situ* condition,[22] these O18-O_{MeOH1} and O5-O_{MeOH1} interatomic distances are slightly longer. This is presumably due to the dynamic measurement in excess flowing methanol in the present study. In addition, for MeOH2 and MeOH3, their derived O18-O_{MeOH} and O5-

O_{MeOH} are substantially longer than those of MeOH1. The interatomic distances between MeOH1 with MeOH2 and MeOH3 fall in the regime of H-bonding. Thus, a strongly bound protonated methanol (MeOH1) and two weakly bound methanol molecules (MeOH2 and MeOH3) inside the H-ZSM-5 cavity are clearly resolved by SXRD under the flowing methanol condition. There is a consistent and steady decrease in the SOF of MeOH1 from 150 °C. The fall in SOF matches with the increasing DME formation, which can clearly reflect the chemical reaction of MeOH1 (see Table 6.2).

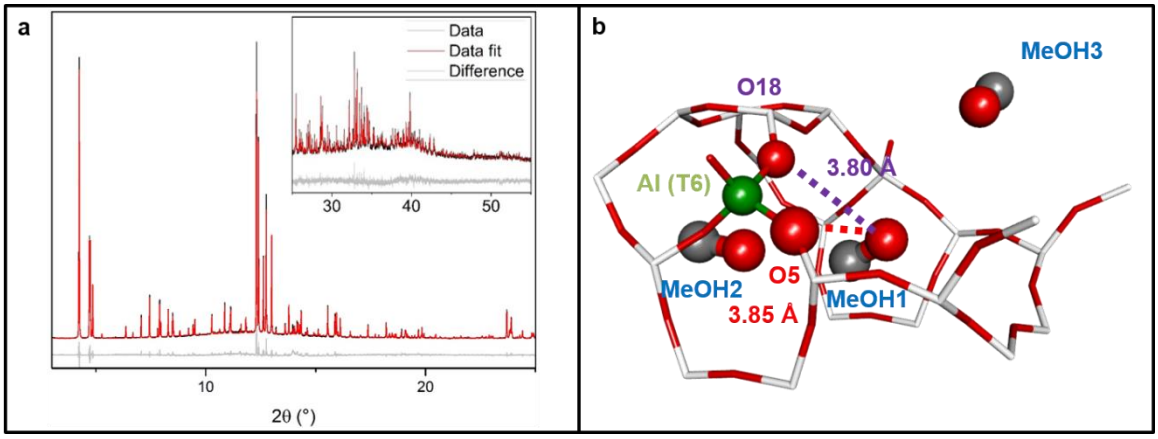

Figure 6.3. (**a**) Rietveld refinement profile of the H-ZSM-5 sample with flowing stream of methanol vapour measured at 25 °C (R_{wp} = 6.524%, χ^2 = 2.680), and (**b**) its corresponding Rietveld derived crystal structure showing an asymmetric unit. The atomic parameters of the complete *operando* SXRD measurements are summarised in Tables A6.1 – A6.6 in Appendix. Atoms are represented in ball/sticks: white = Si/Al, red = O, black = C. No hydrogens are plotted for clarity.

Table 6.2. Comparison of the interatomic distances between the protonated methanol located in sinusoidal-straight cross-channel region and the framework O18 and O5 atoms derived from Rietveld refinements and obtained from AIMD simulations. The numbers in the brackets are estimated standard deviations.

Temperature (°C)	**Interatomic distances from Rietveld refinements**		**Occupancy of MeOH1**	**Isotropic displacement factors of 'C' in MeOH1**	**Interatomic distances from AIMD simulations**	
	$O18\text{-}O_{MeOH1}$ (Å)	$O5\text{-}O_{MeOH1}$ (Å)	SOF of MeOH1	B_{eq} of C_{MeOH1} (Å^2)	$O18\text{-}O_{MeOH1}$ (Å)	$O5\text{-}O_{MeOH1}$ (Å)
25	3.80(4)	3.85(4)	0.763(5)	-	3.85	3.75
50	3.83(4)	3.98(4)	0.741(6)	-	3.95	3.95
100	3.82(5)	3.97(5)	0.648(6)	10.3(11)	3.95	4.05
150	3.63(6)	3.97(6)	0.598(7)	25.3(16)	3.45	3.55
200	3.47(7)	3.50(7)	0.582(8)	34.9(32)	3.45	3.55
250	3.49(7)	3.57(7)	0.519(8)	36.3(38)	3.35	3.55

Interestingly, starting from 150 °C where a significant quantity of DME is produced, O18-O_{MeOH1} and O5-O_{MeOH1} show a clear shortening beyond our experimental errors (see Table 6.2), whereas they remain relatively constant below 100 °C. This observation is in stark contrast to the expected extension of the interatomic distances arisen from thermal vibration at higher temperatures. Most importantly, this unique observation clearly depicts a strengthened adsorbate-framework interaction about the rigid zeolite framework. Obviously, it implies a lesser degree of $\sigma_{C\text{-}O}$ orbital overlap with the increasing covalency of the protonated terminal -O(H_2) moiety during activation at higher temperatures. Furthermore, the significant increase in B_{eq} of C_{MeOH1} atom (notably greater the extent of the reaction temperature effect) about the allegedly rigid C_{MeOH1}-O_{MeOH1} bond also suggests its activation upon increasing temperature. The C_{MeOH1}-O_{MeOH1} bond distance has however not been compared directly due to higher degree of thermal motions of the molecule and additional interactions during bombardment with other methanol molecules under a dynamic condition.

As a result, this activated protonated methanol as [‘CH_3’…OH_2]$^+$ can become more reactive and receptive to another incoming methanol to form DME in the concerted associative mechanism. The associative mechanism has a lower overall apparent Gibbs free energy of activation than that of the dissociative mechanism (115 kJ mol^{-1} vs. 169 kJ mol^{-1}). Eventually, via a simple proton transfer, the formed DME and H_2O will first desorb; then a BAS will be regenerated on the negatively charged framework O atom.

It is worthy to note that at low temperatures, we failed to fit the SXRD data with any CH_3-O_z species (i.e., the intermediate species from the dissociative mechanism). Our Rietveld refinement attempts in placing a ‘C’ atom adjacent to O5 and O18 have

resulted in the SOF approaching zero. In addition, there was no noticeable carbon deposition observed.

Similar results were obtained in a separate methanol flowing experiment where the temperature was kept isothermally at 200 °C. A notable formation of DME was observed in the first hour. We detected the activation of $[\text{'CH}_3\text{'}...\text{OH}_2]^+$ intermediate species is associated with the DME formation under the *operando* condition during the early stage of the methanol conversion. Thus, our DFT prediction of the dominancy of the associative mechanism can be confirmed (which will be discussed in Chapter 6.2.4). It should be noted that such an activated intermediate species and its interactions with neighbouring MeOH molecules at the BAS on the zeolite internal surface resolved in the stereo-specific manner in a 3-D atomic arrangement cannot be easily obtained by other *in situ* spectroscopic techniques.

As the reaction proceeded at 200 °C, we observed a rapid catalyst deactivation as generally reported until <5% residue activity for the DME production after 10 h. The SXRD pattern after 24 h of reaction is displayed in Figure 6.4(a) and the Rietveld derived crystal structure is shown in Figure 6.4(b). The atomic parameters of the H-ZSM-5 with various hours of flowing methanol vapour are summarised in Tables A6.7-A6.9 in Appendix. Interestingly, we herein observe an isolated 'C', presumably the CH_3-O_z species at an interatomic distance of *ca*. 1.6 Å with O5 which is adjacent to the substituted Al site (while the fitting for protonated methanol was unacceptable). The population of CH_3-O_z increased progressively upon longer reaction time, with the SOF increased from 0.43(1) (10 h) < 0.46(1) (18 h) < 0.51(2) (24 h). This suggests the CH_3-O_z became relatively stable once they were formed at the later stage. The detection of CH_3-O_z indicates the dissociation mechanism at this temperature, which is also

suggested by previous DFT[16,25] and spectroscopic[6,18,19] reports. This may imply that some protonated ['CH_3'...OH_2]$^+$ intermediate species did not proceed to form DME via the associative mechanism. They instead underwent the dissociative dehydration route and formed CH_3-O_z on the zeolite framework. As a result, it is evident that two surface intermediates, namely the protonated activated methanol ['CH_3'...OH_2]$^+$ and CH_3-O_z co-exist at 200 °C, where the former dominantly covers the BAS sites. It is therefore envisaged that at higher temperatures, the dissociative mechanism with a higher apparent Gibbs free energy of activation becomes a competing or even dominant mechanism for the DME formation. However, at temperature ≤ 200 °C, the slow but gradual replacement of H^+ on the BAS by the kinetically sluggish CH_3-O_z from the dissociative mechanism will circumvent the associative mechanism and then accumulate. This consequently deactivates the zeolite catalyst, as presently observed.

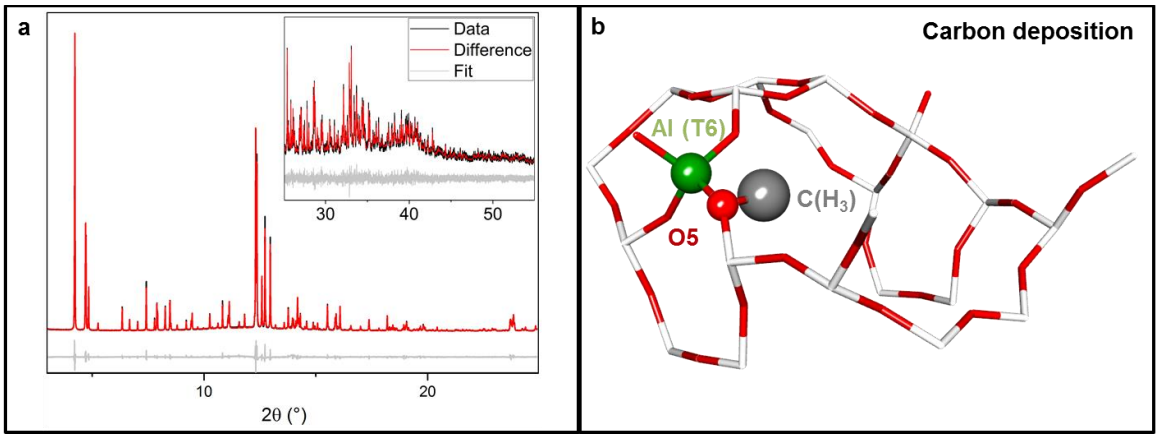

Figure 6.4. (**a**) Rietveld refinement profile of the H-ZSM-5 sample with 24 h of flowing methanol vapour at the reaction temperature of 200 °C (R_{wp} = 7.044%, χ^2 = 1.665), and (**b**) its corresponding Rietveld derived crystal structure showing one asymmetric unit. See Tables A6.7-A6.9 in Appendix for the detailed atomic parameters (10, 18 and 24 h). Atoms are represented in ball/sticks: white = Si/Al, red = O, black = C. No hydrogen or carbon species deep in the channels are plotted for clarity.

6.2.3 **Theoretical Calculations – Interatomic Distances**

Our theoretical calculations derived from *ab initio* molecular dynamics (AIMD) simulations of methanol in H-ZSM-5 at different temperatures indeed support the *operando* SXRD results (see the original crystal structure for theoretical calculations in Figure 6.5). The atomic interactions between the protonated methanol with the framework O atoms in terms of the O_{MeOH1}-O18/O5 interatomic distances at different temperatures are summarised in Table 6.2. The averaged O_{MeOH1}-O18/O5 interatomic distances derived from the radial distribution functions, g(r) between O_{MeOH1} with O18 and O5 (see Figure 6.6) are in excellent agreement with the derived Rietveld analogues. The O_{MeOH1}-O18/O5 interatomic distances display with the same increasing trend at low temperatures, then decrease at high temperatures (up to 250 °C).

A snapshot of three methanol molecules around the active T6 site in the AIMD simulation at 100 °C is displayed in Figure 6.7. We note a slight inconsistency between the experiment and simulation at 150 °C. It might be due to a minor experimental discrepancy over the true sample temperature during the reaction. Again, as previously discussed, this clearly indicates the non-cleaved but activated protonated methanol on the BAS.

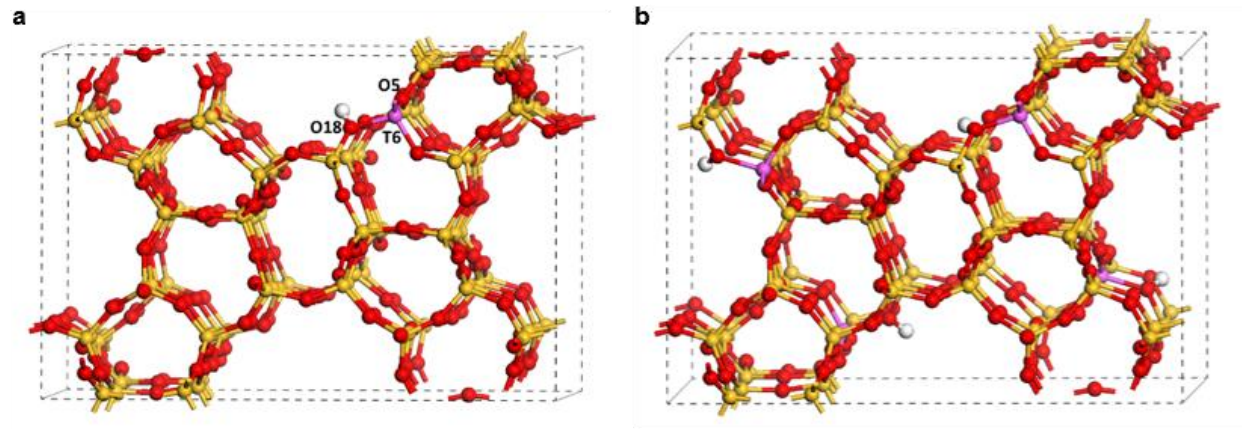

Figure 6.5. The H-ZSM-5 zeolite structure used in the *ab initio* calculations, with the Si/Al ratio of (**a**) 95 and (**b**) 23. Atoms are presented in ball: yellow = Si, magenta = Al, red = O, and white = H.

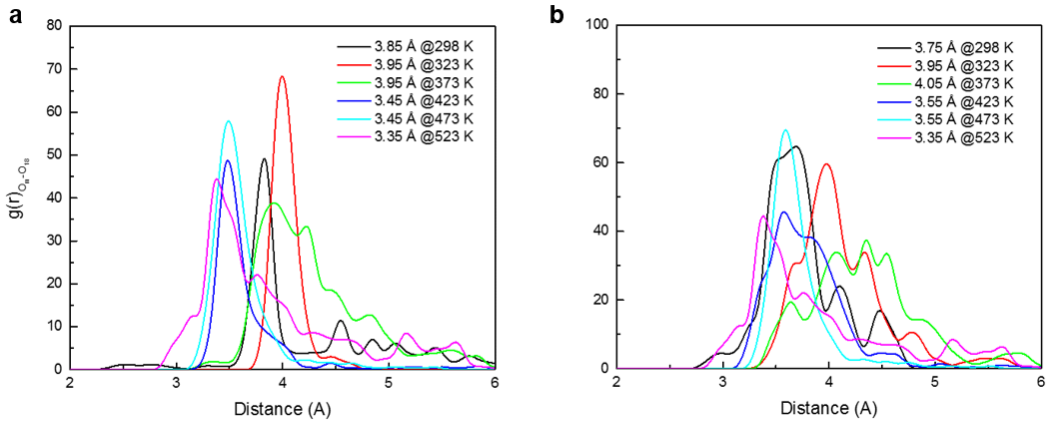

Figure 6.6. Radial distribution functions of the (**a**) O_{MeOH_1}-O18 and the (**b**) O_{MeOH_1}-O5 pairs averaged from 10 ps AIMD trajectories. O_{MeOH_1} is the O atom of the protonated methanol. O18 and O5 are the O atoms of two adjacent framework O atoms of the Al (T6) site.

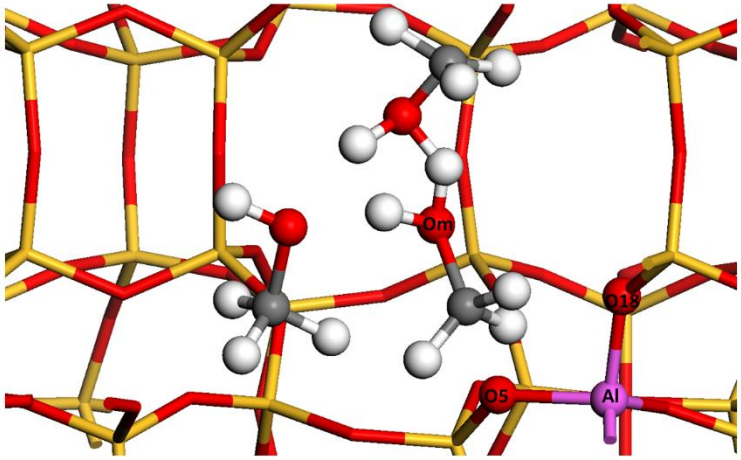

Figure 6.7. A snapshot of three methanol molecules around the Al T6 site in the AIMD simulation at 100 °C. The same colour scheme in Figure 6.5 is applied.

6.2.4 **Theoretical Calculations – Reaction Energy Profile**

The dominancy of the associative mechanism for the DME formation over H-ZSM-5 until 200 °C is further elucidated using DFT calculations. Figure 6.8 shows the Gibbs free energy profiles for methanol conversion to DME via both mechanisms. The corresponding configurational structures are given in Figure 6.9.

The calculated Gibbs free energies of the initiative steps of activation for the dissociative mechanism (TS1 (D-iv), 117 kJ mol^{-1}) and the associative mechanism (TS4 (A-iv), 115 kJ mol^{-1}) for the protonated methanol are comparable. However, the C-O bond scission and subsequent CH_3-O_z cleavage steps in the dissociative mechanism are highly endothermic (+95 and +68 kJ mol^{-1}, respectively), as compared to the mild endothermic concerted step in the associative mechanism of (+21 kJ mol^{-1}). The products formed from the associative mechanism (DME and H_3O^+) appear to be more favourable than the products from the dissociative mechanism (CH_3^+, H_2O and MeOH). In other words, despite both the mechanisms are energetically competitive, the associative mechanism for the DME formation is preferred by a lower apparent energy of activation elementary steps at low temperatures.[15,16,26,27] This supports the direct *operando* observation of the activated [‘CH_3’…OH_2]$^+$ intermediate species (in (A-iv) TS1 in Figure 6.8) for the DME formation at higher coverage without cleaving the C-O bond. In the early stage of the reaction, as reflected by its undetectable coverage at 200 °C, the formation of CH_3-O_z is insignificant. Whereas in the late stage of the reaction, a gradual increase in CH_3-O_z coverage is noted by our SXRD experiment (corresponding to (D-v) and/or activated TS2 (D-vi) in Figure 6.9). This can be attributed to a small quantity of [‘CH_3’…OH_2]$^+$ that have overcome the high-energy

barrier of the C-O cleavage under the reaction temperature. Once formed, the sluggish CH_3-O_z can poison the BAS to regenerate the required intermediates in the associative mechanism, which subsequently further accumulate.

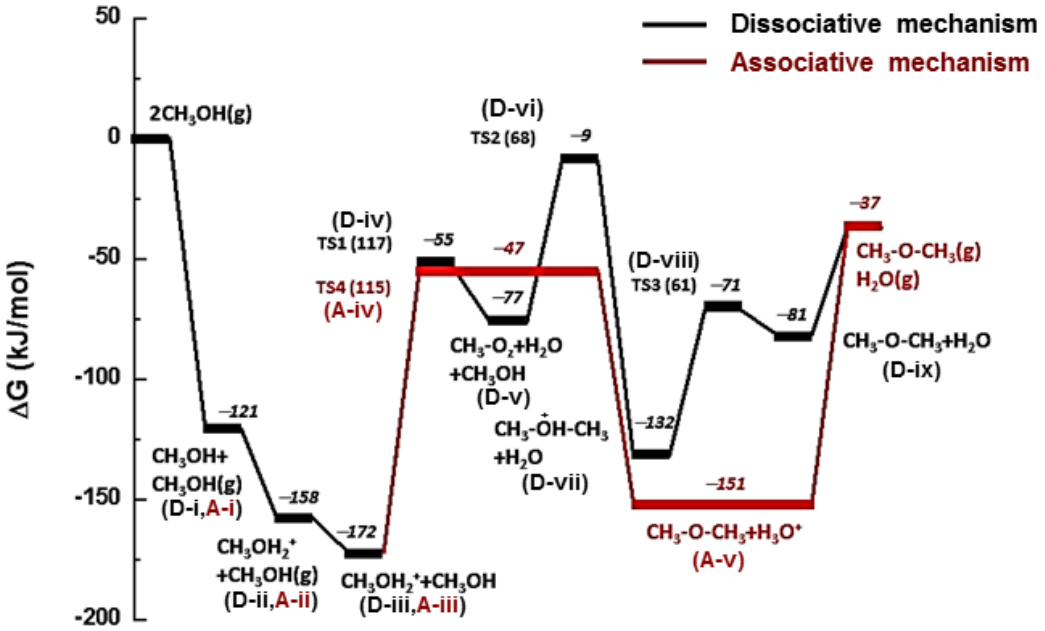

Figure 6.8. DFT calculated Gibbs free energy profile for methanol conversion to DME in the H-ZSM-5 zeolite at 200 °C.

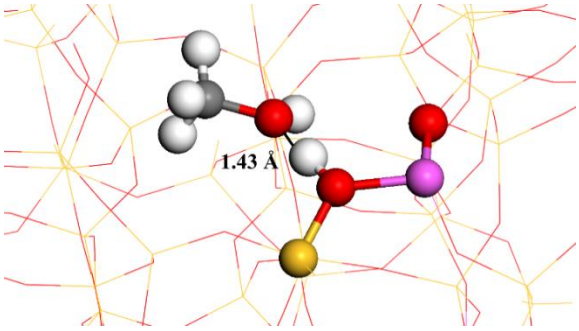

(D-i) $CH_3OH + CH_3OH(g)$

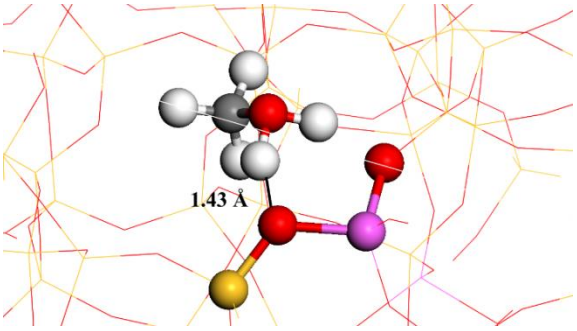

(D-ii) $CH_3OH_2^+ + CH_3OH(g)$

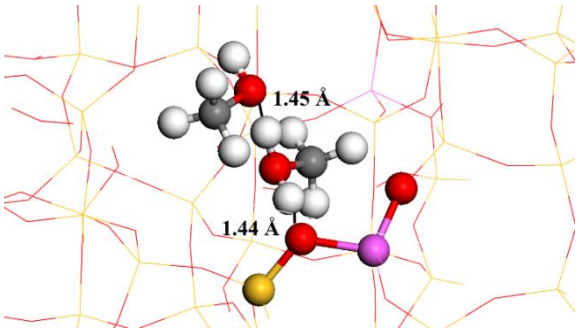

(D-iii) $CH_3OH_2^+ + CH_3OH$

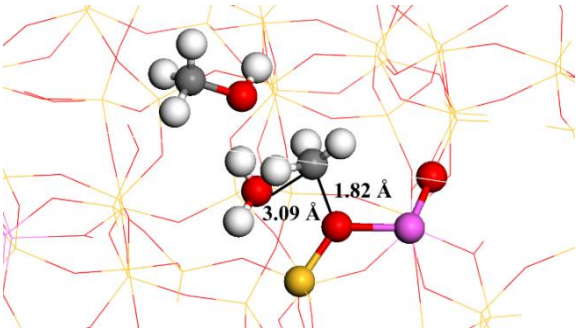

(D-iv) TS1

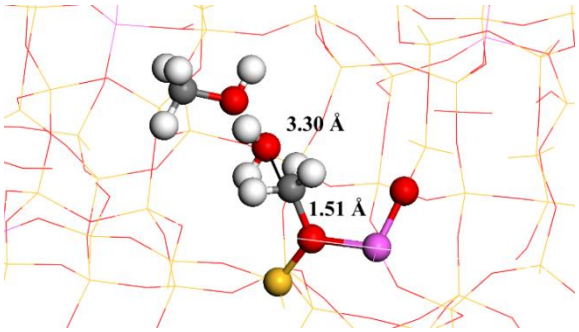

(D-v) $CH_3O_z + H_2O + CH_3OH$

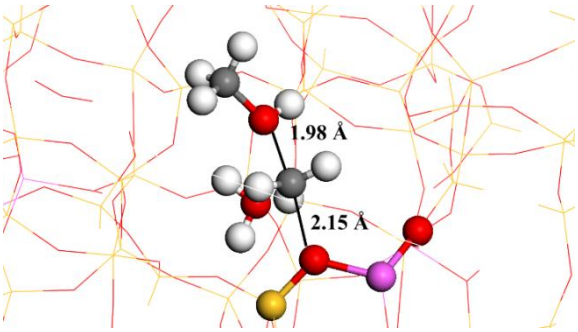

(D-vi) TS2

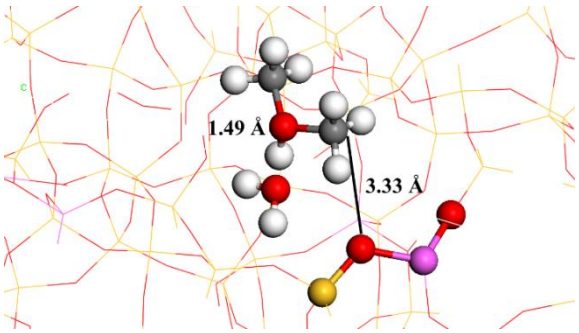

(D-vii) CH_3OH^+-$CH_3 + H_2O$

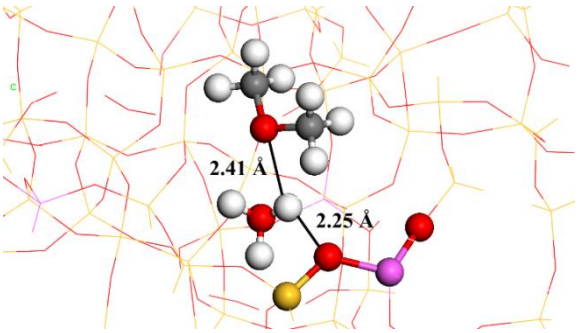

(D-viii) TS3

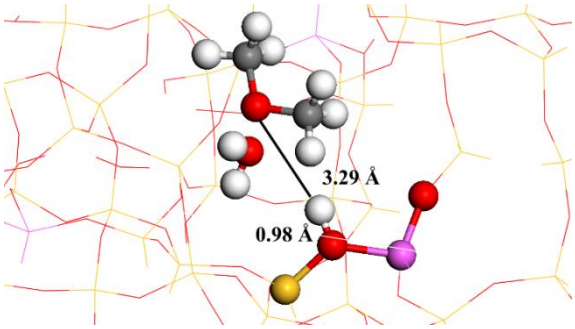

(D-ix) $CH_3OCH_3 + H_2O$

Figure 6.9(a). Configurational structures of all the reaction states and transition states in the **dissociative** mechanism (shown in Figure 6.8) for methanol dehydration to DME over H-ZSM-5 (Si/Al = 23). The C atom is in grey; the same colour scheme in Figure 6.5 is applied.

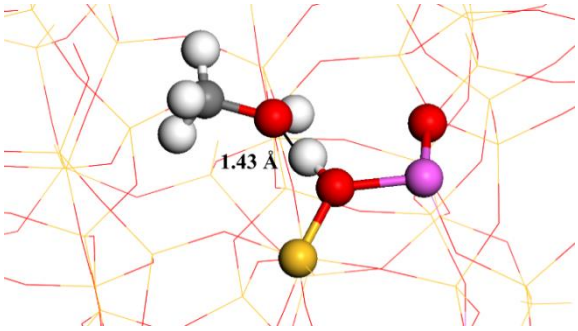

(A-i) CH_3OH + CH_3OH(g)

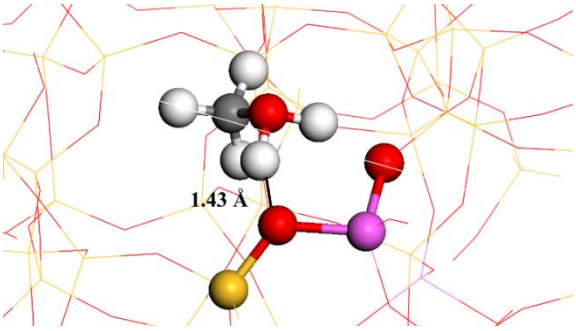

(A-ii) $CH_3OH_2^+$ + CH_3OH(g)

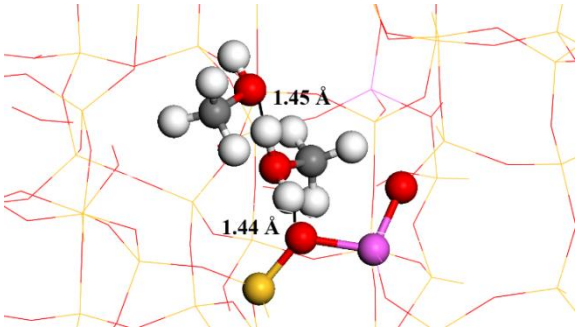

(A-iii) $CH_3OH_2^+$ + CH_3OH

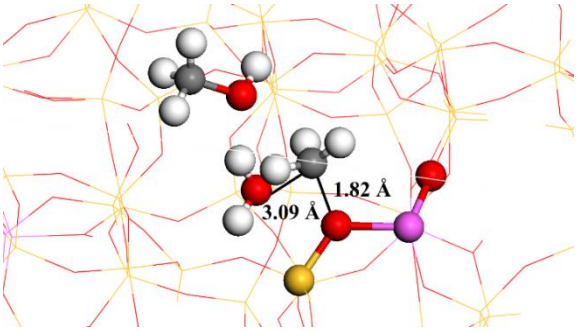

(A-iv) TS1

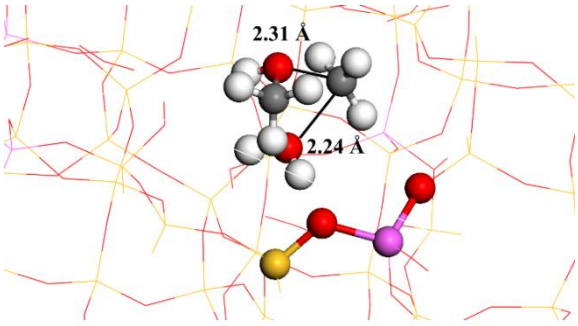

(A-v) TS4

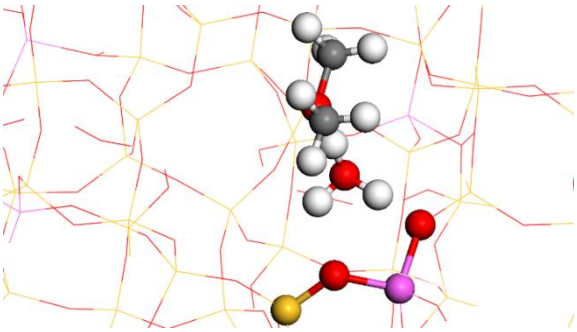

(A-vi) CH_3OCH_3 + H_3O^+

Figure 6.9(b). Configurational structures of all the reaction states and transition states in the **associative** mechanism (shown in Figure 6.8) for methanol dehydration to DME over H-ZSM-5 (Si/Al =23). The C atom is in grey; the same colour scheme in Figure 6.5 is applied.

6.2.5 Carbon Deposition Study

As the reaction proceeded (or when a higher temperature is applied), the sample became notably darker with the dominant surface coverage of the catalyst switching to methoxy. Thus, the build-up of the methoxy species produced by the dissociative mechanism could directly relate to 'HCP' which further leads to 'carbon' deposition or so-called 'heavy coking' in H-ZSM-5 in the late stage of the reaction. In fact, the industrial processes of MTA (H-ZSM-5 based catalysts[28]) and MTO (SAPO based catalysts[3,29]) in conjunction with a large quantity of 'carbon' deposition commonly take place at 400-500 °C. This reaction temperature is in the high-temperature regime to overcome the energy barriers of the cleavage of C_{MeOH1}-O_{MeOH1} and CH_3-O_z bonds (see Figure 6.8) in the dissociative route to produce surface methoxy from methanol. The formation of 'HCP' apparently depends on the stereo-specific pore geometry of zeolites and the reaction temperature required to overcome the energy barriers for a range of fundamental steps for the BAS catalysed reactions to take place, e.g., acetylation, decarboxylation, hydrocarbon radicals formation[30], Diels-Alder reaction[31], polymerisation[32], etc. The possible routes for the formation of C-C bond from the HCP mechanism, originally proposed by Dahl and Kolboe[11] which have been recently verified by Weckhuysen et al.[33], should be consulted.

Nevertheless, the dense electron clouds by 'carbon' deposition in the Fourier contrast map derived from SXRD (see Figure 6.10) can be clearly identified in the sinusoidal and straight (macro-pore) channels of the H-ZSM-5 sample after a flowing stream of methanol vapour treatment for 24 h even at as low as 200 °C. In fact, we observed a good correlation of the progressive build-up of the 'carbon' deposits (TGA analysis,

Table 6.3) with an increasing coverage of methoxy even at this low temperature. Some of these 'carbon' species can be dissolved in cyclohexane to give a yellowish solution. The ultraviolet-visible spectrum shows the presence of conjugated aromatic systems (see Figure 6.11). From the analysis of GC-MS (see Figure 6.12), although the product distribution is rather heterogeneous, most identified products are poly-aromatics, and approaching to a graphitic structure in nature. This implies the participation of the dissociative mechanism with the methoxy species or derivatives for polymerisation in H-ZSM-5. Notice that the H-ZSM-5 cavity is well known for the 'HCP' to undergo aromatisation.[28]

The incorporation of C-O moieties in these poly-aromatic fragments has been occasionally observed from the GC-MS. However, the low O/C ratios in both light products/heavy carbon deposits suggests that the build-up of 'carbon' from methoxy is more reasonable, rather than from oxygenated protonated methanol or DME. The relatively low reactivity of the methoxy on the BAS has raised doubts in the past about the direct route to the 'HCP' and eventually to 'carbon'. Lercher et al.[34] and Weckhuysen et al.[35] have independently suggested that carbonylation (with CO) of the CH_3-O_z on the BAS with a low energy barrier of 80 kJmol^{-1} initiates the first C-C build-up forming 'HCP' by using the ssNMR technique. Indeed, we observed the exit-gas contains CO which is likely obtained from the decomposition of methanol. Thus, the poly-aromatic 'carbon' build-up is likely related to the CH_3-O_z via alternative pathways, such as carbonylation with low activation barriers. However, the more favourable formations of 'HCP', aromatics, and pure graphitic carbon deposit from methanol in zeolites at higher temperature > 400 °C are particularly noted.[34]

Table 6.3. Carbon number estimation by TGA of the H-ZSM-5 samples under various hours of flowing methanol vapour at 200 °C.

Time of H-ZSM-5 under flowing methanol vapour (h)	10	18	24
Number of carbons per unit cell*	41.3(1)	45.6(1)	50.5(1)

*Assuming the entire weight loss as observed from TGA is from carbon.

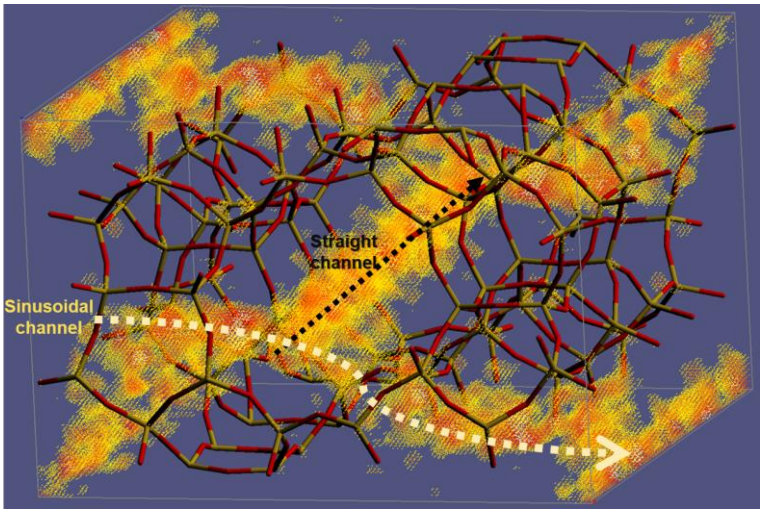

Figure 6.10. The Fourier contrast map of H-ZSM-5 with 24 h of flowing methanol vapour at 200 °C was generated using the TOPAS software by fixing the framework atoms, without the inclusion of any guest species. The density electron cloud indicates the location of the 'carbon' deposit in H-ZSM-5.

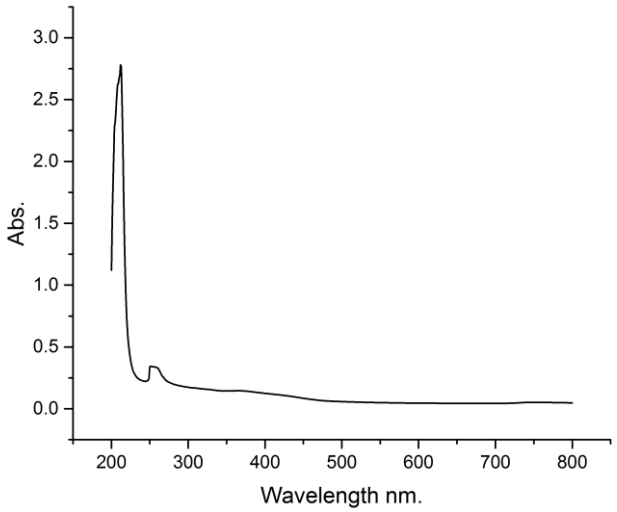

Figure 6.11. Ultraviolet-visible spectrum of the carbon deposit in cyclohexane from H-ZSM-5 with 24 h flowing methanol vapour at 200 °C.

a

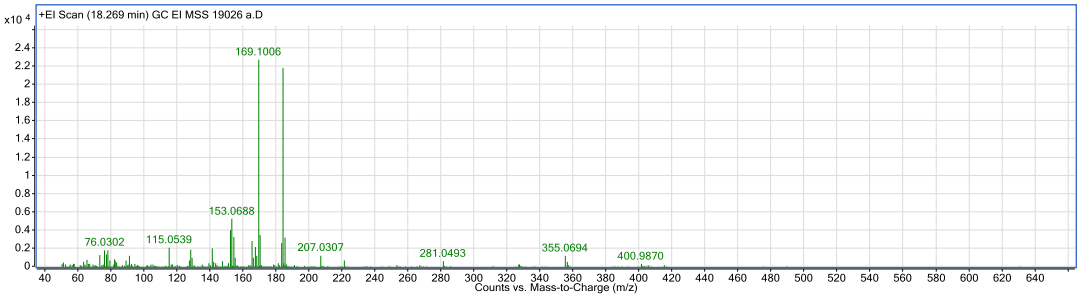

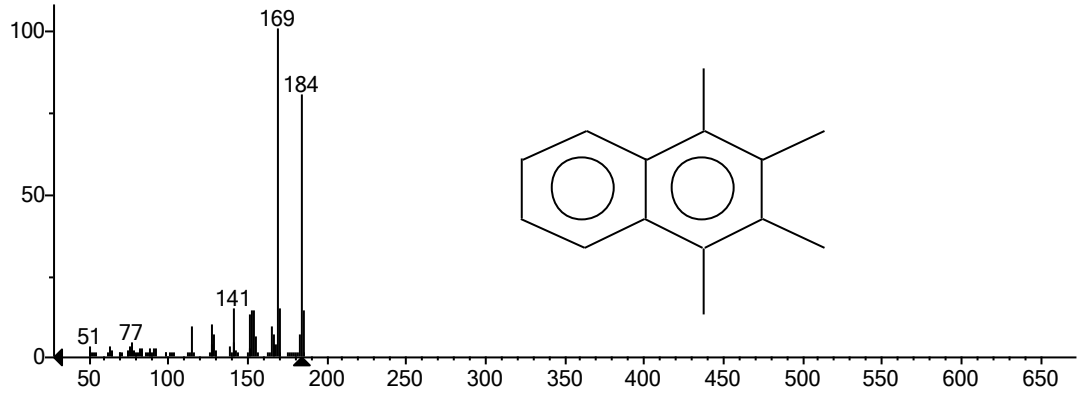

(mainlib) Naphthalene, 1,2,3,4-tetramethyl-

b

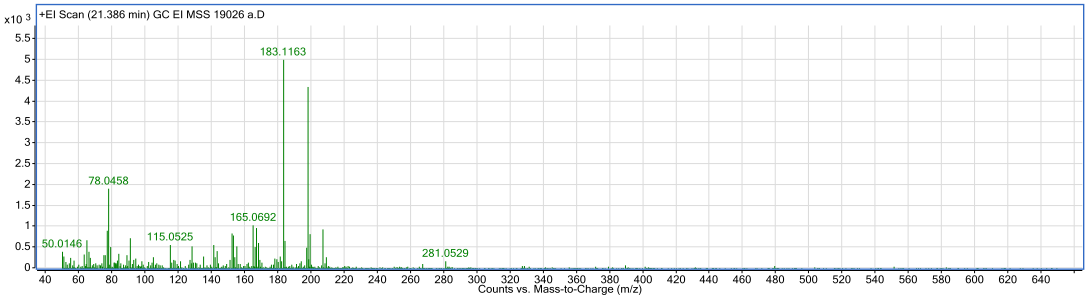

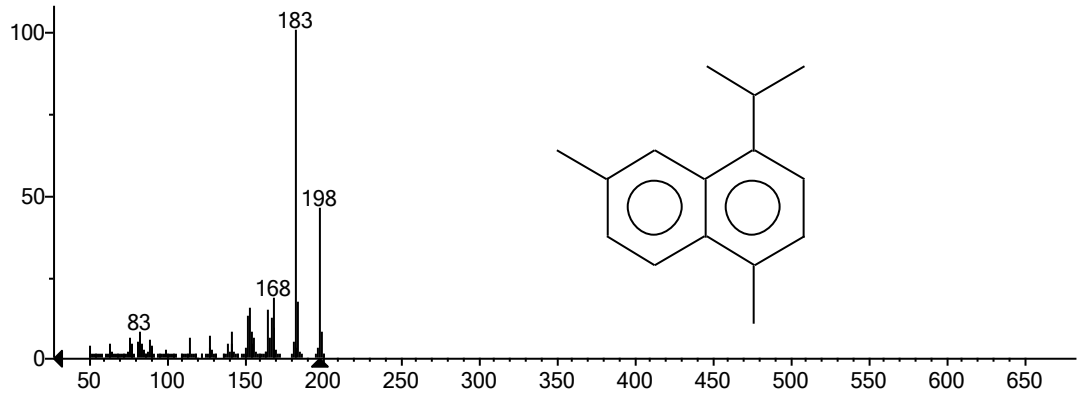

(mainlib) Naphthalene, 1,6-dimethyl-4-(1-methylethyl)-

c

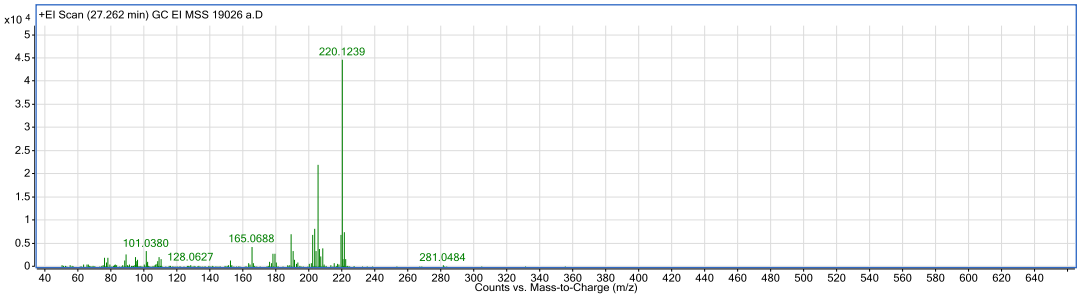

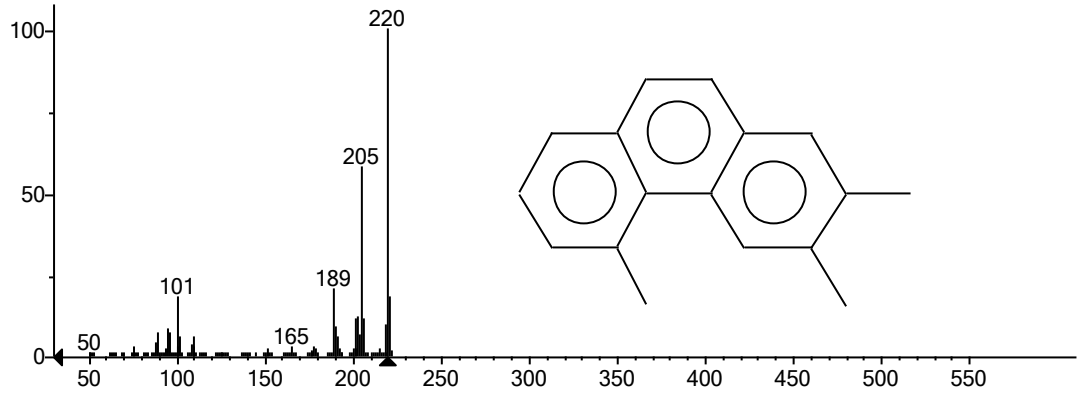

(mainlib) Phenanthrene, 2,3,5-trimethyl-

d

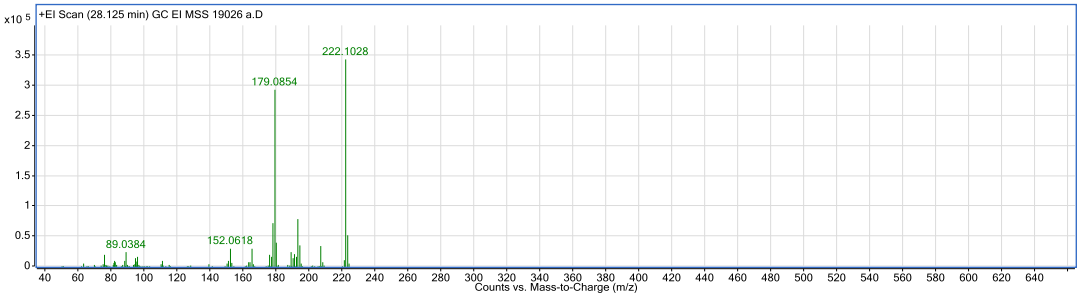

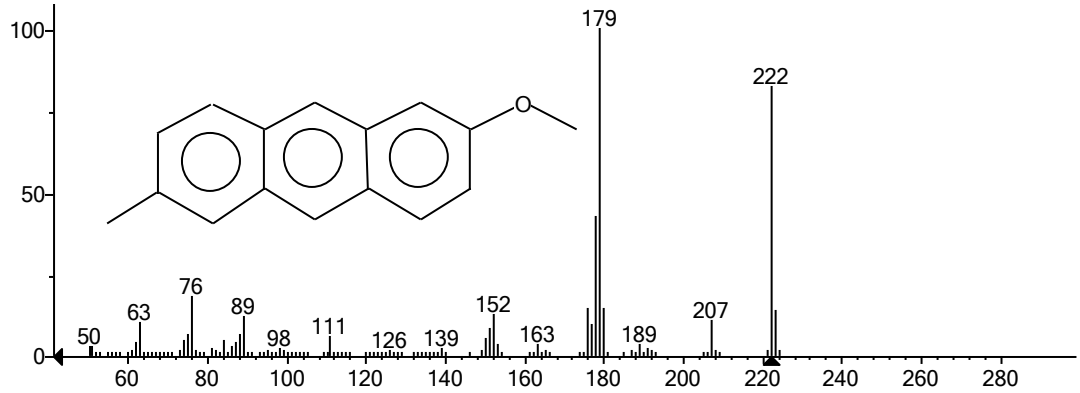

(mainlib) 2-Methoxy-6-methylanthracene

e

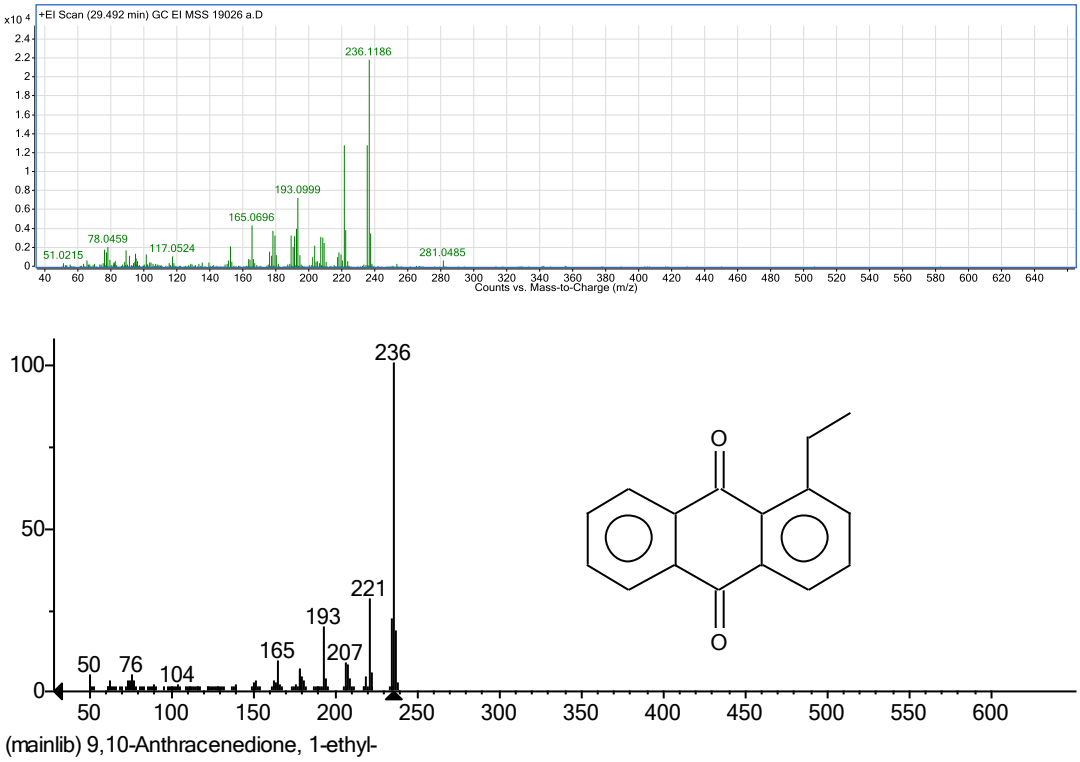

Figure 6.12. GC-MS analysis of some typical 'carbon' deposits from H-ZSM-5 with 24h of flowing methanol vapour at 200 °C. The peaks (**a**)-(**e**) identified by the NIST database and the corresponding MS spectra are presented.

6.3 Conclusion

In short summary, by monitoring the catalytic conversion of methanol using *operando* SXRD, in combination with AIMD simulations and DFT calculations, it is demonstrated with confidence that the concerted associative mechanism is responsible for the DME production over H-ZSM-5 in the early stage of the reaction below 200 °C. The minor contribution from the dissociative mechanism is due to the formation and slow activation of methoxy on the BAS, rendering their accumulation in the H-ZSM-5 during the late stage of the reaction. However, the adsorbed methoxy could also lead to a build-up of HCP and eventually to 'carbon', through the formation of C-C by alternative low energy pathways on the internal zeolite surface. The dissociative mechanism is anticipated to dominate for a greater amount of DME, hydrocarbon and 'carbon' pools formation in the high temperature range. This conclusion and the new toolsets, although presently demonstrated for methanol reactions over H-ZSM-5 under *operando* SXRD, would be expected to be transferable to monitor other catalytic reactions over zeolites, leading to further understanding of structure-activity relationships.

6.4 References

(1) Olah, G. A.; Goeppert, A.; Prakash, G. K. S. *Beyond Oil Gas Methanol Econ. Second Ed.* **2009**, 1–334.

(2) Stöcker, M. *Microporous Mesoporous Mater.* **1999**, *29* (1–2), 3–48.

(3) Tian, P.; Wei, Y.; Ye, M.; Liu, Z. *ACS Catal.* **2015**, *5* (3), 1922–1938.

(4) Bartholomew, C. H. *Appl. Catal. A Gen.* **2001**, *212* (1–2), 17–60.

(5) Xu, M.; Lunsford, J. H.; Goodman, D. W.; Bhattacharyya, A. *Appl. Catal. A Gen.* **1997**, *149* (2), 289–301.

(6) Cheung, P.; Bhan, A.; Sunley, G. J.; Law, D. J.; Iglesia, E. *J. Catal.* **2007**, *245*, 110–123.

(7) Spivey, J. J. *Chem. Eng. Commun.* **1991**, *110* (1), 123–142.

(8) Chang, C. D.; Hellring, S. D.; Pearson, J. A. *J. Catal.* **1989**, *115* (1), 282–285.

(9) Seiler, M.; Schenk, U.; Hunger, M. *Catal. Letters* **1999**, *62* (2), 139–145.

(10) Goguen, P. W.; Xu, T.; Barich, D. H.; Skloss, T. W.; Song, W.; Wang, Z.; Nicholas, J. B.; Haw, J. F. *J. Am. Chem. Soc.* **1998**, *120* (11), 2650–2651.

(11) Dahl, I. M.; Kolboe, S. *Catal. Letters* **1993**, *20* (3–4), 329–336.

(12) Ono, Y.; Mori, T. *J. Chem. Soc. Faraday Trans. 1* **1981**, *77* (9), 2209–2221.

(13) Van Speybroeck, V.; Hemelsoet, K.; De Wispelaere, K.; Qian, Q.; Van der Mynsbrugge, J.; De Sterck, B.; Weckhuysen, B. M.; Waroquier, M. *ChemCatChem* **2013**, *5* (1), 173–184.

(14) Van der Mynsbrugge, J.; Moors, S. L. C.; De Wispelaere, K.; Van Speybroeck, V. *ChemCatChem* **2014**, *6* (7), 1906–1918.

(15) Moses, P. G.; Nørskov, J. K. *ACS Catal.* **2013**, *3* (4), 735–745.

(16) Ghorbanpour, A.; Rimer, J. D.; Grabow, L. C. *ACS Catal.* **2016**, *6* (4), 2287–2298.

(17) Jiang, Y.; Hunger, M.; Wang, W. *J. Am. Chem. Soc.* **2006**, *128* (35), 11679–11692.

(18) Hunger, M.; Horvath, T. *J. Am. Chem. Soc.* **1996**, *118* (49), 12302–12308.

(19) Wang, W.; Buchholz, A.; Seiler, M.; Hunger, M. *J. Am. Chem. Soc.* **2003**, *125* (49), 15260–15267.

(20) Forester, T. R.; Howe, R. F. *J. Am. Chem. Soc.* **1987**, *109* (17), 5076–5082.

(21) Forester, T. R.; Wong, S.; Howe, R. F. *Chem. Commun.* **1986**, 1611–1613.

(22) Lo, B. T. W.; Ye, L.; Qu, J.; Sun, J.; Zheng, J.; Kong, D.; Murray, C. A.; Tang, C. C.; Tsang, S. C. E. *Angew. Chem. Int. Ed.* **2016**, *55* (20), 5981–5984.

(23) Ye, L.; Lo, B. T. W.; Qu, J.; Wilkinson, I.; Hughes, T.; Murray, C. a.; Tang, C. C.;

Tsang, S. C. E. *Chem. Commun.* **2016**, *52* (16), 3422–3425.

(24) Redondo, A.; Hay, P. J. *J. Phys. Chem.* **1993**, *97* (45), 11754–11761.

(25) Helveg, S.; Lauritsen, J.; Laegsgaard, E.; Stensgaard, I.; Norskov, J.; Clausen, B.; Topsoe, H.; Besenbacher, F. *Phys. Rev. Lett.* **2000**, *84* (5), 951–954.

(26) Jones, A. J.; Iglesia, E. *Angew. Chem. Int. Ed.* **2014**, *53* (45), 12177–12181.

(27) Blaszkowski, S. R.; van Santen, R. a. *J. Am. Chem. Soc.* **1996**, *118* (21), 5152–5153.

(28) Ono, Y.; Adachi, H.; Senoda, Y. *J. Chem. Soc. Faraday Trans. 1 Phys. Chem. Condens. Phases* **1988**, *84* (4), 1091–1099.

(29) Liang, J.; Li, H.; Zhao, S.; Guo, W.; Wang, R.; Ying, M. *Appl. Catal.* **1990**, *64*, 31–40.

(30) Kucherov, A. V; Slinkin, A. A.; Kondratyev, D. A.; Bondarenko, T. N.; Rubinstein, A. M.; Minachev, K. M. *J. Mol. Catal.* **1986**, *37* (1), 107–115.

(31) Teixeira, I. F.; Lo, B. T. W.; Kostetskyy, P.; Stamatakis, M.; Ye, L.; Tang, C. C.; Mpourmpakis, G.; Tsang, S. C. E. *Angew. Chem. Int. Ed.* **2016**, *55* (42), 13061–13066.

(32) Derouane, E. G. *Stud. Surf. Sci. Catal.* **1980**, *5*, 5–18.

(33) Schmidt, J. E.; Poplawsky, J. D.; Mazumder, B.; Attila, Ö.; Fu, D.; deWinter, D. A. M.; Meirer, F.; Bare, S. R.; Weckhuysen, B. M. *Angew. Chem. Int. Ed.* **2016**, 11173–11177.

(34) Liu, Y.; Müller, S.; Berger, D.; Jelic, J.; Reuter, K.; Tonigold, M.; Sanchez-Sanchez, M.; Lercher, J. A. *Angew. Chem. Int. Ed.* **2016**, *128* (19), 5817–5820.

(35) Chowdhury, A. D.; Houben, K.; Whiting, G. T.; Mokhtar, M.; Asiri, A. M.; Al-Thabaiti, S. A.; Basahel, S. N.; Baldus, M.; Weckhuysen, B. M. *Angew. Chem. Int. Ed.* **2016**, *55* (51), 15840–15845.

Chapter 7. Conclusions and Future Perspectives

7.1 Conclusions

In this thesis, we have developed a novel methodology to study the molecular chemistry in microporous materials by primarily using modern high-resolution synchrotron powder X-ray diffraction (SXRD) with Rietveld refinement. Using H-ZSM-5 zeolite as an illustration, we systematically studied the Brønsted acid sites (BAS) and its corresponding molecular chemistry.

First, in Chapter 3, we have studied the acid-base interactions between the BAS in H-ZSM-5 with functional molecules (namely pyridine, methanol, and ammonia). The locations of the BAS have been successfully identified, with the substituted Al at the T6 site in H-ZSM-5. We have also verified the relationship between the interatomic distances and the strengths of the acid-base interactions. When a strong base interacts with the BAS, it forms a weak conjugate acid-base pair, hence rendering a long interatomic distance, and *vice versa*.

Second, in Chapter 4, based on the atomic information determined from temperature programmed SXRD and thermogravimetric analysis (TGA), we extensively investigated the ammonia storage capability and sorption kinetics in the H-ZSM-5. The first ammonia molecule interacts with the BAS by forming the chemisorbed NH_4^+ species (O···$^+$HN). Due to the steric effect, there are only two other physisorbed ammonia molecules which can interact with the first chemisorbed NH_4^+ species through its unused H moieties to form a typical H-bonding (N–H···N) along the sinusoidal channel.

Third, in Chapter 5, we reported a novel catalytic conversion of biomass-derived furan and ethanol to aromatics over zeolites. By combining SXRD and theoretical calculations, we demonstrated that structural understanding can guide the rational design of new zeolite catalytic systems and the employment of co-substrates for improvement of other catalysis processes.

Finally, in Chapter 6, we studied the catalytic conversion of methanol using *operando* SXRD, in combination with theoretical calculations. *For the first time*, we demonstrated that the concerted associative mechanism is responsible for dimethyl ether production via an activated protonated methanol intermediate species over H-ZSM-5 in an early stage of the reaction at 200 °C. The minor contribution from the dissociative mechanism of the surface methoxy on the BAS, leads to their accumulation during the late stage of the reaction. This eventually leads to a build-up of the 'hydrocarbon pool' and eventually to 'carbon' through C-C bond formation.

To conclude, the catalysis chemistry in zeolites has been investigated at an atomistic level. Not only have the locations of the active sites been revealed, but the mechanistic aspects of two catalysis reactions have also been extensively studied and understood by making use of SXRD and Rietveld refinement. This thesis has demonstrated that, by using SXRD as the primary characterisation technique and supported with theoretical calculations, some long-standing challenges in zeolite catalysis could be resolved from the structural perspective.

7.2 Future Perspectives

There are two more future directions that can be immediately explored based on the findings from this thesis:

(i) Real-Time Carbon Deposition and Deactivation Study of Zeolite Catalysts

Zeolites have been commonly used as catalysts in the petrochemical industry, where the notable examples are H-ZSM-5 for MTA, SAPO-34 for MTO, and HY for FCC. According to previous studies on the deactivation of zeolite catalysts, the major factor is attributed to carbon deposition in their framework cavity. However, it is difficult to use conventional techniques to extensively study the real-time information of how and where the 'carbon' starts to accumulate.

Future work can be carried out with the real-time study of carbon deposition by SXRD in H-ZSM-5 and SAPO-34 zeolite catalysts, to show the carbon deposition under *in situ* catalytic reaction conditions. Eventually, it is anticipated the change in atomic parameters can be correlated with the catalytic performance, which can provide valuable information for the rational optimisation of zeolite catalysts.

(ii) *In situ* Study of Ethanol/DMF Diels-Alder Reaction

From the Diels-Alder reaction of DMF with ethanol in zeolite catalysts as discussed in Chapter 5, we reported that based on SXRD and PA studies, the preferential protonation of ethanol over DMF is a key step in facilitating the reaction. Future work can be focused on the molecular movements of the DMF and ethanol at different temperatures, studied by *in situ* SXRD experiments. It is anticipated to observe consistent changes in interatomic distances between the reaction molecules at

elevated temperatures, which is expected to provide information critical to investigate the reaction mechanism (in combination with theoretical calculations) of this facilitated Diels-Alder reaction.

Appendix

Supplementary Information for Chapter 3

Table A3.1. Atomic parameters of H-ZSM-5 pre-adsorbed with pyridine measured at 25 °C (R_{wp} = 8.461%, R_{exp} = 6.377%, χ^2 = 1.755).

Species	Atom	*x*	*y*	*z*	SOF	B_{eq} (Å²)	Wychoff
Zeolite framework	O1	0.37066(57)	0.04742(81)	0.77161(78)	1	0.983(12)	8d
	O2	0.30798(67)	0.06124(64)	0.92237(71)	1	0.983(12)	8d
	O3	0.20398(51)	0.05798(66)	0.02338(62)	1	0.983(12)	8d
	O4	0.08950(52)	0.06148(70)	0.92342(79)	1	0.983(12)	8d
	O5	0.11586(62)	0.04562(77)	0.73897(78)	1	0.983(12)	8d
	O6	0.24342(54)	0.05523(90)	0.74881(74)	1	0.983(12)	8d
	O7	0.38410(62)	0.84504(64)	0.76244(89)	1	0.983(12)	8d
	O8	0.30159(71)	0.84258(50)	0.93626(77)	1	0.983(12)	8d
	O9	0.18394(55)	0.84304(48)	0.02067(73)	1	0.983(12)	8d
	O10	0.09090(60)	0.84994(60)	0.91463(90)	1	0.983(12)	8d
	O11	0.12489(62)	0.84355(64)	0.73476(83)	1	0.983(12)	8d
	O12	0.25695(55)	0.84187(60)	0.77994(88)	1	0.983(12)	8d
	O13	0.30270(62)	0.94517(58)	0.82577(60)	1	0.983(12)	8d
	O14	0.07568(50)	0.95810(60)	0.81414(76)	1	0.983(12)	8d
	O15	0.41667(62)	0.13239(59)	0.60535(86)	1	0.983(12)	8d
	O16	0.40296(69)	1.00533(60)	0.59453(90)	1	0.983(12)	8d
	O17	0.39993(66)	0.87963(58)	0.57066(97)	1	0.983(12)	8d
	O18	0.19330(82)	0.12179(58)	0.63042(76)	1	0.983(12)	8d
	O19	0.19718(80)	-0.00118(56)	0.60537(78)	1	0.983(12)	8d
	O20	0.20147(74)	0.86595(55)	0.59518(76)	1	0.983(12)	8d
	O21	0.99674(59)	0.05076(85)	0.79401(77)	1	0.983(12)	8d
	O22	1.00678(65)	0.84299(68)	0.78508(81)	1	0.983(12)	8d
	O23	0.42392(92)	0.75	0.6475(12)	1	0.983(12)	4c
	O24	0.1860(10)	0.75	0.6594(11)	1	0.983(12)	4c
	O25	0.28567(86)	0.75	0.0623(11)	1	0.983(12)	4c
	O26	0.10925(93)	0.75	0.0581(13)	1	0.983(12)	4c
	Si1	0.42505(31)	0.05901(36)	0.66662(44)	1	0.983(12)	8d
	Si2	0.27977(26)	0.05986(35)	1.03477(43)	1	0.983(12)	8d
	Si3	0.30764(38)	0.03246(26)	-0.18020(44)	1	0.983(12)	8d
	Si4	0.12134(27)	0.06479(34)	0.03317(44)	1	0.983(12)	8d
	Si5	0.06914(31)	0.03206(31)	0.81952(48)	1	0.4915(61)	8d

	Si6	0.18739(33)	0.05490(33)	0.68073(41)	1	0.4915(61)	8d
	Si7	0.42683(34)	0.83338(30)	0.67502(50)	1	0.4915(61)	8d
	Si8	0.30879(36)	0.87005(29)	0.82429(40)	1	0.4915(61)	8d
	Si9	0.27475(30)	0.82875(30)	0.04209(44)	1	0.4915(61)	8d
	Si10	0.11670(32)	0.82650(30)	0.03045(50)	1	0.4915(61)	8d
	Si11	0.07330(34)	0.87114(35)	0.81614(49)	1	0.4915(61)	8d
	Si12	0.18913(40)	0.82357(25)	0.68813(45)	1	0.4915(61)	8d
Pyridine 1	H1	1.11245	1.67447	0.52609	0.5050(31)	22.3(16)	8d
	C2	1.06633	1.68274	0.48395	0.5050(31)	16.4(12)	8d
	C3	1.06085	1.73795	0.41998	0.5050(31)	18.8(13)	8d
	C4	1.01311	1.63807	0.49431	0.5050(31)	14.1(10)	8d
	H5	1.10267	1.77305	0.41184	0.5050(31)	24.6(18)	8d
	H6	1.01742	1.59470	0.54458	0.5050(31)	19.9(14)	8d
	N8	0.94895	1.70381	0.37671	0.5050(31)	14.1(10)	8d
	C9	1.00216	1.74848	0.36636	0.5050(31)	16.4(12)	8d
	C10	0.95442	1.64861	0.44069	0.5050(31)	14.1(10)	8d
	H11	0.99786	1.79186	0.31609	0.5050(31)	22.3(16)	8d
	H12	0.90283	1.71209	0.33458	0.5050(31)	19.9(14)	8d
Pyridine 2	H1	-0.2282	0.72262	0.02215	0.2387(26)	4.5(15)	8d
	C2	-0.1897	0.73190	0.07854	0.2387(26)	3.4(12)	8d
	C3	-0.2077	0.75296	0.17426	0.2387(26)	3.0(10)	8d
	C4	-0.1227	0.72267	0.05461	0.2387(26)	3.0(10)	8d
	H5	-0.2604	0.76021	0.19306	0.2387(26)	4.0(14)	8d
	H6	-0.1085	0.70613	0.97941	0.2387(26)	4.0(14)	8d
	N8	-0.0916	0.75555	0.22211	0.2387(26)	2.13(72)	8d
	C9	-0.1587	0.76478	0.24604	0.2387(26)	2.56(87)	8d
	C10	-0.0736	0.73449	0.12639	0.2387(26)	2.56(87)	8d
	H11	-0.1728	0.78132	0.32124	0.2387(26)	3.6(12)	8d
	H12	-0.0210	0.72724	0.10759	0.2387(26)	3.6(12)	8d

*All the adsorbed molecules are described in rigid-body matrices, with the B_{eq} of H atoms set at 1.3 times their corresponding parent atoms.

Table A3.2. Atomic parameters of H-ZSM-5 pre-adsorbed with ammonia measured at 25 °C (R_{wp} = 7.542%, R_{exp} = 3.436%, χ^2= 2.195).

Species	Atom	*x*	*y*	*z*	SOF	B_{eq} (Å^2)	Wyckoff
Zeolite framework	O1	0.37647(44)	0.06083(55)	0.74179(54)	1	1.995(28)	8d
	O2	0.31090(43)	0.06302(44)	0.91920(54)	1	1.995(28)	8d
	O3	0.19373(43)	0.06432(35)	0.02025(42)	1	1.995(28)	8d
	O4	0.09384(35)	0.06111(48)	0.90745(62)	1	1.995(28)	8d
	O5	0.10722(39)	0.04788(54)	0.72441(55)	1	1.995(28)	8d
	O6	0.24360(38)	0.05838(67)	0.75576(50)	1	1.995(28)	8d
	O7	0.37188(45)	0.85025(46)	0.76114(58)	1	1.995(28)	8d
	O8	0.30807(52)	0.84147(37)	0.92935(56)	1	1.995(28)	8d
	O9	0.19679(50)	0.84436(30)	0.02905(49)	1	1.995(28)	8d
	O10	0.09307(44)	0.83956(42)	0.91662(68)	1	1.995(28)	8d
	O11	0.11916(44)	0.84025(45)	0.73614(64)	1	1.995(28)	8d
	O12	0.23590(42)	0.84119(50)	0.75237(61)	1	1.995(28)	8d
	O13	0.31791(35)	0.94636(45)	0.81383(43)	1	1.995(28)	8d
	O14	0.07933(33)	0.95274(50)	0.82350(54)	1	1.995(28)	8d
	O15	0.42212(50)	0.12641(44)	0.60876(67)	1	1.995(28)	8d
	O16	0.41794(51)	1.00549(46)	0.58264(66)	1	1.995(28)	8d
	O17	0.40392(48)	0.86750(45)	0.56592(65)	1	1.995(28)	8d
	O18	0.19089(56)	0.13303(41)	0.60766(56)	1	1.995(28)	8d
	O19	0.19760(61)	0.00031(39)	0.59222(57)	1	1.995(28)	8d
	O20	0.20347(50)	0.86424(42)	0.58718(55)	1	1.995(28)	8d
	O21	0.99653(42)	0.04900(61)	0.79295(56)	1	1.995(28)	8d
	O22	0.99890(46)	0.85617(50)	0.78975(60)	1	1.995(28)	8d
	O23	0.41854(63)	0.75	0.63086(81)	1	1.995(28)	4c
	O24	0.18773(71)	0.75	0.65685(73)	1	1.995(28)	4c
	O25	0.28536(60)	0.75	0.04507(77)	1	1.995(28)	4c
	O26	0.10781(65)	0.75	0.06690(85)	1	1.995(28)	4c
	Si1	0.42482(22)	0.05598(28)	0.66118(30)	1	0.998(14)	8d
	Si2	0.31166(25)	0.03043(18)	0.80709(30)	1	0.998(14)	8d
	Si3	0.27864(19)	0.06270(24)	0.03103(30)	1	0.998(14)	8d
	Si4	0.11702(21)	0.06203(25)	0.02491(32)	1	0.998(14)	8d
	Si5	0.06998(22)	0.03071(21)	0.81261(33)	1	0.998(14)	8d
	Si6	0.18292(20)	0.05889(24)	0.67002(29)	1	0.998(14)	8d
	Si7	0.42261(22)	0.83020(20)	0.67000(36)	1	0.998(14)	8d
	Si8	0.30597(25)	0.86770(21)	0.81222(29)	1	0.998(14)	8d

	Si9	0.27441(22)	0.82555(21)	0.02851(33)	1	0.998(14)	8d
	Si10	0.12253(23)	0.82572(20)	0.02634(35)	1	0.998(14)	8d
	Si11	0.07229(21)	0.87098(23)	0.81901(34)	1	0.998(14)	8d
	Si12	0.18495(24)	0.82579(18)	0.67795(33)	1	0.998(14)	8d
Ammonia 1	N1	0.97164	0.16481	0.54693	0.741(17)	20.0(15)	8d
	H12	1.00238	0.13244	0.58029	0.741(17)	24.0(18)	8d
	H13	0.94991	0.19209	0.60025	0.741(17)	24.0(18)	8d
	H14	0.99904	0.19351	0.50173	0.741(17)	24.0(18)	8d
Ammonia 2	N2	0.48679	0.45790	0.04306	0.570(15)	16.4(16)	8d
	H22	0.51556	0.49103	0.00747	0.570(15)	19.7(19)	8d
	H23	0.51173	0.41458	0.04621	0.570(15)	19.7(19)	8d
	H24	0.47793	0.47610	0.11116	0.570(15)	19.7(19)	8d
Ammonia 3	N2	0.90538	0.71968	0.25856	0.736(11)	20.0(16)	8d
	H22	0.90480	0.66988	0.26709	0.736(11)	24.0(19)	8d
	H23	0.92266	0.72935	0.19023	0.736(11)	24.0(19)	8d
	H24	0.85871	0.73605	0.26677	0.736(11)	24.0(19)	8d
Ammonia 4*	N3	0.75529	0.24006	-0.3810	0.7043(88)	20.0(15)	8d
	H32	0.71376	0.26074	-0.4081	0.7043(88)	24.0(18)	8d
	H33	0.79358	0.25895	-0.4193	0.7043(88)	24.0(18)	8d
	H34	0.75811	0.25212	-0.3089	0.7043(88)	24.0(18)	8d

**Ammonia 4 is located deep inside the straight channel with the weakest interaction with the zeolite framework hence it will be gradually desorbed even at room temperature.

Table A3.3. Atomic parameters of H-ZSM-5 pre-adsorbed with methanol at 25 °C (R_{wp} = 9.005%, R_{exp} = 5.259%, χ^2 = 1.712).

Species	Atom	*x*	*y*	*z*	SOF	B_{eq} (Å^2)	Wychoff
Zeolite framework	O1	0.37499(74)	0.06098(85)	0.75091(95)	1	2.682(34)	8d
	O2	0.31175(72)	0.05779(81)	0.92230(85)	1	2.682(34)	8d
	O3	0.19495(68)	0.06052(63)	0.02140(65)	1	2.682(34)	8d
	O4	0.09911(55)	0.05895(83)	0.91567(94)	1	2.682(34)	8d
	O5	0.11395(73)	0.04951(97)	0.72526(90)	1	2.682(34)	8d
	O6	0.24836(68)	0.0486(11)	0.75288(93)	1	2.682(34)	8d
	O7	0.37288(80)	0.84764(76)	0.7635(11)	1	2.682(34)	8d
	O8	0.30776(83)	0.84938(57)	0.93328(88)	1	2.682(34)	8d
	O9	0.19045(72)	0.84994(46)	0.03369(72)	1	2.682(34)	8d
	O10	0.08631(66)	0.83790(67)	0.9261(11)	1	2.682(34)	8d
	O11	0.11748(78)	0.84021(74)	0.7437(10)	1	2.682(34)	8d
	O12	0.24303(75)	0.84756(87)	0.7620(12)	1	2.682(34)	8d
	O13	0.31642(59)	0.95098(73)	0.81327(67)	1	2.682(34)	8d
	O14	0.07860(53)	0.95362(79)	0.82623(85)	1	2.682(34)	8d
	O15	0.41698(75)	0.12660(70)	0.6080(10)	1	2.682(34)	8d
	O16	0.40988(72)	1.00959(71)	0.5806(11)	1	2.682(34)	8d
	O17	0.40266(82)	0.86938(72)	0.5756(12)	1	2.682(34)	8d
	O18	0.19285(96)	0.12699(69)	0.61269(89)	1	2.682(34)	8d
	O19	0.19975(90)	-0.00631(67)	0.60494(91)	1	2.682(34)	8d
	O20	0.19929(86)	0.87162(67)	0.57942(90)	1	2.682(34)	8d
	O21	0.99697(72)	0.05220(99)	0.79456(86)	1	2.682(34)	8d
	O22	0.99655(79)	0.85037(80)	0.79552(90)	1	2.682(34)	8d
	O23	0.4229(11)	0.75	0.6413(12)	1	2.682(34)	4c
	O24	0.1978(12)	0.75	0.6586(11)	1	2.682(34)	4c
	O25	0.28013(89)	0.75	0.0619(14)	1	2.682(34)	4c
	O26	0.1032(11)	0.75	0.0668(15)	1	2.682(34)	4c
	Si1	0.42204(34)	0.05887(46)	0.66574(51)	1	1.341(17)	8d
	Si2	0.27701(29)	0.05951(42)	1.03284(51)	1	1.341(17)	8d
	Si3	0.31047(45)	0.02887(29)	-0.18899(50)	1	1.341(17)	8d
	Si4	0.11764(32)	0.06373(39)	0.03324(50)	1	1.341(17)	8d
	Si5	0.06929(34)	0.03106(33)	0.81749(53)	1	1.341(17)	8d
	Si6	0.18786(38)	0.05780(37)	0.67765(45)	1	1.341(17)	8d
	Si7	0.42438(37)	0.83078(33)	0.67233(58)	1	1.341(17)	8d
	Si8	0.30684(44)	0.87006(33)	0.82037(47)	1	1.341(17)	8d

	Si9	0.27567(33)	0.82620(31)	0.03335(52)	1	1.341(17)	8d
	Si10	0.12203(35)	0.82521(33)	0.02718(53)	1	1.341(17)	8d
	Si11	0.07259(36)	0.87085(37)	0.81683(55)	1	1.341(17)	8d
	Si12	0.18792(45)	0.82521(28)	0.68244(52)	1	1.341(17)	8d
Methanol1	O1	0.89287	0.70863	0.26235	0.2518(84)	14.7(33)	8d
	H2	0.88144	0.75509	0.29482	0.2518(84)	17.7(40)	8d
	C3	0.94565	0.71959	0.19189	0.2518(84)	19.1(43)	8d
	H4	0.95801	0.76813	0.19157	0.2518(84)	22.1(50)	8d
	H5	0.98515	0.69217	0.21121	0.2518(84)	22.1(50)	8d
	H6	0.93048	0.70610	0.12388	0.2518(84)	22.1(50)	8d
Methanol2	C1	0.24201	0.68380	0.41136	0.2154(81)	7.3(22)	8d
	O2	0.23041	0.71352	0.34922	0.2154(81)	8.7(27)	8d
	C3	0.24979	0.61590	0.37698	0.2154(81)	9.4(29)	8d
	H4	0.24228	0.61411	0.30343	0.2154(81)	10.9(34)	8d
	H5	0.29572	0.59995	0.39238	0.2154(81)	10.9(34)	8d
	H6	0.21677	0.58641	0.41123	0.2154(81)	10.9(34)	8d

Supplementary information for Chapter 4

Table A4.1. Crystallographic parameters of H-ZSM-5 pre-adsorbed with ammonia at various desorption temperatures.

Temperature	100 °C	200 °C	300 °C	400 °C
Crystal system	Orthorhombic	Orthorhombic	Orthorhombic	Orthorhombic
Space group	*Pnma*	*Pnma*	*Pnma*	*Pnma*
NH_3 per unit cell	10.1	5.3	2.1	0
2θ range refinement (°)	3 - 55	3 - 55	3 - 55	3 - 55
Detector	Multi-analyser crystals			
Number of	149	149	143	135
Number of hkls	4174	4174	4172	4172
Refinement methods	Rietveld	Rietveld	Rietveld	Rietveld
a (Å)	20.11851(4)	20.12129(4)	20.11047(3)	20.11098(4)
b (Å)	19.94929(3)	19.95194(3)	19.94394(3)	19.94619(4)
c (Å)	13.43452(3)	13.43445(3)	13.42542(3)	13.42460(3)
V (Å^3)	5391.944(19)	5393.378(19)	5384.694(19)	5385.110(21)
R_{wp} / R_p / R_{exp} (%)	9.048/6.971/3.411	9.047/6.955/3.389	9.413/7.237/3.593	9.623/7.510/4.072
Wavelength (Å)	0.826617(4)	0.826617(4)	0.826209(3)	0.826209(3)
2θ-zero point (°)	0.000254(3)	0.000254(3)	-0.000489(2)	-0.000489(2)
χ^2	2.653	2.669	2.619	2.364

Desorption temperature = 100 °C

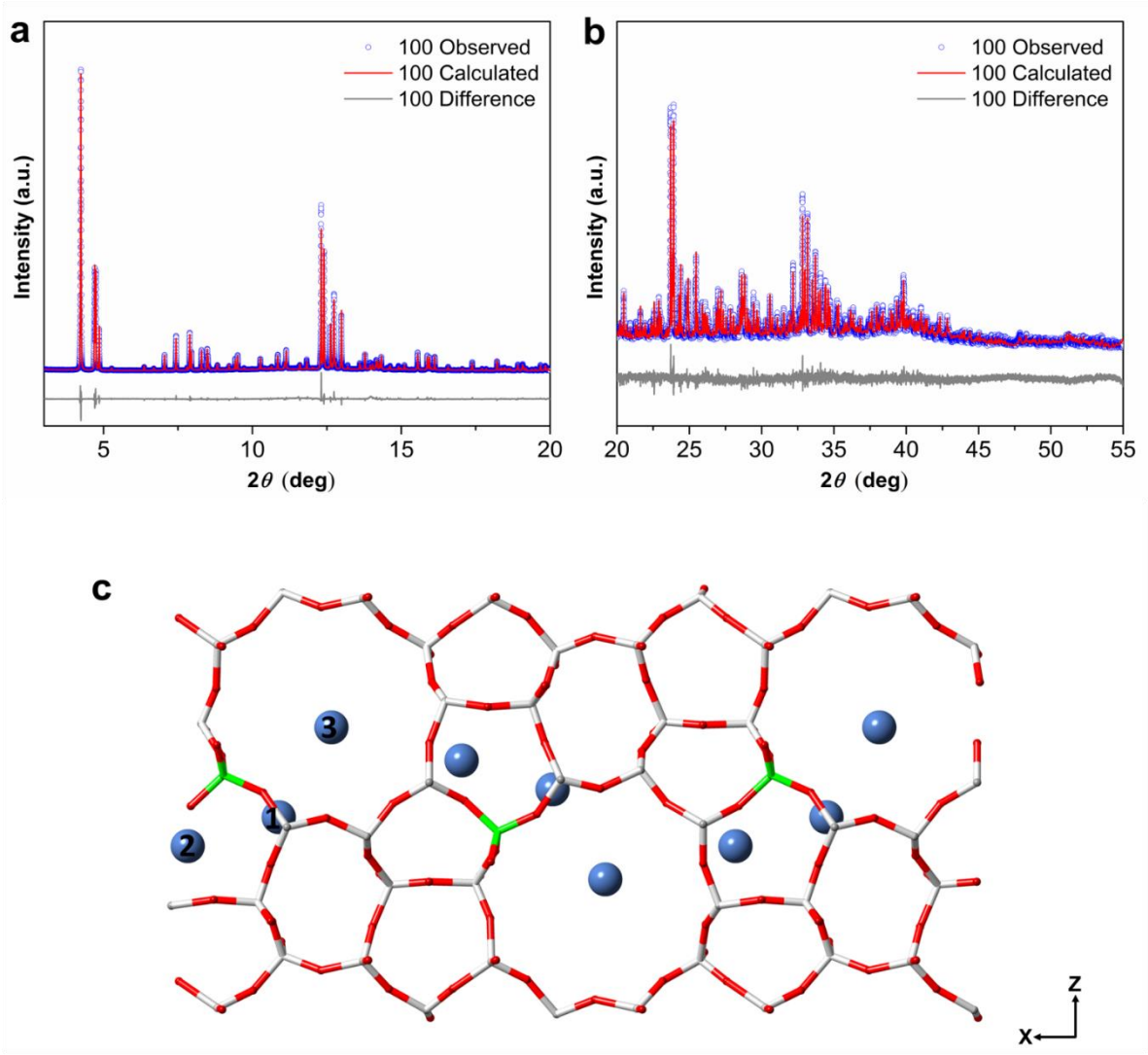

Figure A4.1. Rietveld refinement of the SXRD pattern and the corresponding crystal structure of H-ZSM-5 pre-adsorbed with ammonia, measured at 100 °C. Comparison of the SXRD (blue) and Rietveld refinement (red) profiles and the difference (grey), (**a**) 2θ range of 3-20° and (**b**) 2θ range of 20-55°; (**c**) the corresponding crystal structure (view from [010]). Atoms are represented in ball/sticks: green = Si/Al, red = O, blue = N, black = C. The symmetry for the ammonia molecules is disregarded and no hydrogens are plotted for clarity.

Table A4.2. Atomic parameters of H-ZSM-5 pre-adsorbed with ammonia, measured at 100 °C.

Species	Atom	*x*	*y*	*z*	SOF	B_{eq} (Å²)	Wyckoff
Zeolite framework	O1	0.37560(47)	0.06238(55)	0.74925(60)	1	2.549(35)	8d
	O2	0.30868(46)	0.05882(47)	0.91545(56)	1	2.549(35)	8d
	O3	0.20212(43)	0.05357(51)	0.01532(44)	1	2.549(35)	8d
	O4	0.09788(38)	0.06018(51)	0.91611(64)	1	2.549(35)	8d
	O5	0.11217(44)	0.05436(59)	0.72055(57)	1	2.549(35)	8d
	O6	0.24402(42)	0.05735(67)	0.75728(58)	1	2.549(35)	8d
	O7	0.36958(47)	0.84858(46)	0.76486(61)	1	2.549(35)	8d
	O8	0.30234(52)	0.84204(39)	0.93343(58)	1	2.549(35)	8d
	O9	0.19066(51)	0.84021(36)	0.03428(52)	1	2.549(35)	8d
	O10	0.08708(45)	0.84558(45)	0.90962(70)	1	2.549(35)	8d
	O11	0.11710(49)	0.84402(47)	0.73923(67)	1	2.549(35)	8d
	O12	0.23423(44)	0.84860(50)	0.73986(66)	1	2.549(35)	8d
	O13	0.31310(42)	0.94718(45)	0.81818(46)	1	2.549(35)	8d
	O14	0.07991(37)	0.96168(46)	0.81788(59)	1	2.549(35)	8d
	O15	0.42091(45)	0.12862(49)	0.60634(72)	1	2.549(35)	8d
	O16	0.40159(45)	0.99834(46)	0.57392(78)	1	2.549(35)	8d
	O17	0.40433(49)	0.86100(44)	0.57521(79)	1	2.549(35)	8d
	O18	0.18818(56)	0.12801(43)	0.61915(57)	1	2.549(35)	8d
	O19	0.19668(58)	0.00615(43)	0.58903(63)	1	2.549(35)	8d
	O20	0.19613(56)	0.87802(42)	0.58337(58)	1	2.549(35)	8d
	O21	0.99669(46)	0.04988(66)	0.79030(60)	1	2.549(35)	8d
	O22	0.99387(47)	0.85243(55)	0.79026(63)	1	2.549(35)	8d
	O23	0.42080(64)	0.7500	0.63040(92)	1	2.549(35)	4c
	O24	0.19305(79)	0.7500	0.65964(77)	1	2.549(35)	4c
	O25	0.28418(62)	0.7500	0.05096(87)	1	2.549(35)	4c
	O26	0.10062(67)	0.7500	0.05720(02)	1	2.549(35)	4c
	Si1	0.42288(25)	0.06151(28)	0.65849(36)	1	0.886(18)	8d
	Si2	0.30876(31)	0.02938(22)	0.80744(36)	1	0.886(18)	8d
	Si3	0.27953(22)	0.06112(27)	0.03164(35)	1	0.886(18)	8d
	Si4	0.12180(23)	0.06450(28)	0.02350(37)	1	0.886(18)	8d
	Si5	0.06876(24)	0.03148(24)	0.81544(38)	1	0.886(18)	8d

	Si6	0.18413(24)	0.05587(27)	0.67206(33)	1	0.886(18)	8d
	Si7	0.42375(26)	0.82995(25)	0.66933(40)	1	0.886(18)	8d
	Si8	0.30482(28)	0.86846(24)	0.81327(34)	1	0.886(18)	8d
	Si9	0.27512(25)	0.82829(23)	0.03073(38)	1	0.886(18)	8d
	Si10	0.11984(25)	0.82585(25)	0.02576(40)	1	0.886(18)	8d
	Si11	0.07077(25)	0.87360(27)	0.81519(40)	1	0.886(18)	8d
	Si12	0.18580(28)	0.82649(22)	0.68117(38)	1	0.886(18)	8d
Ammonia 1	N1	0.9160	0.7600	0.2120	0.87(1)	2.48(31)	4c
	H12	0.8800	0.7400	0.1700	0.87(1)	2.98(37)	4c
	H13	0.9100	0.7390	0.2780	0.87(1)	2.98(37)	4c
	H14	0.9600	0.7500	0.1800	0.87(1)	2.98(37)	4c
Ammonia 2	N2	0.7500	0.2430	0.6320	0.67(1)	3.23(40)	4c
	H22	0.7500	0.2800	0.6800	0.67(1)	3.87(48)	4c
	H23	0.7090	0.2500	0.5900	0.67(1)	3.87(48)	4c
	H24	0.7910	0.2500	0.5900	0.67(1)	3.87(48)	4c
Ammonia 3	N3	0.9870	0.3040	0.5410	0.80(1)	3.23(40)	4c
	H32	0.0280	0.3300	0.5500	0.80(1)	3.87(48)	4c
	H33	0.0000	0.2570	0.5300	0.80(1)	3.87(48)	4c
	H34	0.9600	0.3100	0.6000	0.80(1)	3.87(48)	4c

Desorption temperature = 200 °C

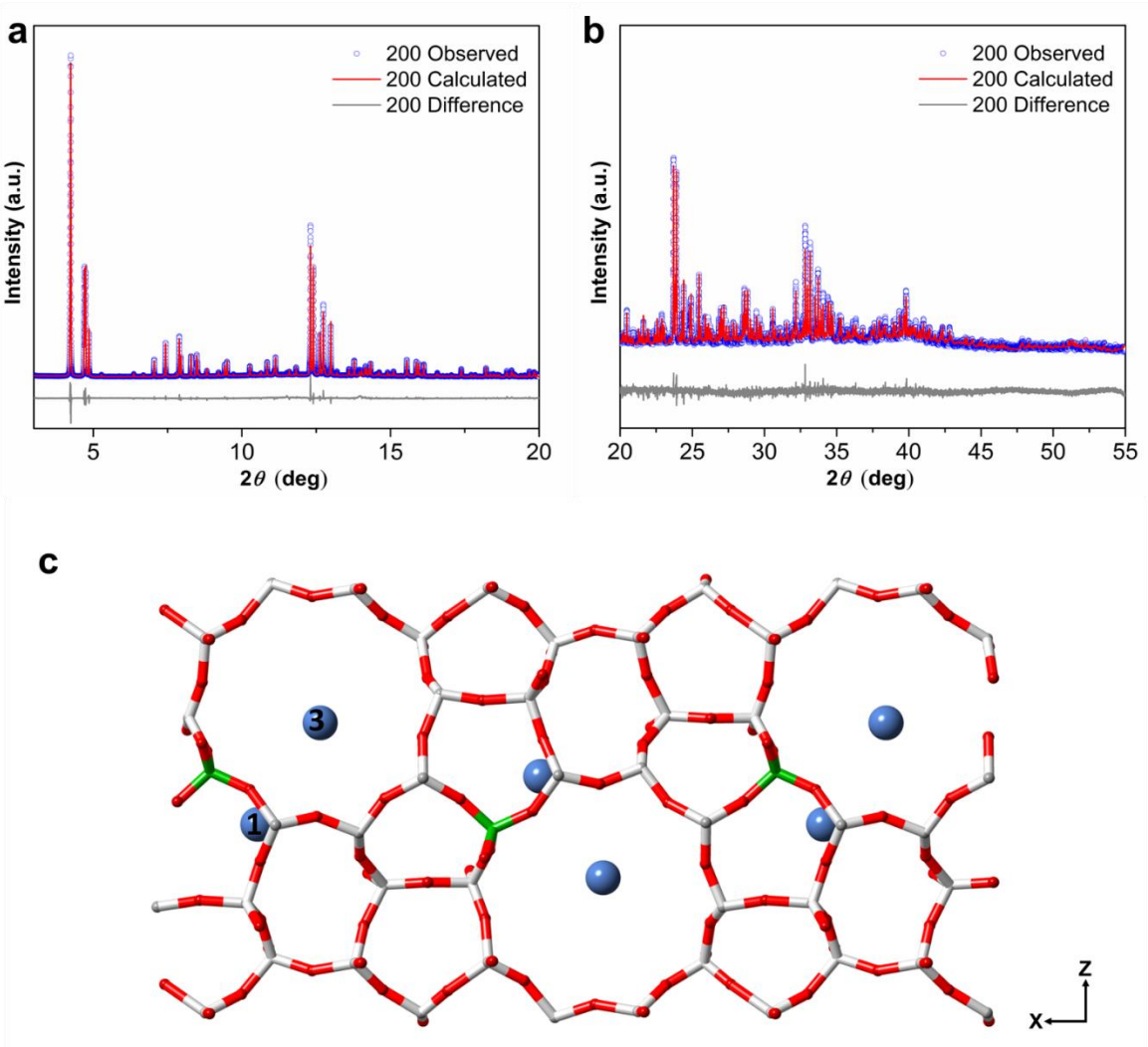

Figure A4.2. Rietveld refinement of the SXRD profile and the corresponding crystal structure of H-ZSM-5 pre-adsorbed with ammonia, measured at 200 °C. Comparison of the SXRD (blue) and Rietveld refinement (red) profiles and the difference (grey), (**a**) 2θ range of 3-20° and (**b**) 2θ range of 20-55°; (**c**) the corresponding crystal structure (view from [010]). Atoms are represented in ball/sticks: green = Si/Al, red = O, blue = N, black = C. The symmetry for the ammonia molecules is disregarded and no hydrogens are plotted for clarity.

Table A4.3. Atomic parameters of H-ZSM-5 pre-adsorbed with ammonia, measured at 200 °C.

Species	Atom	*x*	*y*	*z*	SOF	B_{eq} (Å^2)	Wyckoff
Zeolite framework	O1	0.37642(49)	0.05700(62)	0.75602(64)	1	2.909(35)	8d
	O2	0.31000(48)	0.06301(45)	0.91929(62)	1	2.909(35)	8d
	O3	0.20398(45)	0.06229(42)	0.01724(46)	1	2.909(35)	8d
	O4	0.09666(38)	0.06112(52)	0.91176(68)	1	2.909(35)	8d
	O5	0.11553(46)	0.04679(59)	0.72142(65)	1	2.909(35)	8d
	O6	0.24334(45)	0.05349(68)	0.75356(63)	1	2.909(35)	8d
	O7	0.36961(49)	0.84413(48)	0.76818(64)	1	2.909(35)	8d
	O8	0.30031(52)	0.84737(39)	0.93415(63)	1	2.909(35)	8d
	O9	0.19904(51)	0.84318(33)	0.03084(52)	1	2.909(35)	8d
	O10	0.08606(46)	0.84732(48)	0.91522(74)	1	2.909(35)	8d
	O11	0.11932(50)	0.83941(48)	0.74398(70)	1	2.909(35)	8d
	O12	0.23465(45)	0.84566(51)	0.74176(71)	1	2.909(35)	8d
	O13	0.31350(45)	0.94990(48)	0.82010(47)	1	2.909(35)	8d
	O14	0.08154(38)	0.95987(50)	0.81544(60)	1	2.909(35)	8d
	O15	0.42065(46)	0.12766(51)	0.60059(73)	1	2.909(35)	8d
	O16	0.40184(46)	0.99763(50)	0.58615(81)	1	2.909(35)	8d
	O17	0.40349(49)	0.86710(51)	0.56900(79)	1	2.909(35)	8d
	O18	0.19168(63)	0.12953(45)	0.61812(60)	1	2.909(35)	8d
	O19	0.20038(59)	0.00339(46)	0.59695(67)	1	2.909(35)	8d
	O20	0.19864(57)	0.87113(45)	0.57710(61)	1	2.909(35)	8d
	O21	0.99730(49)	0.05083(67)	0.79317(62)	1	2.909(35)	8d
	O22	0.99490(50)	0.85274(53)	0.79499(66)	1	2.909(35)	8d
	O23	0.41795(66)	0.7500	0.64329(90)	1	2.909(35)	4c
	O24	0.19096(87)	0.7500	0.66020(77)	1	2.909(35)	4c
	O25	0.27431(56)	0.7500	0.06211(90)	1	2.909(35)	4c
	O26	0.09338(62)	0.7500	0.05532(106)	1	2.909(35)	4c
	Si1	0.42292(26)	0.06190(31)	0.66311(40)	1	1.177(17)	8d
	Si2	0.30908(32)	0.03024(23)	0.80952(37)	1	1.177(17)	8d
	Si3	0.27905(23)	0.06354(27)	0.03466(38)	1	1.177(17)	8d
	Si4	0.12102(24)	0.06130(31)	0.02531(40)	1	1.177(17)	8d
	Si5	0.06993(26)	0.02949(25)	0.81652(42)	1	1.177(17)	8d

	Si6	0.18563(26)	0.05675(29)	0.67322(37)	1	1.177(17)	8d
	Si7	0.42370(27)	0.83179(26)	0.66995(45)	1	1.177(17)	8d
	Si8	0.30653(31)	0.86852(26)	0.81783(35)	1	1.177(17)	8d
	Si9	0.27685(25)	0.82796(23)	0.03013(41)	1	1.177(17)	8d
	Si10	0.12199(26)	0.82667(25)	0.02388(42)	1	1.177(17)	8d
	Si11	0.07132(27)	0.87284(30)	0.81453(41)	1	1.177(17)	8d
	Si12	0.18770(31)	0.82481(22)	0.68206(41)	1	1.177(17)	8d
Ammonia 1	N1	0.8990	0.7400	0.1860	0.93(1)	2.94(46)	4c
	H12	0.8540	0.7500	0.1600	0.93(1)	3.52(55)	4c
	H13	0.9330	0.7600	0.1400	0.93(1)	3.52(55)	4c
	H14	0.9000	0.7600	0.2550	0.93(1)	3.52(55)	4c
Ammonia 3	N3	0.9950	0.3100	0.5430	0.43(1)	3.82(60)	4c
	H32	0.0000	0.3600	0.5400	0.43(1)	4.58(72)	4c
	H33	0.0400	0.2900	0.5800	0.43(1)	4.58(72)	4c
	H34	0.9500	0.3000	0.5800	0.43(1)	4.58(72)	4c

Desorption temperature = 300 °C

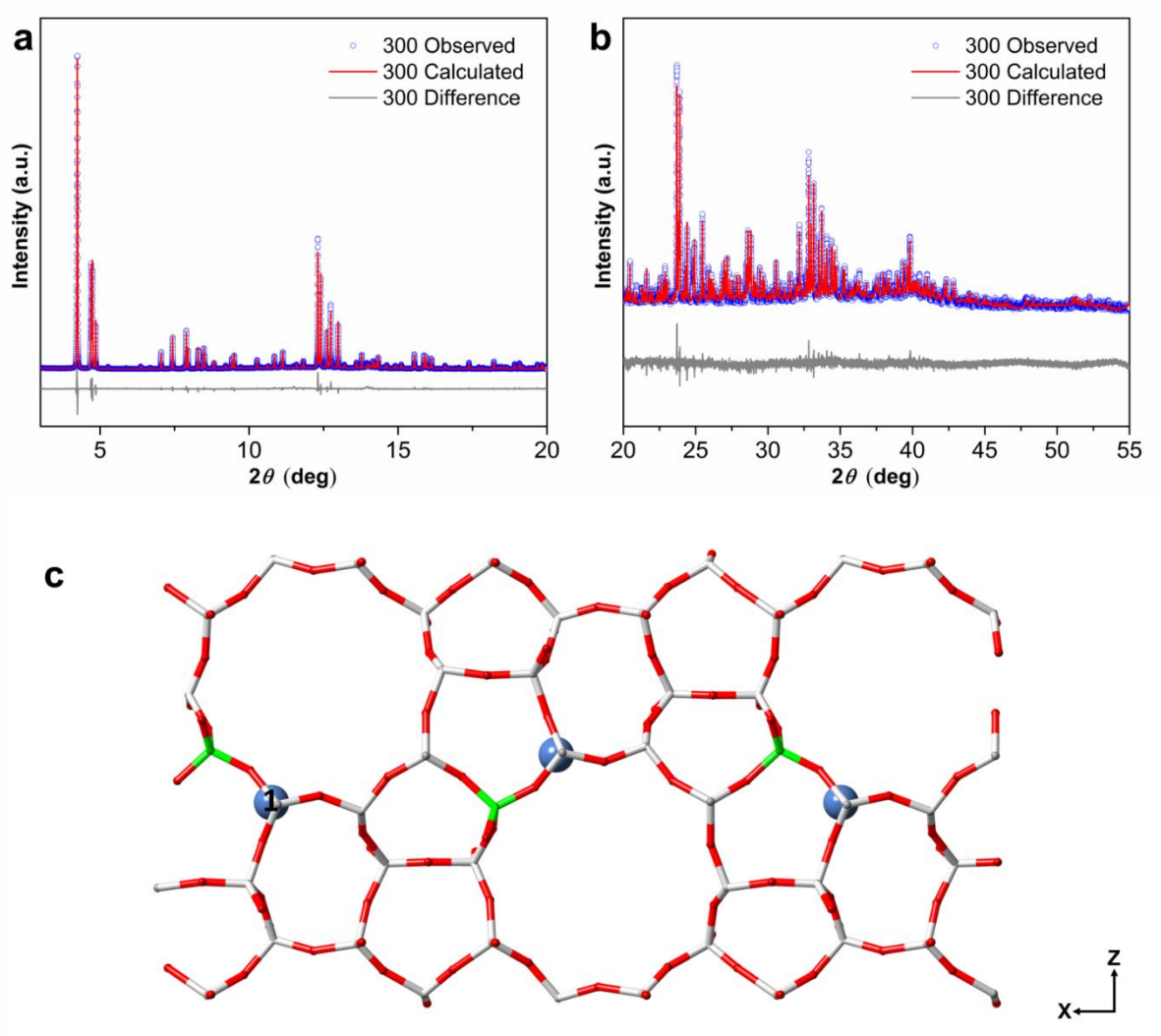

Figure A4.3. Rietveld refinement of the SXRD profile and the corresponding crystal structure of H-ZSM-5 pre-adsorbed with ammonia, measured at 300 °C. Comparison of the SXRD (blue) and Rietveld refinement (red) profiles and the difference (grey), (**a**) 2θ range of 3-20° and (**b**) 2θ range of 20-55°; (**c**) the corresponding crystal structure (view from [010]). Atoms are represented in ball/sticks: green = Si/Al, red = O, blue = N, black = C. The symmetry for the ammonia molecules is disregarded and no hydrogens are plotted for clarity.

Table A4.4. Atomic parameters of H-ZSM-5 pre-adsorbed with ammonia, measured at 300 °C.

Species	Atom	*x*	*y*	*z*	SOF	B_{eq} (Å^2)	Wyckoff
Zeolite framework	O1	0.37520(52)	0.05196(70)	0.75575(67)	1	3.481(36)	8d
	O2	0.30867(55)	0.06262(49)	0.92244(66)	1	3.481(36)	8d
	O3	0.20145(49)	0.05850(49)	0.02160(47)	1	3.481(36)	8d
	O4	0.09524(42)	0.06376(54)	0.91395(71)	1	3.481(36)	8d
	O5	0.11755(49)	0.05735(69)	0.72764(64)	1	3.481(36)	8d
	O6	0.24527(48)	0.05737(70)	0.75535(67)	1	3.481(36)	8d
	O7	0.37101(51)	0.83914(51)	0.76617(70)	1	3.481(36)	8d
	O8	0.30354(60)	0.84506(41)	0.93106(69)	1	3.481(36)	8d
	O9	0.19533(56)	0.84028(35)	0.03070(52)	1	3.481(36)	8d
	O10	0.08822(49)	0.84767(49)	0.92292(79)	1	3.481(36)	8d
	O11	0.11573(54)	0.84648(52)	0.74597(72)	1	3.481(36)	8d
	O12	0.23838(50)	0.84675(54)	0.74786(73)	1	3.481(36)	8d
	O13	0.31376(49)	0.95051(54)	0.81810(49)	1	3.481(36)	8d
	O14	0.07864(39)	0.95596(58)	0.81991(60)	1	3.481(36)	8d
	O15	0.41978(50)	0.12525(52)	0.60703(77)	1	3.481(36)	8d
	O16	0.40299(52)	0.99730(53)	0.59248(79)	1	3.481(36)	8d
	O17	0.40087(52)	0.86477(51)	0.56193(77)	1	3.481(36)	8d
	O18	0.19136(66)	0.13166(47)	0.61882(64)	1	3.481(36)	8d
	O19	0.20282(64)	0.00256(48)	0.59519(70)	1	3.481(36)	8d
	O20	0.19709(64)	0.86900(47)	0.58171(64)	1	3.481(36)	8d
	O21	0.99575(53)	0.04976(69)	0.79451(61)	1	3.481(36)	8d
	O22	0.99404(55)	0.85123(55)	0.79742(65)	1	3.481(36)	8d
	O23	0.41658(72)	0.7500	0.63753(95)	1	3.481(36)	4c
	O24	0.19328(91)	0.7500	0.65918(80)	1	3.481(36)	4c
	O25	0.27832(61)	0.7500	0.05764(96)	1	3.481(36)	4c
	O26	0.09411(69)	0.7500	0.06854(108)	1	3.481(36)	4c
	Si1	0.42278(27)	0.06021(32)	0.66457(41)	1	1.374(16)	8d
	Si2	0.30891(36)	0.02995(22)	0.81037(38)	1	1.374(16)	8d
	Si3	0.27983(24)	0.06382(27)	0.03698(38)	1	1.374(16)	8d
	Si4	0.12083(24)	0.05982(32)	0.02670(40)	1	1.374(16)	8d
	Si5	0.06902(28)	0.02947(27)	0.81822(43)	1	1.374(16)	8d

	Si6	0.18732(29)	0.05534(29)	0.67503(37)	1	1.374(16)	8d
	Si7	0.42392(28)	0.82857(27)	0.67284(47)	1	1.374(16)	8d
	Si8	0.30778(34)	0.87109(26)	0.81977(37)	1	1.374(16)	8d
	Si9	0.27496(26)	0.82978(24)	0.03025(42)	1	1.374(16)	8d
	Si10	0.12126(28)	0.82356(25)	0.02677(43)	1	1.374(16)	8d
	Si11	0.07219(28)	0.87106(32)	0.81548(43)	1	1.374(16)	8d
	Si12	0.18781(33)	0.82624(23)	0.68478(42)	1	1.374(16)	8d
Ammonia 1	N1	0.9202	0.7630	0.1870	0.50(1)	3.19(87)	4c
	H12	0.9600	0.7400	0.1800	0.50(1)	3.82(105)	4c
	H13	0.8900	0.7500	0.1300	0.50(1)	3.82(105)	4c
	H14	0.9000	0.7500	0.2510	0.50(1)	3.82(105)	4c

Desorption temperature = 400 °C

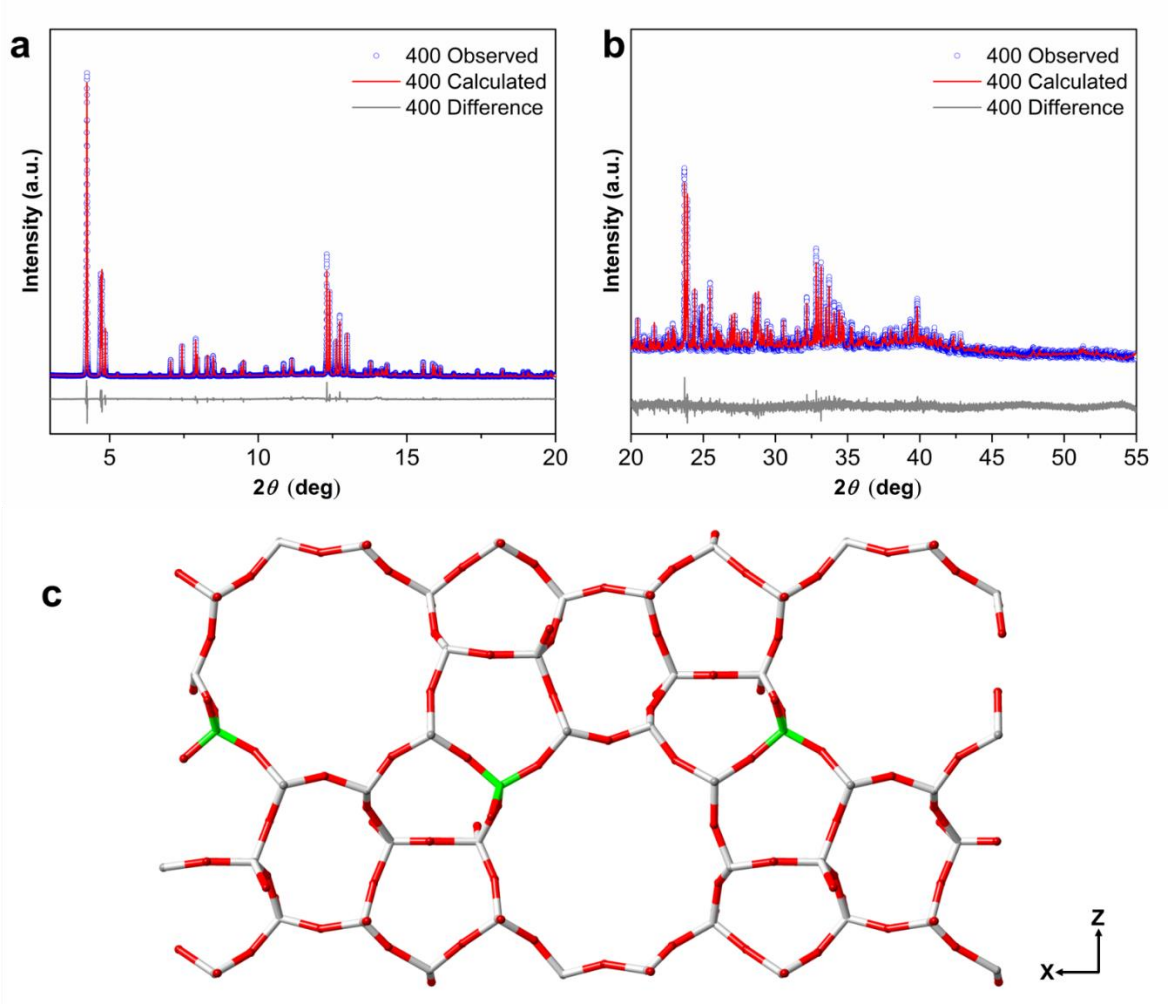

Figure A4.4. Rietveld refinement of the SXRD profile and the corresponding crystal structure of H-ZSM-5 pre-adsorbed with ammonia, measured at 400 °C. Comparison of the SXRD (blue) and Rietveld refinement (red) profiles and the difference (grey), (**a**) 2θ range of 3-20° and (**b**) 2θ range of 20-55°; (**c**) the corresponding crystal structure (view from [010]). Atoms are represented in ball/sticks: green = Si/Al, red = O, blue = N, black = C. The symmetry for the ammonia molecules is disregarded and no hydrogens are plotted for clarity.

Table A4.5. Atomic parameters of H-ZSM-5 pre-adsorbed with ammonia, measured at 400 °C.

Species	Atom	*x*	*y*	*z*	SOF	B_{eq} (Å²)	Wyckoff
Zeolite framework	O1	0.37736(66)	0.05331(72)	0.75523(84)	1	3.865(55)	8d
	O2	0.30947(66)	0.06264(58)	0.92641(80)	1	3.865(55)	8d
	O3	0.20385(57)	0.05641(61)	0.02465(59)	1	3.865(55)	8d
	O4	0.09330(53)	0.06688(60)	0.91660(87)	1	3.865(55)	8d
	O5	0.11922(62)	0.06028(69)	0.73160(80)	1	3.865(55)	8d
	O6	0.24472(61)	0.05458(88)	0.75232(88)	1	3.865(55)	8d
	O7	0.37280(65)	0.83552(57)	0.76765(89)	1	3.865(55)	8d
	O8	0.30362(77)	0.84479(50)	0.92785(85)	1	3.865(55)	8d
	O9	0.18994(64)	0.83699(42)	0.02948(64)	1	3.865(55)	8d
	O10	0.09000(60)	0.85115(58)	0.91709(95)	1	3.865(55)	8d
	O11	0.11578(70)	0.84921(60)	0.74896(90)	1	3.865(55)	8d
	O12	0.24567(68)	0.84861(69)	0.75621(96)	1	3.865(55)	8d
	O13	0.31544(59)	0.94963(64)	0.82147(60)	1	3.865(55)	8d
	O14	0.07905(48)	0.95436(70)	0.81721(73)	1	3.865(55)	8d
	O15	0.42140(61)	0.12475(59)	0.61799(94)	1	3.865(55)	8d
	O16	0.40099(62)	0.99572(62)	0.59388(91)	1	3.865(55)	8d
	O17	0.40166(66)	0.86281(59)	0.56106(90)	1	3.865(55)	8d
	O18	0.19096(78)	0.13676(51)	0.62312(79)	1	3.865(55)	8d
	O19	0.20224(74)	0.00475(55)	0.59570(84)	1	3.865(55)	8d
	O20	0.19859(79)	0.86767(54)	0.58141(83)	1	3.865(55)	8d
	O21	0.99592(66)	0.05110(80)	0.79697(74)	1	3.865(55)	8d
	O22	0.99728(70)	0.85003(66)	0.79661(77)	1	3.865(55)	8d
	O23	0.41574(86)	0.7500	0.62442(124)	1	3.865(55)	4c
	O24	0.19171(09)	0.7500	0.65522(101)	1	3.865(55)	4c
	O25	0.27359(71)	0.7500	0.06908(124)	1	3.865(55)	4c
	O26	0.08904(78)	0.7500	0.08014(123)	1	3.865(55)	4c
	Si1	0.42180(32)	0.05770(39)	0.66422(50)	1	1.455(23)	8d
	Si2	0.30851(42)	0.02973(26)	0.81211(47)	1	1.455(23)	8d
	Si3	0.27992(28)	0.06377(32)	0.04033(44)	1	1.455(23)	8d
	Si4	0.12078(29)	0.05877(38)	0.02634(48)	1	1.455(23)	8d
	Si5	0.06831(33)	0.03048(32)	0.82136(52)	1	1.455(23)	8d
	Si6	0.18719(35)	0.05597(35)	0.67605(46)	1	1.455(23)	8d
	Si7	0.42470(34)	0.82576(32)	0.67469(56)	1	1.455(23)	8d
	Si8	0.31002(40)	0.87134(30)	0.82252(46)	1	1.455(23)	8d

	Si9	0.27526(32)	0.83011(29)	0.02857(50)	1	1.455(23)	8d
	Si10	0.12087(33)	0.82257(30)	0.02942(53)	1	1.455(23)	8d
	Si11	0.07277(36)	0.87088(37)	0.81494(53)	1	1.455(23)	8d
	Si12	0.18886(42)	0.82717(27)	0.68660(50)	1	1.455(23)	8d

Supplementary Information for Chapter 5

Crystallographic and atomic parameters of H-ZSM-5 pre-adsorbed with ethanol, DMF, and an equimolar mixture of both, measured at 25 °C

Table A5.1(a). Atomic parameters of H-ZSM-5 pre-adsorbed with ethanol measured at 25 °C (R_{wp} = 7.649%, R_{exp} = 3.365%, χ^2= 2.274).

Species	Atom	x	*y*	*z*	SOF	B_{eq} (Å^2)	Wyckoff
Zeolite framework	O1	0.37346(45)	0.05149(62)	0.75410(57)	1	2.099(23)	8d
	O2	0.30627(54)	0.05716(52)	0.92008(54)	1	2.099(23)	8d
	O3	0.19923(44)	0.05827(45)	0.02005(40)	1	2.099(23)	8d
	O4	0.09506(38)	0.06229(55)	0.91329(62)	1	2.099(23)	8d
	O5	0.11620(45)	0.04839(55)	0.72565(57)	1	2.099(23)	8d
	O6	0.24673(40)	0.06016(59)	0.75345(55)	1	2.099(23)	8d
	O7	0.37308(47)	0.84215(49)	0.76509(66)	1	2.099(23)	8d
	O8	0.30857(52)	0.84282(39)	0.93245(57)	1	2.099(23)	8d
	O9	0.19539(50)	0.84636(32)	0.03209(49)	1	2.099(23)	8d
	O10	0.08777(43)	0.83897(46)	0.92199(71)	1	2.099(23)	8d
	O11	0.11477(44)	0.83726(45)	0.74053(63)	1	2.099(23)	8d
	O12	0.23986(44)	0.84962(49)	0.75554(69)	1	2.099(23)	8d
	O13	0.31079(46)	0.94840(46)	0.81731(46)	1	2.099(23)	8d
	O14	0.07952(35)	0.95448(51)	0.82108(57)	1	2.099(23)	8d
	O15	0.42233(46)	0.12706(51)	0.60269(64)	1	2.099(23)	8d
	O16	0.40969(50)	1.00129(50)	0.58709(68)	1	2.099(23)	8d
	O17	0.40488(47)	0.86747(49)	0.57131(73)	1	2.099(23)	8d
	O18	0.19211(58)	0.12849(43)	0.61891(54)	1	2.099(23)	8d
	O19	0.20463(54)	0.00367(44)	0.59379(61)	1	2.099(23)	8d
	O20	0.20156(57)	0.87023(46)	0.58355(58)	1	2.099(23)	8d
	O21	0.99693(46)	0.04676(56)	0.79233(58)	1	2.099(23)	8d
	O22	0.99505(48)	0.85142(49)	0.79070(59)	1	2.099(23)	8d
	O23	0.41960(66)	0.75	0.64682(83)	1	2.099(23)	4c
	O24	0.19149(82)	0.75	0.64986(75)	1	2.099(23)	4c
	O25	0.28440(61)	0.75	0.05534(83)	1	2.099(23)	4c
	O26	0.10992(66)	0.75	0.0624(10)	1	2.099(23)	4c
	Si1	0.42491(22)	0.05671(31)	0.66327(31)	1	1.049(11)	8d
	Si2	0.27891(19)	0.06068(24)	1.03346(32)	1	1.049(11)	8d
	Si3	0.30834(30)	0.03098(19)	-0.18939(31)	1	1.049(11)	8d
	Si4	0.11967(22)	0.06401(25)	0.02769(34)	1	1.049(11)	8d
	Si5	0.07071(23)	0.02983(22)	0.81467(35)	1	1.049(11)	8d
	Si6	0.18862(25)	0.05696(25)	0.67589(30)	1	1.049(11)	8d

	Si7	0.42292(24)	0.82909(23)	0.67228(37)	1	1.049(11)	8d
	Si8	0.30910(28)	0.87051(22)	0.81671(30)	1	1.049(11)	8d
	Si9	0.27422(21)	0.82685(21)	0.03309(35)	1	1.049(11)	8d
	Si10	0.12073(24)	0.82612(22)	0.03050(36)	1	1.049(11)	8d
	Si11	0.07261(23)	0.87075(27)	0.82161(35)	1	1.049(11)	8d
	Si12	0.18757(27)	0.82643(19)	0.68213(33)	1	1.049(11)	8d
Ethanol1	O1	-2.10743	0.75557	1.25099	0.3825(68)	20.0(17)	4c
	H2	-2.08704	0.79846	1.28459	0.3825(68)	24.0(20)	4c
	C3	-2.09765	0.76177	1.14514	0.3825(68)	26.0(22)	4c
	H4	-2.07417	0.80486	1.13039	0.3825(68)	30.0(26)	4c
	H5	-2.07024	0.7233	1.12067	0.3825(68)	30.0(26)	4c
	C6	-2.16377	0.76131	1.09357	0.3825(68)	28.0(24)	4c
	H7	-2.16968	0.80418	1.0559	0.3825(68)	34.0(29)	4c
	H8	-2.16578	0.72262	1.04625	0.3825(68)	34.0(29)	4c
	H9	-2.2	0.75683	1.14412	0.3825(68)	34.0(29)	4c
Ethanol2	O1	0.02961	0.32422	1.47871	0.5969(53)	15.12(73)	4c
	H2	-0.00282	0.2861	1.45523	0.5969(53)	18.15(88)	4c
	C3	-0.01034	0.37741	1.51974	0.5969(53)	19.66(95)	4c
	H4	-0.05837	0.36484	1.51561	0.5969(53)	22.7(11)	4c
	H5	0.00216	0.38479	1.59099	0.5969(53)	22.7(11)	4c
	C6	0.00129	0.4407	1.46185	0.5969(53)	21.2(10)	4c
	H7	-0.04156	0.45625	1.432	0.5969(53)	25.7(12)	4c
	H8	0.019	0.47618	1.50733	0.5969(53)	25.7(12)	4c
	H9	0.03419	0.43192	1.40756	0.5969(53)	25.7(12)	4c
Ethanol3	O1	-0.97621	0.17557	0.64367	0.2723(79)	6.5(12)	4c
	H2	-0.94124	0.13727	0.65542	0.2723(79)	7.9(14)	4c
	C3	-0.96682	0.22492	0.72073	0.2723(79)	8.5(16)	4c
	H4	-0.92979	0.2105	0.76555	0.2723(79)	9.8(18)	4c
	H5	-0.95549	0.26912	0.68985	0.2723(79)	9.8(18)	4c
	C6	-1.02957	0.23174	0.78019	0.2723(79)	9.2(17)	4c
	H7	-1.02043	0.22035	0.85143	0.2723(79)	11.1(20)	4c
	H8	-1.04615	0.27894	0.77568	0.2723(79)	11.1(20)	4c
	H9	-1.064	0.20048	0.75318	0.2723(79)	11.1(20)	4c
Ethanol4	O1	-1.08952	0.17105	0.59341	0.4383(63)	20.0(14)	4c
	H2	-1.05627	0.15065	0.64553	0.4383(63)	24.0(17)	4c
	C3	-1.12174	0.22747	0.63985	0.4383(63)	26.0(18)	4c
	H4	-1.10456	0.23299	0.70926	0.4383(63)	30.0(21)	4c
	H5	-1.11226	0.26906	0.60068	0.4383(63)	30.0(21)	4c
	C6	-1.19533	0.21567	0.64292	0.4383(63)	28.0(20)	4c

	H7	-1.21086	0.21594	0.71367	0.4383(63)	34.0(24)	4c
	H8	-1.21855	0.25196	0.60507	0.4383(63)	34.0(24)	4c
	H9	-1.20571	0.17121	0.61208	0.4383(63)	34.0(24)	4c

Table A5.1(b). Translational and rotational axes for the matrices describing the adsorbate ethanol molecules, together with their corresponding systematic errors.

	x	***y***	***z***
Translational			
Ethanol1	-2.1074(18)	0.7556(86)	1.2510(23)
Ethanol2	0.02961(88)	0.32422(63)	1.4787(15)
Ethanol3	-0.9762(16)	0.1756(18)	0.6437(25)
Ethanol4	-1.0895(13)	0.1711(18)	0.5934(29)
Rotational			
Ethanol1	190.7(75)	244.1(82)	52.4(27)
Ethanol2	108.3(26)	17.8(23)	-34.8(11)
Ethanol3	-75.5(25)	53.2(29)	-125.6(36)
Ethanol4	-26.9(47)	41.6(39)	-68.7(29)

Table A5.2(a). Atomic parameters of H-ZSM-5 pre-adsorbed with DMF measured at 25 °C (R_{wp} = 8.457%, R_{exp} = 3.339%, χ^2 = 2.533).

Species	Atom	*x*	*y*	*z*	SOF	B_{eq} (Å^2)	Wychoff
Zeolite framework	O1	0.37684(48)	0.05499(68)	0.75255(65)	1	1.832(25)	8d
	O2	0.30932(50)	0.05871(54)	0.92543(59)	1	1.832(25)	8d
	O3	0.19809(46)	0.06165(43)	0.02543(45)	1	1.832(25)	8d
	O4	0.09579(38)	0.05807(57)	0.91475(65)	1	1.832(25)	8d
	O5	0.11354(48)	0.04504(55)	0.72940(62)	1	1.832(25)	8d
	O6	0.24622(43)	0.05293(70)	0.75865(61)	1	1.832(25)	8d
	O7	0.37427(51)	0.84195(50)	0.75952(71)	1	1.832(25)	8d
	O8	0.30251(56)	0.84755(42)	0.93166(61)	1	1.832(25)	8d
	O9	0.19652(51)	0.84845(33)	0.03241(52)	1	1.832(25)	8d
	O10	0.08424(47)	0.84053(46)	0.92706(73)	1	1.832(25)	8d
	O11	0.11719(47)	0.83640(46)	0.74246(67)	1	1.832(25)	8d
	O12	0.24036(48)	0.84717(52)	0.76361(74)	1	1.832(25)	8d
	O13	0.31361(43)	0.95152(49)	0.81623(49)	1	1.832(25)	8d
	O14	0.07984(36)	0.95337(55)	0.82822(55)	1	1.832(25)	8d
	O15	0.41967(48)	0.12367(51)	0.60807(72)	1	1.832(25)	8d
	O16	0.40289(52)	1.00242(54)	0.58739(76)	1	1.832(25)	8d
	O17	0.40537(49)	0.87167(51)	0.57239(75)	1	1.832(25)	8d
	O18	0.19076(60)	0.12924(45)	0.61922(60)	1	1.832(25)	8d
	O19	0.20281(60)	0.00204(48)	0.59549(66)	1	1.832(25)	8d
	O20	0.19965(60)	0.87055(49)	0.58780(60)	1	1.832(25)	8d
	O21	0.99733(51)	0.04932(64)	0.79526(60)	1	1.832(25)	8d
	O22	0.99596(52)	0.85111(52)	0.79386(67)	1	1.832(25)	8d
	O23	0.41913(73)	0.75	0.64018(89)	1	1.832(25)	4c
	O24	0.19650(83)	0.75	0.65447(80)	1	1.832(25)	4c
	O25	0.28593(62)	0.75	0.04753(82)	1	1.832(25)	4c
	O26	0.11467(68)	0.75	0.06522(96)	1	1.832(25)	4c
	Si1	0.42464(26)	0.05924(33)	0.66587(36)	1	0.916(13)	8d
	Si2	0.27852(20)	0.06072(27)	1.03645(34)	1	0.916(13)	8d
	Si3	0.31074(31)	0.02973(21)	-0.18602(36)	1	0.916(13)	8d
	Si4	0.12108(23)	0.06360(28)	0.02698(36)	1	0.916(13)	8d
	Si5	0.06991(25)	0.03036(24)	0.81778(36)	1	0.916(13)	8d
	Si6	0.18663(26)	0.05780(27)	0.67567(33)	1	0.916(13)	8d
	Si7	0.42310(27)	0.82944(23)	0.66747(38)	1	0.916(13)	8d
	Si8	0.30950(30)	0.86991(24)	0.81522(33)	1	0.916(13)	8d
	Si9	0.27425(23)	0.82715(22)	0.03047(38)	1	0.916(13)	8d
	Si10	0.12082(26)	0.82569(23)	0.03173(39)	1	0.916(13)	8d

	Si11	0.07270(25)	0.87069(28)	0.82009(37)	1	0.916(13)	8d
	Si12	0.18727(30)	0.82621(20)	0.68486(35)	1	0.916(13)	8d
DMF 1	O1	-2.10446	0.77858	1.26435	0.4296(35)	14.40(82)	4c
	C2	-2.09845	0.75538	1.16989	0.4296(35)	17.28(98)	4c
	C3	-2.03265	0.74961	1.14424	0.4296(35)	20.2(11)	4c
	C4	-1.996	0.77064	1.2284	0.4296(35)	20.2(11)	4c
	C5	-2.042	0.78776	1.29952	0.4296(35)	17.28(98)	4c
	C6	-2.0255	0.81297	1.40135	0.4296(35)	20.2(11)	4c
	C7	-2.15541	0.73846	1.10309	0.4296(35)	20.2(11)	4c
	H8	-2.0077	0.70499	1.11431	0.4296(35)	24.5(14)	4c
	H9	-1.95627	0.74283	1.26628	0.4296(35)	24.5(14)	4c
	H10	-1.97068	0.81559	1.41013	0.4296(35)	24.5(14)	4c
	H11	-2.04643	0.77829	1.45799	0.4296(35)	24.5(14)	4c
	H12	-2.04713	0.86376	1.41162	0.4296(35)	24.5(14)	4c
	H13	-2.13617	0.72067	1.03018	0.4296(35)	24.5(14)	4c
	H14	-2.18654	0.7838	1.09154	0.4296(35)	24.5(14)	4c
	H15	-2.18585	0.69834	1.13791	0.4296(35)	24.5(14)	4c
DMF 2	O1	-1.96795	0.86786	1.45559	0.4868(31)	14.58(59)	4c
	C2	-1.99818	0.92089	1.49958	0.4868(31)	17.50(70)	4c
	C3	-2.04431	0.89929	1.56778	0.4868(31)	20.42(82)	4c
	C4	-2.0422	0.82845	1.56539	0.4868(31)	20.42(82)	4c
	C5	-1.99493	0.81181	1.49592	0.4868(31)	17.50(70)	4c
	C6	-1.97592	0.74174	1.46863	0.4868(31)	20.42(82)	4c
	C7	-1.9834	0.99274	1.47705	0.4868(31)	20.42(82)	4c
	H8	-2.04797	0.91419	1.6463	0.4868(31)	24.8(10)	4c
	H9	-2.03544	0.79459	1.62906	0.4868(31)	24.8(10)	4c
	H10	-2.00582	0.70573	1.51307	0.4868(31)	24.8(10)	4c
	H11	-1.9223	0.73394	1.48444	0.4868(31)	24.8(10)	4c
	H12	-1.98548	0.73347	1.38808	0.4868(31)	24.8(10)	4c
	H13	-2.01535	1.02549	1.5238	0.4868(31)	24.8(10)	4c
	H14	-1.99351	1.00284	1.39711	0.4868(31)	24.8(10)	4c
	H15	-1.93033	1.00331	1.49347	0.4868(31)	24.8(10)	4c
DMF 3	O1	-1.85598	0.77216	1.31054	0.3328(35)	19.1(12)	4c
	C2	-1.86218	0.71832	1.37145	0.3328(35)	23.0(14)	4c
	C3	-1.8017	0.70143	1.41159	0.3328(35)	26.8(17)	4c
	C4	-1.75547	0.74793	1.37275	0.3328(35)	26.8(17)	4c
	C5	-1.79099	0.78993	1.31164	0.3328(35)	23.0(14)	4c
	C6	-1.76204	0.84717	1.25442	0.3328(35)	26.8(17)	4c
	C7	-1.92586	0.68239	1.39203	0.3328(35)	26.8(17)	4c

H8	-1.78994	0.69483	1.49083	0.3328(35)	32.6(20)	4c
H9	-1.72077	0.77931	1.41528	0.3328(35)	32.6(20)	4c
H10	-1.70781	0.85022	1.26911	0.3328(35)	32.6(20)	4c
H11	-1.78624	0.89464	1.27807	0.3328(35)	32.6(20)	4c
H12	-1.77056	0.83919	1.17354	0.3328(35)	32.6(20)	4c
H13	-1.91651	0.64031	1.44442	0.3328(35)	32.6(20)	4c
H14	-1.94637	0.66235	1.32122	0.3328(35)	32.6(20)	4c
H15	-1.96205	0.7178	1.42574	0.3328(35)	32.6(20)	4c

Table A5.2(b). Translational and rotational axes for the matrices describing the adsorbate DMF molecules, together with their corresponding systematic errors.

	x	***y***	***z***
Translational			
DMF1	-2.10446(84)	0.7786(13)	1.2643(15)
DMF2	-1.96795(73)	0.86786(65)	1.4556(11)
DMF3	-1.8560(13)	0.7722(18)	1.3105(19)
Rotational			
DMF1	-200.1(12)	-4.65(78)	2.17(31)
DMF2	58.57(84)	-33.31(66)	-131.53(89)
DMF3	52.04(81)	-11.1(13)	1.92(13)

Table A5.3(a). Atomic parameters of H-ZSM-5 pre-adsorbed with limited equimolar DMF and ethanol at 25 °C (R_{wp} = 9.005%, R_{exp} = 5.259%, χ^2 = 1.712).

Species	Atom	*x*	*y*	*z*	SOF	B_{eq} (Å^2)	Wychoff
Zeolite framework	O1	0.36816(50)	0.06015(63)	0.74449(73)	1	1.718(30)	8d
	O2	0.29519(55)	0.06478(49)	0.91155(70)	1	1.718(30)	8d
	O3	0.20000(50)	0.05169(57)	0.02262(55)	1	1.718(30)	8d
	O4	0.09514(48)	0.05082(62)	0.92036(78)	1	1.718(30)	8d
	O5	0.11615(53)	0.04771(65)	0.71605(74)	1	1.718(30)	8d
	O6	0.23764(47)	0.05105(67)	0.74567(68)	1	1.718(30)	8d
	O7	0.36641(50)	0.84642(51)	0.75978(73)	1	1.718(30)	8d
	O8	0.30329(57)	0.84794(43)	0.92707(66)	1	1.718(30)	8d
	O9	0.20262(55)	0.84233(44)	0.03986(60)	1	1.718(30)	8d
	O10	0.09086(50)	0.83272(51)	0.91736(83)	1	1.718(30)	8d
	O11	0.12136(51)	0.84033(50)	0.72749(78)	1	1.718(30)	8d
	O12	0.23326(48)	0.85372(56)	0.74264(79)	1	1.718(30)	8d
	O13	0.30281(53)	0.95322(54)	0.81407(55)	1	1.718(30)	8d
	O14	0.07423(43)	0.95268(59)	0.82301(67)	1	1.718(30)	8d
	O15	0.41283(52)	0.12406(52)	0.59261(83)	1	1.718(30)	8d
	O16	0.41001(57)	1.00514(57)	0.57015(94)	1	1.718(30)	8d
	O17	0.40626(55)	0.87189(57)	0.57146(90)	1	1.718(30)	8d
	O18	0.18609(56)	0.12848(51)	0.61341(67)	1	1.718(30)	8d
	O19	0.19906(64)	-0.00304(50)	0.59427(70)	1	1.718(30)	8d
	O20	0.20508(62)	0.86455(52)	0.57121(77)	1	1.718(30)	8d
	O21	0.99504(53)	0.04374(66)	0.78773(79)	1	1.718(30)	8d
	O22	0.99488(58)	0.85313(59)	0.78702(77)	1	1.718(30)	8d
	O23	0.42169(75)	0.75	0.6357(11)	1	1.718(30)	4c
	O24	0.19631(92)	0.75	0.65161(94)	1	1.718(30)	4c
	O25	0.29415(80)	0.75	0.0652(10)	1	1.718(30)	4c
	O26	0.11518(73)	0.75	0.0661(11)	1	1.718(30)	4c
	Si1	0.42418(26)	0.05246(32)	0.65964(39)	1	0.859(15)	8d
	Si2	0.27955(24)	0.06519(26)	1.02249(39)	1	0.859(15)	8d
	Si3	0.30701(32)	0.02964(23)	-0.19411(40)	1	0.859(15)	8d
	Si4	0.12224(24)	0.05826(32)	0.02829(39)	1	0.859(15)	8d
	Si5	0.06841(27)	0.02989(26)	0.80727(42)	1	0.859(15)	8d
	Si6	0.18370(26)	0.06265(26)	0.66179(36)	1	0.859(15)	8d
	Si7	0.42446(29)	0.82906(26)	0.66408(41)	1	0.859(15)	8d
	Si8	0.30297(33)	0.86993(27)	0.80714(36)	1	0.859(15)	8d
	Si9	0.27728(26)	0.82723(23)	0.03058(38)	1	0.859(15)	8d

	Si10	0.12154(28)	0.82232(25)	0.02161(41)	1	0.859(15)	8d
	Si11	0.07141(28)	0.86702(30)	0.81750(39)	1	0.859(15)	8d
	Si12	0.18798(31)	0.82429(23)	0.67949(37)	1	0.859(15)	8d
Ethanol1	O1	-2.10464	0.75904	1.22838	0.7520(59)	29.32(94)	4c
	H2	-2.07265	0.80007	1.2183	0.7520(59)	35.2(11)	4c
	C3	-2.13891	0.748	1.13569	0.7520(59)	38.1(12)	4c
	H4	-2.12381	0.78179	1.08559	0.7520(59)	44.0(14)	4c
	H5	-2.1288	0.70191	1.11071	0.7520(59)	44.0(14)	4c
	C6	-2.21247	0.75493	1.15161	0.7520(59)	41.1(13)	4c
	H7	-2.23006	0.79178	1.1086	0.7520(59)	49.8(16)	4c
	H8	-2.23504	0.71192	1.1338	0.7520(59)	49.8(16)	4c
	H9	-2.22141	0.76571	1.22306	0.7520(59)	49.8(16)	4c
DMF1	O1	-3.02226	1.85689	0.49902	0.5396(30)	12.91(65)	4c
	C2	-3.0041	1.79275	0.47906	0.5396(30)	15.49(78)	4c
	C3	-2.95026	1.79157	0.41582	0.5396(30)	18.07(91)	4c
	C4	-2.93442	1.85937	0.39574	0.5396(30)	18.07(91)	4c
	C5	-2.97971	1.89716	0.44815	0.5396(30)	15.49(78)	4c
	C6	-2.98177	1.97213	0.44896	0.5396(30)	18.07(91)	4c
	C7	-3.03791	1.73189	0.5201	0.5396(30)	18.07(91)	4c
	H8	-2.92467	1.74696	0.38672	0.5396(30)	21.9(11)	4c
	H9	-2.89405	1.87804	0.3479	0.5396(30)	21.9(11)	4c
	H10	-2.94125	1.99211	0.40091	0.5396(30)	21.9(11)	4c
	H11	-2.97486	1.99051	0.52649	0.5396(30)	21.9(11)	4c
	H12	-3.03074	1.98949	0.4201	0.5396(30)	21.9(11)	4c
	H13	-3.01277	1.68608	0.49154	0.5396(30)	21.9(11)	4c
	H14	-3.09098	1.73168	0.49643	0.5396(30)	21.9(11)	4c
	H15	-3.03511	1.7327	0.60282	0.5396(30)	21.9(11)	4c

Table A5.3(b). Translational and rotational axes for the matrices describing the adsorbate molecules, together with their corresponding systematic errors.

	x	***y***	***z***
Translational			
Ethanol1	-2.05677(87)	0.76004(41)	1.1929(17)
DMF1	-1.97832(66)	0.69500(30)	1.45665(90)
Rotational			
Ethanol1	106.3(25)	-4.07(51)	47.9(25)
DMF1	60.80(40)	33.04(50)	-45.36(63)

Supplementary Information for Chapter 6

Table A6.1. Atomic parameters of H-ZSM-5 with a flowing stream of methanol vapour, measured at 25 °C.

Species	Atom	*x*	*y*	*z*	SOF	B_{eq} (Å^2)	Wychoff
Zeolite framework	O1	0.38107(43)	0.04886(60)	0.75697(56)	1	0.262(30)	8d
	O2	0.30491(48)	0.05760(53)	0.92753(53)	1	0.262(30)	8d
	O3	0.20489(38)	0.05952(45)	0.02246(46)	1	0.262(30)	8d
	O4	0.09426(37)	0.05665(57)	0.91024(58)	1	0.262(30)	8d
	O5	0.11781(44)	0.05789(63)	0.73015(55)	1	0.262(30)	8d
	O6	0.25017(40)	0.05449(65)	0.76112(53)	1	0.262(30)	8d
	O7	0.36835(44)	0.84528(48)	0.77375(62)	1	0.262(30)	8d
	O8	0.30645(52)	0.84243(39)	0.93536(58)	1	0.262(30)	8d
	O9	0.19177(47)	0.84547(31)	0.02251(50)	1	0.262(30)	8d
	O10	0.08819(44)	0.84218(45)	0.91477(67)	1	0.262(30)	8d
	O11	0.11898(48)	0.84653(48)	0.73753(61)	1	0.262(30)	8d
	O12	0.23619(41)	0.84138(45)	0.74486(62)	1	0.262(30)	8d
	O13	0.30070(42)	0.94836(44)	0.82602(48)	1	0.262(30)	8d
	O14	0.07278(34)	0.95782(43)	0.81317(58)	1	0.262(30)	8d
	O15	0.41623(45)	0.12152(43)	0.61102(68)	1	0.262(30)	8d
	O16	0.40540(42)	0.99096(43)	0.58913(67)	1	0.262(30)	8d
	O17	0.40099(46)	0.87185(44)	0.58105(68)	1	0.262(30)	8d
	O18	0.18819(48)	0.13282(39)	0.62073(58)	1	0.262(30)	8d
	O19	0.20095(52)	0.00969(38)	0.60418(57)	1	0.262(30)	8d
	O20	0.20317(53)	0.87065(46)	0.58420(56)	1	0.262(30)	8d
	O21	0.99600(45)	0.04451(52)	0.79673(60)	1	0.262(30)	8d
	O22	0.99957(51)	0.84308(50)	0.78832(61)	1	0.262(30)	8d
	O23	0.42247(64)	0.75	0.64575(90)	1	0.262(30)	4c
	O24	0.19857(72)	0.75	0.64873(84)	1	0.262(30)	4c
	O25	0.28211(58)	0.75	0.06580(88)	1	0.262(30)	4c
	O26	0.10562(64)	0.75	0.05683(97)	1	0.262(30)	4c
	Si1	0.42463(22)	0.05435(30)	0.66394(31)	1	0.254(16)	8d
	Si2	0.27945(20)	0.06012(27)	1.03930(32)	1	0.254(16)	8d
	Si3	0.30791(27)	0.03232(19)	-0.18195(32)	1	0.254(16)	8d
	Si4	0.12004(22)	0.06213(27)	0.02896(35)	1	0.254(16)	8d
	Si5	0.06931(23)	0.02940(23)	0.80958(35)	1	0.254(16)	8d
	Si6	0.19015(26)	0.05945(24)	0.67998(30)	1	0.254(16)	8d
	Si7	0.42491(24)	0.82869(23)	0.67572(37)	1	0.254(16)	8d

	Si8	0.30706(27)	0.87183(22)	0.82157(31)	1	0.254(16)	8d
	Si9	0.27772(23)	0.82699(21)	0.03298(36)	1	0.254(16)	8d
	Si10	0.12220(26)	0.82448(23)	0.03349(37)	1	0.254(16)	8d
	Si11	0.07131(24)	0.86756(27)	0.82255(35)	1	0.254(16)	8d
	Si12	0.18886(27)	0.82530(20)	0.67956(36)	1	0.254(16)	8d
Methanol1	O	0.91982	0.75665	0.21509	0.7657(53)	9.92(85)	4c
	H	0.9019527	0.7513018	0.2880739	0.7657(53)	12.9(11)	4c
	C	0.8635708	0.7539855	0.1491378	0.7657(53)	15.0(12)	4c
	H	0.8221031	0.7477835	0.1889382	0.7657(53)	19.5(15)	4c
	H	0.860625	0.796741	0.1105988	0.7657(53)	19.5(15)	4c
	H	0.868867	0.7155791	0.1020111	0.7657(53)	19.5(15)	4c
Methanol2	O	2.99203	3.6656	0.47422	1	11.29(48)	4c
	H	2.945372	3.666473	0.4395015	1	14.67(62)	4c
	C	3.006649	3.596943	0.4987321	1	8.58(59)	4c
	H	2.969135	3.567678	0.4767922	1	11.15(77)	4c
	H	3.04828	3.582816	0.4641224	1	11.15(77)	4c
	H	3.012699	3.592587	0.5723282	1	11.15(77)	4c
Methanol3	O	1.16367	0.71537	0.30361	0.5598(56)	17.5(17)	4c
	H	1.203777	0.7460321	0.323889	0.5598(56)	22.7(22)	4c
	C	1.105447	0.7411969	0.3524352	0.5598(56)	15.8(19)	4c
	H	1.117686	0.7813773	0.3929198	0.5598(56)	20.5(25)	4c
	H	1.071751	0.7541954	0.301334	0.5598(56)	20.5(25)	4c
	H	1.086412	0.7059787	0.3970062	0.5598(56)	20.5(25)	4c

Table A6.2. Atomic parameters of H-ZSM-5 with a flowing stream of methanol vapour, measured at 50 °C.

Species	Atom	*x*	*y*	*z*	SOF	B_{eq} (Å^2)	Wychoff
Zeolite framework	O1	0.37723(45)	0.05220(62)	0.75777(55)	1	0.422(29)	8d
	O2	0.30352(49)	0.05757(51)	0.92586(51)	1	0.422(29)	8d
	O3	0.20455(37)	0.06114(40)	0.02120(42)	1	0.422(29)	8d
	O4	0.09482(38)	0.05823(55)	0.90981(57)	1	0.422(29)	8d
	O5	0.11764(44)	0.05283(65)	0.72744(55)	1	0.422(29)	8d
	O6	0.24891(40)	0.05517(66)	0.75771(53)	1	0.422(29)	8d
	O7	0.36827(44)	0.84829(47)	0.76854(61)	1	0.422(29)	8d
	O8	0.30565(54)	0.84354(38)	0.93125(56)	1	0.422(29)	8d
	O9	0.19342(46)	0.84665(29)	0.02439(48)	1	0.422(29)	8d
	O10	0.09092(44)	0.84060(44)	0.91450(67)	1	0.422(29)	8d
	O11	0.11899(47)	0.84367(49)	0.73774(61)	1	0.422(29)	8d
	O12	0.23634(41)	0.84160(44)	0.74255(62)	1	0.422(29)	8d
	O13	0.30229(42)	0.94621(42)	0.82299(47)	1	0.422(29)	8d
	O14	0.07316(33)	0.95714(41)	0.81630(59)	1	0.422(29)	8d
	O15	0.41570(44)	0.12263(43)	0.61000(68)	1	0.422(29)	8d
	O16	0.40744(44)	0.99429(44)	0.58614(65)	1	0.422(29)	8d
	O17	0.40320(47)	0.87063(45)	0.57813(66)	1	0.422(29)	8d
	O18	0.18739(48)	0.13259(37)	0.61713(56)	1	0.422(29)	8d
	O19	0.20210(51)	0.00786(37)	0.60241(56)	1	0.422(29)	8d
	O20	0.20257(55)	0.87007(44)	0.58296(56)	1	0.422(29)	8d
	O21	0.99623(44)	0.04399(51)	0.79802(59)	1	0.422(29)	8d
	O22	0.99800(49)	0.84193(48)	0.78954(59)	1	0.422(29)	8d
	O23	0.42206(64)	0.75	0.64361(88)	1	0.422(29)	4c
	O24	0.19594(77)	0.75	0.64519(80)	1	0.422(29)	4c
	O25	0.28566(60)	0.75	0.06153(84)	1	0.422(29)	4c
	O26	0.10655(66)	0.75	0.05531(96)	1	0.422(29)	4c
	Si1	0.42444(21)	0.05489(29)	0.66397(32)	1	0.325(15)	8d
	Si2	0.28000(19)	0.06015(26)	1.03775(31)	1	0.325(15)	8d
	Si3	0.30785(27)	0.03210(18)	-0.18525(32)	1	0.325(15)	8d
	Si4	0.12006(21)	0.06239(26)	0.02774(33)	1	0.325(15)	8d
	Si5	0.06938(22)	0.02925(22)	0.80972(35)	1	0.325(15)	8d
	Si6	0.18960(25)	0.05905(24)	0.67718(30)	1	0.325(15)	8d
	Si7	0.42492(23)	0.82832(22)	0.67324(37)	1	0.325(15)	8d
	Si8	0.30625(27)	0.87242(21)	0.81784(30)	1	0.325(15)	8d

	Si9	0.27730(22)	0.82651(20)	0.03045(34)	1	0.325(15)	8d
	Si10	0.12256(25)	0.82497(23)	0.03246(36)	1	0.325(15)	8d
	Si11	0.07140(23)	0.86826(26)	0.82175(34)	1	0.325(15)	8d
	Si12	0.18807(26)	0.82569(19)	0.67930(35)	1	0.325(15)	8d
Methanol1	O	0.92346	0.74494	0.22237	0.7409(56)	11.95(95)	4c
	H	0.906842	0.743254	0.296424	0.7409(56)	15.5(12)	4c
	C	0.865901	0.751917	0.159637	0.7409(56)	24.3(14)	4c
	H	0.825035	0.753387	0.201856	0.7409(56)	31.6(18)	4c
	H	0.869416	0.794307	0.120325	0.7409(56)	31.6(18)	4c
	H	0.863223	0.712908	0.113105	0.7409(56)	31.6(18)	4c
Methanol2	O	2.99274	3.66834	0.47676	1	14.96(54)	4c
	H	2.945067	3.670086	0.445249	1	19.45(70)	4c
	C	3.006646	3.599492	0.500995	1	10.66(62)	4c
	H	2.967864	3.570966	0.481953	1	13.85(80)	4c
	H	3.046903	3.584313	0.463723	1	13.85(80)	4c
	H	3.014842	3.595318	0.574164	1	13.85(80)	4c
Methanol3	O	1.16154	0.74346	0.34942	0.5264(57)	25.2(16)	4c
	H	1.199108	0.775696	0.324098	0.5264(57)	32.8(21)	4c
	C	1.098782	0.774019	0.325485	0.5264(57)	18.0(22)	4c
	H	1.106644	0.817755	0.291161	0.5264(57)	23.4(29)	4c
	H	1.073012	0.743687	0.280575	0.5264(57)	23.4(29)	4c
	H	1.073045	0.781867	0.388074	0.5264(57)	23.4(29)	4c

Table A6.3 Atomic parameters of H-ZSM-5 with a flowing stream of methanol vapour, measured at 100 °C.

Species	Atom	*x*	*y*	*z*	SOF	B_{eq} (Å^2)	Wychoff
Zeolite framework	O1	0.37630(44)	0.05303(64)	0.75494(56)	1	0.485(29)	8d
	O2	0.30391(52)	0.05751(50)	0.92405(52)	1	0.485(29)	8d
	O3	0.20513(37)	0.06146(40)	0.02053(42)	1	0.485(29)	8d
	O4	0.09463(39)	0.05969(53)	0.91054(58)	1	0.485(29)	8d
	O5	0.11846(45)	0.05035(62)	0.72613(56)	1	0.485(29)	8d
	O6	0.24980(40)	0.05562(71)	0.75428(54)	1	0.485(29)	8d
	O7	0.37034(46)	0.84842(48)	0.76768(60)	1	0.485(29)	8d
	O8	0.30525(57)	0.84405(38)	0.92989(57)	1	0.485(29)	8d
	O9	0.19499(47)	0.84537(29)	0.02857(48)	1	0.485(29)	8d
	O10	0.09173(46)	0.84117(44)	0.91702(69)	1	0.485(29)	8d
	O11	0.11691(46)	0.84214(48)	0.74172(62)	1	0.485(29)	8d
	O12	0.23479(40)	0.84301(44)	0.74104(61)	1	0.485(29)	8d
	O13	0.30449(44)	0.94569(40)	0.81932(47)	1	0.485(29)	8d
	O14	0.07438(35)	0.95947(38)	0.81973(62)	1	0.485(29)	8d
	O15	0.41444(45)	0.12398(45)	0.61106(68)	1	0.485(29)	8d
	O16	0.40741(45)	0.99476(44)	0.58594(67)	1	0.485(29)	8d
	O17	0.40424(49)	0.86998(45)	0.57845(66)	1	0.485(29)	8d
	O18	0.18678(48)	0.13139(38)	0.61805(57)	1	0.485(29)	8d
	O19	0.20388(51)	0.00483(39)	0.59766(58)	1	0.485(29)	8d
	O20	0.20248(58)	0.87041(44)	0.58365(57)	1	0.485(29)	8d
	O21	0.99615(43)	0.04595(55)	0.79798(59)	1	0.485(29)	8d
	O22	0.99784(49)	0.84325(50)	0.78986(59)	1	0.485(29)	8d
	O23	0.42109(65)	0.75	0.64303(89)	1	0.485(29)	4c
	O24	0.19415(82)	0.75	0.64602(79)	1	0.485(29)	4c
	O25	0.28728(63)	0.75	0.05734(82)	1	0.485(29)	4c
	O26	0.10475(65)	0.75	0.04904(94)	1	0.485(29)	4c
	Si1	0.42461(21)	0.05561(29)	0.66431(32)	1	0.349(15)	8d
	Si2	0.28012(19)	0.06098(26)	1.03490(31)	1	0.349(15)	8d
	Si3	0.30918(28)	0.03154(18)	-0.18477(33)	1	0.349(15)	8d
	Si4	0.12069(21)	0.06237(26)	0.02645(33)	1	0.349(15)	8d
	Si5	0.06991(22)	0.02941(22)	0.80914(34)	1	0.349(15)	8d
	Si6	0.18959(25)	0.05902(24)	0.67523(30)	1	0.349(15)	8d
	Si7	0.42461(24)	0.82835(22)	0.67207(37)	1	0.349(15)	8d
	Si8	0.30603(27)	0.87188(21)	0.81568(30)	1	0.349(15)	8d

	Si9	0.27746(22)	0.82615(20)	0.03080(34)	1	0.349(15)	8d
	Si10	0.12241(25)	0.82555(23)	0.03259(37)	1	0.349(15)	8d
	Si11	0.07177(23)	0.86867(25)	0.82230(34)	1	0.349(15)	8d
	Si12	0.18659(26)	0.82604(19)	0.67961(35)	1	0.349(15)	8d
Methanol1	O	0.9339442	0.7401096	0.2329602	0.6480(54)	18.6(13)	4c
	H	0.9122571	0.720672	0.2979407	0.6480(54)	24.2(17)	4c
	C	0.8808886	0.7571188	0.1656136	0.6480(54)	10.3(11)	4c
	H	0.8372246	0.7462755	0.1972693	0.6480(54)	13.4(15)	4c
	H	0.8827359	0.8060736	0.1500888	0.6480(54)	13.4(15)	4c
	H	0.8858088	0.7308362	0.1026477	0.6480(54)	13.4(15)	4c
Methanol2	O	2.995267	3.673169	0.4701096	0.8064(52)	13.38(76)	4c
	H	2.946972	3.675955	0.4408439	0.8064(52)	17.40(99)	4c
	C	3.006154	3.605093	0.5015747	0.8064(52)	6.95(69)	4c
	H	2.965464	3.577884	0.4878146	0.8064(52)	9.03(90)	4c
	H	3.044645	3.585821	0.4642111	0.8064(52)	9.03(90)	4c
	H	3.015924	3.604231	0.5745803	0.8064(52)	9.03(90)	4c
Methanol3	O	1.162034	0.7518436	0.3643717	0.4380(63)	27.3(23)	4c
	H	1.195826	0.7830717	0.3270498	0.4380(63)	35.5(29)	4c
	C	1.096669	0.7670871	0.3271409	0.4380(63)	20.0(28)	4c
	H	1.099835	0.8031626	0.2756941	0.4380(63)	26.0(36)	4c
	H	1.076834	0.7260087	0.2966106	0.4380(63)	26.0(36)	4c
	H	1.067881	0.7826907	0.3832265	0.4380(63)	26.0(36)	4c

Table A6.4. Atomic parameters of H-ZSM-5 with flowing stream of methanol vapour, measured at 150 °C.

Species	Atom	*x*	*y*	*z*	SOF	B_{eq} (Å^2)	Wychoff
Zeolite framework	O1	0.37809(42)	0.05650(55)	0.76019(50)	1.1663(19)	2.059(23)	8d
	O2	0.30360(46)	0.05760(47)	0.92397(50)	1.1663(19)	2.059(23)	8d
	O3	0.20231(37)	0.06257(34)	0.02352(37)	1.1663(19)	2.059(23)	8d
	O4	0.09562(35)	0.06083(49)	0.91265(55)	1.1663(19)	2.059(23)	8d
	O5	0.11555(40)	0.05398(55)	0.73103(52)	1.1663(19)	2.059(23)	8d
	O6	0.24815(37)	0.05490(65)	0.75371(49)	1.1663(19)	2.059(23)	8d
	O7	0.37489(49)	0.85407(45)	0.76365(58)	1.1663(19)	2.059(23)	8d
	O8	0.30830(49)	0.84349(34)	0.93036(52)	1.1663(19)	2.059(23)	8d
	O9	0.19586(43)	0.84817(26)	0.03138(42)	1.1663(19)	2.059(23)	8d
	O10	0.08770(41)	0.83692(40)	0.91849(64)	1.1663(19)	2.059(23)	8d
	O11	0.12320(47)	0.83950(45)	0.73401(55)	1.1663(19)	2.059(23)	8d
	O12	0.24315(46)	0.84017(45)	0.76210(59)	1.1663(19)	2.059(23)	8d
	O13	0.30000(37)	0.94869(41)	0.82675(42)	1.1663(19)	2.059(23)	8d
	O14	0.07306(29)	0.95265(44)	0.81584(48)	1.1663(19)	2.059(23)	8d
	O15	0.41535(40)	0.12719(42)	0.61356(62)	1.1663(19)	2.059(23)	8d
	O16	0.40946(42)	1.00137(44)	0.59138(62)	1.1663(19)	2.059(23)	8d
	O17	0.40260(44)	0.86848(43)	0.57957(63)	1.1663(19)	2.059(23)	8d
	O18	0.18515(41)	0.13165(37)	0.61607(51)	1.1663(19)	2.059(23)	8d
	O19	0.20383(48)	0.00117(38)	0.60071(53)	1.1663(19)	2.059(23)	8d
	O20	0.20309(51)	0.86968(40)	0.58293(52)	1.1663(19)	2.059(23)	8d
	O21	0.99538(40)	0.04566(49)	0.79881(52)	1.1663(19)	2.059(23)	8d
	O22	0.99793(47)	0.84443(48)	0.78886(53)	1.1663(19)	2.059(23)	8d
	O23	0.41578(58)	0.75	0.65330(79)	1.1663(19)	2.059(23)	4c
	O24	0.19547(74)	0.75	0.64707(68)	1.1663(19)	2.059(23)	4c
	O25	0.28618(56)	0.75	0.06411(74)	1.1663(19)	2.059(23)	4c
	O26	0.10382(58)	0.75	0.05223(84)	1.1663(19)	2.059(23)	4c
	Si1	0.42295(20)	0.05603(29)	0.66607(31)	1.1179(13)	1.030(12)	8d
	Si2	0.27908(18)	0.06142(24)	1.03525(31)	1.1179(13)	1.030(12)	8d
	Si3	0.30859(26)	0.03113(17)	-0.18494(30)	1.1179(13)	1.030(12)	8d
	Si4	0.11941(19)	0.06142(25)	0.03086(32)	1.1179(13)	1.030(12)	8d
	Si5	0.06961(21)	0.02879(20)	0.81335(33)	1.1179(13)	1.030(12)	8d
	Si6	0.18952(25)	0.05851(23)	0.67789(29)	1.1179(13)	1.030(12)	8d
	Si7	0.42453(22)	0.82813(20)	0.67316(37)	1.1179(13)	1.030(12)	8d
	Si8	0.30927(25)	0.87225(20)	0.81861(28)	1.1179(13)	1.030(12)	8d

	Si9	0.27652(20)	0.82679(19)	0.03404(32)	1.1179(13)	1.030(12)	8d
	Si10	0.12367(22)	0.82524(21)	0.03081(36)	1.1179(13)	1.030(12)	8d
	Si11	0.07132(22)	0.86924(24)	0.82165(34)	1.1179(13)	1.030(12)	8d
	Si12	0.18961(27)	0.82690(17)	0.68013(34)	1.1179(13)	1.030(12)	8d
Methanol1	O	0.911176	0.749888	0.238448	0.5982(71)	23.2(14)	4c
	H	0.903615	0.797525	0.269614	0.5982(71)	30.1(18)	4c
	C	0.883975	0.750903	0.13928	0.5982(71)	25.3(16)	4c
	H	0.864937	0.79619	0.125162	0.5982(71)	32.9(20)	4c
	H	0.919879	0.740862	0.090033	0.5982(71)	32.9(20)	4c
	H	0.848191	0.716363	0.133681	0.5982(71)	32.9(20)	4c
Methanol2	O	2.996748	3.669088	0.480709	0.8469(70)	20.00(97)	4c
	H	2.946196	3.680901	0.488549	0.8469(70)	26.0(13)	4c
	C	3.004238	3.598761	0.501801	0.8469(70)	19.0(12)	4c
	H	2.959935	3.579063	0.518424	0.8469(70)	24.7(15)	4c
	H	3.02296	3.57553	0.44209	0.8469(70)	24.7(15)	4c
	H	3.035028	3.592782	0.559558	0.8469(70)	24.7(15)	4c
Methanol3	O	1.138352	0.771785	0.38031	0.5672(76)	30.0(25)	4c
	H	1.187723	0.783547	0.362159	0.5672(76)	39.0(32)	4c
	C	1.096192	0.805301	0.309445	0.5672(76)	20.0(22)	4c
	H	1.12419	0.831061	0.261305	0.5672(76)	26.0(29)	4c
	H	1.069231	0.771383	0.272436	0.5672(76)	26.0(29)	4c
	H	1.065836	0.836769	0.345311	0.5672(76)	26.0(29)	4c

Table A6.5. Atomic parameters of H-ZSM-5 with a flowing stream of methanol vapour, measured at 200 °C.

Species	Atom	*x*	*y*	*z*	SOF	B_{eq} (Å^2)	Wychoff
Zeolite framework	O1	0.37759(42)	0.05759(52)	0.76091(52)	1.1721(19)	2.329(24)	8d
	O2	0.30521(47)	0.05773(47)	0.92601(52)	1.1721(19)	2.329(24)	8d
	O3	0.20153(39)	0.06329(34)	0.02361(37)	1.1721(19)	2.329(24)	8d
	O4	0.09566(35)	0.05978(51)	0.91305(56)	1.1721(19)	2.329(24)	8d
	O5	0.11570(41)	0.05558(53)	0.73171(53)	1.1721(19)	2.329(24)	8d
	O6	0.24763(39)	0.05035(59)	0.75303(51)	1.1721(19)	2.329(24)	8d
	O7	0.37647(47)	0.85432(45)	0.75870(59)	1.1721(19)	2.329(24)	8d
	O8	0.30854(51)	0.84446(35)	0.92920(53)	1.1721(19)	2.329(24)	8d
	O9	0.19550(45)	0.84835(27)	0.03370(43)	1.1721(19)	2.329(24)	8d
	O10	0.08710(42)	0.83721(40)	0.92049(66)	1.1721(19)	2.329(24)	8d
	O11	0.12181(48)	0.84175(45)	0.73412(57)	1.1721(19)	2.329(24)	8d
	O12	0.24538(45)	0.83538(41)	0.76353(57)	1.1721(19)	2.329(24)	8d
	O13	0.30169(39)	0.94863(42)	0.82538(43)	1.1721(19)	2.329(24)	8d
	O14	0.07389(29)	0.95273(44)	0.81711(50)	1.1721(19)	2.329(24)	8d
	O15	0.41394(42)	0.12898(41)	0.61465(63)	1.1721(19)	2.329(24)	8d
	O16	0.41173(42)	1.00440(42)	0.58648(62)	1.1721(19)	2.329(24)	8d
	O17	0.40335(44)	0.86879(44)	0.58016(67)	1.1721(19)	2.329(24)	8d
	O18	0.18665(46)	0.12979(38)	0.61288(51)	1.1721(19)	2.329(24)	8d
	O19	0.20581(44)	-0.00276(39)	0.60608(53)	1.1721(19)	2.329(24)	8d
	O20	0.20288(49)	0.86813(40)	0.58263(52)	1.1721(19)	2.329(24)	8d
	O21	0.99654(42)	0.04810(52)	0.79806(52)	1.1721(19)	2.329(24)	8d
	O22	0.99741(48)	0.84704(49)	0.79095(55)	1.1721(19)	2.329(24)	8d
	O23	0.41504(58)	0.75	0.65080(79)	1.1721(19)	2.329(24)	4c
	O24	0.19145(72)	0.75	0.64979(68)	1.1721(19)	2.329(24)	4c
	O25	0.28539(55)	0.75	0.06019(79)	1.1721(19)	2.329(24)	4c
	O26	0.10328(59)	0.75	0.05735(90)	1.1721(19)	2.329(24)	4c
	Si1	0.42311(20)	0.05629(29)	0.66942(33)	1.1226(13)	1.165(12)	8d
	Si2	0.27892(18)	0.06082(25)	1.03613(31)	1.1226(13)	1.165(12)	8d
	Si3	0.30960(27)	0.03088(17)	-0.18376(32)	1.1226(13)	1.165(12)	8d
	Si4	0.11922(19)	0.06305(24)	0.03187(32)	1.1226(13)	1.165(12)	8d
	Si5	0.07059(22)	0.02857(20)	0.81446(35)	1.1226(13)	1.165(12)	8d
	Si6	0.18998(26)	0.05879(24)	0.67601(29)	1.1226(13)	1.165(12)	8d
	Si7	0.42491(23)	0.82707(20)	0.67460(39)	1.1226(13)	1.165(12)	8d
	Si8	0.30972(25)	0.87218(21)	0.81859(30)	1.1226(13)	1.165(12)	8d

	Si9	0.27688(20)	0.82630(19)	0.03275(33)	1.1226(13)	1.165(12)	8d
	Si10	0.12326(22)	0.82567(21)	0.03020(36)	1.1226(13)	1.165(12)	8d
	Si11	0.07140(22)	0.86913(25)	0.82194(35)	1.1226(13)	1.165(12)	8d
	Si12	0.18944(28)	0.82698(18)	0.68281(34)	1.1226(13)	1.165(12)	8d
Methanol1	O	0.90918	0.728856	0.229734	0.5818(76)	26.7(22)	4c
	H	0.885176	0.76328	0.276622	0.5818(76)	34.7(29)	4c
	C	0.880241	0.73534	0.132165	0.5818(76)	35.0(32)	4c
	H	0.844964	0.770586	0.133546	0.5818(76)	45.4(41)	4c
	H	0.91543	0.748338	0.083307	0.5818(76)	45.4(41)	4c
	H	0.860203	0.691606	0.111791	0.5818(76)	45.4(41)	4c
Methanol2	O	2.993593	3.669263	0.486112	0.6935(85)	30.0(18)	4c
	H	2.943159	3.675215	0.468314	0.6935(85)	39.0(23)	4c
	C	3.004307	3.599474	0.507922	0.6935(85)	18.6(15)	4c
	H	2.961528	3.574494	0.500726	0.6935(85)	24.2(19)	4c
	H	3.037808	3.580724	0.460547	0.6935(85)	24.2(19)	4c
	H	3.021037	3.59467	0.577659	0.6935(85)	24.2(19)	4c
Methanol3	O	1.138566	0.773011	0.380188	0.4701(89)	30.0(28)	4c
	H	1.185724	0.794933	0.387384	0.4701(89)	39.0(37)	4c
	C	1.098853	0.816905	0.319414	0.4701(89)	30.0(36)	4c
	H	1.125841	0.856775	0.299556	0.4701(89)	39.0(47)	4c
	H	1.083975	0.792445	0.258389	0.4701(89)	39.0(47)	4c
	H	1.059125	0.832019	0.358033	0.4701(89)	39.0(47)	4c

Table A6.6. Atomic parameters of H-ZSM-5 with a flowing stream of methanol vapour, measured at 250 °C.

Species	Atom	*x*	*y*	*z*	SOF	B_{eq} (Å^2)	Wychoff
Zeolite framework	O1	0.37165(47)	0.05987(60)	0.75690(57)	1.1870(22)	2.137(30)	8d
	O2	0.30656(49)	0.05571(55)	0.91919(58)	1.1870(22)	2.137(30)	8d
	O3	0.20138(43)	0.06214(41)	0.02126(42)	1.1870(22)	2.137(30)	8d
	O4	0.09914(38)	0.05766(58)	0.91070(65)	1.1870(22)	2.137(30)	8d
	O5	0.11518(45)	0.05878(57)	0.72713(59)	1.1870(22)	2.137(30)	8d
	O6	0.24523(42)	0.04972(61)	0.74734(59)	1.1870(22)	2.137(30)	8d
	O7	0.37365(50)	0.85684(49)	0.75362(62)	1.1870(22)	2.137(30)	8d
	O8	0.31002(54)	0.84139(41)	0.92816(60)	1.1870(22)	2.137(30)	8d
	O9	0.19701(49)	0.84967(30)	0.03169(47)	1.1870(22)	2.137(30)	8d
	O10	0.08982(48)	0.83839(46)	0.91787(74)	1.1870(22)	2.137(30)	8d
	O11	0.11993(50)	0.84351(49)	0.73445(64)	1.1870(22)	2.137(30)	8d
	O12	0.24132(47)	0.83945(48)	0.75367(64)	1.1870(22)	2.137(30)	8d
	O13	0.30124(42)	0.94540(48)	0.81307(48)	1.1870(22)	2.137(30)	8d
	O14	0.07389(34)	0.95555(47)	0.81676(58)	1.1870(22)	2.137(30)	8d
	O15	0.41500(49)	0.12541(45)	0.61025(72)	1.1870(22)	2.137(30)	8d
	O16	0.41597(48)	1.00313(47)	0.58287(71)	1.1870(22)	2.137(30)	8d
	O17	0.40405(49)	0.86669(50)	0.57275(77)	1.1870(22)	2.137(30)	8d
	O18	0.18342(46)	0.13136(40)	0.60607(60)	1.1870(22)	2.137(30)	8d
	O19	0.20643(49)	0.00068(44)	0.59724(63)	1.1870(22)	2.137(30)	8d
	O20	0.20350(52)	0.86906(46)	0.57847(61)	1.1870(22)	2.137(30)	8d
	O21	0.99493(43)	0.04789(55)	0.79957(58)	1.1870(22)	2.137(30)	8d
	O22	0.99774(50)	0.84554(49)	0.79358(61)	1.1870(22)	2.137(30)	8d
	O23	0.41429(62)	0.75	0.64317(90)	1.1870(22)	2.137(30)	4c
	O24	0.19063(75)	0.75	0.64685(78)	1.1870(22)	2.137(30)	4c
	O25	0.28470(61)	0.75	0.05348(87)	1.1870(22)	2.137(30)	4c
	O26	0.09642(67)	0.75	0.0519(10)	1.1870(22)	2.137(30)	4c
	Si1	0.42206(22)	0.05672(32)	0.66693(38)	1.1303(15)	1.068(15)	8d
	Si2	0.27894(20)	0.06105(28)	1.03064(34)	1.1303(15)	1.068(15)	8d
	Si3	0.30815(29)	0.03049(20)	-0.19070(36)	1.1303(15)	1.068(15)	8d
	Si4	0.12042(21)	0.06087(29)	0.02892(36)	1.1303(15)	1.068(15)	8d
	Si5	0.06925(23)	0.02905(23)	0.81162(39)	1.1303(15)	1.068(15)	8d
	Si6	0.18652(25)	0.05901(27)	0.67183(35)	1.1303(15)	1.068(15)	8d
	Si7	0.42533(24)	0.82676(23)	0.67111(44)	1.1303(15)	1.068(15)	8d
	Si8	0.30758(28)	0.87157(23)	0.81353(33)	1.1303(15)	1.068(15)	8d

	Si9	0.27710(24)	0.82696(21)	0.02947(35)	1.1303(15)	1.068(15)	8d
	Si10	0.12675(24)	0.82375(24)	0.02739(38)	1.1303(15)	1.068(15)	8d
	Si11	0.07055(24)	0.86875(28)	0.81917(40)	1.1303(15)	1.068(15)	8d
	Si12	0.18794(29)	0.82768(20)	0.67849(40)	1.1303(15)	1.068(15)	8d
Methanol1	O	0.908583	0.734197	0.235559	0.5190(83)	18.9(20)	4c
	H	0.959165	0.743617	0.222344	0.5190(83)	24.6(26)	4c
	C	0.874224	0.741044	0.142099	0.5190(83)	36.4(38)	4c
	H	0.906782	0.752912	0.088704	0.5190(83)	47.4(50)	4c
	H	0.851965	0.6978	0.124953	0.5190(83)	47.4(50)	4c
	H	0.840031	0.777182	0.147645	0.5190(83)	47.4(50)	4c
Methanol2	O	3.005474	3.667797	0.480527	0.6352(81)	18.8(15)	4c
	H	2.960706	3.688474	0.50638	0.6352(81)	24.5(19)	4c
	C	3.008068	3.5994	0.514118	0.6352(81)	16.8(17)	4c
	H	2.967063	3.588892	0.553174	0.6352(81)	21.9(22)	4c
	H	3.010868	3.568839	0.455328	0.6352(81)	21.9(22)	4c
	H	3.048076	3.592905	0.557213	0.6352(81)	21.9(22)	4c
Methanol3	O	1.128572	0.795968	0.395691	0.4183(96)	26.5(31)	4c
	H	1.17704	0.814904	0.402599	0.4183(96)	34.5(41)	4c
	C	1.10722	0.807858	0.294942	0.4183(96)	20.7(33)	4c
	H	1.143487	0.830892	0.257296	0.4183(96)	26.9(44)	4c
	H	1.096694	0.7642	0.262129	0.4183(96)	26.9(44)	4c
	H	1.066631	0.83675	0.295338	0.4183(96)	26.9(44)	4c

Table A6.7. Atomic parameters of H-ZSM-5 with 10 hours of flowing stream of methanol vapour, measured at 200 °C.

Species	Atom	*x*	*y*	*z*	SOF	B_{eq} (Å^2)	Wychoff
Zeolite framework	O1	0.37049(51)	0.05615(67)	0.75474(71)	1	2.107(28)	8d
	O2	0.31405(49)	0.05594(55)	0.91931(67)	1	2.107(28)	8d
	O3	0.20186(48)	0.06015(48)	0.01357(49)	1	2.107(28)	8d
	O4	0.10043(40)	0.06034(58)	0.91002(73)	1	2.107(28)	8d
	O5	0.12040(55)	0.05081(67)	0.73374(67)	1	2.107(28)	8d
	O6	0.24158(45)	0.05668(69)	0.75365(67)	1	2.107(28)	8d
	O7	0.37601(53)	0.83804(50)	0.75805(74)	1	2.107(28)	8d
	O8	0.30985(60)	0.84422(45)	0.92572(67)	1	2.107(28)	8d
	O9	0.20197(56)	0.84674(37)	0.03723(56)	1	2.107(28)	8d
	O10	0.08822(50)	0.83937(51)	0.92007(91)	1	2.107(28)	8d
	O11	0.12081(55)	0.84913(52)	0.74288(78)	1	2.107(28)	8d
	O12	0.24257(52)	0.85500(57)	0.74807(79)	1	2.107(28)	8d
	O13	0.31860(42)	0.95201(54)	0.81473(52)	1	2.107(28)	8d
	O14	0.07955(39)	0.95102(63)	0.82234(63)	1	2.107(28)	8d
	O15	0.41745(49)	0.12262(56)	0.60355(84)	1	2.107(28)	8d
	O16	0.41434(54)	1.00241(56)	0.57611(80)	1	2.107(28)	8d
	O17	0.40626(53)	0.86823(51)	0.56053(76)	1	2.107(28)	8d
	O18	0.18265(51)	0.13303(47)	0.61022(73)	1	2.107(28)	8d
	O19	0.20864(49)	-0.00135(51)	0.59632(70)	1	2.107(28)	8d
	O20	0.20218(58)	0.87116(50)	0.58283(69)	1	2.107(28)	8d
	O21	0.99626(50)	0.05073(67)	0.80074(67)	1	2.107(28)	8d
	O22	0.99412(56)	0.84799(54)	0.79101(74)	1	2.107(28)	8d
	O23	0.41324(70)	0.75	0.65036(97)	1	2.107(28)	4c
	O24	0.19483(82)	0.75	0.65115(88)	1	2.107(28)	4c
	O25	0.28738(69)	0.75	0.05875(95)	1	2.107(28)	4c
	O26	0.11531(66)	0.75	0.0716(11)	1	2.107(28)	4c
	Si1	0.42231(25)	0.05655(35)	0.66659(37)	1	1.053(14)	8d
	Si2	0.30993(33)	0.02838(22)	0.80829(38)	1	1.053(14)	8d
	Si3	0.27861(23)	0.06144(30)	0.03229(37)	1	1.053(14)	8d
	Si4	0.12086(25)	0.06235(31)	0.02799(38)	1	1.053(14)	8d
	Si5	0.07104(27)	0.02786(26)	0.81425(43)	1	1.053(14)	8d
	Si6	0.18707(27)	0.05998(28)	0.66935(35)	1	1.053(14)	8d
	Si7	0.42286(27)	0.83002(26)	0.66442(39)	1	1.053(14)	8d
	Si8	0.30535(31)	0.86966(26)	0.81332(36)	1	1.053(14)	8d

	Si9	0.27465(26)	0.82589(25)	0.02909(39)	1	1.053(14)	8d
	Si10	0.12373(30)	0.82728(29)	0.03107(42)	1	1.053(14)	8d
	Si11	0.07041(26)	0.87024(29)	0.81824(43)	1	1.053(14)	8d
	Si12	0.18414(28)	0.82760(23)	0.68656(36)	1	1.053(14)	8d
Carbon species	Ca	-0.0206(13)	0.71486(96)	0.5362(21)	0.693(23)	8	4c
	Cb	0.2256(15)	0.28280(78)	0.9119(24)	0.437(11)	8	4c
	Cc	0.4351(10)	0.2174(33)	0.5522(47)	0.276(16)	8	4c
	Cd	0.0165(17)	0.4350(20)	0.4846(27)	0.441(12)	8	4c
	Ce	0.4043(16)	0.2145(11)	0.8594(22)	0.630(19)	8	4c
	Ch	0.5172(22)	0.2902(20)	0.8113(51)	0.422(20)	8	4c
	Cj	0.0288(10)	0.64449(69)	0.4350(18)	0.929(17)	8	4c
	Cm	0.0439(12)	0.28179(63)	0.7946(23)	0.677(23)	8	4c
	Cn	0.3030(34)	0.2175(11)	0.7834(30)	0.294(12)	8	4c
	Cp	0.0317(30)	0.71512(86)	0.4498(48)	0.390(24)	8	4c
Framework carbon	Cl	0.1201(22)	0.1431(22)	0.7305(27)	0.434(17)	8	4c

Table A6.8. Atomic parameters of H-ZSM-5 with 18 hours of flowing methanol vapour, measured at 200 °C.

Species	Atom	x	y	z	SOF	B_{eq} (Å^2)	Wychoff
Zeolite framework	O1	0.37107(38)	0.05963(50)	0.73621(52)	1	2.001(22)	8d
	O2	0.30731(41)	0.05928(43)	0.91241(54)	1	2.001(22)	8d
	O3	0.19950(40)	0.05293(43)	0.02014(43)	1	2.001(22)	8d
	O4	0.10328(35)	0.06375(46)	0.90275(58)	1	2.001(22)	8d
	O5	0.11205(39)	0.05380(52)	0.71555(54)	1	2.001(22)	8d
	O6	0.24002(35)	0.05478(54)	0.74877(49)	1	2.001(22)	8d
	O7	0.37151(41)	0.83868(38)	0.75636(52)	1	2.001(22)	8d
	O8	0.30914(44)	0.84499(34)	0.91918(53)	1	2.001(22)	8d
	O9	0.19523(46)	0.84297(32)	0.03285(45)	1	2.001(22)	8d
	O10	0.09778(41)	0.83661(40)	0.91250(65)	1	2.001(22)	8d
	O11	0.11865(41)	0.84696(39)	0.73267(59)	1	2.001(22)	8d
	O12	0.23585(37)	0.85413(42)	0.73557(58)	1	2.001(22)	8d
	O13	0.29975(37)	0.94951(43)	0.80460(41)	1	2.001(22)	8d
	O14	0.07192(31)	0.95193(48)	0.81550(51)	1	2.001(22)	8d
	O15	0.42271(37)	0.12673(40)	0.59558(64)	1	2.001(22)	8d
	O16	0.40826(42)	1.00565(42)	0.56708(67)	1	2.001(22)	8d
	O17	0.40476(40)	0.86775(43)	0.56306(67)	1	2.001(22)	8d
	O18	0.17881(37)	0.13225(39)	0.60243(55)	1	2.001(22)	8d
	O19	0.19982(51)	0.00066(38)	0.58106(54)	1	2.001(22)	8d
	O20	0.19360(43)	0.86933(39)	0.57341(52)	1	2.001(22)	8d
	O21	0.99611(37)	0.05120(52)	0.79936(54)	1	2.001(22)	8d
	O22	0.99486(41)	0.85278(41)	0.79066(56)	1	2.001(22)	8d
	O23	0.41159(53)	0.75	0.63470(82)	1	2.001(22)	4c
	O24	0.19054(69)	0.75	0.63538(74)	1	2.001(22)	4c
	O25	0.28309(51)	0.75	0.05094(78)	1	2.001(22)	4c
	O26	0.10242(60)	0.75	0.05074(95)	1	2.001(22)	4c
	Si1	0.42146(20)	0.05622(28)	0.65737(30)	1	1.001(11)	8d
	Si2	0.30559(24)	0.02825(17)	0.79784(30)	1	1.001(11)	8d
	Si3	0.27987(18)	0.06215(23)	0.02355(29)	1	1.001(11)	8d
	Si4	0.12109(19)	0.06284(24)	0.02153(32)	1	1.001(11)	8d
	Si5	0.07054(20)	0.02765(19)	0.80964(35)	1	1.001(11)	8d
	Si6	0.18179(19)	0.06093(23)	0.66200(29)	1	1.001(11)	8d
	Si7	0.42359(21)	0.83033(21)	0.66066(32)	1	1.001(11)	8d
	Si8	0.30123(24)	0.86992(19)	0.80471(27)	1	1.001(11)	8d

	Si9	0.27598(21)	0.82731(18)	0.02265(30)	1	1.001(11)	8d
	Si10	0.12265(22)	0.82448(20)	0.02147(33)	1	1.001(11)	8d
	Si11	0.06761(19)	0.86973(22)	0.80988(33)	1	1.001(11)	8d
	Si12	0.18199(21)	0.82866(19)	0.67397(28)	1	1.001(11)	8d
Carbon species	Ca	-0.01892(59)	0.71354(57)	0.52404(83)	1.072(12)	8	4c
	Cb	0.2245(16)	0.28573(94)	0.9140(27)	0.346(12)	8	4c
	Cc	0.51511(81)	0.21479(74)	0.71532(74)	0.499(16)	8	4c
	Cd	0.01264(93)	0.4481(11)	0.4843(14)	0.7059(92)	8	4c
	Ce	0.40289(57)	0.21448(65)	0.86223(86)	0.783(14)	8	4c
	Ch	0.5564(14)	0.28594(96)	0.7973(24)	0.465(13)	8	4c
	Cj	0.04068(68)	0.63870(48)	0.4302(13)	0.964(14)	8	4c
	Cm	0.0870(10)	0.28395(50)	0.8956(14)	0.652(10)	8	4c
	Cn	0.26432(92)	0.21722(46)	0.7910(15)	0.605(12)	8	4c
	Cp	0.04738(61)	0.71422(51)	0.4346(19)	0.651(17)	8	4c
Framework carbon	Cl	0.1295(16)	0.1313(17)	0.7202(21)	0.466(14)	8	4c

Table A6.9. Atomic parameters of H-ZSM-5 with 24 hours of flowing methanol vapour, measured at 200 °C.

Species	Atom	*x*	*y*	*z*	SOF	B_{eq} (Å^2)	Wychoff
Zeolite framework	O1	0.37079(71)	0.05831(89)	0.73340(96)	1	1.572(37)	8d
	O2	0.30317(73)	0.06081(66)	0.90845(98)	1	1.572(37)	8d
	O3	0.20091(71)	0.06018(68)	0.03372(80)	1	1.572(37)	8d
	O4	0.10361(65)	0.05192(85)	0.9029(11)	1	1.572(37)	8d
	O5	0.10718(66)	0.05158(85)	0.7059(10)	1	1.572(37)	8d
	O6	0.24132(71)	0.0548(12)	0.73862(99)	1	1.572(37)	8d
	O7	0.37718(86)	0.84417(71)	0.75577(94)	1	1.572(37)	8d
	O8	0.31404(69)	0.84712(57)	0.92224(91)	1	1.572(37)	8d
	O9	0.19941(80)	0.84614(52)	0.03381(87)	1	1.572(37)	8d
	O10	0.10019(75)	0.83019(66)	0.9188(11)	1	1.572(37)	8d
	O11	0.12218(75)	0.84380(71)	0.73558(95)	1	1.572(37)	8d
	O12	0.23606(70)	0.85305(77)	0.72606(98)	1	1.572(37)	8d
	O13	0.29419(62)	0.94539(72)	0.81002(76)	1	1.572(37)	8d
	O14	0.06859(59)	0.95642(73)	0.81400(97)	1	1.572(37)	8d
	O15	0.41627(63)	0.12942(73)	0.5953(11)	1	1.572(37)	8d
	O16	0.42007(63)	1.01293(68)	0.5545(12)	1	1.572(37)	8d
	O17	0.40053(72)	0.87020(78)	0.5574(11)	1	1.572(37)	8d
	O18	0.17242(64)	0.13048(71)	0.60262(90)	1	1.572(37)	8d
	O19	0.20707(74)	0.00121(63)	0.5867(10)	1	1.572(37)	8d
	O20	0.20497(75)	0.86398(67)	0.56612(94)	1	1.572(37)	8d
	O21	0.99374(64)	0.0513(11)	0.8020(10)	1	1.572(37)	8d
	O22	0.99398(74)	0.84792(81)	0.7896(11)	1	1.572(37)	8d
	O23	0.41761(96)	0.75	0.6326(15)	1	1.572(37)	4c
	O24	0.1886(12)	0.75	0.6228(14)	1	1.572(37)	4c
	O25	0.3140(11)	0.75	0.0597(13)	1	1.572(37)	4c
	O26	0.1014(10)	0.75	0.0434(17)	1	1.572(37)	4c
	Si1	0.42367(36)	0.05666(48)	0.65519(56)	1	0.786(19)	8d
	Si2	0.30421(42)	0.03179(30)	0.79558(54)	1	0.786(19)	8d
	Si3	0.27932(32)	0.06154(43)	0.01952(53)	1	0.786(19)	8d
	Si4	0.12288(35)	0.06437(41)	0.02021(59)	1	0.786(19)	8d
	Si5	0.06610(37)	0.02672(34)	0.80595(61)	1	0.786(19)	8d
	Si6	0.17862(32)	0.05855(42)	0.66436(54)	1	0.786(19)	8d
	Si7	0.42421(37)	0.82984(36)	0.65954(60)	1	0.786(19)	8d
	Si8	0.30095(43)	0.87016(34)	0.80111(50)	1	0.786(19)	8d

	Si9	0.27546(36)	0.82643(30)	0.01978(53)	1	0.786(19)	8d
	Si10	0.12649(39)	0.82528(38)	0.01991(57)	1	0.786(19)	8d
	Si11	0.06800(37)	0.86743(40)	0.80947(58)	1	0.786(19)	8d
	Si12	0.18258(38)	0.82585(32)	0.66911(50)	1	0.786(19)	8d
Carbon species	Ca	-0.0378(11)	0.6566(11)	0.5371(15)	1.294(32)	8	4c
	Cb	0.1739(25)	0.28110(99)	0.9141(27)	0.599(24)	8	4c
	Cc	0.5076(25)	0.22078(82)	0.6645(33)	0.624(25)	8	4c
	Cd	0.0089(25)	0.4586(14)	0.4898(39)	0.564(19)	8	4c
	Ce	0.4004(13)	0.21136(73)	0.8676(17)	1.126(25)	8	4c
	Ch	0.5681(18)	0.27981(85)	0.7783(29)	0.667(25)	8	4c
	Cj	0.04744(82)	0.6274(11)	0.4199(13)	1.490(27)	8	4c
	Cm	0.0927(17)	0.2764(17)	0.8589(25)	0.848(32)	8	4c
	Cn	0.2649(10)	0.21934(83)	0.7667(14)	1.039(23)	8	4c
	Cp	0.0127(14)	0.7040(12)	0.4588(20)	1.073(35)	8	4c
Framework carbon	Cl	0.1640(25)	0.0436(28)	0.7897(40)	0.505(25)	8	4c